REPUBLIC OF TURKEY

YILDIZ TECHNICAL UNIVERSITY GRADUATE SCHOOL OF SCIENCE AND ENGINEERING

SOLUTION PROCESSABLE INVERTED TYPE PEROVSKITE SOLAR CELLS

HAMED MOEINI ALISHAH

DOCTOR OF PHILOSOPHY THESIS

Department of Physics

Physics Program

Supervisor

Prof. Dr. Serap GÜNEŞ

November, 2021

REPUBLIC OF TURKEY

YILDIZ TECHNICAL UNIVERSITY

GRADUATE SCHOOL OF SCIENCE AND ENGINEERING

SOLUTION PROCESSABLE INVERTED TYPE PEROVSKITE SOLAR CELLS

A thesis submitted by Hamed MOEINI ALISHAH in partial fulfillment of the requirements for the degree of DOCTOR OF PHILOSOPHY is approved by the committee on 12.11.2021 in Department of Physics, Physics Program.

Prof. Dr. Serap GÜNEŞ Yıldız Technical University Supervisor

Approved By the Examining Committee

Prof. Dr. Serap GÜNEŞ, Supervisor	
Yildiz Technical University	
Prof. Dr. Nilgün YAVUZ, Member	
Istanbul Technical University	
Doç. Dr. Murat ÇALIŞKAN, Member	
Yildiz Technical University	
Prof. Dr. Fatih ONGÜL, Member	
,	
Ardahan University	
Prof. Dr. Serço Serkis YEŞİLKAYA, Member	
Yildiz Technical University	

I hereby declare that I have obtained the required legal permissions during data collection and exploitation procedures, that I have made the in-text citations and cited the references properly, that I haven't falsified and/or fabricated research data and results of the study and that I have abided by the principles of the scientific research and ethics during my Thesis Study under the title of Solution Processable Inverted Type Perovskite Solar Cells supervised by my supervisor, Prof. Dr. Serap GÜNEŞ. In the case of a discovery of false statement, I am to acknowledge any legal consequence.

Hamed MOEINI ALISHAH

Signature

I want to take this opportunity to express my most heartfelt thanks and a deep sense of gratitude to my supervisor, Prof. Dr. Serap Güneş for giving me the chance to study a Ph.D. degree under her supervision. It has been my great honor and privilege to learn and work with her. Her passion for research and immense knowledge has kept me motivated to conduct research in a scientific way and this will help me to succeed in my career. All this research could not have come true without her constant support, patient guidance, and valuable suggestions. I feel myself very fortunate to have a supervisor like her. I couldn't have dreamt of a better mentor for my graduate study.

Beside my supervisor, I would like to extend my appreciation to dear Dr. Fatma Pınar Gökdemir Choi for assisting me in the laboratory works and related research. My Ph.D. study would not be completed smoothly without her support and help. She is so smart and one of the best researchers I have ever known. Moreover, she is an excellent role model for the time management and perfect balancing of work and family.

A special thanks to Assoc. Prof. Dr. Fatih Ongül, Dr. Mehmet Kazici, and Dr. Sinem Bozar for their help. I have learned a lot about technical and experimental setups from them.

I would like to thank Prof. Dr. Nilgün Yavuz, Assoc. Prof. Dr. Murat Çalışkan, Assoc. Prof. Dr. Serço Serkis Yeşilkaya and Assoc. Prof. Dr. Fatih Ongül. They are so kind in becoming members of my thesis committee. The knowledge that they impacted me made the finalization of this manuscript possible.

Additionally, I would like to show my gratitude to my external collaborators and co-authors: Dr. Ugur Deneb Menda from Universidad NOVA de Lisboa and CEMOP, for her inspiration, and discussion on the BCP study; Assist. Prof. Dr. Furkan Kuruoğlu and Prof. Dr. Ayşe Erol from Istanbul University for their assistance on the Zn-doped PEDOT:PSS characterizations; Assist. Prof. Dr. Macide

Rodop Cantürk who always kept us hopeful to continue on the path with her good advice; Miss. Ceylan Doyranlı for synthesizing BTBT molecule that is employed in the published work; and Mr. Cihangir Kahveci for troubleshooting technical problems.

I would also like to thank Mr. Hasan Güneş the person who treated me like a member of his family with warm hospitality. Also, very thanks to all my friends, department faculties and stuffs for making my stay in Istanbul a great memory in my life.

Finally, I must express my profound gratitude to my parents and family members for their unfailing support and continuous encouragement throughout my years of study.

Last but not the least, I would like to thank my funding resources: Turk abroad and related communities (YTB), and FBA-2019-3583 NAP Project of Yildiz Technical University.

Hamed Moeini Alishah

TABLE OF CONTENTS

LIST OF SYMBOLS	IX
LIST OF ABBREVIATIONS	X
LIST OF FIGURES	XII
LIST OF TABLES	XVIII
ABSTRACT	XIX
ÖZET	XXI
1 INTRODUCTION	1
1.1 Literature Review	1
1.1.1 Background	1
1.1.2 Energy	2
1.1.3 Renewable Energy	2
1.1.4 Photovoltaics (PV)	3
1.1.5 PV Technologies	4
1.1.5.1 PV Technologies of the First Generation: Cryst Solar Cells	
1.1.5.2 Second-Generation PV Technologies: Thin-File	m Solar Cells 6
1.1.5.3 Third-Generation PV Technologies: High Efficand Novel PV Concepts	-
1.1.6 Perovskite Solar Cells	7
1.2 Objective of the Thesis	8
1.3 Hypothesis	10
2 DEROVSKITE SOLAR CELLS	11

2.1	His	tory and development	11
2.2	Pro	perties of perovskite	14
2.	2.1	Crystal structure of perovskites	14
2.2	2.2	Absorption coefficient, α	15
2.	2.3	Bandgap	16
2	2.4	Diffusion length	18
2.	2.5	Defect density	19
2.3	Wo	rking principle of PSCs	21
2.4	Adv	vantages of PSCs	22
2.5	Lin	nitation of PSCs	23
2.	5.1	Recombination of charge carriers	23
2	5.2	Hysteresis	24
2.	5.3	Device stability	25
2.	5.4	Toxicity	27
2.6	Dev	vice architectures	28
2.	6.1	Conventional n-i-p structure	29
2.	6.2	Inverted p-i-n structure	30
2.7	Fab	prication methods	30
2.	7.1	One-step solution method	31
2.	7.2	Two-Step solution method	32
2.	7.3	Vapor-assisted solution method	33
2.	7.4	Dual-source vapor method	33
2.8	Ele	ctron Transport Layer (ETL)	33
20	Нο	a Transport Layer (HTL)	25

	2.9.1	Organic hole transport materials	36
	2.9.2	Polymer hole transport materials	36
	2.9.3	Inorganic hole transport materials	37
2	.10	Device characterization of solar cells	38
	2.10.	1 Current-Voltage (I-V) measurement	38
	2.10.	2 Light I-V measurement	39
	2.10.	3 Dark I-V measurement	42
	2.10.	4 Quantum Efficiency	44
3 II	МРАС	T OF UV EXPOSURE OF ITO/PEDOT:PSS SUBSTRATES ON	
TH	E FUN	ICTIONALITY OF INVERTED-TYPE PSCS	48
3	.1 Ir	ntroduction	48
3	.2 E	xperimental	49
3	.3 R	esults and discussion	51
3	.4 C	onclusion	65
4 E	NHAN	NCEMENT OF FILL FACTOR OF P-I-N TYPE OF PEROVSKITE	
SO	LAR C	ELLS BY EMPLOYMENT OF ZN-DOPED PEDOT:PSS AS A H	
			67
4	.1 Ir	ntroduction	67
4	.2 E	xperimental	69
4	.3 R	esult and discussion	71
4	.4 C	onclusion	87
5 T	HE R	OLE OF BATHOCUPROINE CONCENTRATIO ON THE PV	
PEI	RFOR	MANCE OF NIO _x -BASED PSCS	88
5	.1 Ir	ntroduction	88
5	2 F	xperimental procedure	89

	5.2	.1	Materials	89
	5.2	.2	Device fabrication	89
5.	.3	Res	ult and discussion	90
5.	.4	Cor	nclusion	99
6 C	E A	ND	ZN CO-DOPED NIO _x -BASED HTLS FOR USING IN PSCS	100
6.	.1	Intr	oduction	. 100
6.	.2	Exp	perimental	. 102
	6.2	.1	Materials	. 102
	6.2	.2	Precursor solutions	. 102
	6.2	.3	Device fabrication	. 104
6.	.3	Res	ults and discussion	. 104
6.	.4	Cor	nclusion	. 118
7 R	ESU	JLT	S AND DISCUSSION	119
7.	.1	Cor	nclusions	. 119
7.	.2	Fut	ure work	. 120
REI	FER	ENC	CES	121
PUI	BLIC	CAT	IONS FROM THE THESIS	159

LIST OF SYMBOLS

 $E_g \hspace{1cm} Band \hspace{1cm} gap \hspace{1cm}$

ε₀ Dielectric constant of vacuum

e Electron

eV Electron volt

FF Fill Factor

HCl Hydrochloric acid

HNO₃ Nitric acid

 V_{OC} Open-circuit voltage

h Planck's constant

I_{SC} Short-circuit current

J_{SC} Short-circuit current density

Ag Silver

C Speed of light

H₂O Water

W Watt

LIST OF ABBREVIATIONS

AFM Atomic Force Microscopy

BCP Bathocuproine

CB Chlorobenzene

DI Deionized (water)

DMF Dimethylformamide

DSSC Dye Sensitized Solar Cell

EQE External Quantum Efficiency

ETL Electron Transport Layer

HF Hysteresis Factor

HOMO Highest Occupied Molecular Orbital

HTL Hole Transport Layer

IPA Isopropanol

ITO Indium Tin Oxide

J-V Current density-voltage

LUMO Lowest Unoccupied Molecular Orbital

MAI Methylammonium Iodide

NREL National Renewable Energy Laboratory

P3HT Poly(3-hexylthiophene-2,5-diyl)

PbI₂ Lead iodide

PCBM [6,6]-phenyl-C61-butyric acid methyl ester

PCE Power Conversion Efficiency

PEDOT:PSS Poly(3,4-ethylenedioxythiophene)-poly(styrenesulfonate)

PL Photoluminescence

PSC Polymer Solar Cells

rpm Revolutions per minute

SEM Scanning Electron Microscopy

 $Spiro-OMetad~2,2',7,7'-tetrakis-(N,N-di-p-methoxyphenylamine)\lambda,\lambda'-spirobifluorene$

UV-Vis Ultraviolet-visible

VB Valance Band

XRD X-ray Diffraction

 $\lambda \qquad \qquad Wavelength$

LIST OF FIGURES

Figure 1.1 Solar panels cost and worldwide deployment in the last 40 years
[10]
Figure 1.2 NREL's efficiency chart is reprinted with permission by the National
Renewable Energy Laboratory [13]
Figure 2.1 Development of PCE of PSCs in comparison with other solar
technologies [26]
Figure 2.2 Structure of Perovskite [41]
Figure 2.3 Absorption coefficient of various PV materials at various wavelength
[44]
Figure 2.4 To evaluate the bandgap of perovskite, (Quantum efficiency \times
Energy) ² vs Energy was achieved. It points to a bandgap of 1.58 eV [46] 16
Figure 2.5 Absorption coefficient of mixed-halide perovskite with varied Iodine
and Bromine relative compositions [47]
Figure 2.6 Diffusion length of carrier in perovskite at various temperatures
[50]
Figure 2.7 PSC with sub-gap quantum efficiency. Urbach energy is estimated to
be around 15 meV [52]
Figure 2.8 Two defect levels can be seen in an Arrhenius plot utilizing
Capacitance-Frequency-Temperature (CFT) measurements: the activation energy
of shallower traps is about 0.24 eV and the activation energy of deeper traps is
about 0.66 eV [46]
Figure 2.9 Capacitance vs Frequency profile of PSC (a) Density of states (t-
DOS) distribution within the perovskite bandgap (b) t-DOS of the midgap state
fitted by Gaussian distribution [46]
Figure 2.10 A conventional p-i-n (inverted) perovskite solar cell's energy band
diagram. The Basic functioning principle is as follow: 1. Light absorption and

production of exciton, 2. Separation of charge carrier, 3. Extraction of charge
carrier [53]
Figure 2.11 Hysteresis phenomenon of a solar cell. Forward and reverse
voltage sweeps have different current-voltage properties [80]
Figure 2.12 Effect of decomposition when the film exposed to air for seven
days. Black perovskite films become yellow [84]
Figure 2.13 (a) n-i-p mesoscopic, (b) n-i-p planar, (c) p-i-n planar, and (d) p-i-n mesoscopic architectures of PSCs [34]
Figure 2.14 Representative manufacturing approaches for perovskite thin layers: (a) one-step solution method; (b) two-step solution method; (c) vapor-assisted solution method; (d) dual-source vapor method [34]
Figure 2.15 Materials for ETL in PSCs showing conduct band minimum/LUMO levels [112]
Figure 2.16 Representative HTMs utilized in PSCs, evolving the most efficient perovskite light absorbers, are shown in schematic energy diagram [113] 35
Figure 2.17 Stability of perovskite materials with various hole transport layers [116]
Figure 2.18 Equivalent circuit of solar cells with double-diode model under illumination [118]
Figure 2.19 Light IV curve and output power vs. voltage curve of a solar cell [119]
Figure 2.20 A comparison of IV curves of an ideal solar cell (blue curve) and a solar cell with resistance issues (red curve) [119]
Figure 2.21 In a solar cell, the dark IV curve can be utilized to provide information on the recombination mechanism and resistance issue [120] 43
Figure 2.22 A diagram of the QE experimental setup. D.U.T is a reference solar cell or a sample solar cell [123]
Figure 2.23 An ideal QE curve and a typical QE curve [124]

Figure 3.1 SEM images of a PEDOT: PSS, b PEDOT: PSS (UV: 5 min.), c
PEDOT: PSS (UV: 10 min.), and d PEDOT: PSS (UV: 15 min.) [138]
Figure 3.2 AFM images of PEDOT: PSS films a non-treated b UV-treated for
5 min c UV treated for 10 min d UV-treated for 15 min [138]
Figure 3.3 SEM images of perovskite layers coated on top of a , b PEDOT: PSS,
c, d PEDOT: PSS (UV: 5 min.), e, f PEDOT: PSS (UV: 10 min.), and g, h
PEDOT: PSS (UV: 15 min) in 500 nm and 1 μm scales, respectively [138] 54
Figure 3.4 XRD pattern of perovskite (CH3NH3PbI _{3-x} Cl _x) film [138] 55
Figure 3.5 Sheet resistances of non-treated and UV-treated PEDOT: PSS film
[138]56
Figure 3.6 XRD Spectra of a nontreated b PEDOT: PSS (5 min UV treated) c
PEDOT: PSS (10 min UV treated) d PEDOT: PSS (15 min UV treated) films
[138]57
Figure 3.7 FTIR spectra of non-treated and UV treated ITO/PEDOT: PSS films
for different time intervals [138]
Figure 3.8 Semi-logarithmic J-V curves of devices employing non-treated,
5 min, 10 min, and 15 min UV-treated PEDOT: PSS films. The graph at the
bottom is the comparison of J-V curves in linear scale. Inset is the J-V curve of
perovskite solar cells under reverse and forward bias [138] 60
Figure 3.9 Comparison of external quantum efficiency of devices and
absorption of non-treated and UV-treated PEDOT: PSS films (bold lines are
absorption) [138]
Figure 3.10 Fitted EIS spectra of ITO/PEDOT:PSS electrodes without UV
treatment of PEDOT:PSS film and ITO/PEDOT:PSS electrodes with 5, 10, and
15 min UV-treated PEDOT:PSS films [138]
Figure 3.11 KPFM surface potential images of PEDOT: PSS films a non-
treated, \boldsymbol{b} UV treated for 5 min, \boldsymbol{c} UV treated for 10 min \boldsymbol{d} UV treated for
15 min. (Insets are the surface potential histograms) [138] 65

Figure 4.1 (a) Schematic configuration (b) photograph (c) estimated energy
level diagram of the produced perovskite solar cells [170]
Figure 4.2 Schematic demonstration of the Zn-doped PEDOT: PSS film
preparation process [170]
Figure 4.3 (a) Demonstration of the possible composition of the Zn-doped
PEDOT:PSS with water drop test (b) AFM images over 3 \times 3 μ m ² (c) KPFM
measurements of PEDOT:PSS and Zn-doped PEDOT:PSS films [170]
Figure 4.4 (a) Current-voltage curves of PEDOT:PSS films with a ITO/HTL/Ag
structure (b) UV-Vis transmittance spectra of the ITO coated glass and
PEDOT:PSS layers on ITO coated glass substrates [170]
Figure 4.5 Comparison of the PEDOT:PSS layers' cyclic voltammograms
between 1.5 V to - 1.0 V vs Ag in 0.1 M LiClO $_4$ /ACN under various scan rates
[170]
Figure 4.6 Cyclic voltammograms of the (a) PEDOT:PSS (b) Zn-doped
PEDOT:PSS layers between 1.5 V to - 1.0 V vs Ag in 0.1 M LiClO ₄ /ACN under
various scan rates (c) Anodic and cathodic peak currents vs scan rate [170] 79
Figure 4.7 Chronoamperograms of the PEDOT:PSS and Zn-doped PEDOT:PSS
layers during 180 seconds at (a) - 900 mV (b) 1200 mV vs Ag in 0.1 M
LiClO ₄ /ACN (c) pictures of reduced and oxidized states of PEDOT:PSS films on
ITO coated glass substrates during CA experiments [170] 80
Figure 4.8 FE-SEM images of perovskite films on (a) PEDOT:PSS and (b) Zn-
doped PEDOT:PSS films under 100000 X and 30000 X magnifications [170] 81 $$
Figure 4.9 (a) Illuminated current density-voltage curves of the solar cell
devices with different HTLs (b) Hysteresis curves of the corresponding solar cell
devices [170]
Figure 4.10 Box chart graphics of photovoltaic parameters of the solar cell
devices [170]

Figure 4.11 (a) Dark current density-voltage characteristics of the hole-only
devices with ITO/HTL/perovskite/P3HT/Ag configuration, and (b) dark J-
V ² curves of high voltage region for hole mobility extraction [170] 85
Figure 4.12 (a) Photoluminescence curves with a
ITO/HTL/perovskite/PCBM/BCP configuration (b) normalized PCE values of the
PSCs as a function of time [170]
Figure 5.1 (a) Schematic description and (b) Energy level diagram for the
device [208]
Figure 5.2 XRD graph of perovskite (MAPbI ₃) film [208]
Figure 5.3 UV-Vis absorption spectra and photoluminescence (PL) of
perovskite (MAPbI ₃) film [208]
Figure 5.4 FTIR spectra of ITO/perovskite (MAPbI ₃) film [208]
Figure 5.5 Current density-voltage curves of the solar cell devices as a function of BCP precursor concentration cast at (a) 1500 rpm and (b) 4000 rpm spinning speeds [208]
Figure 5.6 (a) Power conversion efficiency and (b) series resistance of the solar cell devices as a function BCP layer coating parameters [208]
Figure 5.7 Dark current density-voltage characteristics of (a) perovskite solar cells (b) e-only devices (ITO/TiO ₂ /MAPbI ₃ /PCBM/BCP/Ag) with and without BCP (0.5 mg/ml, 4000 rpm) layers [208]
Figure 5.8 Distribution of the open circuit voltage, short circuit current density, fill factor and power conversion efficiency values over 15 solar cell devices as a function of different BCP concentrations cast at 1500 rpm and 4000 rpm [208]
Figure 5.9 EQEs and corresponded integrated photocurrent densities of the solar cell devices with BCP (0.5 mg/ml, 4000 rpm) and without BCP layers

Figure 6.1 Precursor preparation and fabrication steps for NiO _x layers [240]
Figure 6.2 Perovskite precursor formation and solar cell fabrication steps [240]
Figure 6.3 (a) AFM images (b) Current-voltage curves (c) KPFM measurements
of NiO_x layers onto ITO coated glass substrates [240]
Figure 6.4 (a) UV-vis transmittance spectra (b) Tauc plots for NiO _x layers
[240]
Figure 6.5 The wide survey XPS spectra of the (a) NiO _x (b) Zn-Ce co-doped
NiO_x (c) deconvolution of Ni $2p_{3/2} \text{for NiO}_x$ and (d) Zn-Ce co-doped NiO $_x$ (e)
deconvolution of Zn $2p_{\rm 3/2}$ (f) deconvolution of Ce $4p_{\rm 3/2}$ and $4p_{\rm 1/2}$ for Zn-Ce co-
doped layers [240]
Figure 6.6 SEM surface images of the perovskite layers growth on (a) NiO _x and
(b) Zn-Ce co-doped NiO _x HTLs under different magnifications and corresponded
grain size distribution [240]
Figure 6.7 (a) Estimated energy level diagram of the devices (b) Illuminated J-
V curves (c) Dark J-V curves (d) EQE spectra along with the corresponding
integrated J_{SC} curves of the ITO/HTL/CH $_3NH_3PbI_3/PCBM/BCP/Ag$ Solar Cells
[240]
Figure 6.8 (a) Dark J-V curves of the hole-only devices with a
ITO/HTL/CH ₃ NH ₃ PbI ₃ /P3HT/Ag configuration (b) Hall mobility measurements
for various NiO_x HTLs (c) Photoluminescence spectra for the perovskite layers on
various NiO _x HTLs (d) Absorbance spectra with Tauc plots (e) Urbach energy
plots for various NiO _x HTLs [240]
Figure 6.9 Box chart graphics of the photovoltaic parameters for various NiO _x
HTL employed PSCs [240]
Figure 6.10 Short term device stability curves for NiO _x and Ce-Zn co-doped
NiO_{x} employed PSCs stored under aging conditions with RH around 70 $\%$ and
temperature; 23-25.0°C [240]

LIST OF TABLES

Table 3.1 Photovoltaic parameters of fabricated devices [138]
Table 3.2 Electrochemically active surface areas and fitted impedance values of
UV-treated and non-treated PEDOT: PSS electrodes at different time intervals of
5 min., 10 min, and 15 min
Table 4.1 PV characteristics of produced cells (Champion efficiency, Average
efficiency values for 20 cells: PCE*, standard deviation) [170]
Table 5.1 Photovoltaic parameters of fabricated devices [208]
Table 6.1 Device Parameters of the PSCs Based on various NiO _x HTLs (doping:
mmol %) [240]

Solution Processable Inverted Type Perovskite Solar Cells

Hamed MOEINI ALISHAH

Physics Department

Doctor of Philosophy Thesis

Supervisor: Prof. Dr. Serap GÜNEŞ

For more than one decade, perovskite-based solar cells have attracted considerable attention due to its particular features, which include low price, long carrier diffusion length, high absorption coefficient, low-temperature preparation, low charge recombination, high electron and hole mobility, controllable bandgap, and a fast improvement from 3.9 % to more than 25%, which is not typical for solar cells to progress so quickly in such a short time.

In perovskite solar cells, charge transport layers (CTL) are significantly vital to the device's performance. Therefore, choosing a suitable and cost-effective CTL is inevitable. Despite being one of the most commonly applied hole transporters in solar cell research, PEDOT:PSS must still meet the performance criteria of solar cells. Consequently, PEDOT: PSS has become of the most popular due to its improved morphology, conductivity, and durability. In this thesis by using a simple method we investigate the performance of PSCs when PEDOT: PSS layers are exposed to UV radiation. In addition, the influence of dopants also on electrooptical properties and performance of PEDOT: PSS based perovskite solar cells has been investigated.

Bathocuproine (BCP) is a well-known material used in perovskite solar cells as a hole-blocking layer. Vacuum or solution processing can be used to process thin BCP films as buffer layers. In this thesis, the effect of BCP layers prepared using sol-gel method on the performance of perovskite solar cells is investigated. On the other hand, inorganic charge transport materials are preferred because they are plentiful, inexpensive, and have high hole mobility and chemical stability. Because of its high optical transmittance, broad direct bandgap, deep valance band, and high conduction band, non-stoichiometric nickel oxide (NiO_x) is widely used as a HTL for inverted PSCs. For the first time in the literature, we demonstrate a research based on Ce and Zn co-doping into NiO_x HTLs for inverted type PSCs.

Key Word: Perovskite Solar Cells, BCP, PEDOT:PSS, NiO_X

Çözüm İşlenebilir Ters Çevrilmiş Perovskit Güneş Pilleri

Hamed MOEINI ALISHAH

Fizik Bölümü

Doktora Tezi

Danışman: Prof. Dr. Serap GÜNEŞ

On yıl boyunca perovskite güneş pilleri, düşük maliyetli, uzun taşıyıcı difüzyon uzunluğu, yüksek absorpsiyon katsayısı, düşük sıcaklıkta işleme, düşük rekombinasyon oranı, yüksek elektron ve boşluk hareketliliği ve ayarlanabilir band aralığı gibi olağanüstü özellikleri nedeniyle çok dikkat çekmiştir. Fotovoltaic güç dönüşüm verimlerinin %3,9'dan %25'in üzerine hızlı bir şekilde artması, ki bu bir fotovoltaik cihazın bu kadar kısa bir sürede son derece hızlı bir gelişme göstermesi yaygın değildir, perovskit güneş pillerini ilgi çekici hale getirmiştir.

Perovskit güneş pillerinde yük taşıma katmanları (YTK), cihazın performansında çok önemli bir rol oynar. Enerji açısından uygun ve uygun maliyetli bir YTK seçimi kaçınılmazdır. Gelişmiş morfoloji, iletkenlik ve stabiliteye sahip olması PEDOT:PSS'i öne çıkarması ve güneş pili araştırmalarında en yaygın olarak kullanılan boşluk taşıyıcılardan biri olmasına rağmen, PEDOT:PSS'nin yine de güneş pillerinin performans kriterlerini karşılaması gerekmektedir . Bu tez

çalışmasında, basit bir yöntem kullanarak, PEDOT: PSS katmanları UV radyasyonuna maruz kaldığında PSC'lerin performansını araştırılmıştır. Ayrıca PEDOT:PSS tabanlı perovskit güneş pillerinin elektro-optik karakteristikleri ve performansı üzerine katkılamanın etkisi araştırılmıştır.

Bathocuproine (BCP), perovskite güneş pillerinde sıklıkla kullanılan bir malzemedir. İnce BCP filmlerini tampon katmanlar olarak işlemek için vakum veya çözelti işleme teknikleri kullanılabilir. Vakumla işlenmiş BCP katmanlarına dayalı literatürde çok sayıda çalışma olmasına rağmen, çözeltiden işlenmiş BCP katmanlarına odaklanan çalışmaların sayısı nispeten sınırlıdır. Bu tezde sol-jel yöntemiyle hazırlanan BCP katmanlarının perovskit güneş pillerinin performansına etkisi araştırılmıştır. Öte yandan, anorganik yük taşıma malzemeleri bol, ucuz, yüksek boşluk hareketliliği ve kimyasal kararlılığa sahip oldukları için tercih edilmektedir. Yüksek optik geçirgenliği, geniş doğrudan bant aralığı, derin değerlik bandı ve yüksek iletim bandı nedeniyle, stokiyometrik olmayan nikel oksit (NiOx), tersine çevrilmiş PSC'ler için boşluk seçici bir malzeme olarak yaygın olarak kullanılmıştır. Literatürde ilk kez, tersine çevrilmiş tip PSC'ler için NiOx HTL'lere Ce ve Zn birlikte katkılanmasına dayanan bir araştırma gerçekleştirilmiştir.

Anahtal kelimeler: Perovskit Güneş pilleri, BCP, PEDOT:PSS, NiO_X

1.1 Literature Review

1.1.1 Background

Since the worldwide usage of energy has risen as a result of population growth and industrial development, demand for sustainable and viable energy sources is unavoidable. Alternative resources should strike a balance between productivity, cost, technological issues, and environmental impacts. The use of photovoltaic systems to collect energy from the sunlight provides a new pathway to generate energy on a worldwide scale. Even if silicon-based solar cells have been employed for several years and now dominate the photovoltaic market, their high cost prevents them from being a significant replacement for fossil-fuel resources on a large scale[1]. Secondgeneration solar cells' large-scale production is also restricted due to the presence of hazardous compounds (e.g. Cd) and the requirement for high vacuum and temperature for manufacturing [2]. As a result, a new generation providing low-cost, high-flexibility, low molecular weight, and high-efficiency is demanded. All of these criteria are met by third-generation solar cells[3,4]. Though third-generation solar cells have prompted interest, their efficiencies are still inadequate to keep up with first- and second-generation solar cells which commercially available[5]. Perovskitebased solar cells have recently received considerable attention owing to a significant increase in efficiency from 3.9% to over 25% during the last decade. Perovskite-based solar cells seem to have a lot of promise in terms of overcoming the drawbacks of first, second, and third generation solar cells and possibly outperforming them. Perovskites are affordable, abundantly available and can be solution processed.

1.1.2 Energy

As a result of the population growth and improved industrialization, global energy use has increased, and the limited amount of fossil fuels on the planet will no longer be able to meet the demand for energy in a few decades. Between 2017 and 2040, the International Energy Agency (IEA) predicts a 30% rise in global energy demand[6]. Global energy consumption has grown from 495 quadrillion British thermal unit (Btu) in 2007, to around 739 quadrillion Btu in 2035[7]. On the other hand, the more fossil energy sources we expend, the more global temperature rises, affecting the climate and unpredictable weather changes. In many regions, for instance, heat waves, extreme flood events, and severe drought are observed. This raises a crucial question, how do we overcome the difficult issue of obtaining renewable energy sources to replace fossil fuels. As a result, demand for sustainable and feasible sources of energy is unavoidable, and the use of renewable and clean sources of energy has become progressively important and urgent for humanity.

1.1.3 Renewable Energy

Renewable energy is a long - term solution for the issue of energy supply and demand as well as reducing the environmental effect of the present energy system. Renewable energy comes from unrestricted resources such as wind, sunlight, biomass, tidal waves, ground-source heat, and etc. [8] The majority of renewable energy sources are viable and environmentally friendly. Renewable energy sources have the potential to promote long-term alternatives to possible energy crises. Even though wind and hydroelectric sources dominated recently, different types of renewable energy, especially solar photovoltaic systems, have been rapidly expanding in terms of cost and capabilities. Solar power is nearly limitless as compared to other sustainable resources such as wind and biomass, because the daily illuminated solar energy on the globe is around 10,000 times more than the total energy consumption

in the world per day[9]. Due to its availability on Earth's surface and in space, non-destructive ecological impacts, and feasibility to install solar cell systems in remote areas, solar energy is a common renewable and sustainable energy source. Attempts have been devoted with the aim of increasing power conversion efficiency and lowering cost of photovoltaic devices. PV prices have fallen drastically in the last 40 years, from around \$100/watt to 0.3\$/watt[10], as seen in Figure 1.1. The reduction in PV prices has resulted in a significant rise in PV installations around the world.

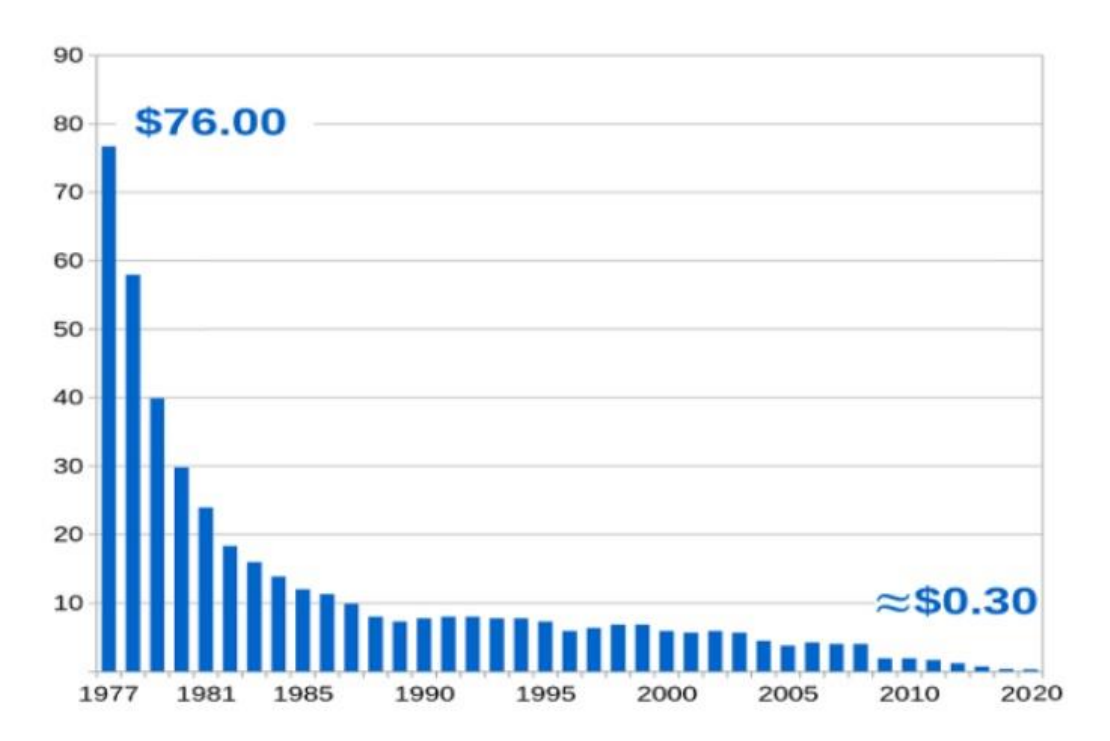


Figure 1.1 Solar panels cost and worldwide deployment in the last 40 years [10]

1.1.4 Photovoltaics (PV)

Photovoltaic cells, known as solar cells, turn solar energy directly into electrical energy. Edmond Becquerel was the first to observe the photovoltaic effect in 1839

and he presented the idea of the solar cell for the first time[11]. New York inventor Charles Fritts developed the first photovoltaic cells with a 1-2 % PCE in 1883 by covering selenium with a thin film of gold [6]. Photovoltaic devices first time were revealed by a group of Bell Telephone researchers who noticed that silicon could generate an electric current when exposed to sunlight. Scientists at Bell Telephone laboratories employed silicon to produce photovoltaic cells with a 6% PCE in 1954[6]. Later, in 1956, Western Electric started to sell licenses for commercial use of silicon PV technology[12]. Particles of solar energy which is called photons can be absorbed in a photovoltaic system by semiconductor materials. The energy of the incident photons from the sunlight varies according to the solar spectrum wavelengths. Several events can occur when photons approach a PV cell: A photon can be reflected completely, pass fully without any interaction through the device, or be absorbed by the semiconductor compounds. Only photons that have been absorbed can participate in generation of electricity. The efficiency of solar cell devices presently varies from 10.6 % to 47.1 %, as shown in the National Renewable Energy Laboratory's (NREL) performance diagram (figure 1.2) [13].

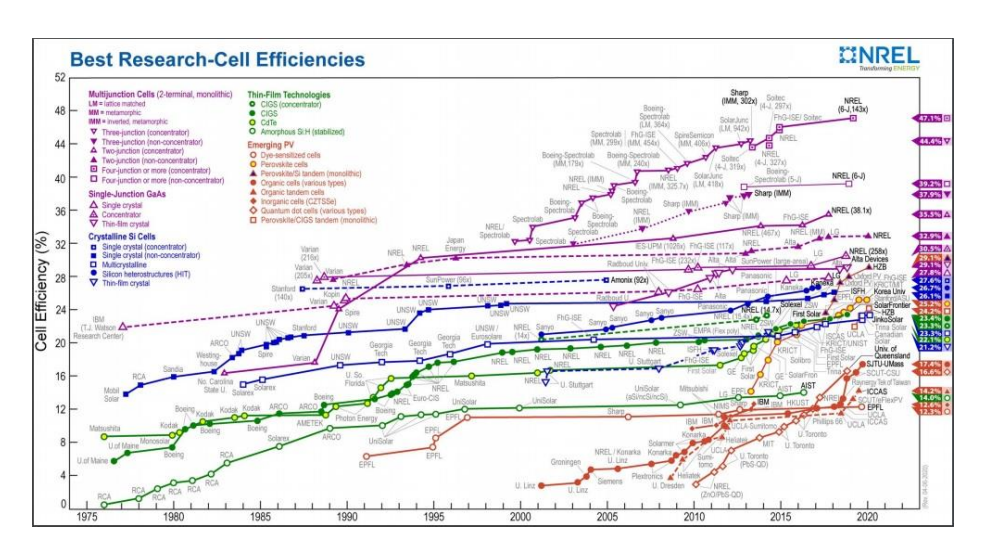


Figure 1.2 NREL's efficiency chart is reprinted with permission by the National Renewable Energy Laboratory [13]

1.1.5 PV Technologies

Solar cells are normally divided into three categories: first-generation, second-generation, and third-generation. Solar cells in the first generation are comparatively costly to manufacture and have high efficiencies. Second-generation solar cells have a lower performance but are less expensive to manufacture than first-generation manufacturing processes. Third-generation solar cells are impactful and plausibly economical, but they are not yet widely available due to low stability of materials employed in the device configuration.

1.1.5.1PV Technologies of the First Generation: Crystalline Silicon Solar Cells

The dominance of crystalline silicon technology in the photovoltaic market can be attributed to a number of aspects: Si is a cheap and abundant component, devices provide a high durability, and crystalline silicon photovoltaic technology was able to properly incorporate developments in microelectronic industry. With a passivated emitter rear locally-diffused (PERL) cell, the world champion performance (25%) was obtained after improving bulk crystal formation in the 1950s and system enhancement in many aspects, such as bulk diffusion length, design, and passivation of surface in the 1980s[14]. Several companies, including Suntech (19 % PCE), SANYO Electric Co., Ltd. (20.7 % PCE), and SunPower (22 % PCE), have commercially produced crystalline silicon PV devices as a result of extensive investigation in this field [15]. Multicrystalline silicon photovoltaic devices were introduced in the 1980s as a cheaper option to monocrystalline PV cells. Since this new technology was of lower quality than crystalline-Si one[15], device improvement was taken into account in order to boost the share of multicrystalline-Si in the market by attaining greater efficiencies at minimal expenses. The recent search for affordable photovoltaic technologies has switched the focus to solar grade silicon (SoG-Si), which is considered to involve high metal. Silicon materials developed SoG-Si solar cells with a 16 % efficiency due to system optimization[15].

1.1.5.2 Second-Generation PV Technologies: Thin-Film Solar Cells

Despite the fact that photovoltaics based on silicon exhibit better energy conversion efficiency, their high cost has prompted researchers to look at alternative technologies and methods for producing more cost-effective photovoltaic devices. Ergo, thin film Si cells were recommended, contributing for less than 10% of the worldwide Photovoltaic module sales. In this technique plasma-enhanced chemical vapor deposition (PECVD) method is commonly used for coating the active layer. Thin-film Si photovoltaic cells were commercially produced in a variety of different ways, which include single, double, triple, and tandem-junction amorphous silicon PV systems. The special optical and electrical properties of selenides, tellurides, and sulphides (also known as chalcogenides) have shifted focus to copper indium gallium selenides (CIGS) and cadmium telluride (CdTe) photovoltaic devices. In contrast to silicon, these substances can be employed as thin film absorbers due to their high absorption coefficient and direct bandgap. Additionally, these substances have a bandgap of 1.5 eV (based on the stoichiometry), which is closely perfect for matching with the spectrum of solar radiation. They can tolerate much more against defects and impurities and could be also developed at low temperature. Solar cells made up of CIGS have efficiencies of up to 20%, which are comparable to the ideal crystalline silicon solar cells[16]. Nevertheless, due to the scarcity and high cost of these materials, researchers have been looking for suitable and more cost-effective Photovoltaic technology.

1.1.5.3Third-Generation PV Technologies: High Efficiency Solar Cells and Novel PV Concepts

This generation of solar cells intends to reach high efficiency cells by using innovative materials and new processing techniques and procedures, which are currently at the forefront of thorough scientific investigations. These novel photovoltaics indicate a

different perspective for producing cost-effective solar cells. Developed thin-film technologies, such as dye-sensitized solar cells, multi-junction solar cells, organicbased solar cells, and, not long ago, perovskite solar cells (PSCs), are included in this category. Dye-sensitized solar cells are organic dye-based PV devices, while in organic solar cells polymers or small molecules are used. Around 12% efficiency has been attained using single junction organic photovoltaics (OPVs) and dye-sensitized solar cells (DSSCs)[13]. Commercial devices, on the other hand, have much lower efficiencies. Low-cost materials and manufacturing can compensate for low efficiency of these kind of solar cells. Optimizing cell efficiency to improve the power-to-cost ratio is pivotal for multi-junction photovoltaic devices, which are composed of multiple cells laying on top of each other. Each layer in the stack in these multijunction cells has a various bandgap to boost the amount of solar spectrum that the photovoltaic cell can accumulate. Also, it may be noteworthy to mention that multijunction OPVs have been studied and shown to be more efficient than single-junction OPVs [17]. Perovskite solar cells are a groundbreaking technology that has increasingly been investigated. Within just a few years of prosperity, PCEs in PSCs have increased from 3.9% to more than 25%, making them equivalent to commercially accessible crystalline silicon solar cells.

1.1.6 Perovskite Solar Cells

Gustav Rose discovered perovskite in 1839, and was named after it was characterized by Lew A. Perowski [18,19]. Perovskites are a wide category of materials with the same crystalline structure as the calcium titanium oxide (CaTiO3). Perovskites with a halide basis can be divided into two classes, perovskites containing alkali-halide and organometal halide. Moller (1958) identified photoconductivity in the first alkali-halide perovskite (CsPbX3, X= Cl, Br, or I), implying that such compounds could act as semiconductors[20]. In 1978, Weber and Naturforsch developed the first organometal halide perovskites by substituting the organic cation methylammonium for the cesium cation [21]. In comparison to oxide-based

perovskites, halide equivalents gained little attention until Mitzi and colleagues used coated organic-inorganic halide perovskites (OIHP) in thin-film transistors and light-emitting diodes (LEDs) in the 1990s [22,23]. It took until 2009 to reveal the use of these materials in photovoltaic devices [24].

The main purpose of this graduation thesis is to use the spin-coating approach to

1.2 Objective of the Thesis

produce solution processable photovoltaic devices that are cost effective, remarkably stable, repeatable, and productive. The current research objectives are focused on preparation and optimization of different type of perovskite and improved hole transport layers and utilization of them in planar architecture of perovskite solar cells. In practice, an effective charge transport layer (CTL) must meet a number of requirements, including the following: (a) a desirable energy level configuration that allows for successful blocking of one form of charge carrier while allowing for efficient transfer of the other, (b) to prevent negative reactions with the surrounding layers, good physical and chemical properties, as well as appropriate surface characteristics, are needed, (c) To achieve maximum absorption in the perovskite layer, the transparency should be as high as possible, (d) excellent transport features to guarantee that charge carriers are transported quickly to the collecting electrode. The purpose of this thesis is to investigate how to improve the performance of perovskite solar cells by using and enhancing various charge transport materials and interlayers. The inverted-type perovskite solar cells employing CH3NH3PbI3-xClx perovskite have been fabricated. UV radiation's effects on ITO/PEDOT:PSS substrates have been studied for PSCs. As compared to perovskite solar cells manufactured on non-treated PEDOT:PSS surfaces, those fabricated on UV-irradiated ITO/PEDOT:PSS surfaces performed much better. In addition, in this thesis, the conductivity and morphological features of UV-treated and non-treated PEDOT:PSS and perovskite layers were improved by adding Zn to the PEDOT:PSS solution as an additive, which improved the stability and performance of the MAPbI3 based devices.

In perovskite solar cells, employing BCP as a buffer layer between the ETL and the cathode electrode has been shown to be highly effective. Also, BCP layers that were processed using wet preparation methods and the sol-gel approach with varying concentrations were used, resulting in improved device performance.

Inorganic hole transporters are preferred for inverted planar PSCs, where the structure of cell begins with HTL manufacturing. They exhibit high hole mobility, low-cost, simple to make, and better chemical stability. Non-stoichiometric nickel oxide (NiO_x) seems to be the most environmentally friendly and promising candidate among them because of its abundance, cost effectiveness, chemical stability, high optical transmittance, ideal energy level configuration with perovskite, and high conduction band, which provides to prevent unwanted electron leakage. In this thesis, to improve the efficiency and stability of inverted methylammonium lead triiodide (CH3NH3PbI3) based solar cells, cerium and zinc co-doped nickel oxide (NiO_x) were developed. PCEs and stability were improved under aging conditions by combining our humidity-resistant GBL-based perovskite deposition method with an optimal doping ratio of NiOx:Zn-Ce layers.

In order to analyze the thin films and devices developed in this research, several techniques were used, including:

- X-ray diffraction patterns and UV-vis spectroscopy are used to evaluate the structural and optical properties of thin films, respectively.
- The surface morphologies of the developed thin films are investigated using atomic force microscopy (AFM) and scanning electron microscope (SEM).
- The surface chemistry and surface potential of thin films are studied using X-ray photoelectron spectroscopy (XPS) and Kelvin probe force microscopy (KPFM), respectively.

- FTIR and photoluminescence PL are used to examine the internal configurations of the composite perovskite as well as its optical properties.
- The performance of manufactured solar cells is determined through current density-voltage (J-V) characterization and external quantum efficiency (EQE) measurements.

1.3 Hypothesis

In this work by employing and tailoring both organic (PEDOT:PSS) and inorganic (NiO_x) charge transport materials with different methods such as UV irradiation and doping technique, the performance and stability of organic/hybrid perovskite solar cells can be improved. In addition, utilizing an optimized concentration of bathocuproine (BCP) as a hole-blocking interlayer influence the performance of fabricated devices positively.

2.1 History and development

Silicon is still the most commonly used photovoltaic material. Albeit notably reduction on the expense of silicon-based solar panels in the past few decades, replacing new type of materials to lessen the cost of panels fabrication and improve the power conversion efficiency (PCE) seems inevitable. Perovskite solar cells can be considered as an alternative which possess these criteria. Perovskite solar cells are an interesting prospect for coming generations of solar cells because of their ease of fabrication, minimal material costs, and simple roll-to-roll manufacturing. Moreover, achieving power conversion efficiency (PCE) more than 25% was reported by several research groups [25]. Figure 2.1 compares perovskite solar cells to other kinds of solar cells in terms of power conversion efficiency [26].

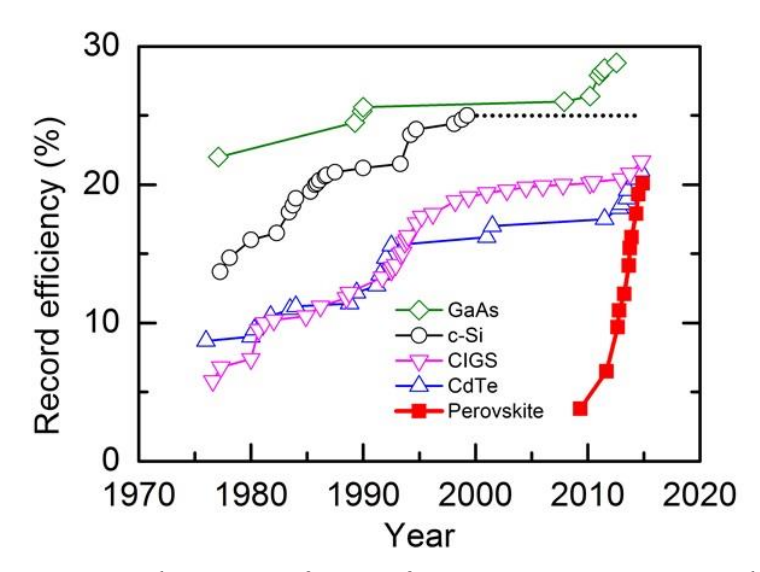


Figure 2.1 Development of PCE of PSCs in comparison with other solar technologies [26]

The name of "perovskite" which was referred to the crystal structure of CaTiO₃ (calcium titanate), firstly discovered by Gustav Rose, a German mineralogist, in 1839 and later was named by Lev Perovski [27].

A comprehensive research with the aim of study on the optoelectronic properties of organic-inorganic perovskite was performed by Mitzi, et al in early 90s [28]. The primary investigation concentrated on tin (II)-based halide perovskite due to superb charge carrier mobility and metallic feature in comparison with lead (II)-based perovskite. These properties play a pivotal role in the utilization of thin film transistor (TFT), superconductor and organic light-emitting diode (OLED) [23,29]. Miyasaka et al. reported the first implementation of it in solar cell in 2009 which dye-sensitized solar cell architecture was used resulted in 3.8% of power conversion efficiency (PCE) [24]. A dye-sensitized solar cell (DSSC) consist of three parts, a porous layer, a dye for absorbing of light and redox-active electrolyte. In Miyasaka's work, to increase the area of the surface and adhere perovskite sensitizer, a mesoporous TiO2 was used as a scaffold. The efficiency of a methylammonium lead triiodide sensitized solar cell was increased to 6.5 % by Nam-Gyu Park and colleagues in 2011 [30]. In their study, perovskite nanocrystal as a sensitizer was used in size of 1-2 nm. In addition, they suggested that by applying a thinner mesoporous layer of TiO2 and perovskite material with higher absorption coefficient, a higher photocurrent density can be achieved. This idea paved the way for the development of planar structure. Nevertheless, due to use of corrosive electrolyte, the stability of the cell was the issue. In order to increase the device stability, Snaith et al in 2012 used Spiro-OMeTAD in solid-state DSSC as a hole transport layer instead of liquid [31]. By using this structure, the efficiency increased to almost 10% [31]. Appealingly, by replacing TiO₂ layer with inert Al₂O₃, a higher efficiency gained [31]. In comparison to TiO₂, more experiments have shown that using Al₂O₃ results in an increase in open-circuit voltage and efficiency. This proved that the scaffold layer is not essential for electron extraction. Further studies revealed that achieving efficiency over 10% in the perovskite solar cells with planar structure were reachable [32–35]. In the same year, Gratzel and Park *et al.* showed an efficiency almost 10% with mesoscopic structure [36].

In 2013 a fast growth was observed for both planar and mesoporous structure of perovskite solar cells. A sequential deposition method was introduced by Burschka and coworkers resulted in an average efficiency over 15%. Liu *et al.*, at the same year, indicated a new technique for fabrication of planar solar cells by dual source thermal evaporation and got a PCE more than 15% [37]. Docampo et al. presented inverted type of perovskite solar cells with a PCE of 10%. Further, by carrying out sintering process at low temperature, the practicality of flexible substrate was conceived. This is a significant breakthrough and it eliminates hurdles to approval of the perovskite technology in the photovoltaic community.

In 2014, a variety of new deposition techniques with even higher efficiencies were published. Yang et al. attained a PCE of 19.3% by manipulating on the formation of the perovskite layer and materials for interlayer to reduce carrier recombination in a planar structure[38]. In 2014, Seok et al, made significant progress in their investigation and accomplished highly uniform perovskite films by solvent engineering methods which led to a PCE of 16.5% [39]. With more experimental works by the same group a higher PCE (19%) was acquired by using compositional engineering method[40]. In order to stabilize the perovskite phase, MAPbBr3 was added into FAPbI3 which led to this high efficiency[40]. Subsequently, the device of Seok et al with an efficiency of 20.1% was certificated by NREL.

In April 2021, a novel record PCE of 25.6% was achieved by the researchers at EPFL [25] in which the highest single junction PSC efficiency to date was achieved using this cutting-edge technology. The device is composed of formamidinium lead iodide, a variety of metal halide perovskite, which has a narrow bandgap and is considered for its good thermal stability. The researchers enhanced the cell's efficiency by using

formate in the precursors, which helped to reduce the number of defects in the structure of perovskite film and thereby increase its efficiency [25].

2.2 Properties of perovskite

In order to optimize the performance of device and figure out the transportation of carrier and mechanism of device degradation, the electro-optical properties of the film has to be studied. The properties of perovskite are summarized below.

2.2.1 Crystal structure of perovskites

The crystal structure of perovskite is generally shown with ABX₃ formula, where A is a cation with one electron vacancy, B is a cation with two vacancies, and X is an anion (oxygen or halogen). The crystalline structure of perovskite is depicted in Figure 2.2 [41].

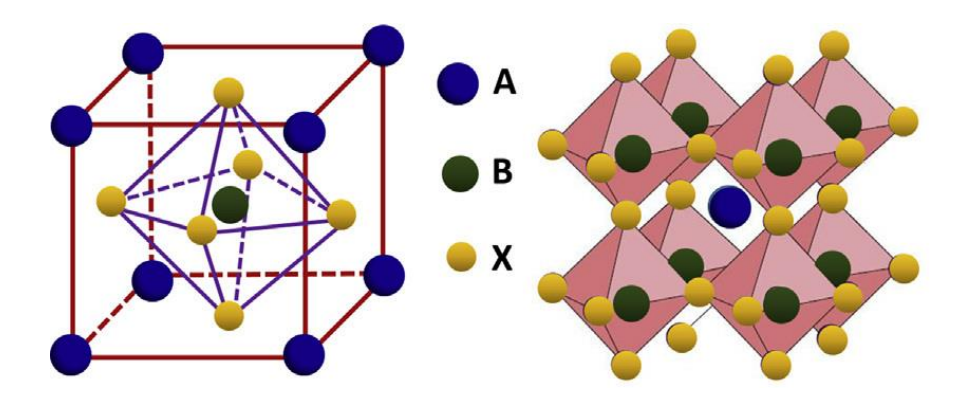


Figure 2.2 Structure of Perovskite [41]

To get perovskite structure, the ionic radii of A, B, and X must fulfill the tolerance and octahedral factors shown below [42].

$$t = \frac{R_A + R_X}{\sqrt{2(R_B + R_X)}} \quad 0.81 < t < 1.1$$
 (2.1)

$$\mu = \frac{R_B}{R_X} \qquad 0.44 < t < 0.9 \tag{2.2}$$

To form perovskite structure, the radii of A element should be between around 1.6 $\,$ A° and 2.5 A°. due to its 1.8 A° ionic radius, the methylammonium is appropriate for using as a cation in lead halide perovskite [43].

2.2.2 Absorption coefficient, α

The absorption coefficient of an absorber layer is a crucial feature. By having a layer with high absorption coefficient, the required thickness for absorbing incident light adequately will decrease. Figure 2.3 depicts the relationship between absorption coefficient and wavelength for several photovoltaic materials [44]. As is seen from Figure 2.3 that the absorption coefficient of perovskite (10^5 – 10^6 cm⁻¹) is substantially higher than that of crystalline silicon, implying that only around 100 nm– 1μ m of perovskite layer is required to collect the vast majority of incident photons.

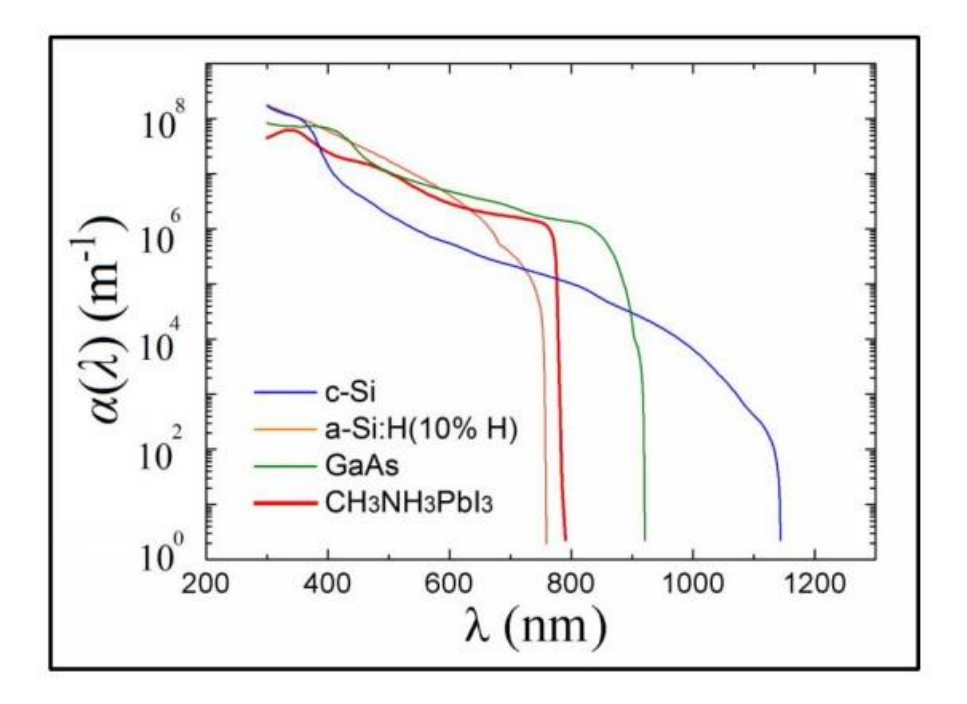


Figure 2.3 Absorption coefficient of various PV materials at various wavelength [44]

2.2.3 Bandgap

The bandgap of a photovoltaic material plays pivotal role since, the highest theoretical efficiency that can be obtained is determined by the bandgap of the material, based on the Shockley–Queisser limit. Perovskite has a direct bandgap. We can achieve the bandgap of materials by employing the "Tauc plot" of α^2 vs hv. For energy near to the bandgap, quantum efficiency can be expressed as the following equations [45]

$$QE(\lambda) = c\alpha(\lambda) \tag{2-3}$$

Where c is a constant and α is the absorption coefficient at incident wavelength of λ . Then, by measuring the quantum efficiency we can use it for finding absorption coefficient.

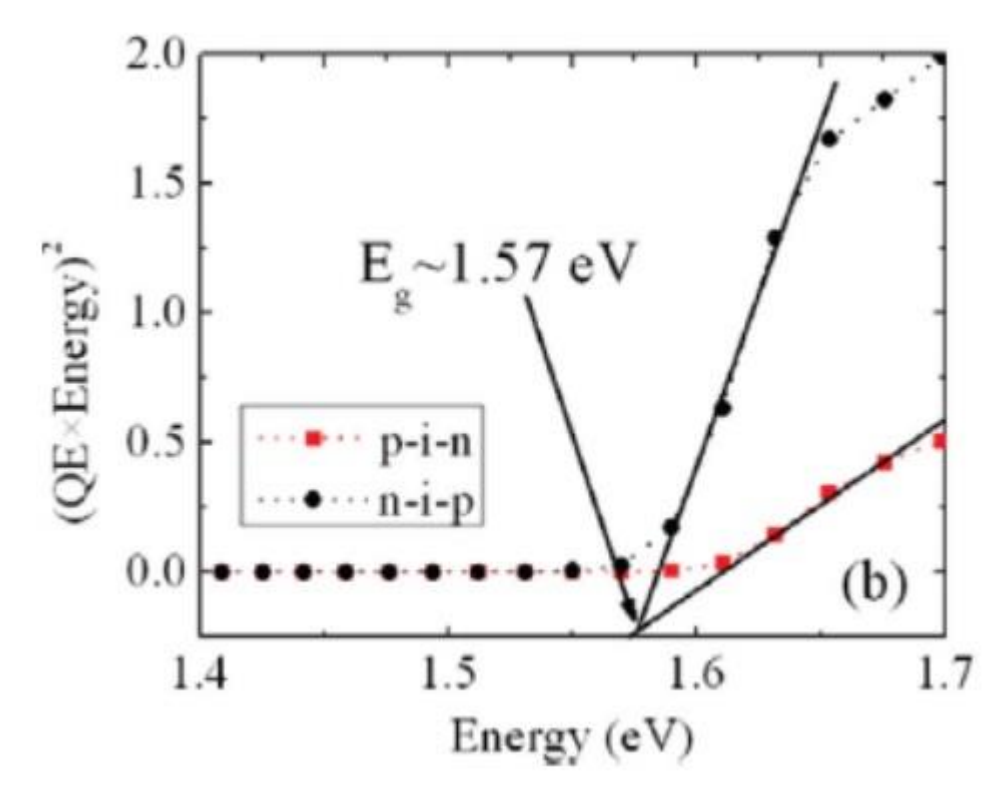


Figure 2.4 To evaluate the bandgap of perovskite, (Quantum efficiency \times Energy)² vs Energy was achieved. It points to a bandgap of 1.58 eV [46]

In figure 2.4 for calculating the bandgap of perovskite the (Quantum Efficiency \times Energy)² vs Energy is plotted. As shown in this diagram, the bandgap of perovskite is approximately 1.58 eV [46]. According to the Shockley–Queisser limit, a single junction perovskite solar cell can have a maximum efficiency of 31 %. A double-junction tandem solar cell can achieve a maximum efficiency of 44 %. As a result, perovskite will significantly improve power conversion efficiency. In 2015, Hoke et al. demonstrated an intriguing feature of perovskite [47]. They demonstrated that the bandgap of a mixed halide perovskite could be altered by changing the relative components of Iodine and Bromine. $CH_3NH_3PbI_{3-x}Br_x$ was the formula for representing perovskite with mixed halides. The bandgap of perovskite can be adjusted from about 1.55 eV to about 2.20 eV by adjusting the relative composition of Bromine and Iodine (see Figure 2.5) [47].

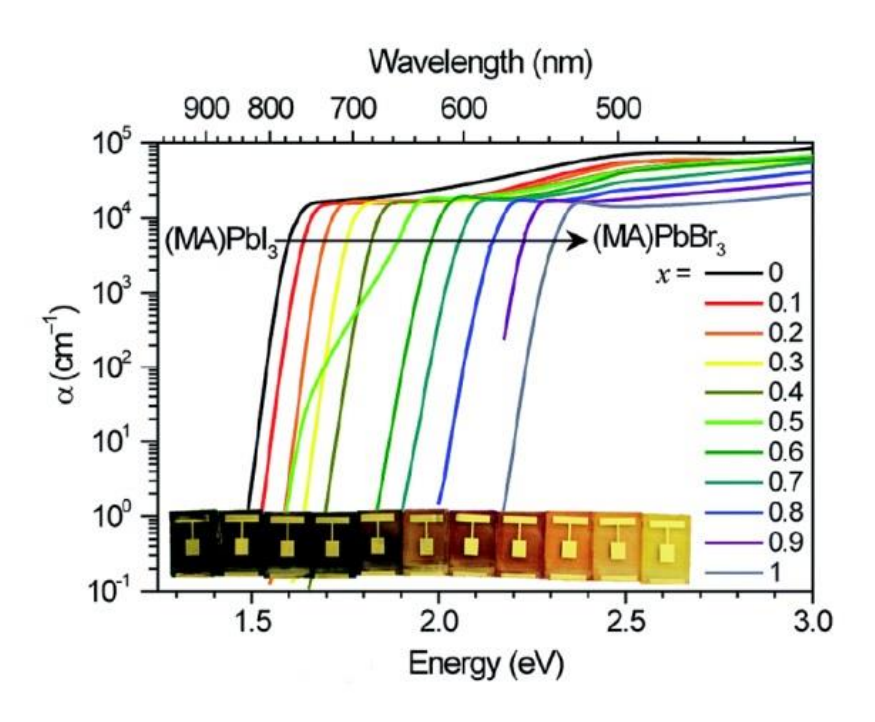


Figure 2.5 Absorption coefficient of mixed-halide perovskite with varied Iodine and Bromine relative compositions [47]

2.2.4 Diffusion length

The carrier diffusion lengths in perovskite are considered to be extremely long. The diffusion length has been reported to be on the order of micrometers by several groups [48–50]. By implementation of time-resolved terahertz spectroscopy technique, the diffusion length of the carrier was measured by La-o-vorakiat et al. at different temperatures (figure 2.6) [50]. They demonstrated that the diffusion length can exceed $1\,\mu\text{m}$. diffusion length at different temperatures has different value, which reveals the relation between recombination mechanism and temperature [50]. According to the research results from literature [48,49,51], high carrier lifetime and carrier mobility are properties of the perovskite which leads to high collection efficiency and long diffusion length.

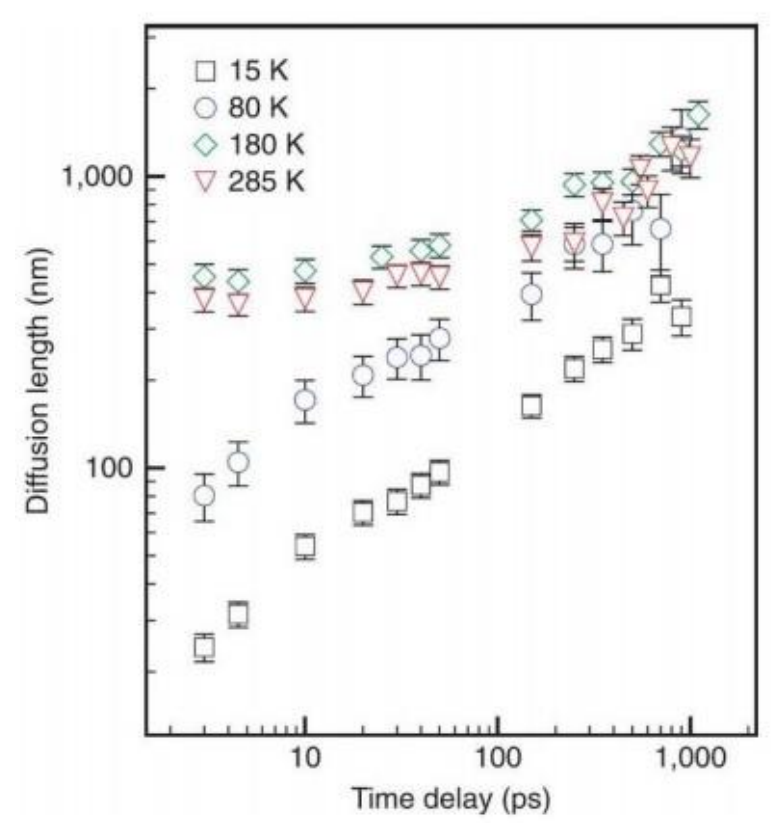


Figure 2.6 Diffusion length of carrier in perovskite at various temperatures [50]

2.2.5 Defect density

The density of defects within the bandgap of a photovoltaic material is vital since the recombination process is dependent on the trap density of states. Figure 2.7 exhibits the calculated Urbach energy of a perovskite solar cell from the quantum efficiency measurement which is around 15 meV [52]. While, for Si materials is \sim 50 meV. This illustrates the crystallinity of perovskite is better.

Mehran et al. demonstrated the existence of two levels of defects inside the perovskite bandgap by implementation of Capacitance-Frequency-Temperature (CFT) technique as shown in figure 2.8[46]. The activation energy of shallow trap level is 0.24 eV, while for deeper trap this amount is around 0.66 eV.

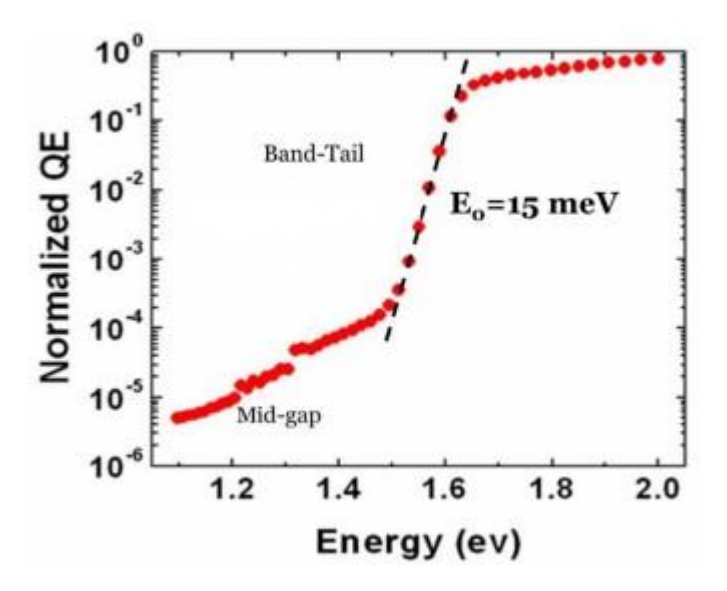


Figure 2.7 PSC with sub-gap quantum efficiency. Urbach energy is estimated to be around 15 meV [52]

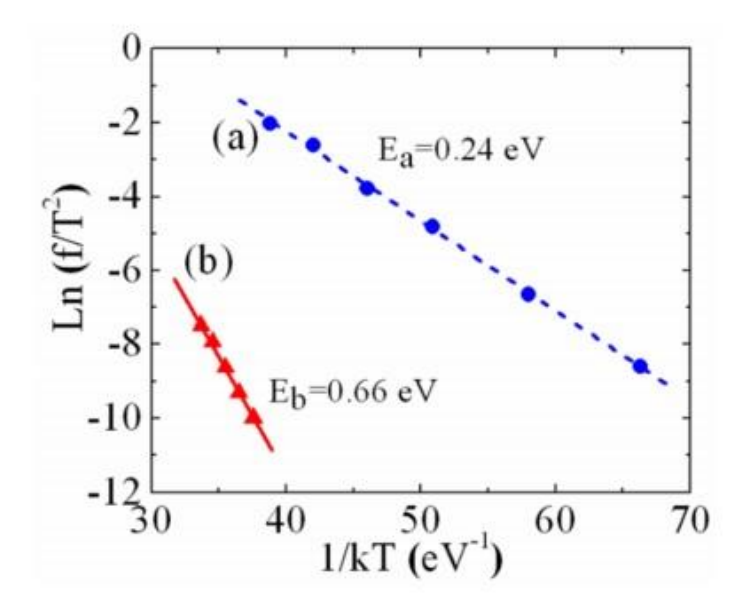


Figure 2.8 Two defect levels can be seen in an Arrhenius plot utilizing Capacitance-Frequency-Temperature (CFT) measurements: the activation energy of shallower traps is about 0.24 eV and the activation energy of deeper traps is about 0.66 eV [46]

They involved the Capacitance vs Frequency measurement to determine the trap density of states profile as well (figure 2.9). As shown in figure 2.9 (a) A peak at 0.66 is found below the conduction band of midgap states, which is in good accord with the plot in figure 2.8. Figure 2.9 (b) shows how a Gaussian distribution can be used to fit the trap density of state of the midgap state.

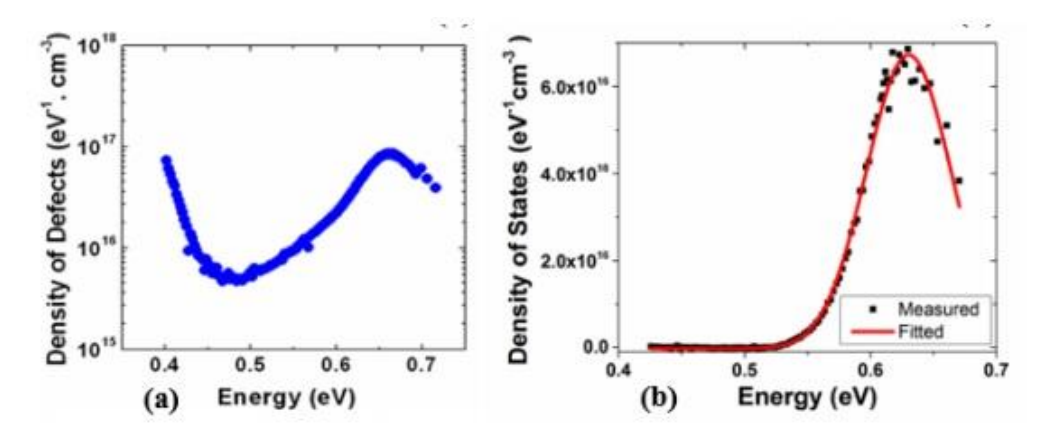


Figure 2.9 Capacitance vs Frequency profile of PSC (a) Density of states (t-DOS) distribution within the perovskite bandgap (b) t-DOS of the midgap state fitted by Gaussian distribution [46]

2.3 Working principle of PSCs

Generally, a perovskite solar cell consists of electrodes (as an anode and cathode), active layer, and layers for charge transportation. As previously stated, the inverted p-i-n device architecture is the foundation of this thesis work. As shown in figure 2.10 [53], perovskite employs as an active layer for light absorption which is inserted between two charge transport layers such as PEDOT: PSS, a p-type material for hole transport, and a n-type layer like PCBM as an electron transport layer. For back contact a transparent conductive layer such as FTO or ITO and for front contact a metal layer for instance Al or Ag are used. MAPbI₃ is the perovskite material frequently used in literature. Our work mainly focuses on MAPbI3 and MAPbI_{3-x}Cl_x based perovskite solar cells.

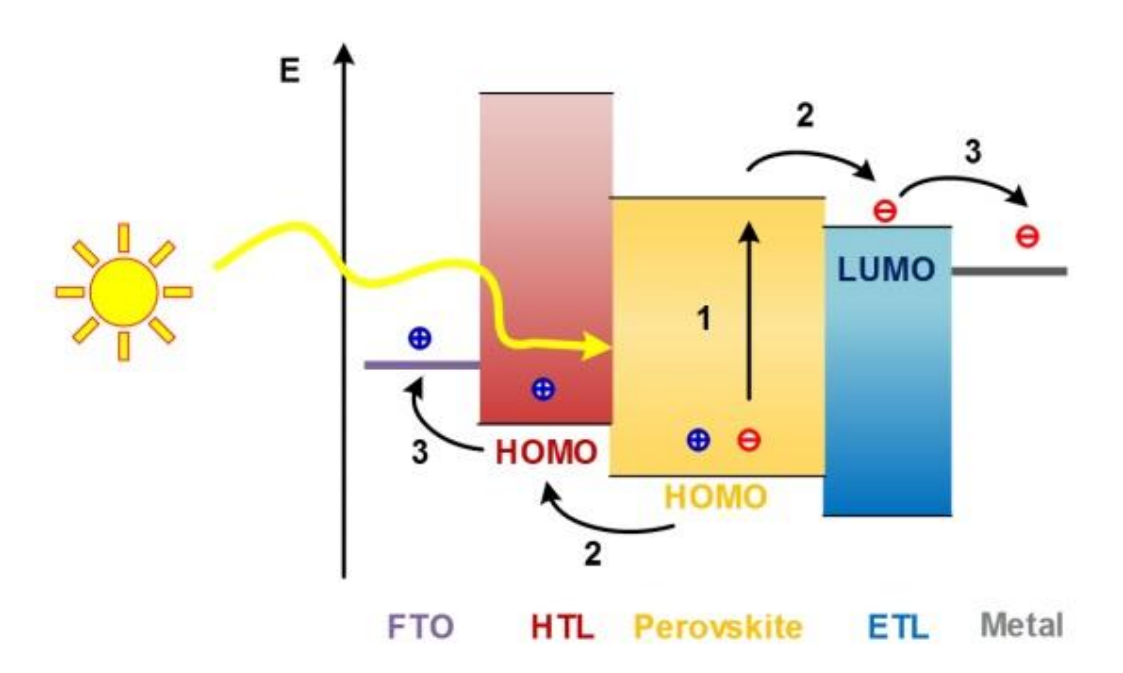


Figure 2.10 A conventional p-i-n (inverted) perovskite solar cell's energy band diagram. The Basic functioning principle is as follow: 1. Light absorption and production of exciton, 2. Separation of charge carrier, 3. Extraction of charge carrier [53].

As perovskite absorbs light, a transfer from HOMO (highest occupied molecular orbital) to LUMO (lowest unoccupied molecular orbital) will happen for an electron. In organic semiconductors, HOMO and LUMO are analogous to the valence band and conduction band. A hole is formed when an electron is transferred from HOMO, causes the creation of an electron-hole pair. This pair of electron and hole is called excitons[53]. In excitons electrons and holes are bound to each other with a binding energy between 0.3 and 1 eV[53]. By absorbing light and overcoming the binding energy, free charges of both electrons and holes that is called photocurrent will be generate. In perovskite solar cells, p-type and n-type interfaces are the places that the dissociation of exciton happens. After dissociation, diffusion of free charges to the proper transport layer occurs (holes to HTL and electrons to ETL) and electrodes will collect them and produce a photocurrent.

2.4 Advantages of PSCs

Due to their excellent optoelectronic properties, hybrid organic-inorganic perovskites have received a lot of attention recently [49,54–60] and paved the way for other applications in optoelectronic area such as light emitting diode (LED) [61], lasers [62,63], photovoltaics [36–39,64,65], and photodetectors [66]. Perovskite materials have obtained PCE more than 25% in photovoltaic field. Less than a decade, perovskites have been considered as a competent candidate for next generation of solar cells. Fabrication processes and inventive device engineering not only improved our understanding of solar cell physics, but also enhanced the efficiency of devices to more than 20%. An extensive research reveals that long diffusion length, high absorption coefficient, and high hole and electron mobility are only a few of the electrical and optical features of perovskites. Due to large absorption coefficient of perovskite materials, only a thin film of perovskite (around 300 nm) is enough to efficiently absorb and utilize the energy of the photon to achieve a high current from device. It was shown that by focusing electron beam on one side of perovskite layer,

on both electrodes charge carriers collected. This firmly confirms MAPbX3 perovskites have ambipolar behavior [57]. Furthermore, the long diffusion length of MAPbX3 which passes more than 175 μ m [58], can be used in evidence of non-radiative recombination process. Moreover, mixed halide perovskite is a tunable bandgap which supplies a broad variety of bandgaps from 1.48 to 2.53 eV [67].

2.5 Limitation of PSCs

Although perovskite solar cells have marvelous optoelectronic properties, there are some formidable challenges that must be solved before making them commercially available. The PCE of a perovskite solar device that theoretically calculated exceeds 30%[68]. But, in fact, approaching to such a high efficiency is not possible in reality. For application of perovskite solar cells in industry there are some hurdles include hysteresis, low PCE, recombination of charge carriers at the interfaces, and, more specifically, device stability.

2.5.1 Recombination of charge carriers

One of the key reasons that the efficiency of PSCs is not as high as the theoretical calculation is the recombination of free charges in device which causes a reduction in fill factor (FF) and open circuit voltage (V_{OC}) of the perovskite solar cells. There are two types of recombination mechanisms: radiative and non-radiative recombination. In radiative mechanism a recombination occurred between an electron from conduction band and a hole from valence band. In non-radiative recombination, On the other hand, the development of defect states in the crystalline lattice occurs when an electron or hole is confined in the forbidden regions. Non-radiative recombination causes a limitation on the efficiency of PSCs. At the surfaces and at the grain boundaries of polycrystalline perovskite thin films, defects or impurities can be observed. In the structure of the device, the perovskite layer is sandwiched between ETL and HTL. Then, the formation of an interface contains impurities and defect or

trap states seems inevitable. The performance of the device is negatively affected due to non-radiative recombination at the interface.

2.5.2 Hysteresis

The photocurrent hysteresis is another important factor that affects the efficiency of perovskite solar devices. The hysteresis is determined as difference between the behavior of current-voltage (J-V) characterization of the device in forward and reverse scan mode which causes a challenge for defining the precise amount of PCE in PSCs. This means there is a mismatching in the efficiency of perovskite solar cells between forward scan and reverse scan (Fig. 2.11) [69,70]. PSCs' J-V hysteretic activity is influenced by a number of factors such as configurations of perovskite solar cells, voltage range, scan rate, and scan direction [71–77]. The cause of photocurrent hysteresis in PSCs is currently the subject of heavy discussions. The hysteresis phenomenon is believed to be caused by the movement of excess ions and a ferroelectric polarization when a bias voltage is applied [78–80]. Moreover, electron charge traps at grain boundaries or surfaces are suggested as a possible explanation for the prominent hysteresis phenomenon [78]. The reason behind the hysteresis and non-steady state photocurrent is assumed to be slow capacitive charging and discharging during current-voltage measurements [72–75]. Although the hysteresis effect can be influenced by non-steady state photocurrent caused by capacitive charging and discharging, the performance of device with different bias cannot be accounted for entirely by the capacitive effect. It's possible that band bending is what's causing the change in the efficiency. Band bending occurs as a result of ferroelectric polarization, ion migrations, or trapped charges. The hysteresis performance is affected by the electron and hole extraction efficiency. The trapping and detrapping of the charge at the grain boundaries and interface impacts extraction efficiency, and for controlling hysteresis, improving charge extraction is of paramount importance. a depletion region at the interfaces of perovskite will be created due to the partially trapped states. Under forward bias, this results in an alteration in the band structure and decreases charge extraction. By applying large forward bias, the band bending and the depletion region decrease since filling of trap states. Then hysteresis in perovskite solar cells is related to the charge trapping and detrapping. Ion migration causes ion accumulation at interfaces near the electrodes, resulting in the generation of an electric field. Another source of band bending is ion migration, which has a negative impact on photogenerated charge separation and extraction. Another potential cause of modulation of the distribution of the electric field is ferroelectric polarization, which leads to different output in reverse and forward scan.

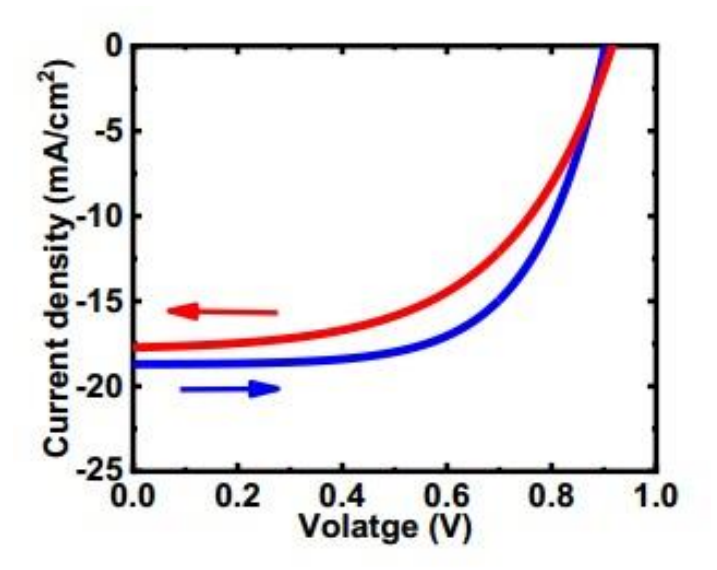


Figure 2.11 Hysteresis phenomenon of a solar cell. Forward and reverse voltage sweeps have different current-voltage properties [80].

2.5.3 Device stability

Recently, the efficiency of a perovskite solar cells approached to more than 20%. Although this efficiency of device in lab-scale is an admirable achievement, stability is one of most important issues of PSCs to make them commercially available. The usual PV modules on the market come with a guarantee that they will maintain their

efficiency for at least 20 years. However, PSCs suffer from degradation when exposed to heat, ambient air, UV radiation, light soaking, and a variety of other variables [81–83]. Various extrinsic and intrinsic factors influence the devices stability. Environmental effects such as moisture and air, not only decompose the perovskite film but also the entire system, are the main extrinsic factors. The stability of PSCs can be adversely affected by exposure to moisture and oxygen in the atmosphere. under moisture conditions, CH₃NH₃PbI₃ begins to hydrolyze (Fig. 2.12) [84], which resulting to perovskite decomposition as follow [85]:

$$CH_3NH_3PbI_3$$
 (s) $\leftrightarrow PbI_2$ (s) $+ CH_3NH_3I$ (aq) (2-4)

$$CH_3NH_3I (aq) \leftrightarrow CH_3NH_2 (aq) + HI (aq)$$
 (2-5)

$$4HI (aq) + O_2 (g) \leftrightarrow 2I_2 (s) + 2H_2O (1)$$
 (2-6)

$$2HI (aq) \leftrightarrow H_2 (g) + I_2 (s) \tag{2-7}$$

Humidity, oxygen, and UV light may induce deterioration. The intrinsic instability of perovskite solar cells is the most serious stability problem. Three main intrinsic factors that contribute to the instability of PSCs are ion migration, thermal instability, and hygroscopicity. Environmental factors determine the degree of hygroscopicity. Under heating, thermal instability causes perovskite to decompose into methylammonium iodide, and lead iodide. Finally, due to the high ionic mobility and using a strong external field through thin layers to assess current-voltage, in all halide perovskites ion migration is practically unavoidable [86]. Furthermore, at interfaces, and grain boundaries the problem is worsened.

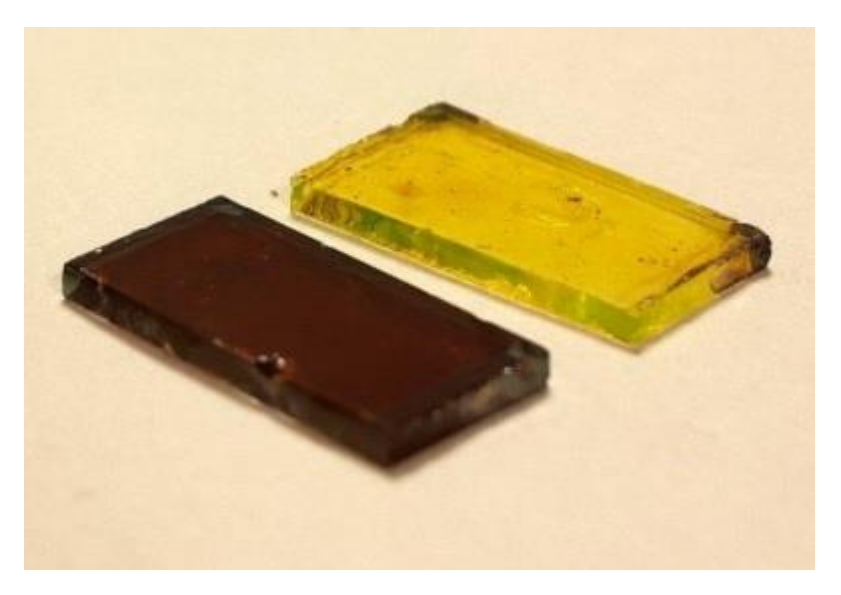


Figure 2.12 Effect of decomposition when the film exposed to air for seven days. Black perovskite films become yellow [84].

2.5.4 Toxicity

In lab-scale, the efficiency of PSCs has approached to silicon PV which commercially available. But, the presence of heavy metals which are used as cations is a significant source of concern in these materials. A PSC with a high performance is composed of lead, which is very hazardous to the ecosystem. While in batteries lead and other harmful chemicals are used, the risk of lead poisoning in the environment is a major issue for the ecosystems. Long-term exposure to hazardous substances, whether from the workplace or the environment, is extremely harmful to human health. Then, perovskite solar cells should be regarded from toxicity point of view. Though tin could be considered as an alternative, the efficiency of these type of PSCs is much lower in comparison with lead-based PSCs. Moreover, in tin-based PSCs, Sn⁺² degrades to Sn⁺⁴ [87]. Consequently, appropriate encapsulation for protection is a great demand for perovskite technology. For recycling modules of PSC suitable standard protocols should be defined.

2.6 Device architectures

Initially, organic-hybrid perovskite solar cells emerged by replacing halide perovskite, as a light absorber, and spiro-OMeTAD, as a solid-state hole layer, with dye and liquid electrolyte respectively in the mesoscopic structure (figure 2.13a) [31,34]. This pioneering merit attracted interest from OPV community. Later, by inserting organic-hybrid perovskite materials between HTM and ETM, the planar structure was introduced [38,88,89]. Depending on which material meets incident light first, the planar structure can be categorized into conventional n-i-p (figure 2.13b) and inverted p-i-n (figure 2.13c). Afterwards, a mesoscopic p-i-n structure (Figure 2.13d) was introduced as well [90]. The architecture of the device specifies the selection of electrodes (cathode and anode), charge transport materials (CTM), fabrication procedure, and, consequently, device performance.

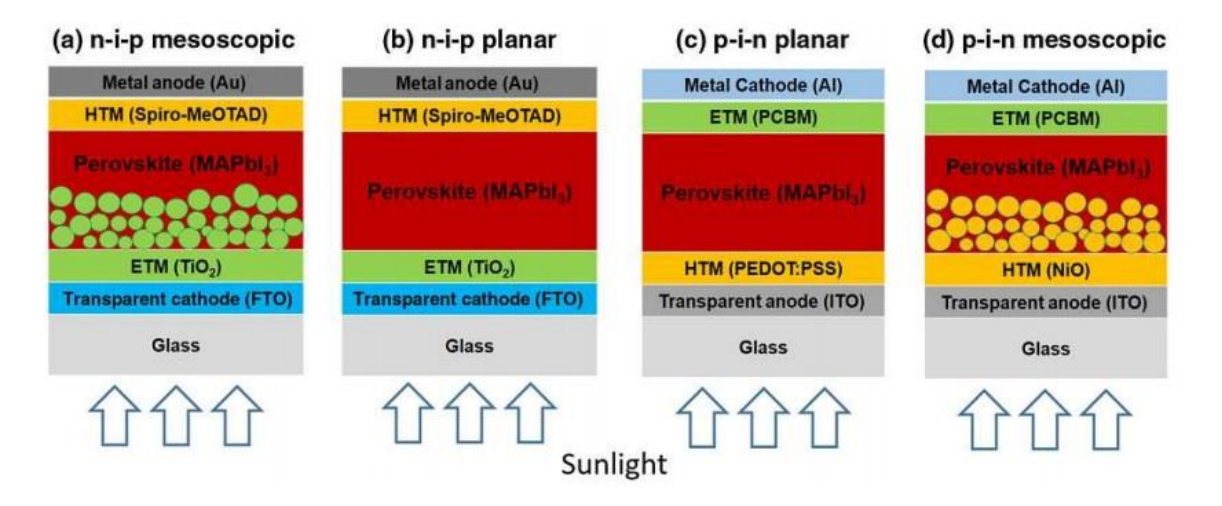


Figure 2.13 (a) n-i-p mesoscopic, (b) n-i-p planar, (c) p-i-n planar, and (d) p-i-n mesoscopic architectures of PSCs [34].

2.6.1 Conventional n-i-p structure

The first PSC architecture was n-i-p mesoscopic structure and it is also commonly used in the manufacturing of perovskite devices [40,91]. As is shown in figure 2.13a, the structure is composed of a fluorine doped tin oxide (FTO) coated glass as a cathode, a thin layer of ETM (\sim 50 nm) such as TiO₂, a thick film of mesoporous metal oxide (~150-300 nm) such as Al₂O₃, or TiO₂ that has been pierced by perovskites, perovskite film (300 nm and more), a hole transport layer (HTL) (~200 nm) like spiro-OMeTAD, and finally 70-110 nm of Ag or Au as a metal anode. To get rid of current leakage between interfaces and to enhance charge collection and light harvesting, the mesoporous layer is utilized. By using mesoscopic layer with a 150-200 nm thickness, the device shows better efficiency than a device with a thick (> 500 nm) porous layer due to improvement in the crystallinity of perovskite film [32,92]. In addition, the thickness of mesoporous layer has an influence on the morphology of the perovskite layer [32]. It is reported that by employing mp-TiO₂ layer with thickness less than 300 nm, a uniform and homogenous perovskite film can be achieved and filling of nanopores has been improved as well. Filling nanopores and fully coverage of perovskite film increases separation of charge and collection of them at the interface. The n-i-p mesoscopic structure is still commonly used and a high PCE (22.1%) of this structure is reported [93].

The mesoscopic structure has been developed into the planar structure (Figure 2.13b). By precisely controlling the interfaces, perovskite formation, electrodes and charge transport layers, some researcher discovered that high efficiency can be achieved even without applying a mesoporous layer [38]. After accurate tuning of the interfaces, a 19.3% PCE was obtained in the planar n-i-p device [38]. Although open circuit voltage (V_{OC}) and short circuit current (J_{SC}) of planar n-i-p devices are better than mesoscopic devices, the hysteresis behavior of planar device is more severe due to unbalanced transportation of electron and hole [34]. Thus, commonly

a thin mesoporous layer (\sim 150 nm) is coated as a buffer layer in the n-i-p devices [89].

2.6.2 Inverted p-i-n structure

The p-i-n structure can be acquired when first HTL is deposited (figure 2.13c). A typical inverted p-i-n device includes indium tin oxide (ITO) coated glass as a substrate, conducting polymer like poly(3,4 ethylenedioxythiophene) poly(styrene-sulfonate) (PEDOT:PSS) as a HTL with thickness of 50-100 nm, perovskite layer (~300 nm), an organic ETL (hole blocker) for instance [6,6]-phenyl-C61- butyric acid methyl ester (PCBM) (~60 nm), and Al or Ag as a metal contact. In fact, the planar structure has made it simple for OPV researchers to move into the perovskite field. The efficiency of this type of PSCs increase quickly by progressing on material preparation and deposition process. For example, the using of NiO and ZnO semiconductors were reported successfully as a HTL and ETL respectively [94,95]. Moreover, PSCs with the mesoscopic p-i-n structure (figure 2.13d) is fabricated by engagement of oxide hole transport materials.

2.7 Fabrication methods

To reach a high performance in PSC devices, perovskite films need to a have good morphology and uniformity, proper crystallinity, and high purity. To approach these quality requirements, keeping the crystallinity under control, engineering of composition and interfacial layers are of paramount importance. As a serious issue, the deposition method plays a significant role on the performance of device even when the materials are same. Generally, deposition processes are divided into four different approaches as follow: one-step method [31], two-step method [91], vapor-assisted method [96], and dual-source vapor method [37].

2.7.1 One-step solution method

Due to low-cost fabrication and simple preparation, one-step solution method (figure 2.14a) is frequently used for PSCs production. To form the precursor solution in this method, lead halide materials (PbX2, X = Cl, Br, or I) are mixed with an organic halide like methylammonium iodide (MAI) inside of dimethylformamide (DMF) or γbutyrolactone (GBL) or dimethyl sulfoxide (DMSO) as a solvent. Spin coating method is the most commonly method used for deposition of precursor on the substrate. Although for solution-based deposition approaches there are other techniques such as doctor blade [97], spray coating [98], and inject printing, perovskite devices in which these techniques are employed exhibit lower efficiency in comparison to that of devices in which spin coating method is employed. The main reason is that in those techniques controlling on morphology of the film is hard. In this method some major factors should be precisely controlled such as the level of oxygen and humidity in environment, substrate, processing temperature, and etc. Though a PCE over 20% has been achieved [38], attaining a homogeneous and uniform thickness over large areas is a drawback of this method that can be improved by employment of additives and anti-solvent.

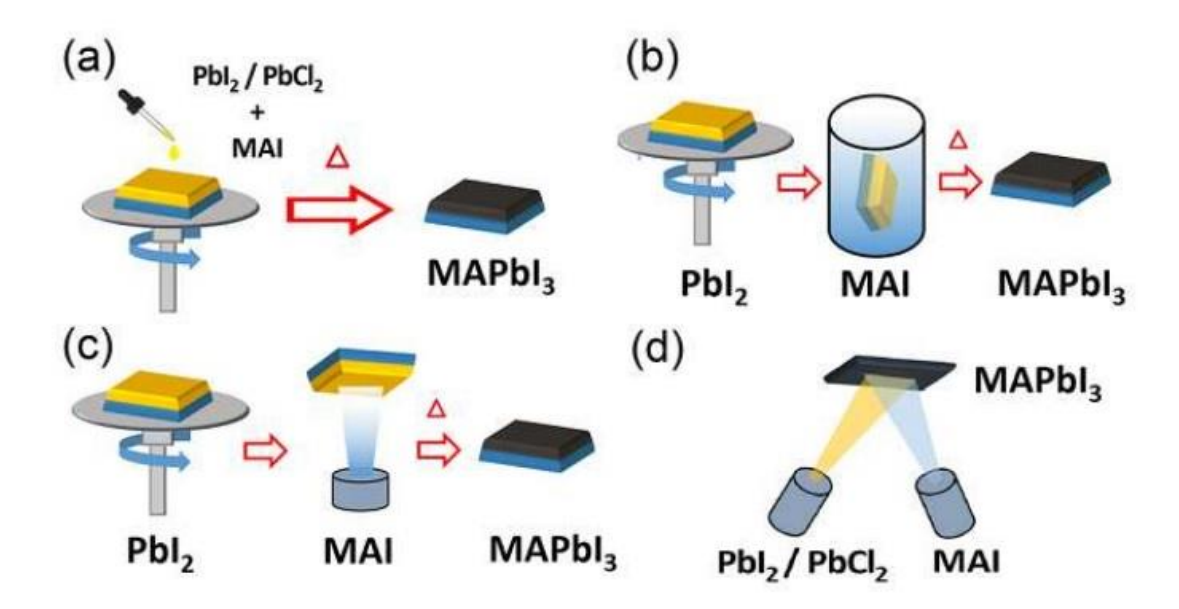


Figure 2.14 Representative manufacturing approaches for perovskite thin layers: (a) one-step solution method; (b) two-step solution method; (c) vaporassisted solution method; (d) dual-source vapor method [34].

Additives and antisolvent leads to formation of uniform perovskite layer be formed due to growing grains and decoupling nucleation. By incorporation of additives or antisolvents, the crystallization process is retarded, which leads to a uniform intermediate phase [90]. In order to have perovskite phase with improved crystallinity with pinhole-free films, thermal annealing is essential [34].

2.7.2 Two-Step solution method

This method firstly was applied by Grätzel's group [91] to fabricate a high efficiency PSC. In this process which also is also called sequential deposition process, the PbI₂ precursor is first spin coated and the coated substrate is subsequently immersed in the MAI solution. For deposition of MAI on PbI₂ layer, spin coating method is used as well. The film produced using this method is more uniform and denser as compared to that of the one step deposition method [99]. Inadequate mixing of precursors

during sequential deposition results in incomplete conversion of precursors to perovskite, which can be regarded one of disadvantages of this method. Recently, some new techniques solved this problem. mixing some additives such as H₂O [100] or DMSO [101] inside PbI₂ precursor form intermediate state that can modify the speed of a chemical reaction between MAI and PbI₂.

2.7.3 Vapor-assisted solution method

As is shown in figure 2.14c, in this method MAI is deposited on PbI_2 layer by a vapor technique [96]. The obtained morphology and grain size in this process is well-controlled and peeling of film is successfully hindered. In vapor-assisted deposition method accomplishing a fully conversion perovskite layer is possible, but one of the drawbacks for practical form is that the whole procedure normally takes several hours to complete. Moreover, the PCE of perovskite devices fabricated using this method is comparatively low (\sim 12%) [102].

2.7.4 Dual-source vapor method

In 1999 Mitzi's group used dual-source vapor method for perovskite film preparation [103]. After some progresses in this method (Figure 2.14d), the first planar perovskite solar cell with an efficiency over 15% was fabricated by Snaith's group [37]. The advantages of this method are perfectly homogenous and pinhole-free perovskite layers, completely coverage of surface [104]. The big issue of this process is thermal stability, means for precisely deposition, temperature controlling is needed.

2.8 Electron Transport Layer (ETL)

The task of transferring the generated electron in perovskite layer is done by an electron transport layer (ETL). Based on their functions, electron transport layers are divided into three different types. The only duty of the first type of ETLs, which are

n-type materials, is the transfer of electron. Mesoporous TiO₂ is a good example for this type. Conventionally, between ETL and conductive glass a blocking layer is embedded to prevent recapturing of electrons by hole transport layer. Nonstructural materials are typically used in this type of ETL, such as nanorod, nanotube, nanowire, or nanocrystalline mesoporous layer [105,106]. Mesoporous TiO₂ is usually used as an ETL. By using mesoporous TiO₂ in PSCs some issues have arisen. It requires a high annealing temperature (500 °C), which increases fabrication cost and is not suitable for flexible devices. Also, TiO₂ can function like a catalyst to decompose perovskite The role of the second type of electron transport layer is as same materials [107]. as first type, however, it is employed in inverted structure of perovskite solar cells. Normally a dense thin film, as a blocking layer, is used between this layer and metal contact. Organic [6,6]-phenyl-C61 -butyric acid methyl ester (PCBM) is an instance for this type of electron transport material [108,109]. The third kind of electron transport layer acts both as blocking layer and electron transferring layer. It is typically located between conductive glass and perovskite layer. SnO_x in planar structure is a good example [110]. To maximize the shunt resistant, the layer needs to be dense and thin enough to minimize series resistance of device. There are three types of materials in the electron transport layer as follow: organic materials, inorganic materials, and polymers. The conduction band (CB) of an ideal electron transport material lines up with the conduction band edge of perovskite materials. This causes an electron transfer before the recombination of electron and hole, and formation of uniform contact with perovskite layer as well. Besides, in n-i-p structure of PSCs, to maximize the absorption of incident photon by perovskite, the electron transport layer requires to be transparent [111]. Figure 2.15 shows various materials as the ETL in PSCs [112].

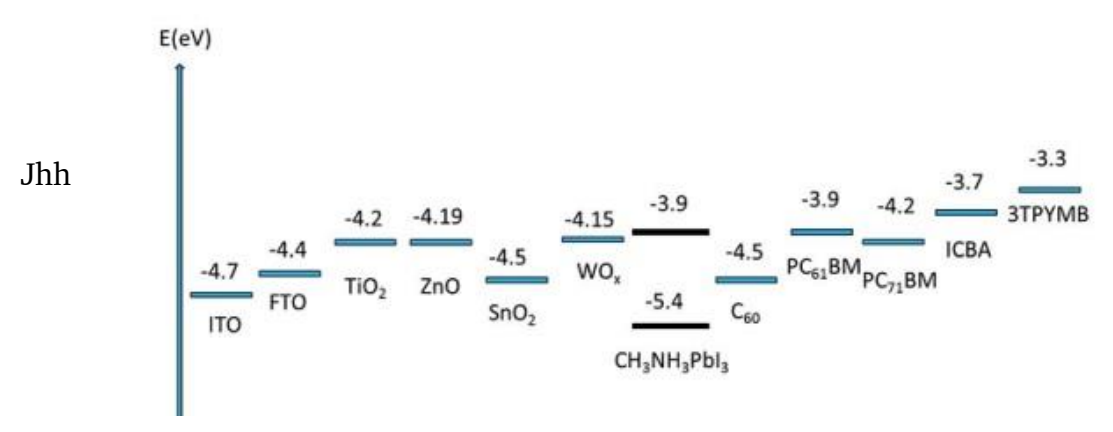


Figure 2.15 Materials for ETL in PSCs showing conduct band minimum/LUMO levels [112]

2.9 Hole Transport Layer (HTL)

An ideal hole transport layer (HTL) should have high conductivity, high stability, high hole mobility, and line up with valance band (VB) of perovskite. In perovskite solar cells all polymer, organic, and inorganic materials can be utilized as a hole transport layer meeting the energy level alignment criteria. Figure 2.16 depicts band diagram with highest efficiency of HTL which are used in PSCs [113].

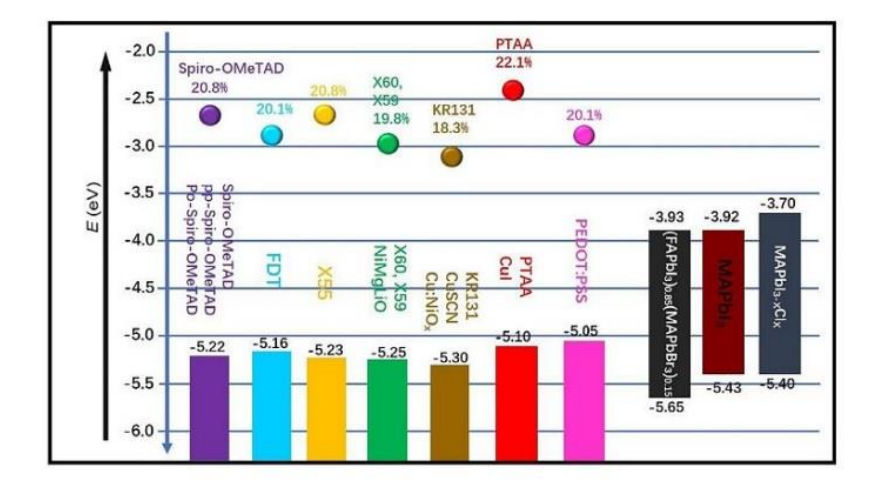


Figure 2.16 Representative HTMs utilized in PSCs, evolving the most efficient perovskite light absorbers, are shown in schematic energy diagram [113]

2.9.1 Organic hole transport materials

Organic solvents can dissolve small organic molecules efficiently. Due to small size, they can have a good contact with perovskite layer regardless of perovskite morphology. Adjusting its functional groups will alter all of its physical properties. Further, since most of elements are available plentifully like hydrogen, nitrogen, and carbon, the price of these type of hole transport layer is potentially low.

2,2,7,7-tetrakis(N,N-di-p-methoxyphenylamine)-9,9-spirobifluorene (Spiro-OMeTAD) is one of the most common organic hole transport materials used in PSCs. Before its employment in PSCs, this material had been used in dye-sensitized solar cells. It shows low conductivity (10⁻⁵ S cm⁻¹) and hole mobility (<10⁻⁴ cm² V⁻¹ s⁻¹). To enhance these properties, additives are required. 4-tert pyridine (tBP) and lithium bistrifluoromethanesulfonimidate (LiTFSI) were used in combination with Spiro-OMeTAD to improve performance. However, PSCs' stability is also affected. Since LiTFSI is hygroscopic and tBP is corrosive, perovskite materials suffer from these deleterious effects. Consequently, new organic hole transport materials have been proposed such as thiophene derivatives, triazine derivatives, and pyrene derivatives. The efficiency of some of them is consistent with Spiro-OMeTAD [114].

2.9.2 Polymer hole transport materials

The mobility and conductivity of polymer hole transport materials are great. Attaining the suitable organic solvent for dissolving polymers without dissolving perovskite materials is more difficult than finding the proper organic solvent to dissolve organic hole transport materials. Consequently, many polymer hole transport materials have an alkyl side chain to improve solubility in commonly used solvents. The contact area among perovskite and polymer, on the other hand, is restricted due to the size, specifically in PSCs with a meso-porous electrode [39,60]. Nevertheless, polymer hole transport materials are usually more stable than small organic

materials, especially in terms of thermal stability. The band structure can be adjusted by modifying the functional group of the units as well as the degree of polymerization. Poly(3-hexylthiophene-2,5-diyl) (P3HT) and Poly[bis(4- phenyl)(2,4,6-trimethylphenyl)amine] (PTAA) are the most widely used polymeric hole transport materials. The highest efficiency employing PTAA in PSC devices is 22.1% [115]. However, in order to enhance the performance of device, P3HT and PTAA require dopants such as tBP and LiTFSI. These polymer materials' stability also needs to be improved. As figure 2.17 shows, the stability of the perovskite with the PTAA is lower than that of the perovskite with doped Spiro-OMeTAD [116].



Figure 2.17 Stability of perovskite materials with various hole transport layers [116]

2.9.3 Inorganic hole transport materials

Crystallization of the HTL could decrease contact at the perovskite/HTL interface. Inorganic hole transport materials are typically amorphous semiconductors. After deposition on the substrate, some inorganic materials require

heat treatment. Since high temperature process can deteriorate perovskite, most inorganic hole transport materials can only be used in PSCs with an inverted configuration. Inorganic hole transport materials have a higher stability in comparison to that of polymer/organic materials HTL, which is an advantage in PSCs.

The two inorganic hole transport materials commonly used in PSCs with high efficiency and stability are CuSCN and NiOx. Reactivity of CuSCN with metal contacts had previously been an issue, later on it was improved by introducing a graphene layer between CuSCN and Au [117].

2.10 Device characterization of solar cells

2.10.1 Current-Voltage (I-V) measurement

One of the most fundamental measurements in semiconductor devices is the current-voltage (I-V) measurement. This is achieved by recording the current passing through the device while voltage across it is changing. To provide an understanding of how this process works, equivalent circuit model of solar cells is presented. A solar cell's equivalent circuit with a double-diode model is shown in Figure 2.18 [118]. Here, R_{SH} and R_{S} represent shunt and series resistances, respectively, I_{L} is photo current generated by incident photon. These two diodes present recombination in solar cell. By applying a voltage V through the circuit, the current I can be obtained as

$$I = I_{01} \exp(\frac{V - IR_S}{2kT/q}) + I_{02} \exp(\frac{V - IR_S}{kT/q}) + \frac{V - IR_S}{R_{SH}} + -I_L$$
(2-8)

Here, I_{01} and I_{02} show diode saturation currents. Equation (2-8) is the primary equation that defines a solar cell's current response in both light and dark conditions.

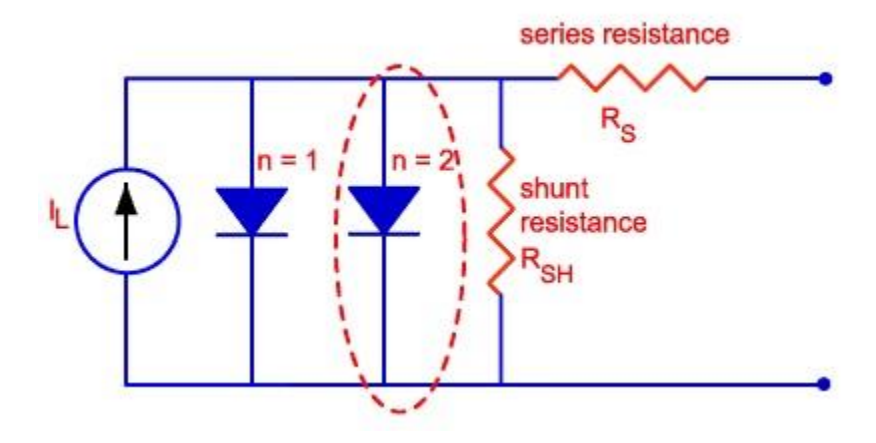


Figure 2.18 Equivalent circuit of solar cells with double-diode model under illumination [118].

2.10.2 Light I-V measurement

The measurement to define the power conversion efficiency of a solar cell under light is called light I-V. The photocurrent will be induced when the cell is exposed to light. The IV curve we get in this case, according to equation above, will be the red curve in Figure 2.19. An IV curve has four essential parameters. The first is the open-circuit voltage (V_{OC}), which is the voltage when there is no current. Short-circuit current (I_{SC}) is the second one that determines the current flow when the voltage across the device is zero. P = I*V is the formula for calculating the output power of a solar cell. So, as blue curve in figure 2.19 depicts, the output power of the solar cell vs. voltage can be acquired. Obviously, it depends on voltage and that the impedance has to be matched to achieve optimum output power. Fill factor (FF) is the third parameter that defines how square the IV curve is, and can be achieved as

$$FF = \frac{P_{max}}{V_{OC} \times I_{SC}} = \frac{\max(I \times V)}{V_{OC} \times I_{SC}}$$
(2-9)

As shown in figure 2.19, fill factor can be acquired from area ratio of A and B as well [119]. The last and most important parameter of a solar cell is efficiency, which is described as

$$\eta = \frac{P_{max}}{P_{irradiation}} \tag{2-10}$$

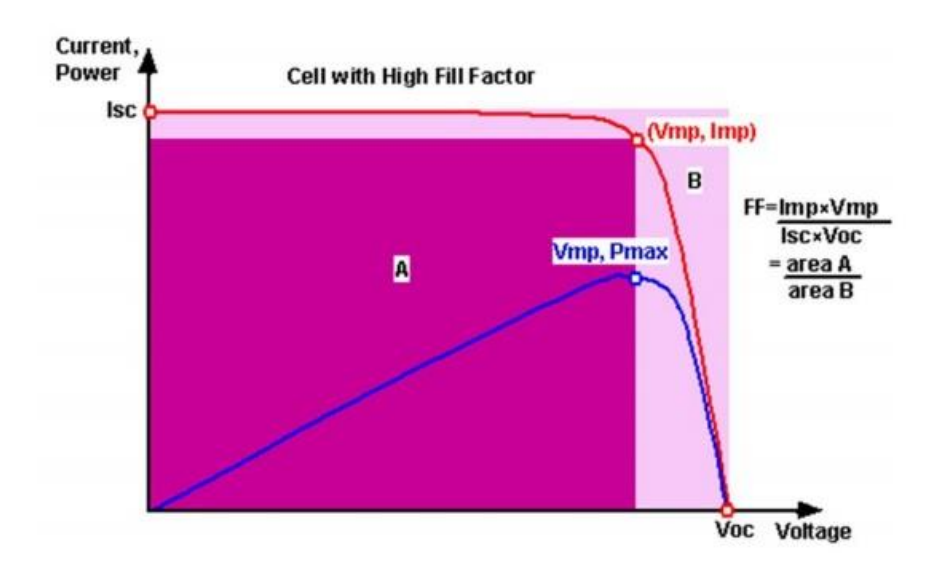


Figure 2.19 Light IV curve and output power vs. voltage curve of a solar cell [119].

IV measurement can also be used to diagnose a solar cell's resistance problem. To achieve higher efficiency, the product of FF, V_{OC} and I_{SC} should be as high as possible, in accordance with equation (2-10). Material properties and device structure play a major role in determining V_{OC} and I_{SC} . Whereas, the series resistant R_S and shunt resistance R_{SH} have a major impact on FF.

According to equation (2-8), from slope of the IV curve, the R_S and R_{SH} can be accomplished as follow:

$$R_{S} = \frac{\partial V}{\partial I} |_{V=VOC}$$
 (2-11)

$$R_{SH} = \frac{\partial V}{\partial I} |_{V=0}$$
 (2-12)

The difference in the IV curve between an ideal solar cell and a solar cell with a resistance is shown in Figure 2.20. The solar cell with a resistance issue (the red curve) has a substantially lower fill factor as compared to that of the ideal curve. R_S =0, and R_{SH} = ∞ for an ideal solar cell. The section of the IV curve near to the open-circuit voltage will shift to the left as the series resistance increases. As is seen in Figure 2.20, the part close to the short-circuit point will decrease as the shunt resistance decreases.

So, by measuring the IV curve of the solar cell, series and shunt resistances can be calculated.

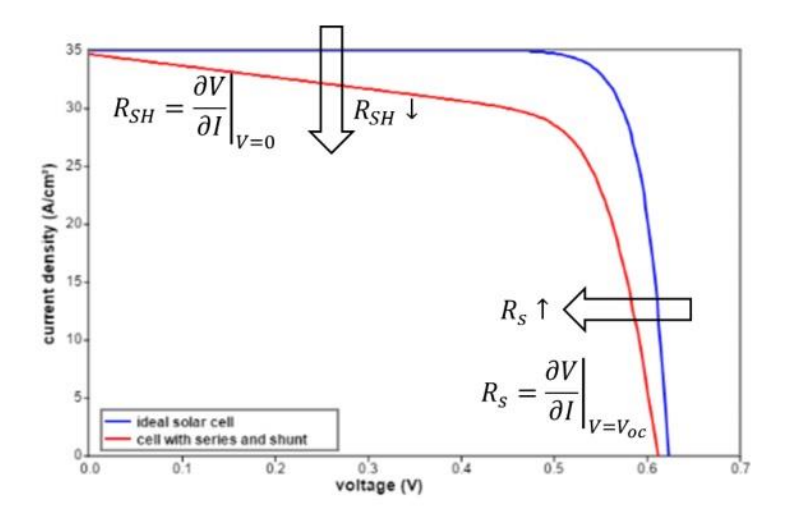


Figure 2.20 A comparison of IV curves of an ideal solar cell (blue curve) and a solar cell with resistance issues (red curve) [119].

2.10.3 Dark I-V measurement

For calculation of shunt and series resistances dark IV can be employed. It is more precise than the resistance measurement based on the IV curve under illumination due to influence of light IV curve by other factors. For instance, even when there is no resistance issue, but if the device has a low diffusion length and low charge collection, the IV curve will move down, leading to an underestimation of R_{SH} and an overestimation of R_S if we use light IV measurements are used. By applying dark IV we will not have this problem.

The recombination mechanism in solar devices can also be studied employing dark IV. In the dark mode, when we impose a bias across the solar cell, the current that flows through the cell should be

$$I = I_{01} \exp(\frac{V - IR_S}{2kT/q}) + I_{02} \exp(\frac{V - IR_S}{kT/q}) + \frac{V - IR_S}{R_{SH}}$$
 (2-13)

In this equation unlike equation 2-8, there is no photocurrent term (I_L). Figure 2.21 demonstrates a standard dark IV curve [120]. At low bias, the shunt current, which is the third term of equation (2-13), dominates the dark current. Low shunt resistance in solar cells is usually caused by pinholes in the i-layer or an undesired shunt direction. There will be two exponential zones as the applied bias increases, which are dominated by those two exponential terms in equation (2-13). The dark current will be saturated and restricted by the series resistance as the bias increases more. We can derive information about shunt resistance and series resistance from the low bias and high bias zones, respectively, because those territories are dominated by shunt and series resistances, respectively.

The ideality factor for the first exponential region is 2. This is the current in a solar cell's depletion zone that is dominated by recombination. As shown in equation (2-14), I_{01} which is called the diode saturation current, has information about minority lifetime in the depletion zone [121]. Then, the minority lifetime in solar cell can be evaluated by using first exponential region.

The recombination in the neutral zone dominates the second exponential term, resulting in 1 ideality factor. The recombination rate is also determined by the saturation current in this region, which is exhibited in equation (2-11) [121,122].

$$I_{01} = \frac{qAn_i x'}{2\tau}$$
 (2-14)

$$I_{02} = qA \left\{ \frac{D_n n_{p0}}{L_n} + \frac{D_p p_{n0}}{L_p} \right\}$$
 (2-15)

In the two equations above, x' is effective width of depletion layer, n_i is the concentration of intrinsic carrier, τ is the recombination lifetime in the depletion region, D_n and D_p are the diffusion coefficient of electrons and holes respectively, n_{p0} and p_{n0} are the concentration of minority in the neutral region, L_n and L_p are the minority diffusion length of electrons and holes.

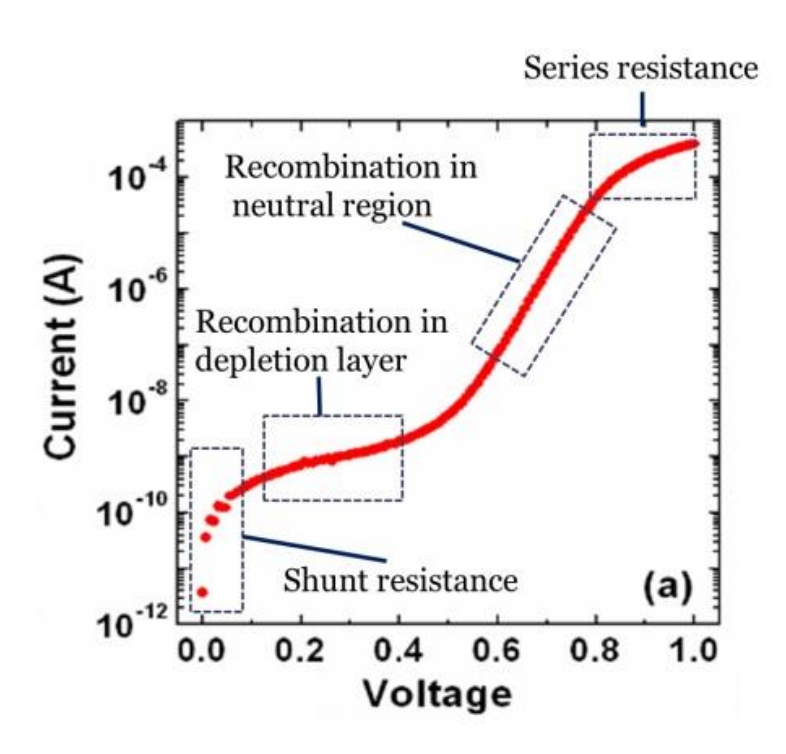


Figure 2.21 In a solar cell, the dark IV curve can be utilized to provide information on the recombination mechanism and resistance issue [120].

2.10.4 Quantum Efficiency

External Quantum efficiency (EQE) is a diagnostic method for troubleshooting photon absorption and charge collection issues in solar cells. It is described as the ratio of extracted carriers to number of incident photons at each wavelength:

$$EQE = \frac{\text{number od collected carriers }(\lambda)}{\text{number od incident photons }(\lambda)}$$
 (2-16)

The EQE of a solar cell indicates how effectively photons are harvested at each wavelength. It provides key information about the carrier loss locations and indicates where we can optimize the device. The experimental setup of the EQE measurement utilized in this thesis study is shown in Figure 2.22 [123]. Photons with various wavelengths are produced by using a white halogen bulb. Photons of specific wavelengths are obtained using a monochromator and optical filters. After being diffracted on the slits, the wanted wavelength will pass through the monochromator by setting a suitable incident angle. The optical filter in the monochromator is used to block unwanted harmonics induced by higher orders of light diffraction. In order to convert D.C signal to A.C signal, an optical chopper is applied. Commonly, a chopper with a frequency of 13 Hz is used to reduce noise from the environment. The signal is gathered from D.U.T and sent to the pre-amplifier. Thereafter, by synchronizing the signal with the chopper, a lock-in amplifier is used to minimize noise.

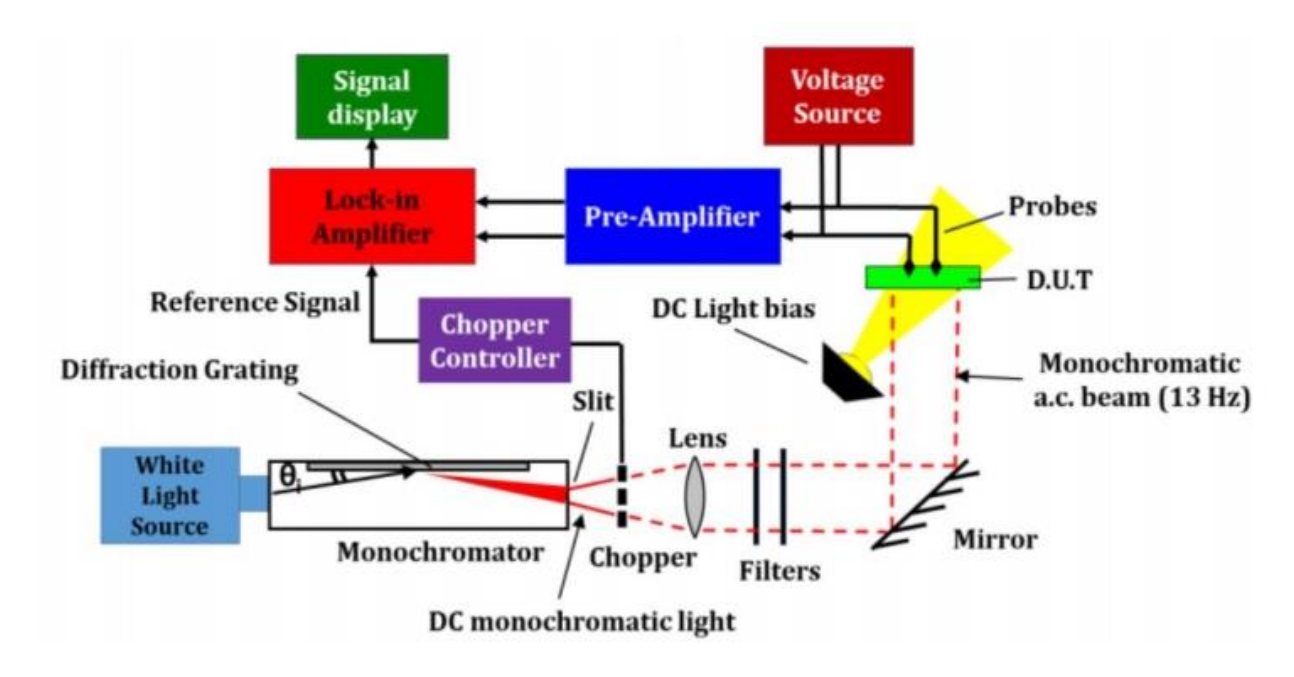


Figure 2.22 A diagram of the QE experimental setup. D.U.T is a reference solar cell or a sample solar cell [123].

The EQE signal should ideally be 100%, as shown in Figure 2.23 by the brown curve. Solar cells, on the other hand, suffer from a number of energy losses, including absorption and recombination losses. The black curve in Figure 2.23 illustrates a common EQE [124]. In both the short and long wavelength regions, we can see a noticeable signal reduction. Signal loss in EQE measurements can emerge for a variety of reasons, then we should interpret the EQE data based on the solar cell structure and material properties. The signal loss in the short wavelength region in Figure 2.23 may be due to front-layer parasitic absorption or front-surface recombination. Inadequate absorption and thus signal loss in the long wavelength zone may be the consequence of insufficient main layer thickness. The total EQE signal loss may be due to short diffusion length or a reflection loss in the main layer. Since there is no absorption above a certain wavelength, there would be no EQE signal.

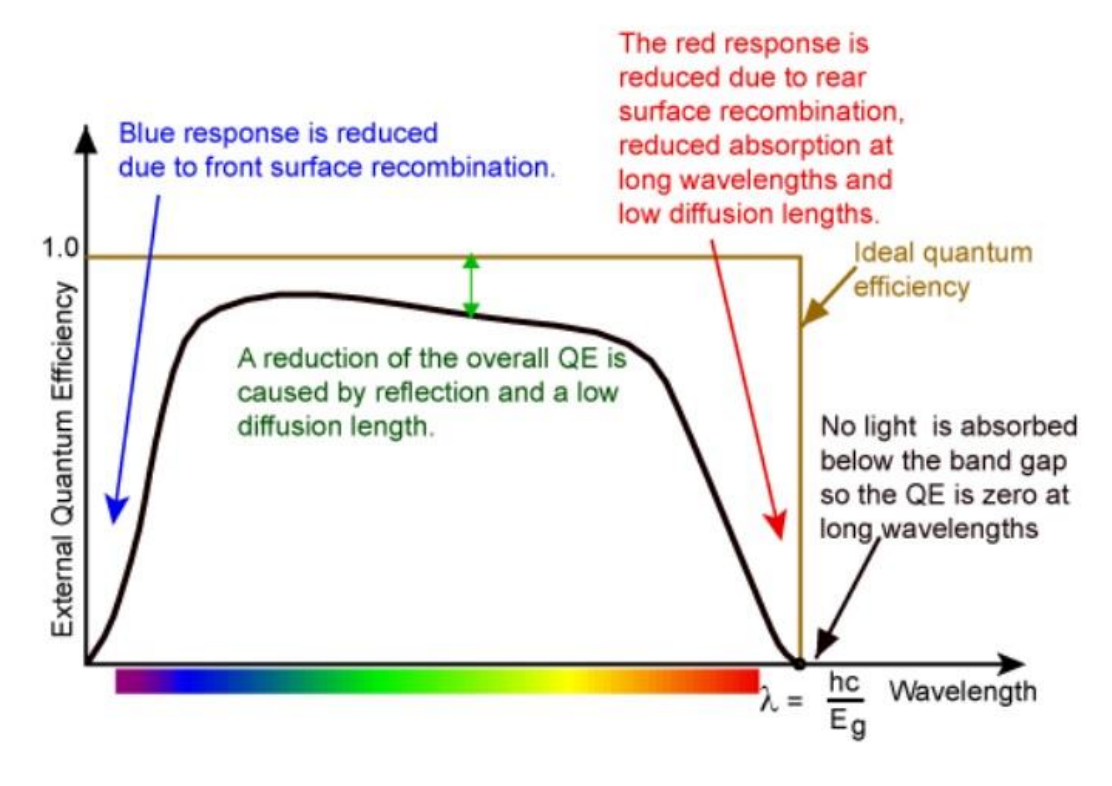


Figure 2.23 An ideal QE curve and a typical QE curve [124].

The EQE can be represented in the following way using mathematical model on a finite solar cell with back surface recombination[125].

$$EQE = \frac{1}{1 - \frac{1}{\alpha^2 L^2}} \left\{ 1 - \frac{1}{\alpha L} \left[\frac{\frac{SL}{D} \left\{ \cosh\left(\frac{t}{L}\right) - e^{-\alpha t} \right\} + \sinh\left(\frac{t}{L}\right) + \alpha L e^{-\alpha t}}{\frac{SL}{D} \sinh\left(\frac{t}{L}\right) + \cosh\left(\frac{t}{L}\right)} \right] \right\}$$
(2-17)

By fitting this equation to the measurement data, QE measurement can reveal further information about the device, including the back-surface recombination velocity and diffusion length.

In several practical cases, equation (2-17) can also be more clarified. For instance, when a solar cell has a high absorption coefficient and is illuminated by high energy

incident photons. In this situation, t \gg L, α L \gg 1. Equation (2-17) can be simplified to

$$EQE = \frac{\alpha L}{1 + \alpha L} \tag{2-18}$$

The diffusion length can be determined from the slope of the curve if EQE vs. absorption coefficient (α) curve is drawn.

IMPACT OF UV EXPOSURE OF ITO/PEDOT:PSS SUBSTRATES ON THE FUNCTIONALITY OF INVERTED-TYPE PSCs

3.1 Introduction

PEDOT: PSS is commonly used as a conducting hole transport layer for producing inverted-type perovskite solar cells. By applying DMSO (dimethyl sulfoxide) and zonyl as additives in PEDOT: PSS the PCE of device was increased to 12% in inverted configuration with PCBM as a ETL as was reported by Adam et al [126]. Low hysteresis and outstanding stability were attributed to the well-designed devices. By altering the perovskite of Methylammonium Lead Iodide (MAPbI₃) perovskite with FAPbI₃, the PCE has surpassed 20% [60].

The efficiency of inverted-type PSCs has been improved using a variety of techniques since the manufacturing of the first inverted PSCs, including interface design [127,128], control of the perovskite layer morphology [129,130], employment of various HTLs [131] and ETLs [111,128], and optimization of the structure [132]. Perovskite solar cells in inverted type, on the other hand, have a lower PCE than conventional PSCs. Initially, PEDOT: PSS was used to improve the extraction of hole as a hole transport layer by reducing electron leakage between active layer and ITO in organic solar cells. Despite the fact that PEDOT: PSS is a frequently utilized hole transporter in organic photovoltaics, it still needs to be improved. As a result, PEDOT: PSS with improved morphology, conductivity, and stability is attracting a lot of attention. To achieve these purposes, a variety of techniques have been applied for instance doping PEDOT: PSS with additives [133], adding solvent in PEDOT: PSS [134,135], thermal annealing [136]. PEDOT: PSS treatment has been illustrated in

the literature to have a major impact on the performance of organic as well as inverted type perovskite solar cells [133–135].

In this chapter by using a simple method we investigate the performance of PSCs when PEDOT: PSS layers are exposed to UV radiation is investigated. UV radiation was used to illuminate the PEDOT: PSS surface coated on ITO substrate for 5 to 15 minutes, and the impact of the illumination period on the performance of device was studied.

3.2 Experimental

Initially, all ITO glasses used as a substrates were etched by employing the mixture of HCl: H2O: HNO3 (4.6:5:0.4) for 45 min. In order to clean substrates entirely, all substrates were ultrasonicated with acetone at room temperature for 20 min and then with isopropanol at 60 °C for 45 min respectively. UV light was applied for 30 min on all ITO coated glasses. As a HTL, the solution of PEDOT: PSS was spin-coated at 1000 rpm for 40 s and then to eliminate any remaining moisture, thermal annealing for 30 min at 120 °C was carried out at ambient air. Later, UV radiation with different time interval from 5 to 15 min was applied on PEDOT: PSS films. Non-treated PEDOT:PSS films on non-treated ITO substrates were also used as references. CH₃NH₃PbI_{3-x}Cl_x Perovskite films were produced according to the procedures in the literature [137]. For preparing the CH₃NH₃PbI_{3-x}Cl_x solution, the mixture of PbCl₂, PbI₂, and CH₃NH₃I was dissolved in DMF with1:1:4.4 molar ratio. Prior to use, the precursor solution of perovskite was stirred at 50 °C for one night and filtered with a PTFE filter (0.45 µm). The solution of perovskite was coated at 1500 rpm for 25 s and 2000 rpm for 6 s at room temperature and thermal annealing at 105 °C for 40 min was carried out. To make the PCBM layer, 20 mg of PCBM was dissolved in chloroform and chlorobenzene mixture (500 µl: 500 µl) and then coated at 1500 rpm for 15 s and 2000 rpm for 15 s. Finally, 100 nm of Al was deposited with the evaporation method in vacuum system under 2×10^{-6} mbar.

For recording I-V measurements, Keithley appliance with software of LabVIEW was used. In order to have AM 1.5 circumstances, a xenon arc lamp-based solar simulator, which produce white light with the power of 100 mW/cm2 was used that can be calibrated with a silicon diode. LabVIEW software can measure not only the photovoltaic characteristics of devices such as FF, Voc, Jsc, and efficiency but also parasitic resistances including the shunt resistance (R_{SH}) and the series resistance (R_S) from the J–V graphs. The hysteresis factor (HF) of devices was obtained by measuring J-V in reverse and forward bias from -1.5 to 1.5 V and vice versa under irradiation of light. With internals of 5 nm, the EQE was attained at wavelengths ranging from 300 to 900 nm. A two-point probe tool was used to determine the sheet resistances of the coated PEDOT: PSS layers. The ohmic functioning of the I-V graphs in the dark was used to assess the resistances of UV-treated and non - treated PEDOT: PSS layers. To record the absorption spectra of PEDOT: PSS films, Perkin Elmer UV-VIS spectrometer was used. In order to analyze the surface morphology of both PEDOT: PSS and perovskite films, FEI Quanta FEG 250 scanning electron microscope (SEM) applied. XRD technique was used to investigate the crystallinity of perovskite films, as well as pristine and UV-induced PEDOT: PSS layers. Electrochemical impedance spectroscopic (EIS) experiments were performed with the Gamry Reference 3000 model appliance and a three-electrode device that included an electrochemical cell. PEDOT: PSS films with different treatment were used as a working electrode. For the counter and reference electrodes platinum wire and saturated calomel electrode (SCE) were employed, respectively. As an electrolyte, 0.1 m LiClO4 was chosen. The all spectra were matched with an equivalent circuit model. EIS spectra were recorded at frequencies ranging from 0.01 to 105 Hz.

The Shimadzu SPM-9600 device was used to launch AFM and KPFM analyses. For AFM measurement, the dynamic mode was engaged. In KPFM probe was employed to determine potential of the surface.

3.3 Results and discussion

Surface morphology images of original and UV induced PEDOT: PSS samples for various time durations ranging from 5 to 15 minutes which are achieved from SEM analysis are illustrated in Figure 3.1 [138]. As shown in the figure 3.1, all of the films have a smooth morphology. In order to better comprehend and analyze the modifications in the morphological properties of the obtained PEDOT: PSS layers, AFM measurements were performed. AFM samples of pristine and UV-treated PEDOT: PSS layers for various time periods are shown in Figure 3.2a–d [138].

The roughness average and the root mean square roughness (Rq) attained from AFM analysis are identical, with the major difference being the absolute values of mean squared of the surface roughness profile. Due mainly to the amplitude squaring in its evaluation, the Rq is more susceptible than the mean roughness to valleys and peaks [139]. The values of rms roughness for untreated and UV-induced PEDOT: PSS layers for 5, 10, and 15 min were as 1.434 nm, 2.31 nm, 1.250 nm, and 1.240 nm, respectively. All of the surfaces seemed perfectly smooth. The vertical length between the minimum valleys and the maximum peaks on profiles of the film is depicted on the graphs. For nontreated PEDOT: PSS layer the maximum height scale is 21.42 nm, while for UV-treated PEDOT: PSS layer for 5, 10, and 15 min the values are 26.64 nm, 12.46 nm, and 16.42 nm, respectively. Though profiles of the height scale differ slightly, the height ranges are analogous. The films' features, on the other hand, were lightly dissimilar. The nontreated PEDOT: PSS films had a compact film morphology, while the surface of UV-treated PEDOT: PSS films had various sizes of glossy grains. According to the literature, by applying electric field on the PEDOT: PSS films the surface morphology of films can be changed [140]. Lim et al. noticed irregularly formed grains upon the layer of PEDOT: PSS which was already exposed to an electric field as well [140]. The structure of grains we distinguished in this experimental study was almost identical to the reported structure (see Fig. 3.2 [138]). We employed electrochemical impedance spectroscopy to investigate the properties of the surface films for nontreated and UV-treated PEDOT: PSS layers, and noticed that PEDOT: PSS films' active surface area enhanced electrochemically after applying of UV radiation. This will be presented in more detail later.

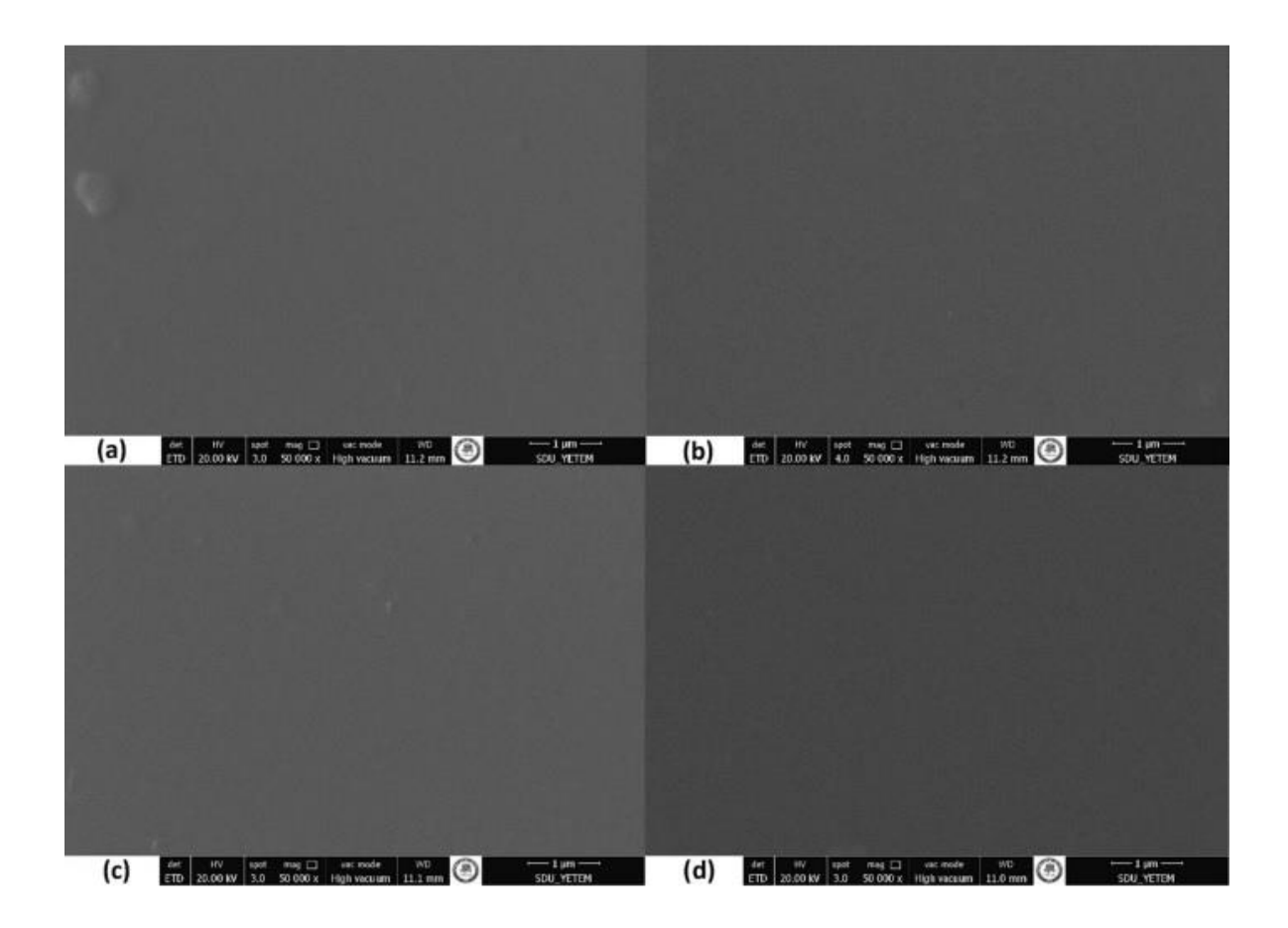


Figure 3.1 SEM images of **a** PEDOT: PSS, **b** PEDOT: PSS (UV: 5 min.), **c** PEDOT: PSS (UV: 10 min.), and **d** PEDOT: PSS (UV: 15 min.) [138]

Figure 3.3 displays SEM images which are belong to the perovskite layers on normal and UV-induced PEDOT: PSS layers for 5 to 15 minutes at different scales (500 nm and 1 μ m) [138]. The perovskite films appear to develop larger grains when PEDOT: PSS layers are exposed to UV radiation for 15 minutes. According to the literature, by applying UV radiation, the surface of PEDOT: PSS is improved and have a tendency for becoming hydrophobic. As a result, the surface's wettability is

increased. Surface energy is crucial in controlling the growing of perovskite successfully and thereby the efficiency of PSCs [141]. Deposition of perovskite layer on a hydrophilic surface causes film with tiny grain sizes, which consequently lead to low performance of PV device [141]. On the hydrophobic and non-wetting of HTLs surfaces, it is hard to accomplish consistent film of hydrophilic perovskite without any pinholes, since overall grain sizes are greater on hydrophobic surfaces [141]. For high-performance PSCs, developing a uniform and smooth perovskite film is crucial. Then, it is essential to be aware of grain size and connections between grains.

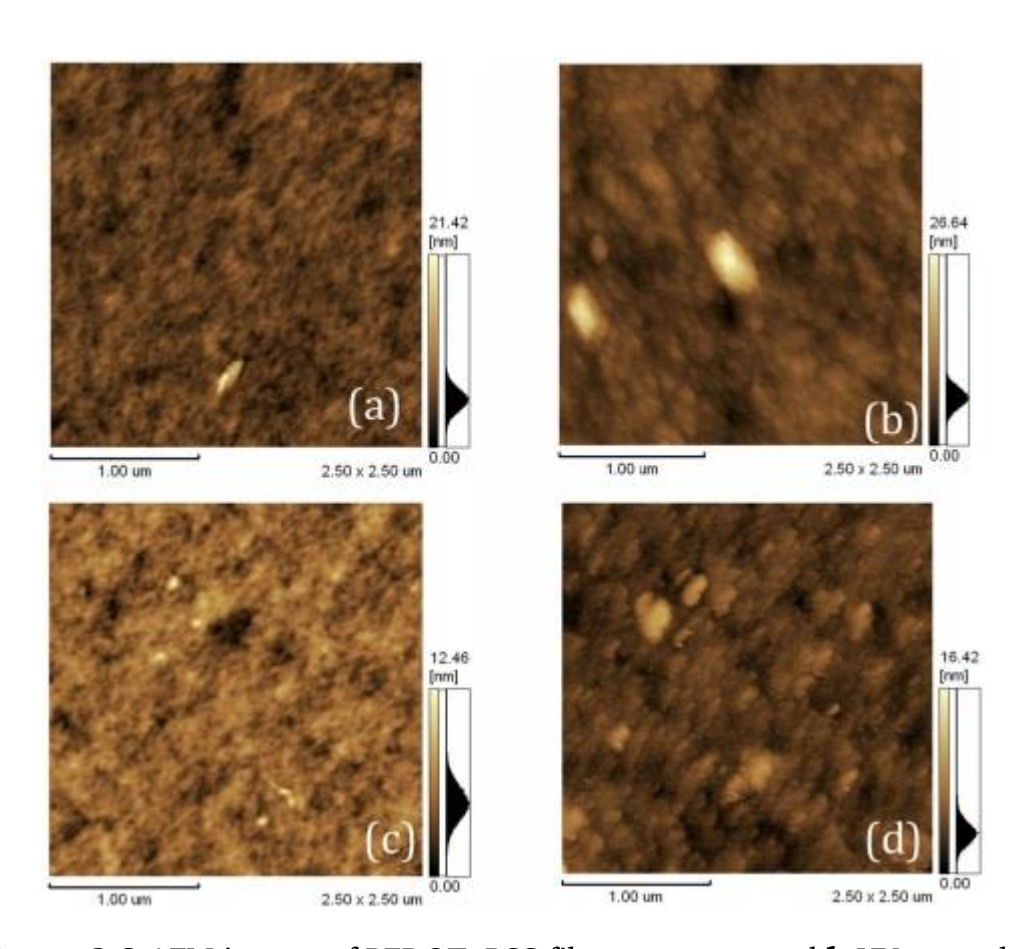


Figure 3.2 AFM images of PEDOT: PSS films **a** non-treated **b** UV-treated for 5 min **c** UV treated for 10 min **d** UV-treated for 15 min [138]

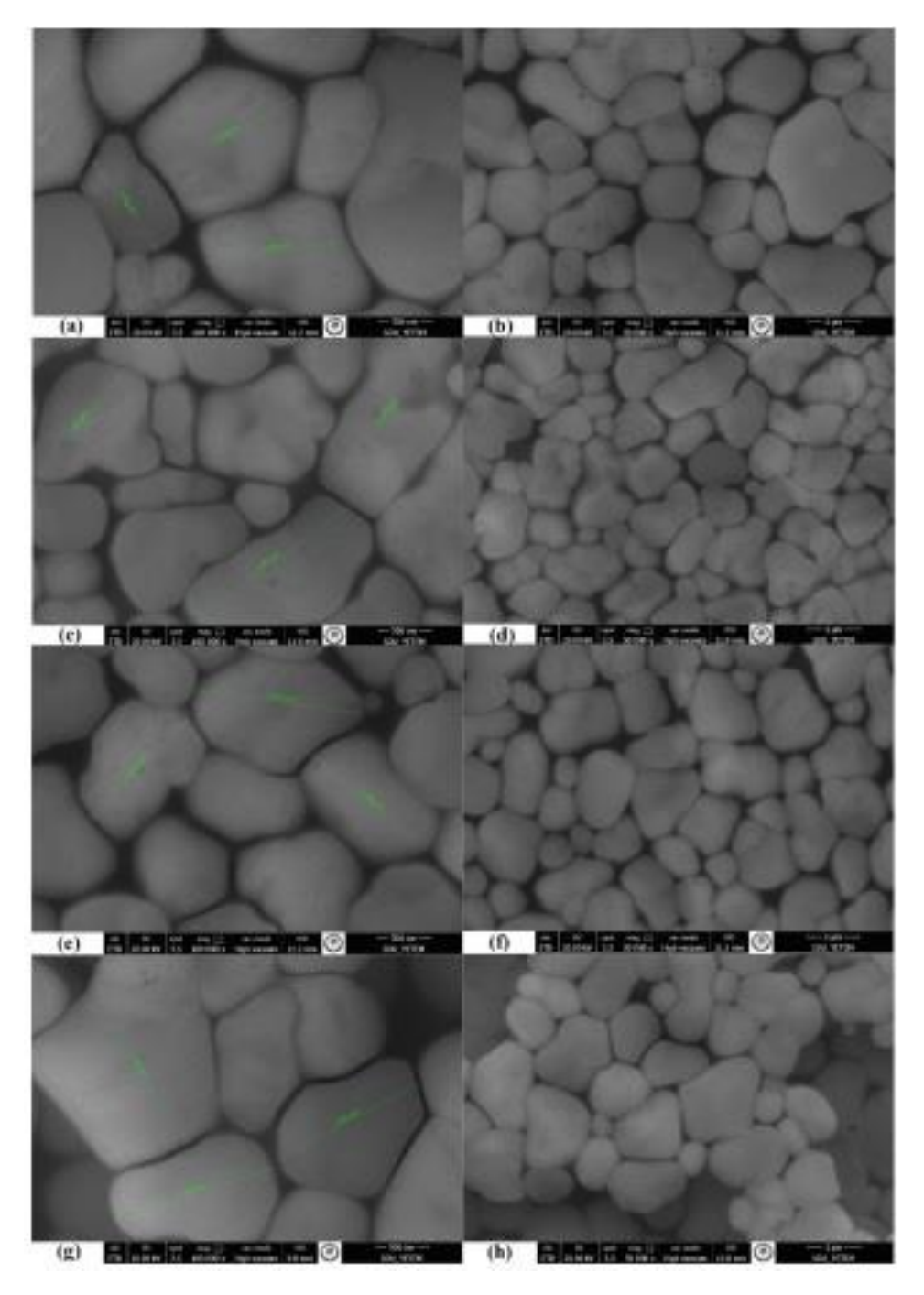


Figure 3.3 SEM images of perovskite layers coated on top of **a**, **b** PEDOT: PSS, **c**, **d** PEDOT: PSS (UV: 5 min.), **e**, **f** PEDOT: PSS (UV: 10 min.), and **g**, **h** PEDOT: PSS (UV: 15 min) in 500 nm and 1 μ m scales, respectively [138]

The process by which the perovskite grows on the surface is the factor that controls the grain size. Theoretical reports show that large and great grain size associated with a uniform distribution of grains will result in high values of current [142]. In this work, SEM analysis exhibits that UV radiation improves the grain size. Nonetheless, the distribution of the grains is not homogeneous. In addition, the samples subjected to UV radiation for 15 minutes, include holes between the grains. The more voids between grains leads to the low contact between them.

XRD analysis was used to verify the productive deposition of perovskite layer on the ITO/PEDOT: PSS substrate. The XRD pattern of a CH3NH3PbI3-xClx perovskite film is displayed in Figure 3.4 [138]. The characteristic peaks referring to (110), (220), and (314) planes reflect the formation of perovskite structure which is consistent with the literature [143]. The values of full width half maximum (FWHM) for (110) and (200) planes at 14.22° and 28.37°, respectively, were 0.0738, revealing a crystalline structure of perovskite [143].

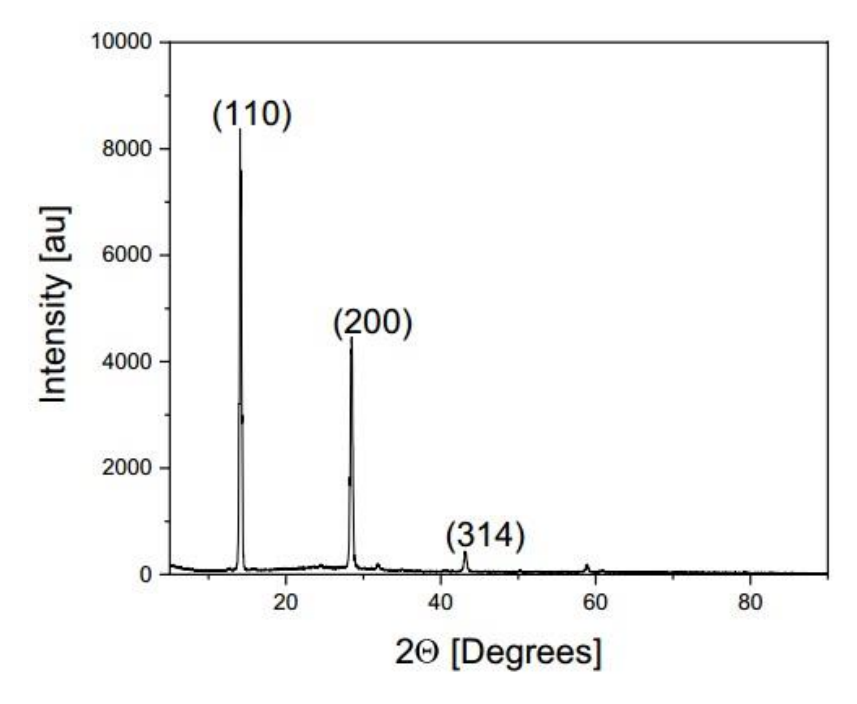


Figure 3.4 XRD pattern of perovskite (CH3NH3PbI_{3-x}Cl_x) film $\lceil 138 \rceil$

Figure 3.5 depicts the sheet resistance diagram of PEDOT: PSS layers for various UV exposure time intervals [138]. It was revealed after 5 to 10 minutes exposure of UV, the sheet resistance was reduced, then increased after 15 minutes. PEDO:PSS is composed of a hydrophobic and conductive PEDOT with a insulating and hydrophilic PSS compounds [144].

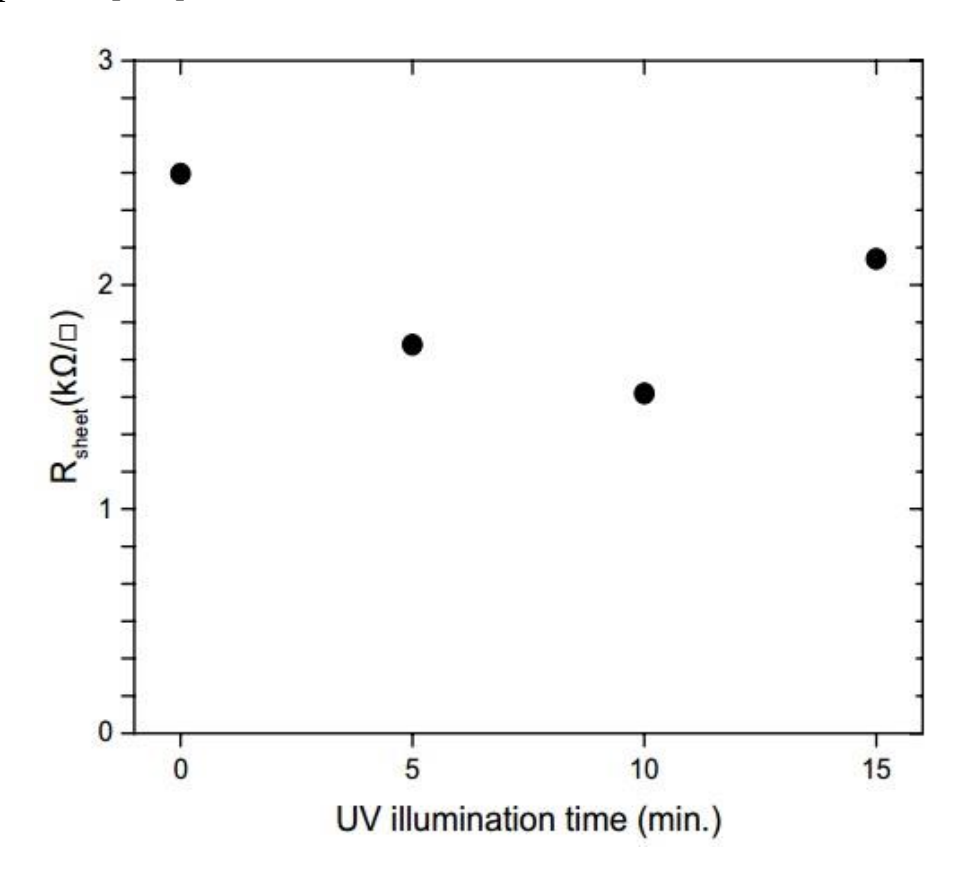


Figure 3.5 Sheet resistances of non-treated and UV-treated PEDOT: PSS film [138]

The consistency of material is supported by the hydrogen bonds of the PSS chains [144]. External factors, for example an electric field, can induce PEDOT: PSS separation [140]. We have an external influence here in the form of UV irradiation. It is conceivable that UV irradiation causes a detachment between PSS and PEDOT, with either PEDOT or PSS being predominant, as well as movement of one of these parts from deeper regions to the surface of the PEDOT:PSS layers, as has

been reported in the literature when an electric field is applied [141]. Sheet resistances may be influenced due to different opto-electrical features of PEDOT and PSS. The implementation of UV irradiation has a direct effect on sheet resistances. It dropped for the first 5 to 10 minutes of UV treatment, then increased for the once more for 15 minutes. PSS acts as an insulator, while PEDOT acts as a conductor segment in PEDOT: PSS [144]. The growth in the resistance of sheet for the surfaces irradiated with UV radiation for 15 minutes may be explained by an accumulation of PSS close to the surface caused by the impact of UV light.

XRD analysis was used on variously treated PEDOT: PSS surfaces to examine the impact of UV treatment on the PEDOT: PSS crystallinity. The XRD patterns of nontreated and UV-treated PEDOT: PSS layers are indicated in Figure 3.6. At around 25 degrees, a wide peak can be seen that corresponding to the (020) plane of the PEDOT: PSS backbone. Even though there is a slight variation in intensities, the PEDOT: PSS maintains its amorphous structure.

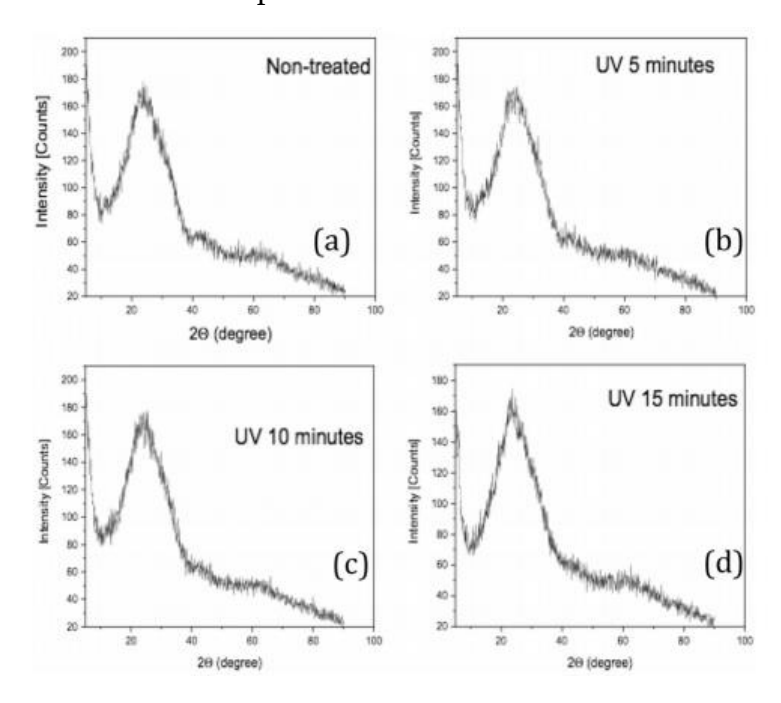


Figure 3.6 XRD Spectra of **a** nontreated **b** PEDOT: PSS (5 min UV treated) **c** PEDOT: PSS (10 min UV treated) **d** PEDOT: PSS (15 min UV treated) films [138]

from 500 cm⁻¹ to 2500 cm⁻¹, the FTIR spectra of pristine and UV-modified PEDOT: PSS layers are shown in figure 3.7 [138]. The C–S stretching bond is primarily responsible for the IR band at 818 cm⁻¹. The C–O–C band stretching in the ethylene dioxy units is accountable for the IR bands at 1010 cm⁻¹ and 1164 cm⁻¹. The C–C and C=C stretching of thiophene rings, as well as the sulfonic acid groups of PSS, are responsible for the IR bands of 1369 cm⁻¹ and 1529 cm⁻¹.

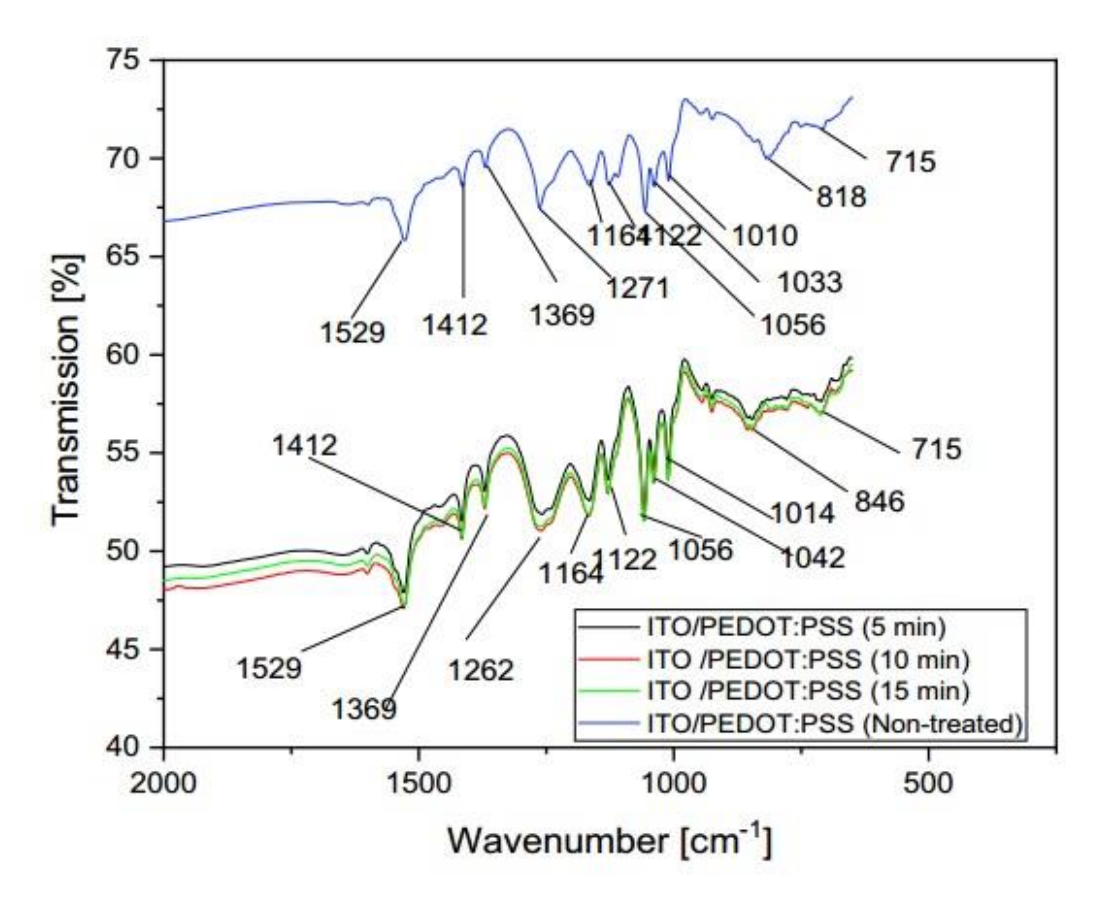


Figure 3.7 FTIR spectra of non-treated and UV treated ITO/PEDOT: PSS films for different time intervals [138]

Figure 3.8 presents the J–V curves of cells including pristine and UV-induced PEDOT: PSS layers [138]. For the reference device in which non-treated PEDOT: PSS film is employed, a J_{SC} of 16.4 mA/cm⁻² and a V_{OC} of 0.88 V were obtained. A 0.72 FF was evaluated which resulted in a PCE of 10.4%. The devices employing UV treated

PEDOT: PSS film for 5 minutes demonstrated a J_{SC} of 16.6 mA/cm⁻², 0.75 of FF, with a 0.89 V of V_{OC} which resulted in a PCE of 11.1%. Devices with PEDOT:PSS film exposed to UV radiation for 10 minutes, 17.2 mA/cm⁻² of J_{SC} and 0.89 V of V_{OC} with a 0.74 of FF were achieved leading to a PCE of 11.3%. Devices with PEDOT:PSS film exposed to UV radiation for 15 minutes, 15.5 mA/cm⁻² of J_{SC} and 0.89 V of V_{OC} with a 0.76 of FF were achieved resulting in a PCE of 10.5%. The efficiency of the devices increased after 10 minutes of UV exposure. The performance of devices in which PEDOT: PSS layers with 15 minutes UV exposure was employed was nearly identical to the reference device. Table 3.1 presents the PV parameters, which include the hysteresis factor [138]. Duration of UV irradiation on the PEDOT: PSS has a major impact on the performance of the herein investigated devices. In literature several explanations for the chemical and physical modifications in PEDOT: PSS caused by UV irradiation was described as a reduction in defects involving charge trapping [145], work function increasing [146], UV light causes the PEDOT: PSS chains to modify from benzoid to quinoid, restricting the generation of a hole extraction boundary between the PEDOT: PSS and the active layer [147]. Every one of these factors improve the efficiency of extraction and, as a result, reduce the recombination chance between holes and electrons, leading to performance enhancement of device. In this study, the lowest PCE was achieved for the devices employing PEDOT:PSS treated by UV light for 15 minutes, and the J_{SC} was the major loss. Developing a uniform and homogeneous perovskite film is important for having a highperformance PSC, as previously stated. J_{SC} can be lowered if there is poor connection between the grains as well as a weak linkage to the back contact. The process by which perovskite is obtained on the surface is the aspect that influences grain size. The AFM results in this research showed that UV irradiation affects the morphology of PEDOT: PSS films, resulting in different growth of perovskite film on different PEDOT: PSS surfaces. Scientific reports show that large and great grain size associated with a uniform grain distribution will lead to high values of current [148]. In this research, UV irradiation enhances the grain size, as is seen in SEM results. Nevertheless, the distribution of grain size is not homogeneous. Further, predominantly for the samples subjected to UV light for 15 minutes, there are pinholes between the grains. The growth of voids among the grains means low connection between the grains, resulting in a reduction in J_{SC} .

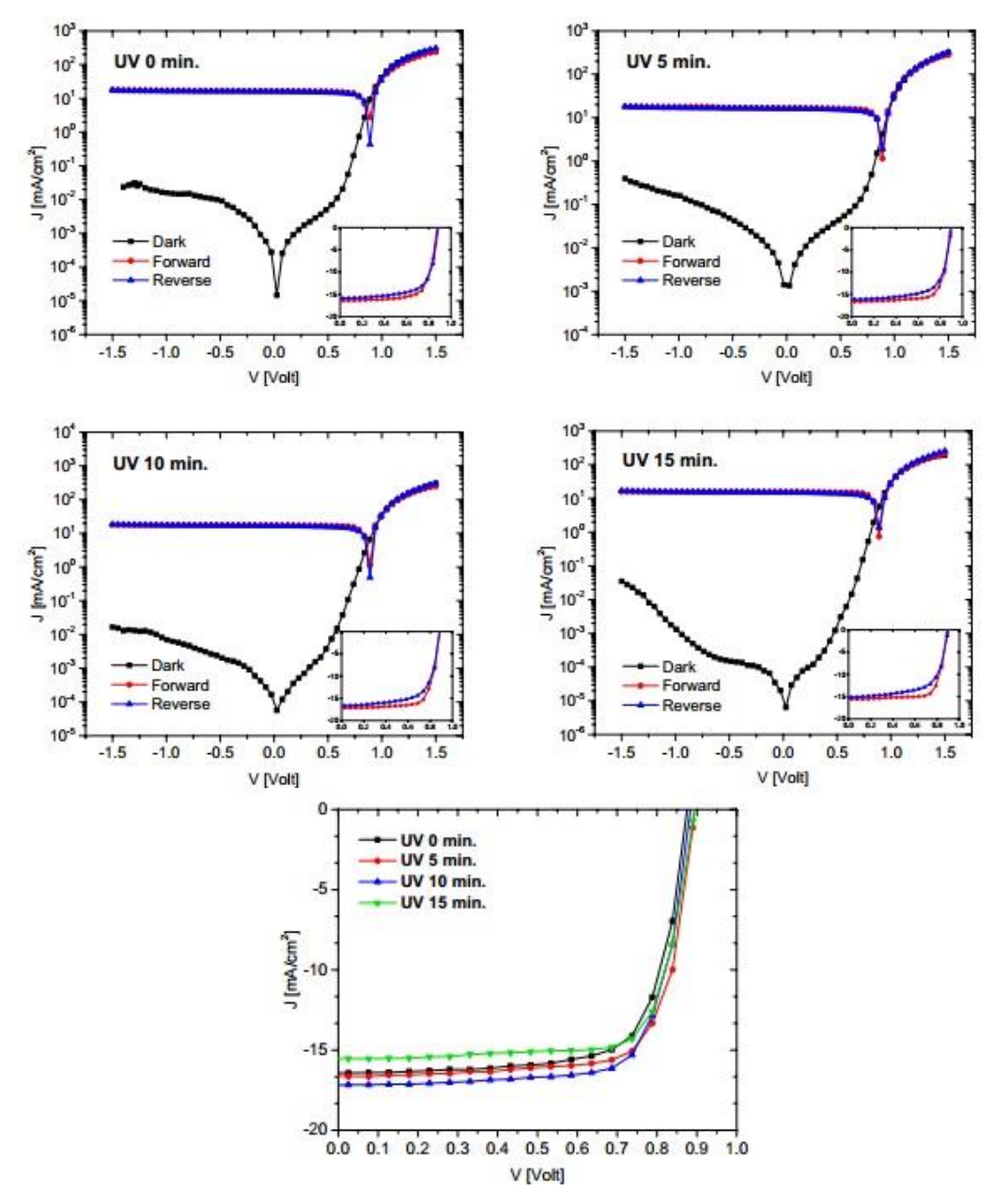


Figure 3.8 Semi-logarithmic J-V curves of devices employing non-treated, 5 min, 10 min, and 15 min UV-treated PEDOT: PSS films. The graph at the bottom is the comparison of J-V curves in linear scale. Inset is the J-V curve of perovskite solar cells under reverse and forward bias [138]

Table 3.1 Photovoltaic parameters of fabricated devices [138]

	UV 0 min	UV 5 min	UV 10 min	UV 15 min	
V_{oc} (V)	0.88	0.89	0.89	0.89	
$J_{\rm sc}$ (mA/cm ²)	16.4	16.6	17.2	15.5	
FF	0.72	0.75	0.74	0.76	
$R_{\rm s}\left(\Omega\right)$	20	20	22	23	
$R_{\rm sh}(\Omega)$	6261	37077	159953	16875	
PCE (%)	10.4	11.1	11.3	10.5	
HF	0.07	0.10	0.12	0.15	

Figure 3.9 depicts the EQE of devices using pristine and UV-treated films of PEDOT: PSS for various time period as well as the absorption of PEDOT: PSS films for both pristine and UV-treated for various time duration (right scale) [138]. External quantum efficiency stands for the quantity of charge carriers which are generated with incident photon devoting to the photocurrent per received photon and is employed to determine the photons energy that lead to current generation in PV devices [149]. The external quantum efficiency and absorption spectra of specific elements used in the cell architecture can be compared to determine which collections supply the generation of charge carrier. EQE has a wavelength range of 350 nm to 800 nm. In the EQE data, a shoulder can be seen around 484 nm. In the absorption data of PEDOT: PSS layers, a certain type of shoulder is identified around 526 nm, which is consistent with previous studies [150,151]. The absorption shape of PEDOT: PSS layers on ITO-coated glasses is identical to the distinctive shoulder at 484 nm in the external quantum efficiency spectrum. The participation of perovskite and PCBM to production of photocurrent is responsible for the wavelength alternation. It may be inferred that all of the elements in the device configuration play a role on the photocurrent generation as concluded by comparing the absorption profile and EQE. But, in the range of 500 nm to 700 nm, a shift in the absorption spectrum was observed. When the oxidation state of PEDOT: PSS varies, the absorption spectrum of PEDOT: PSS is modified in the near infrared zone, according to the literary works [152]. While the wavelength range of 550 nm to 750 nm does not fall exactly inside the NIR zone, it is close to it, and because the tests were performed in ambient air, the PEDOT:PSS film might have been oxidized, leading to changes in the absorption profile of different PEDOT:PSS [152,153].

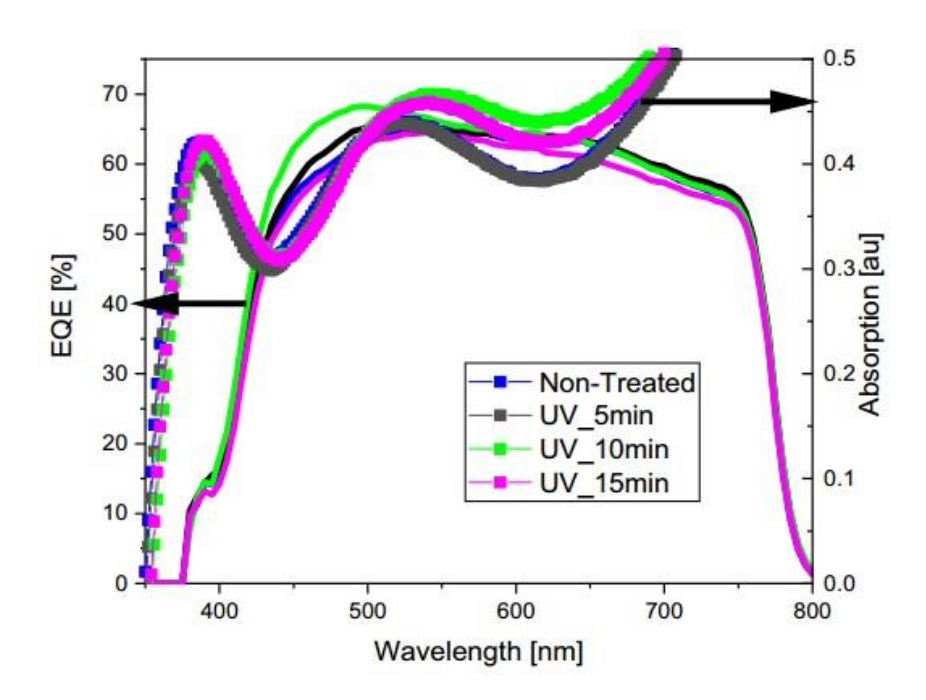


Figure 3.9 Comparison of external quantum efficiency of devices and absorption of non-treated and UV-treated PEDOT: PSS films (bold lines are absorption) [138]

The resistance properties of the pristine and UV-treated electrodes in the configuration of ITO/PEDOT: PSS were determined by using electrochemical impedance spectroscopy (EIS) method. Figure 3.10 [138] displays the EIS spectra that have been fitted to an equivalent circuit model as is shown in figure 3.10 where C_{dl} , R_s , R_{ct} , and W express capacitance of two layers, resistance of solution, resistance of charge transfer, and values of Warburg impedance, respectively [154,155].

The solution resistance and the electrodes' contact resistance determine the value of Rs[154]. Since EIS measurements were performed in the identical electrolyte, the values were close for each kind of electrode (Table 3.2 [138]). However, because of the increased surface conductivity of the electrode caused by UV treatment procedure, a reducing trend was observed for UV-treated electrodes (Table 3.2) [155]. R_{ct} is related to electron transfer and resistance of electrochemical reaction

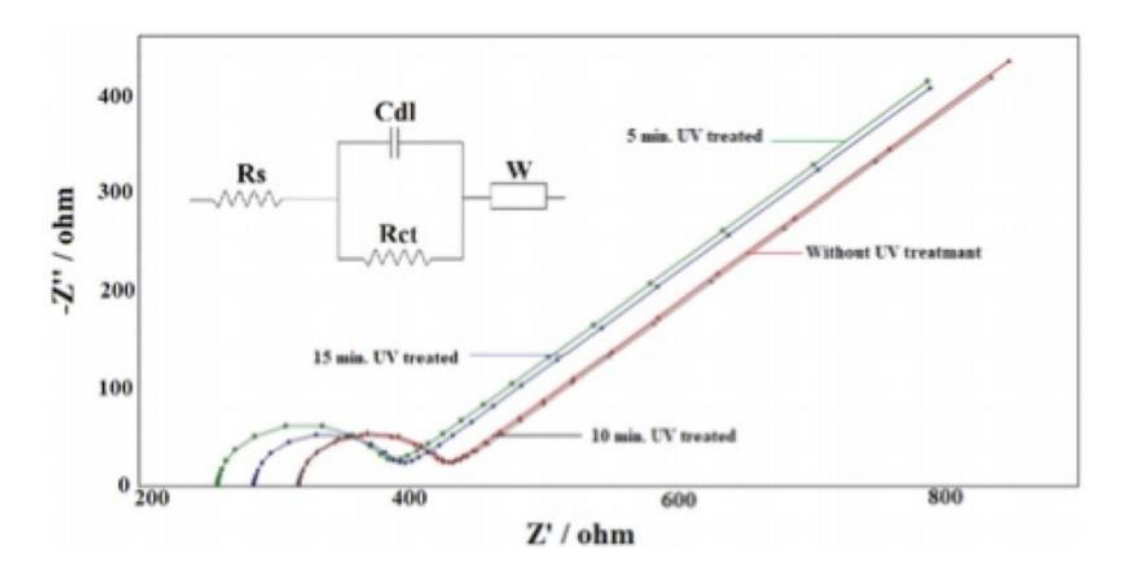


Figure 3.10 Fitted EIS spectra of ITO/PEDOT:PSS electrodes without UV treatment of PEDOT:PSS film and ITO/PEDOT:PSS electrodes with 5, 10, and 15 min UV-treated PEDOT:PSS films [138]

Table 3.2 Electrochemically active surface areas and fitted impedance values of UV-treated and non-treated PEDOT: PSS electrodes at different time intervals of 5 min., 10 min, and [138].

Electrode	Electrochemically active surface area (cm ²)	Normalized R_s (Ω cm ⁻²)	Normalized $R_{\rm ct}$ (Ω cm ⁻²)	Normalized W	Normalized C _{dl} (F cm ⁻²)
Non-treated PEDOT:PSS	3.06	25.96	7.81	0.00103	1.017×10^{-7}
ITO/PEDOT:PSS UV-treated for 5 min	3.47	18.53	7.33	0.00106	1.210×10^{-7}
ITO/PEDOT:PSS UV-treated for 10 min	3.44	23.03	7.20	0.00107	1.211×10^{-7}
ITO/PEDOT:PSS UV-treated for 15 min	3.39	20.93	7.19	0.00110	1.352×10^{-7}

 R_{ct} values decreased for UV-treated electrodes (Table 3.2 [138]), indicating that the electrocatalysis activity of electrodes grew after using UV light [155]. The induced double layer capacitance upon the surface of electrode and the rate of flow of the ions to the surface are described by the C_{dl} and Warburg impedance values, respectively [154,155]. After UV procedure, there were some rises in C_{dl} and Warburg values. The growth of electrochemically active areas on the surface of electrodes as a result of UV irradiation was linked to a boost in the values [155]. The Randles–Sevcik formula was used to determine the rate of surface zones (Table 3.2) [156]. The growth of electrochemically active areas on the surface of electrode as a consequence of UV irradiation was corroborated by the AFM studies (see figure 3.2). The active area on the surface of electrode was found to rise as a result of applying UV light.

The surface potential of nontreated and UV-treated PEDOT:PSS films was studied by means of KPFM measurements as are shown in Figure 3.11 [138]. For defining the difference potential on the different surfaces, KPFM can be used. Because of its especially high surface sensitivity, this approach is generally employed [157]. This approach is used to investigate polymer energy-level adjustment on various electrodes [157]. The contact potential difference (V_{CPD}) between the tip of KPFM and nontreated PEDOT: PSS surface was obtained to be -0.43 V whereas, for PEDOT: PSS layers which were annealed under UV light for 5, 10, and 15 minutes, the V_{CPD} of them were -0.19 V, -0.24 V, and -0.135 V, respectively. The variation in work function between the sample and the KPFM tip is comparable to V_{CPD}. Due to the use of same tip throughout all the test, it may concluded that the use of UV radiation increases the work function of PEDOT: PSS film. The barrier between the PEDOT: PSS layer and active layer can be influenced by increasing work function, which is pivotal for solar cell operation. Our findings are consistent with studies in the literature claiming that UV radiation increases the work function of PEDOT: PSS [145,153].

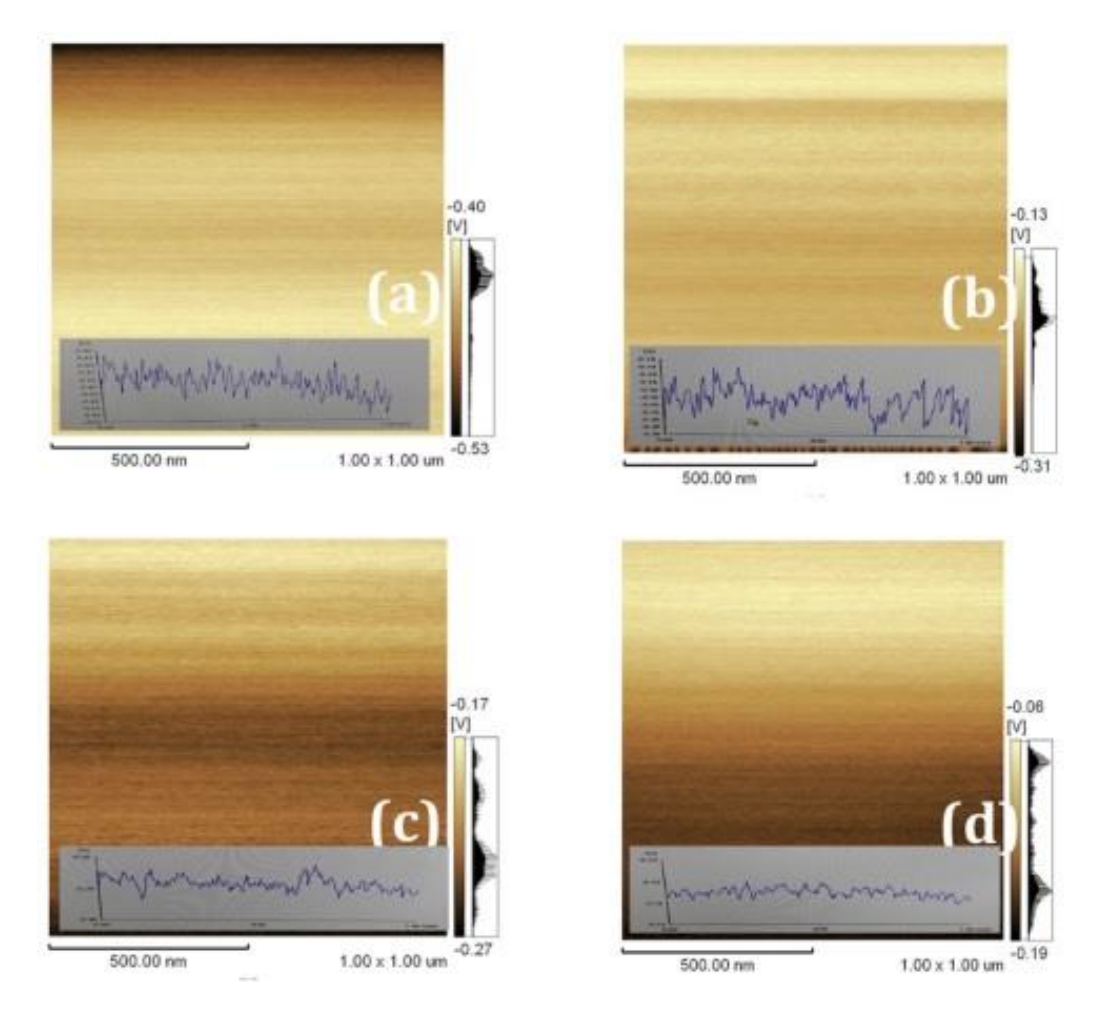


Figure 3.11 KPFM surface potential images of PEDOT: PSS films **a** nontreated, **b** UV treated for 5 min, **c** UV treated for 10 min **d** UV treated for 15 min. (Insets are the surface potential histograms) [138]

3.4 Conclusion

The impact of UV irradiation on ITO/PEDOT: PSS samples in p-i-n type of PSCs was studied. It is demonstrated that exposing PEDOT: PSS coated substrates to UV irradiation for a certain period of time (up to 10 minutes) improves the PCEs of the PSCs. To analyze the consequences of UV radiation on the system, we used XRD, SEM, I-V, resistivity, absorption, and EQE analyzes were performed. The performance of PV deteriorates after 15 minutes of UV illumination. The performance of a solar

cell depends directly on photovoltaic parameters such as J_{SC} , V_{OC} , and FF. The reduction in J_{SC} was the most significant loss for the cells employed UV-treated PEDOT: PSS layers for 15 minutes. The issue of controlling the morphology of perovskite layers is the main reason for poor J_{SC} in PSCs. EIS results revealed that UV light enhanced the electrochemically active surface areas of the PEDOT: PSS films, which is consistent with AFM observations. The surface on which the perovskite layer is coated has an influence on the film growth features of the perovskites, according to the literature. In this research, it was also observed that the UV treatment of the substrates affects perovskite grain growth and thus morphology of perovskite film.

The impact of UV light on the efficiency of organic photovoltaics has been analyzed in the past. Nevertheless, its influence on PSCs has never been investigated in the literature. Lee et al. noticed a better performance for cells using UV-modified PEDOT: PSS layers, that they linked to modification of work function and low series resistance of device after UV radiation, which we also observed in this study. Nevertheless, they noticed a slight change in the morphology of surface. In this thesis, it was demonstrated that UV radiation alters PEDOT: PSS morphology, which in turn alters the film forming features of perovskites on various PEDOT:PSS surfaces. Moreover, as a significant benefit, it was revealed in our research that for observing the impact of UV light on the operation of the cells, a long UV radiation time is not required. Although Xing et al. [59] reported an enhancement in the conductivity of PEDOT: PSS layers, which were exposed to UV light, a long UV radiation time (25 h) was required. In our study, we were capable of achieving high PCEs for PSCs with shorter UV exposure times.

4

ENHANCEMENT OF FILL FACTOR OF P-I-N TYPE OF PEROVSKITE SOLAR CELLS BY EMPLOYMENT OF Zn-DOPED PEDOT:PSS AS A HTL

4.1 Introduction

In the inverted structure, the requirement for low resistivity and high transparency of the HTL appears to be unavoidable. As previously mentioned, PEDOT:PSS is a prevalent HTL among specific sorts of conductive polymers [138,158,159]. In 2013, Jeng et al. were the first to use PEDOT: PSS in an inverted type of perovskite solar cell[160]. PEDOT: PSS can be considered an advantageous HTL for flexible devices owing to its excellent transparency and solution processing at low temperatures [161,162].

PEDOT: PSS is made up of the conductive and insulating groups PEDOT and PSS, respectively. The orientation and concentration of PEDOT and PSS affect the conductivity degree of PEDOT:PSS. Furthermore, a portion of the PSS in the PEDOT:PSS layer is removed during the solvent injection procedure, resulting in a greater proportion of PEDOT to PSS [163,164]. By manipulating the volume ratios of dimethylsulfoxide (DMSO) in the PEDOT: PSS solution, Huang et al.[165] enhanced photocurrent and extraction of charge in PSCs.

By using of additives, the electrical conductivity of PEDOT: PSS can be boosted[150]. The morphology of PEDOT: PSS and perovskite layer can be improved by applying additives inside the layer. Huang et al. showed that utilizing polyethylene oxide as an addition to PEDOT: PSS film resulted in a considerable increase in the conductivity of PEDOT: PSS film [166]. The doped-PEDOT: PSS speeds up the

transport of holes from the perovskite film to the anode, resulting in improved perovskite solar cell performance. Improvements in the morphological properties of the modified film and an increase in the quantity of PEDOT in the bipolaron state are responsible for the rise in electrical conductivity. Because of the rough surfaces of pristine or excessively doped PEDOT:PSS layers with PEO, trap states that induce recombination rate and losses at the interfaces can occur at the interfaces between perovskite and HTL [167]. Qian et al. observed a positive improvement in the PV characteristics of PSCs by using Ag-nanoparticles as a dopant in PEDOT: PSS due to enhancements in PEDOT: PSS conductivity and morphological characteristics of active layer.[168]. By adding sodium chloride (NaCl) inside PEDOT: PSS, Hu et al increased the performance of perovskite solar cells [169]. The addition of NaCl to PEDOT:PSS not only improved conductivity and hole extraction, but also increased FF and V_{OG} , resulting in a better efficiency.

In this chapter, to enhance the electrical conductivity and surface morphology of coated HTL and perovskite films, PEDOT:PSS solution was doped by Zn, which the significantly improved the device performance. As is shown in Figure 4.1 [170], the device architecture used in this research was ITO/PEDOT:PSS/MAPbI₃/PCBM/BCP/Ag. All of the tests were performed in out of glove box with a humidity level of 40-50 %.

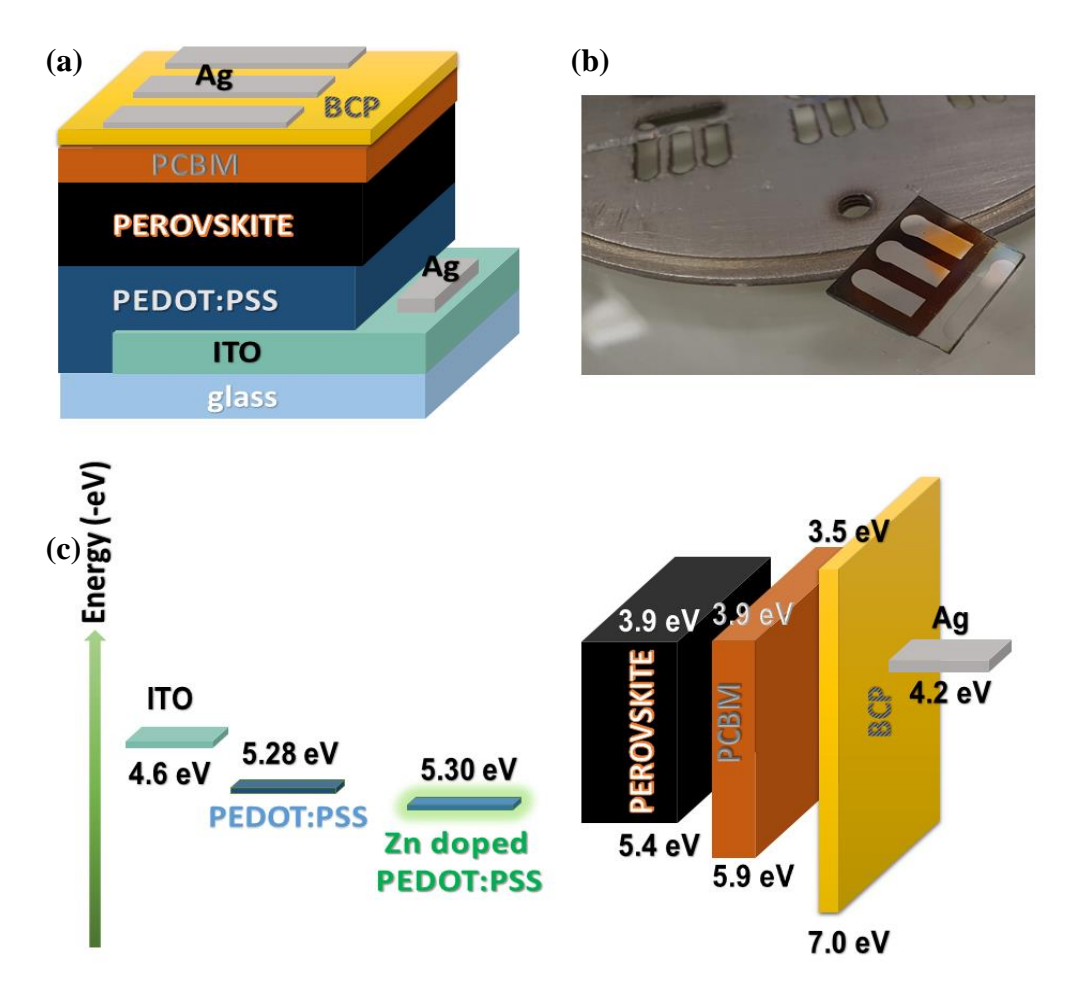


Figure 4.1 (a) Schematic configuration (b) photograph (c) estimated energy level diagram of the produced perovskite solar cells [170]

4.2 Experimental

20 mg PCBM powder was dissolved in 1ml chlorobenzene and stirred at 45°C for a few hours to make the ETL solution. A perovskite solution was obtained by combining PbI2 and MAI in a 1:1 molar ratio in 1 ml of GBL and heated at 65°C for at least 12 hours, then filtered through a 0.45 μ m PVDF filter before coating. 1 ml absolute ethanol was used to dissolve 0.5 mg bathocuproine, which was mixed for 12 hours to make the BCP solution. Prior to the use of HTL, a 0.45 μ m PTFE filter was used to filter the PEDOT: PSS solution. To make Zn-doped PEDOT:PSS solution, 0.05

M Zn(CH₃CO₂)₂·2H₂O was dissolved in 1ml of distilled water, and the solvent was combined with PEDOT:PSS at a volume ratio of (7.5:100) and agitated for two hours prior to use (Figure 4.2 [170]).

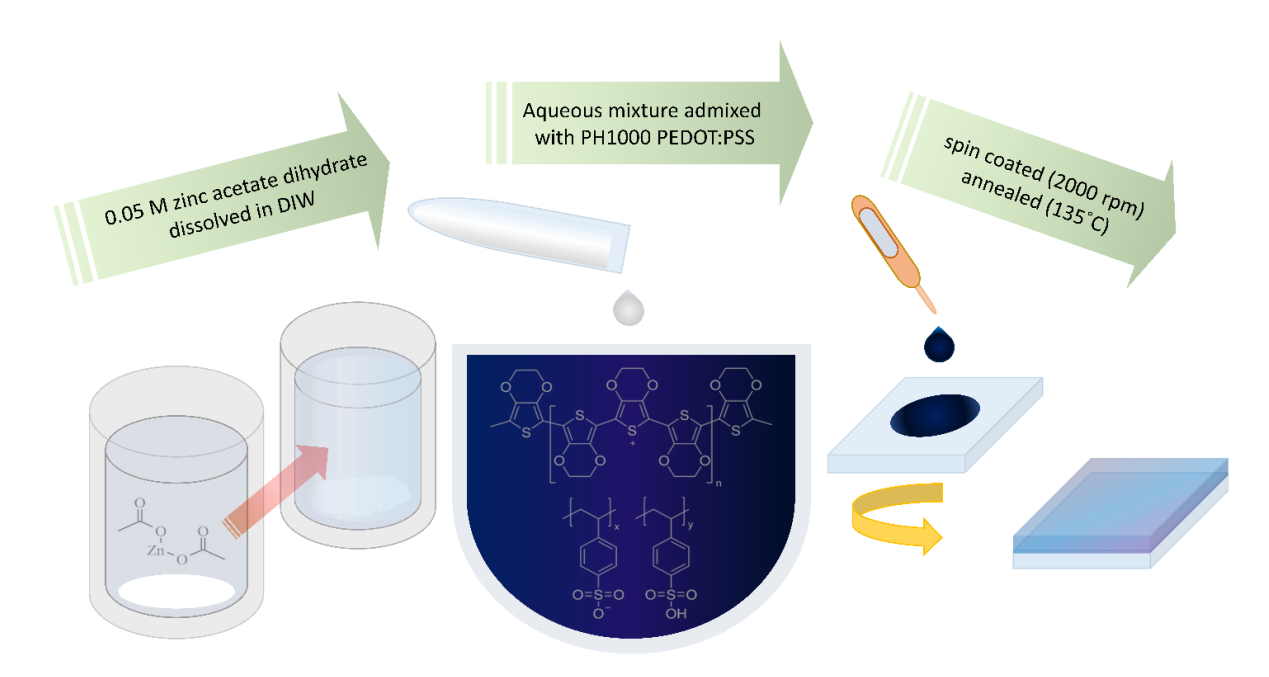


Figure 4.2 Schematic demonstration of the Zn-doped PEDOT: PSS film preparation process [170]

HCl: HNO₃: H₂O (4.6:0.4:5) mixture was used for 45 minutes to etch ITO-coated glasses before being sliced into 1.5×1.5 cm². To prepare ITO coated glasses for HTL coating, they were washed in ethanol, acetone, and isopropanol. They were sonicated in acetone and IPA for 25 and 40 minutes respectively to extract particles and dust from the surface. Finally, N₂ gas was used to dry the substrates. HTLs were coated for 50 seconds at 2000 rpm, then thermally annealed for 10 minutes at 140 °C. The perovskite film was coated by spinning a perovskite solution at 2200 rpm for 15 seconds and 4000 rpm for 25 seconds. 60 μ l of toluene was dropped on the substrate five seconds after the spin coater approached 4000 rpm, as an anti-solvent, to acquire a quick and better crystalline layer. Afterwards, perovskite layer was

annealed for 20 minutes on a heating plate at about 105 ° C. PCBM layer was coated on the perovskite layer for 15 seconds at 1500 rpm and 20 seconds at 2000 rpm, then dried for 90 seconds at 90 °C. Hole blocking layer (BCP) was coated at 4000 rpm for 40 s. Ultimately, silver was formed in 110 nm of thickness by using the thermal evaporation system. In addition, for hole-only devices, rather than PCBM and BCP films, a quite thin film of P3HT classified as an HTL was placed on the surface of perovskite. P3HT film was achieved by dissolving 10 mg P3HT in CB and coating at 4000 rpm for 25 seconds, followed by annealing at 90°C for 90 seconds on a hot plate.

4.3 Result and discussion

AFM was utilized to analyze the roughness of HTL surface. AFM technique was used for pristine and Zn-PEDOT: PSS films to investigate their morphologies as are displayed in Figure 4.3 [170]. pristine and doped PEDOT: PSS films possess the RMS roughness values of 1.56 and 0.95 nm, respectively. The roughness of the doped film is decreased, leading to a flat and smooth form of PEDOT: PSS layer. PEDOT: PSS and Zn-doped PEDOT: PSS maximum heights, expressed as the difference in height between the highest and lowest peak, are 15.92 nm and 11.67 nm, respectively [171].

Based on AFM images, the doped PEDOT:PSS film has a significantly better particle agglomeration than the pristine PEDOT:PSS film. The RMS roughness can be increased by increasing particle diameter and accumulation of primary particles (cluster), and by removing the extra PSS layer, the diameter of the main particles in the cluster should indeed be reduced [172]. Round-shaped fine-grained regions can be seen on the surface of the layers, as can be noticed in the AFM images. In comparison to pure films, the portion of these granular regions grows and is uniformly distributed all over Zn-doped PEDOT:PSS films. In the literature, these broad regions have been related to higher conducting PEDOT groups [173]. However, thermal annealing of PEDOT:PSS films to 135°C for 10 minutes can cause PEDOT to

migrate to the film surface and aggregate, as a result, vertical phase separation occurs, and larger grains form [174]. The roughness of doped PEDOT:PSS film is reduced by reorienting PEDOT and PSS chains. Since surface quality has a significant impact on organic semiconductor devices, using a rapid and simple Zn doping method to reduce surface roughness of organic layers is a highly promising outcome. The softness parameter of metal ions has been demonstrated in the literature that have a critical role and is relevant to the energy between the ion with other compounds that bind them together. PEDOT:PSS is a polyelectrolyte with PEDOT chains that are positively charged and PSS chains that are negatively charged, and salt can cause interactions between polycations and polyanions. The softness parameters of cations are related to the strength of bond between cations and PSS, according to the literature [175]. Thus, The PSS anions in PEDOT:PSS can connect to metal ions. Zn⁺² pierces PEDOT:PSS and binds to PSS anions in our case (Figure 4.3 (a) [170]). As stated earlier, in this case, removing excess PSS can result in a reduction in the diameter of the cluster's dominating particles [172]. However, the binding of the positively Zn ion to negatively charged PSS has the potential of causing charge screening and rearrangements [176]. Electrical properties of PEDOT and PSS are different from each other. PEDOT acts as a conductor while PSS acts as an insulator in PEDOT: PSS [144]. Furthermore, PEDOT:PSS film is made up of hydrophobic core (PEDOT) and hydrophilic shell (PSS), with the PSS chains' hydrogen bonds providing the material's consistency. Interaction of Zn⁺² ion with PSS causes a conformational transition, and removing the hydrophilic PSS component of the film ends up making it hydrophobic. Water drop testing on the pristine and doped HTLs (Figure 4.3 (a) [170]) revealed that the PEDOT:PSS layers became significantly more hydrophobic after doping with Zn, which could be interpreted as evidence of Zn ion binding to hydrophilic PSS and potential elimination of PSS from the surface leading to the surface be more hydrophobic. According to what is identified, perovskites deposited on hydrophilic surfaces have smaller grains, although perovskites covered on hydrophobic surfaces have larger grains. It seems to be vital for PSC success to try to manage grain size and connectivity between perovskite grains [141]. Perovskites with larger grain sizes and a consistent grain spread have higher current values, according to theoretical studies [142]. Our finding that Zn doping results in a more hydrophobic PEDOT:PSS layer, which is also supported by SEM analyzes (see Figure 4.8 [170]), which reveal that compared to pristine PEDOT:PSS substrates, perovskites formed on doped PEDOT:PSS substrates have higher grain sizes.

Due to improved charge transport, the device performs better with a film that is more homogeneous and smoother. Low HTL roughness and uniformity are favorable not only for better hole transport and lower recombination and leakage current, but also for the development of perovskite layers with less pin-holes, which are crucial for solar cell performance. KPFM analysis was employed to measure the work function of HTLs, utilizing V_{CPD} formula (contact potential difference), where "e" represents the elementary charge;

$$V_{CPD} = \frac{\varphi_{sample} - \varphi_{tip}}{e} \tag{4-1}$$

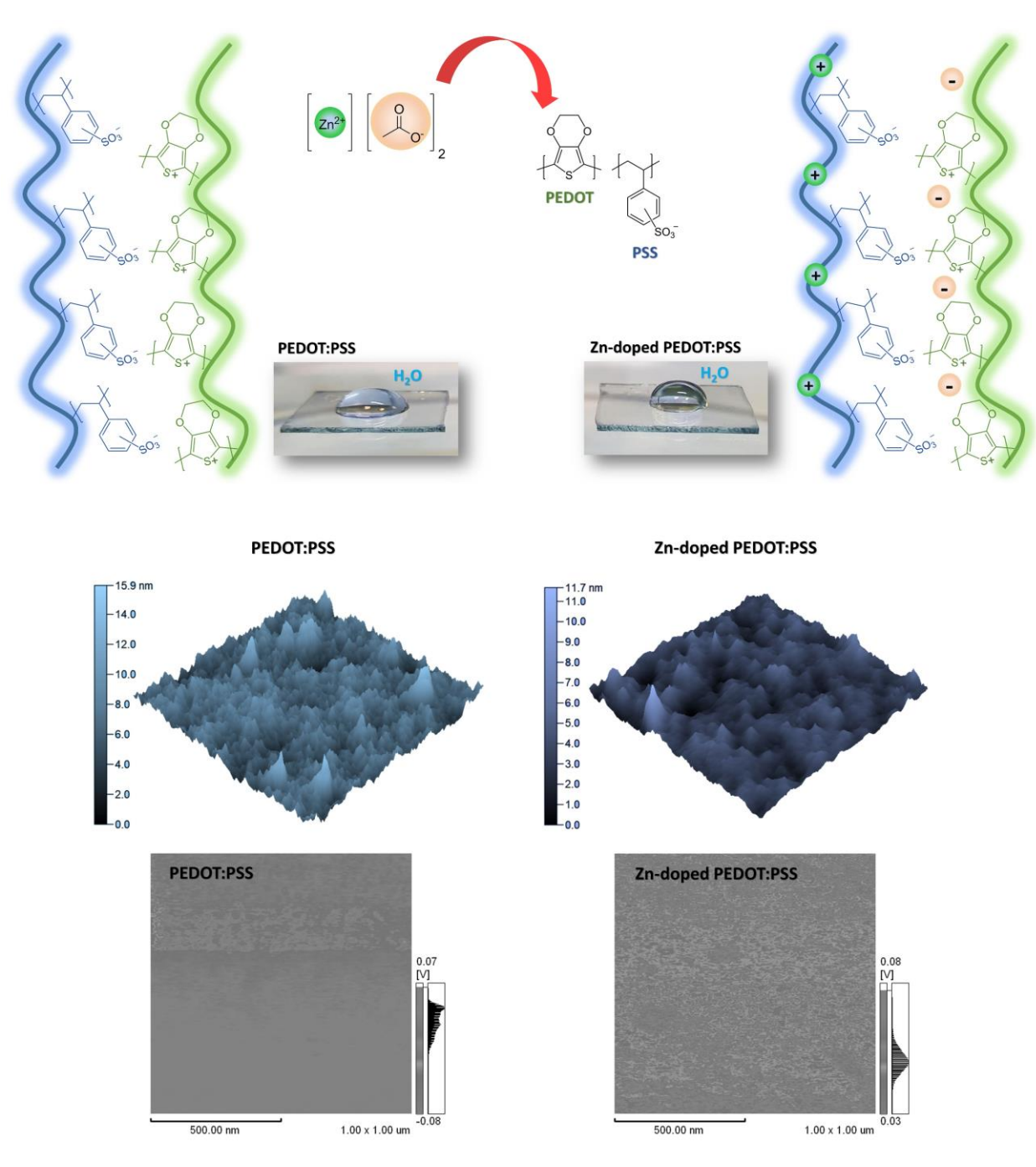


Figure 4.3 (a) Demonstration of the possible composition of the Zn-doped PEDOT:PSS with water drop test (b) AFM images over $3 \times 3 \, \mu \text{m}^2$ (c) KPFM measurements of PEDOT:PSS and Zn-doped PEDOT:PSS films [170]

Figure 4.3 (c) [170] illustrates the changing potential of HTLs on the surface beside the corresponding AFM images (right). For pristine and doped PEDOT: PSS layers, measured values were 5.28 eV and 5.30 eV, respectively. The modest enhancement in work function is estimated to lower the difference between HTL and the perovskite's valence bands, resulting in a greater electric field and hence charge transfer. Since the $V_{\rm OC}$ is proportional to the gap between HOMO level of hole transport layer and LUMO level of electron transport layer, higher values are forecast.

Current-voltage measurements were taken for the cells in the ITO/HTL/Ag configuration shown in Figure 4.4 (a) [170] to evaluate the conductivity of pristine and doped HTLs. In accordance with the following formula [43], the conductivity " σ_E " of PEDOT:PSS films was obtained.

$$I = \frac{\sigma_E AV}{I} \tag{4-2}$$

Where A is active area (0.1 cm^2) , L presents the thickness of the HTL. The conductivity of the undoped and doped HTLs were evaluated as $1.48 \times 10^{-4} \text{ S cm}^{-1}$ and $3.35 \times 10^{-4} \text{ S cm}^{-1}$, respectively, indicating that the Zn-doped HTL films have a higher conductivity [177]. Conductivity improvement matches the softness parameter of the cation of the salts, analogous to the explanation on morphology mentioned [178]. $\text{Zn}(\text{CH}_3\text{COO})_2$ is a salt in which Zn ions connect to the PSS. Charges of PEDOT and PSS could be screened because salt can cause charge screening and rearrangements in polyelectrolyte compounds [175], which weaken the Coulombic force between the two complexes. As a consequence, the conductivity rises due to the removal of PSS which is insulating part of PEDOT:PSS. The increase in conductivity caused by PSS reduction has also been observed in the literature [179].

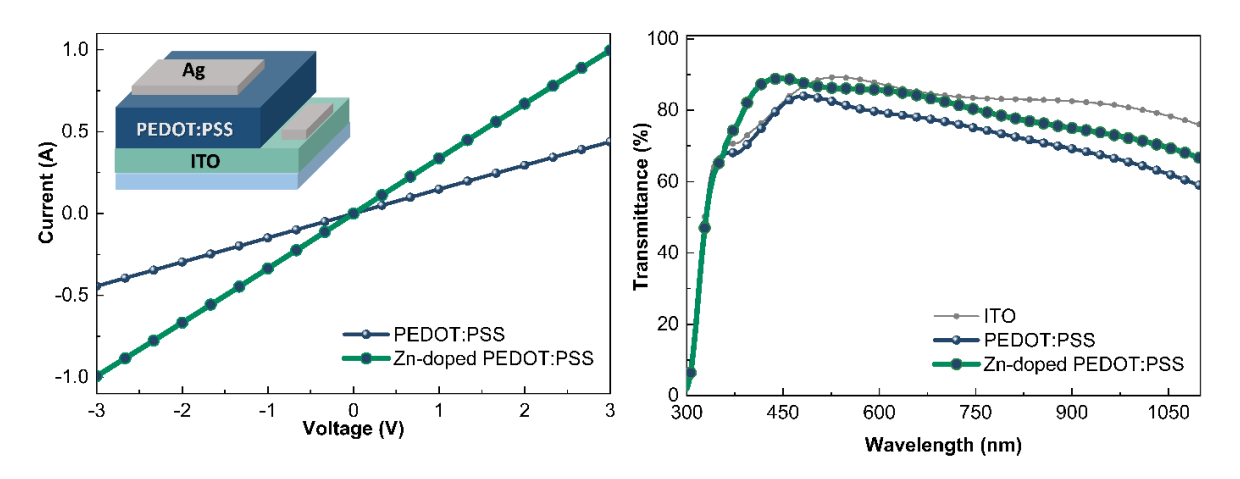


Figure 4.4 (a) Current-voltage curves of PEDOT:PSS films with a ITO/HTL/Ag structure (b) UV-Vis transmittance spectra of the ITO coated glass and PEDOT:PSS layers on ITO coated glass substrates [170]

Enhanced HTL conductivity does not only prevent electron-hole recombination, resulting in an increase in FF and J_{SC} , but also accounts for greater hole extraction from the active layer [38,180], leading to improved device performance. The transmittance profiles of ITO substrate and HTLs on ITO are shown in Figure 4.4 (b) [170]. Since light passes through the HTL, its transmittance plays a critical role in perovskite film as a light-harvesting layer. The transmittance of the HTLs was increased by Zn-doping, as is shown by the transmittance curves. Furthermore, doped hole transport layers provided a greater transmittance result around 450 nm than ITO-coated glass, which is comparable with reported research related to the less surface roughness of the Zn-doped HTLs [171,181].

The electrochemical characteristics of the HTLs were evaluated using cyclic voltammetry (CV) and chronoamperometry (CA) within a system involving electrodes of ITO/PEDOT:PSS as the working electrode, silver (Ag) as the reference electrode, and platinum (Pt) metal as the counter electrode. As illustrated in Figure 4.5 [170], CV experiments were performed in 0.1 M of LiClO4: ACN over a potential

from -0.9 V to +1.2 V employing PEDOT:PSS as electrodes swept from 0 V to positive potentials and vice versa at different scan rates.

Both pristine and doped PEDOT:PSS electrodes demonstrated growing cathodic

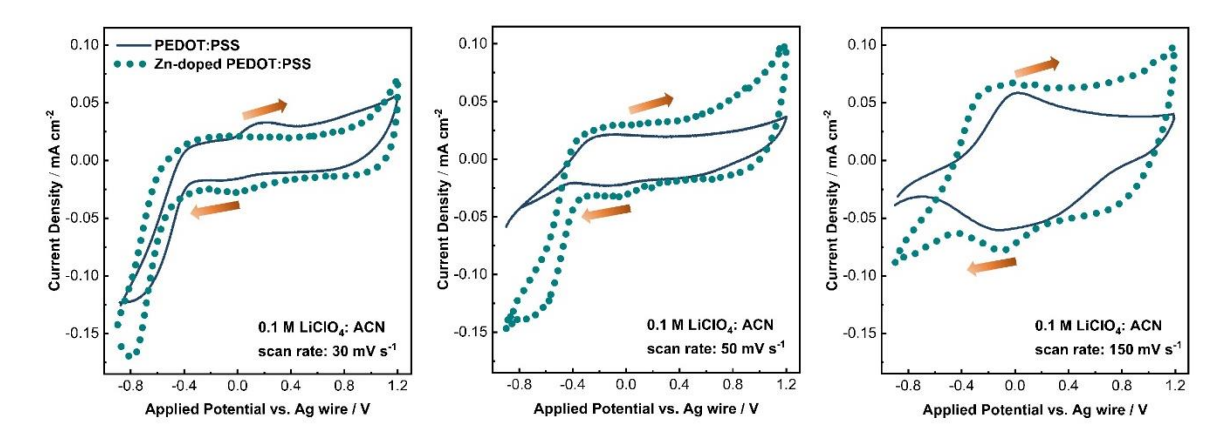


Figure 4.5 Comparison of the PEDOT:PSS layers' cyclic voltammograms between 1.5 V to - 1.0 V vs Ag in 0.1 M LiClO₄/ACN under various scan rates [170].

current densities. Kumar et al. observed a similar trend when measuring the electrochemical reduction of PEDOT:PSS surfaces during CV experiments under air purging [182]. The rapid reoxidation caused by oxygen decomposition explains this action. The doped PEDOT:PSS layer clearly presents a substantially cyclic voltammogram with a rectangular shape at 150 mV s-1, demonstrating that the response of the electric double layer to charge-discharge are quick, revealing a highly reversible and kinetically straightforward activity [183]. At faster scan rates, the cells were capable of providing firmly rectangular shapes since active material and the current collector are more strongly coupled [184]. Furthermore, current increased in doped PEDOT:PSS electrodes, which could be attributed to improved activity of surface and electron transport after doping [185]. At a scan rate of 150 mV s⁻¹, the inserted (Qi) and extracted (Qe) charge values for pristine and doped films were estimated to be 517.97 C cm⁻²: 464.93 C cm⁻² and 888.64 C cm⁻²: 762.26 C cm⁻², respectively. Furthermore, as illustrated in Figure 4.6, cyclic voltammetry analyzes were performed for larger potential ranges. When the potential range was

expanded to "1.5 V to - 1.0 V" rather than "1.2 V to - 0.9 V," greater and much more balanced current densities were achieved. For lower scan rates, more analogous cyclic voltammogram forms were detected compared to the initial observation. However, greater current and much more rectangular curves were met with Zn-doped PEDOT:PSS electrodes. Figure 4.6. (a) and (b) [170] display 50 cycles for pristine and Zn-doped PEDOT:PSS films for 1000 mV s⁻¹ scan rate. As depicted by the yellow arrows, both layers had strong cycling stability with a small decrease in current. The apex current densities of doped PEDOT:PSS films decreased, although the anodic and cathodic peak current densities of pristine PEDOT:PSS layers also reduced. At a scan rate of 150 mV s⁻¹, the inserted (Qi) and extracted (Qe) charge quantities for pure and doped layers were determined to be 847.649 C cm⁻²: 766.235 C cm⁻² and 1.961 mC cm⁻²: 1.901 mC cm⁻², respectively. The better conductivity of the doped HTLs as electrodes (Figure 4.4 (a)) may be the explanation for the increased charge capacity [186]. Figure 4.6 (c) [170] also depicts that the cathodic and anodic peak current densities are dependent on the square root of the scan rate. The demonstrated linear relationship indicates explicit diffusion for both electrodes. The doped PEDOT:PSS electrodes having a higher slope reflecting improved diffusion quality. The CV findings indicate that the electrical conductivity of the doped HTL has improved, as shown before by current-voltage results.

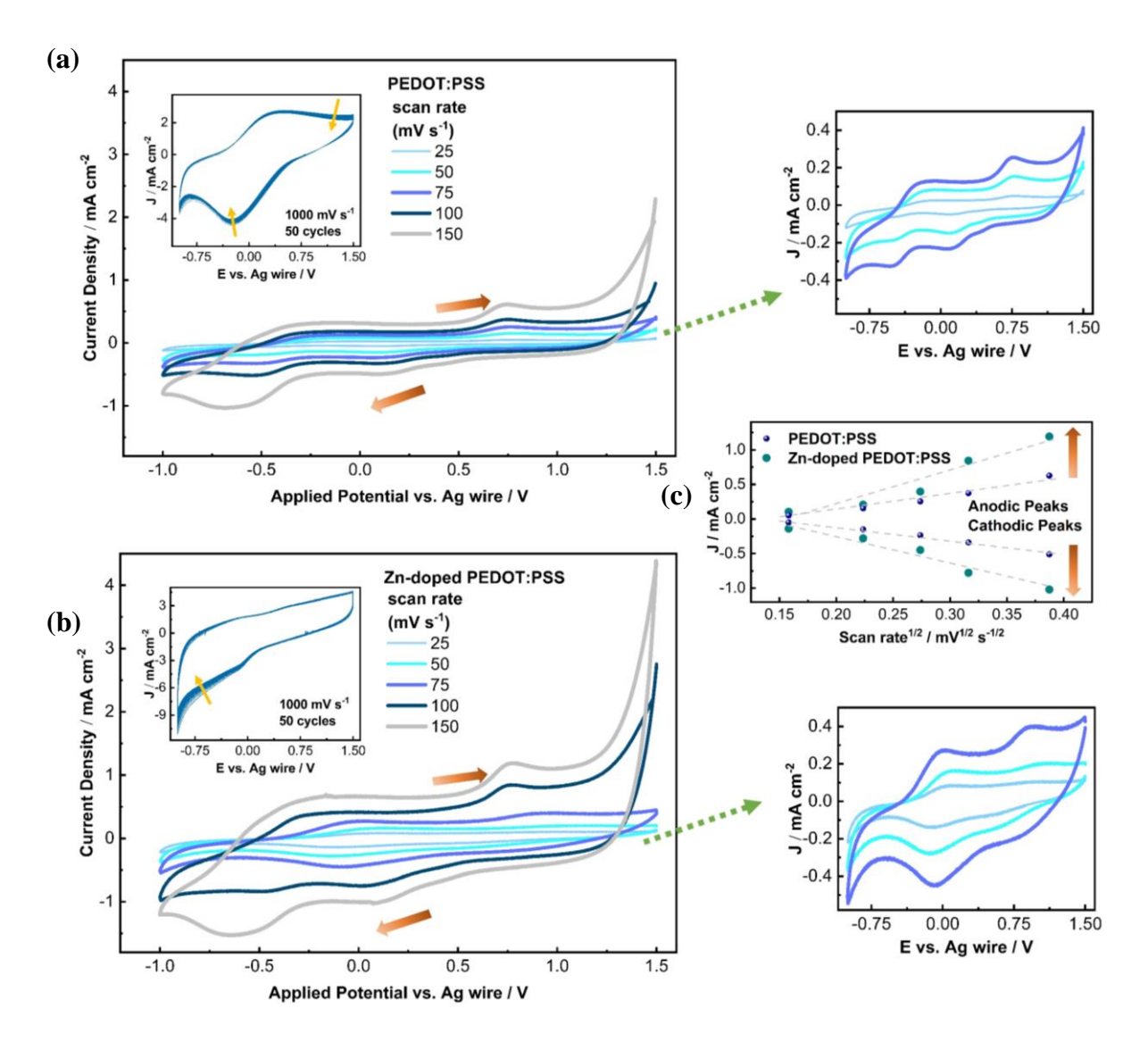


Figure 4.6 Cyclic voltammograms of the (a) PEDOT:PSS (b) Zn-doped PEDOT:PSS layers between 1.5 V to - 1.0 V vs Ag in 0.1 M LiClO₄/ACN under various scan rates (c) Anodic and cathodic peak currents vs scan rate [170].

Figure 4.7 (a)-(b) [170] shows the chronoamperograms obtained by using -0.9 V and 1.2 V for 180 s. Although the thin layer of PEDOT:PSS-based films (about 100 nm), a notable color variation was detected during chronoamperometry experiments, Figure 4.7 (b) [187].

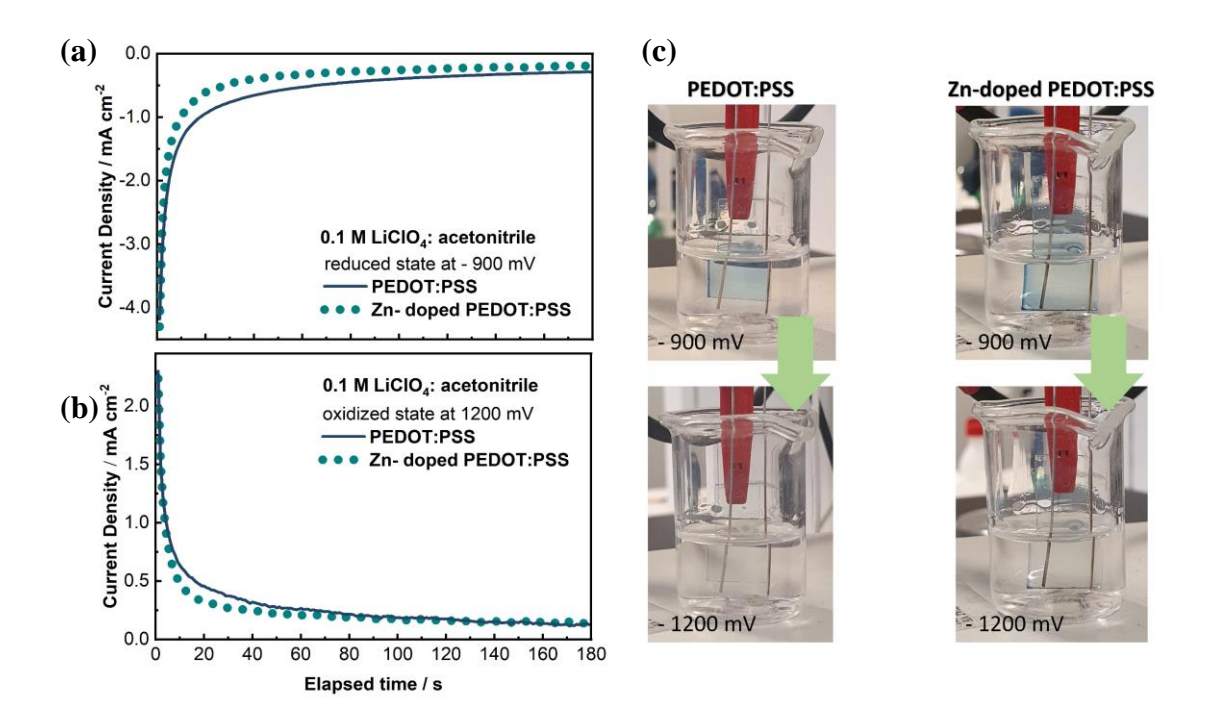


Figure 4.7 Chronoamperograms of the PEDOT:PSS and Zn-doped PEDOT:PSS layers during 180 seconds at (a) - 900 mV (b) 1200 mV vs Ag in 0.1 M LiClO₄/ACN (c) pictures of reduced and oxidized states of PEDOT:PSS films on ITO coated glass substrates during CA experiments [170].

Furthermore, when compared to pristine PEDOT:PSS electrodes, doped PEDOT:PSS electrodes showed stronger carrier diffusion, implying a shorter time to achieve steady-state, indicating the improved conductivity once more.

FE-SEM was used to study the morphological properties of surface of perovskite films from top, which is quite important in the functioning of photovoltaic devices. Figure 4.8 [170] displays two separate scales of FE-SEM representations of the perovskite films on pristine and doped PEDOT: PSS. As illustrated in Figure 4.8 [170], the perovskite layer developed on the top of doped film has a higher grain size than those produced on the surface of pristine film. The average and prevalent grain sizes of the perovskite layer produced on the undoped film are 142 nm and 103 nm, respectively,

whereas these parameters were obtained as 197 nm and 183 nm for the perovskite layer coated on the Zn-doped layer, respectively. The perovskite layer formed on the doped HTL becomes more uniform and homogeneous as the quality of the interface between the perovskite and the HTL improves, which can also be confirmed by the proximity of the average and prevalent grain sizes, as well as the presence of smaller pin-holes, which can assist in the improvement of PV characteristics, resulting in an improvement in the performance of photovoltaic device. Increased grain size leading to perovskite film with grain boundaries without holes improving the perovskite film, is beneficial to the fill factor and short-circuit current.

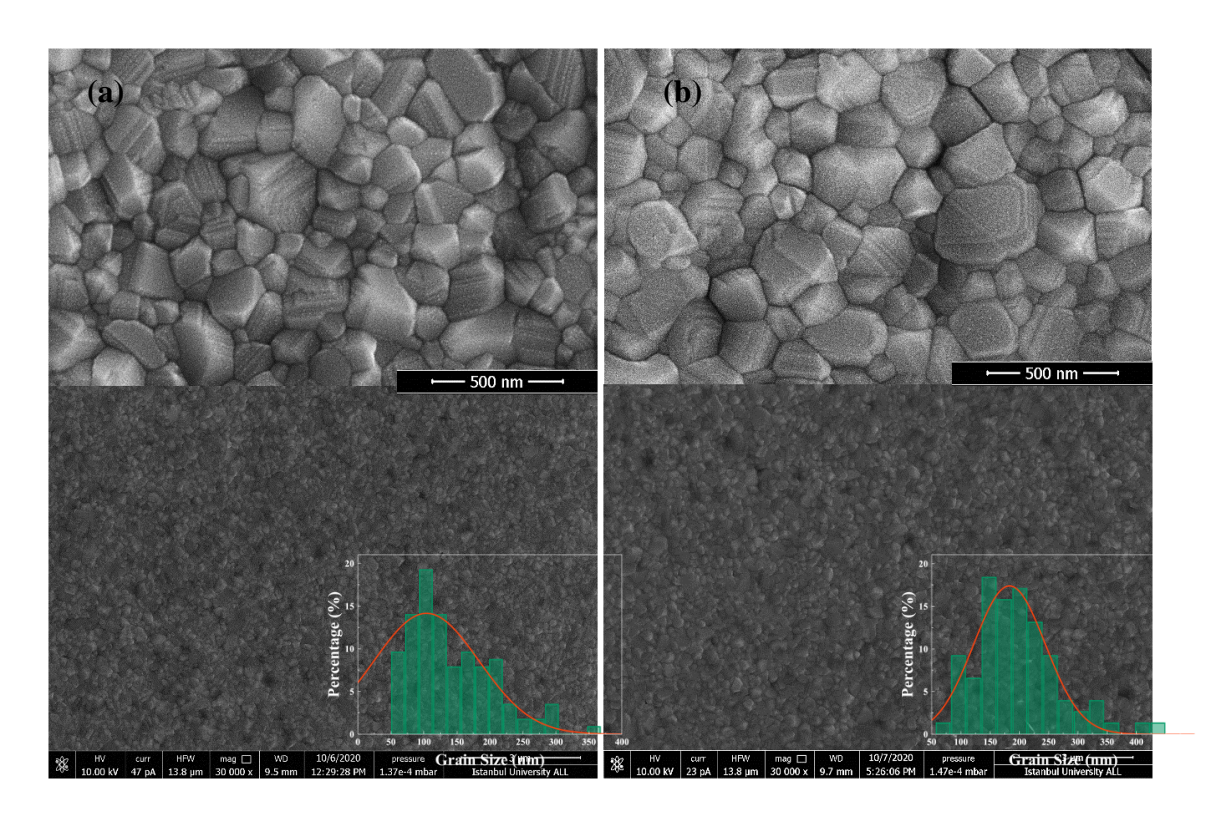


Figure 4.8 FE-SEM images of perovskite films on (a) PEDOT:PSS and (b) Zndoped PEDOT:PSS films under 100000 X and 30000 X magnifications [170].

The J-V curves of photovoltaic devices under illumination, are depicted in Figure 4.9 [170]. As compared to the pristine device, the devices employing zinc doped HTL displayed remarkable improvement. The photovoltaic parameters of the devices are exhibited in Table 4.1.

Table 4.1 PV characteristics of produced cells (Champion efficiency, Average efficiency values for 20 cells: PCE*, standard deviation) [170]

HTL	V _{OC} (mV)	J _{SC} (mA/cm ²)	FF (%)	PCE (%)	PCE*	σ	R_{Series} (Ω/cm^2)	R _{Shunt} (kΩ/cm ²)	HF
PEDOT:PSS	890	15.4	70	9.6	8.9	0.40	4.8	1.7	0.08
Zn-doped PEDOT:PSS	925	17.2	83	13.2	12.5	0.39	4.1	35	0.02

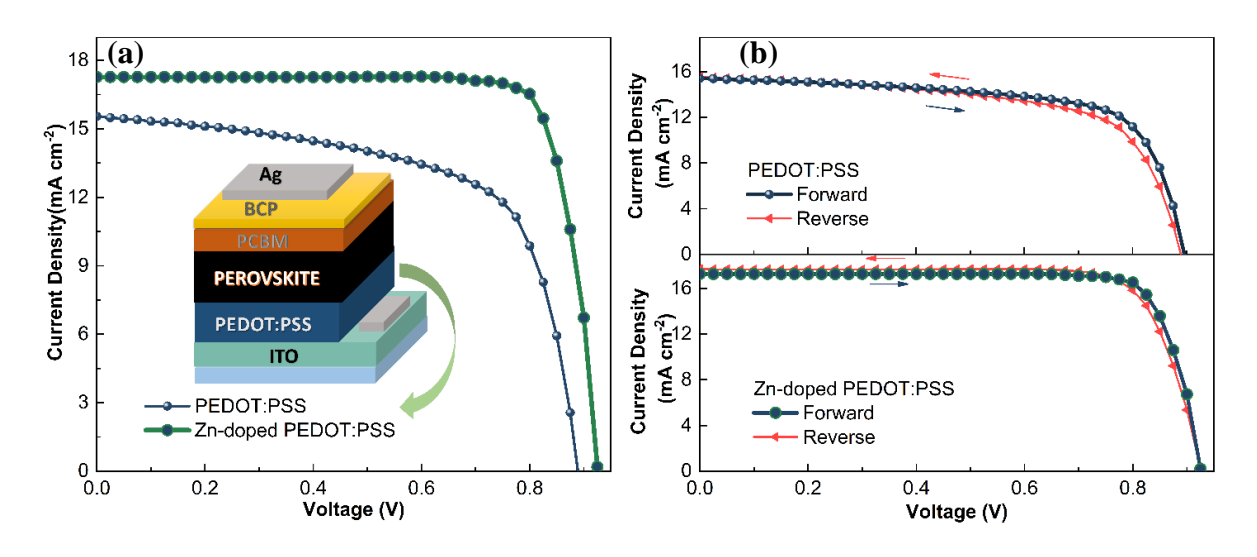


Figure 4.9 (a) Illuminated current density-voltage curves of the solar cell devices with different HTLs (b) Hysteresis curves of the corresponding solar cell devices [170].

The device employing pristine PEDOT: PSS exhibited a J_{SC} of 15.4 mA cm⁻², an open-circuit voltage V_{OC} of 890 mV, and a fill factor FF of 0.7, leading to a PCE of 9.6 %. Whereas, the devices employing the Zn-doped HTL showed a J_{SC} of 17.2 mA cm⁻², an open-circuit voltage V_{OC} of 925 mV, and a fill factor FF of 0.83, leading to a PCE of 13.2 %. Improvement in the morphology of perovskite layer and HTL, and also increased conductivity accounted for the improvement in the photovoltaics parameters of the devices with Zn doped PEDOT:PSS layers. Despite the mechanism of hysteresis is not clearly determined, it is supposed to have something to do with trap states and charge accumulation at the interface between active layer and the carrier selective layer (ETL and/or HTL) [77,188,189].

Figure 4.6 (b) [170] shows that our devices have a very low level of hysteresis, with slightly different J-V curves for forward and reverse scanning results. Table 4.1 [170] shows the derived hysteresis factors, which indicate the hysteresis of doped HTL involved cells is lower than that of devices with pristine HTL. Consequently, it can be noted the hysteresis of the device was reduced with the assistance of Zn. Shunt resistance is the impedance of PV devices to leakage current. To put it another way, the lower shunt resistance, the higher leakage current. The improved short-circuit current values can be attributed to the measured shunt resistances (R_{Shunt}), which are substantially higher in the doped PEDOT:PSS device than in the pure PEDOT:PSS device.

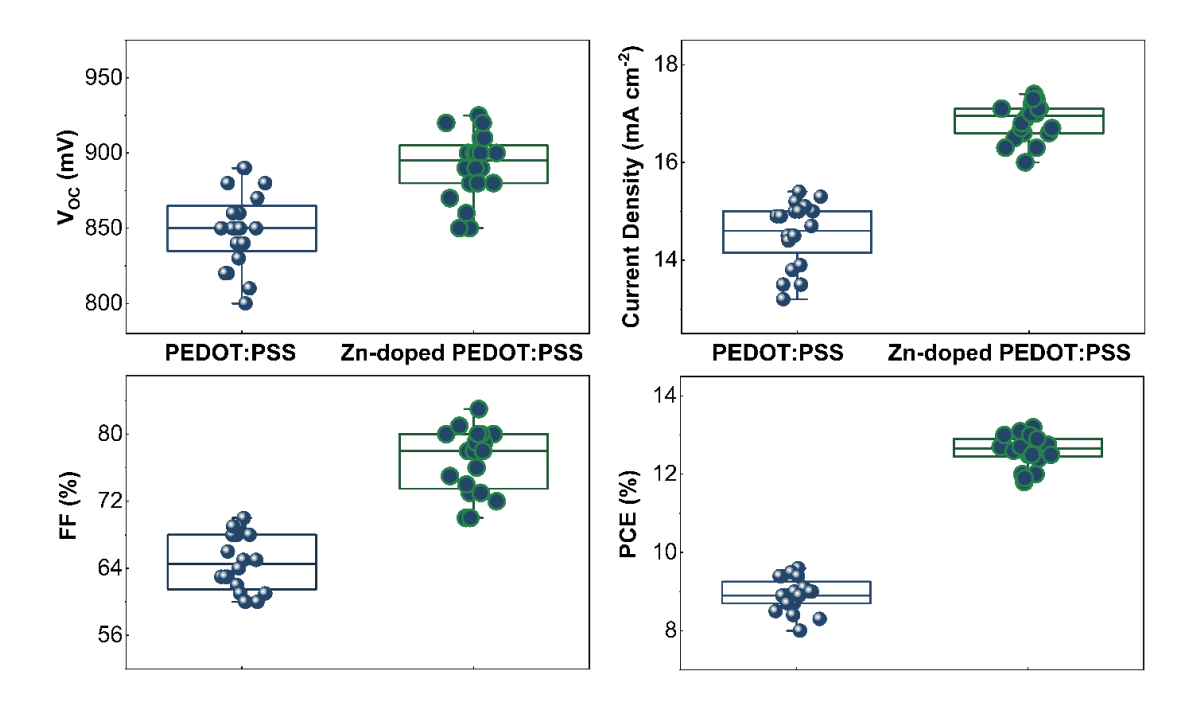


Figure 4.10 Box chart graphics of photovoltaic parameters of the solar cell devices [170]

The statistics of PV parameters (V_{OC} , J_{SC} , FF, PCE) of the devices employing pristine and Zn-doped HTL are shown in Figure 4.10 for 20 cells. The fill factor and current density values have been considerably enhanced by using additive within HTL, as shown in Figure 4.10. The narrowed boxes also reflect that the doped PEDOT:PSS-based devices fabricated in this study are more reproducible.

We fabricated hole-only cells with an architecture of ITO/HTL/perovskite/P3HT/Ag to investigate the density of trap states inside the perovskite using the SCLC technique. The dark J-V plots of hole-only cells are illustrated in Figure 4.11 [170]. Low bias voltages provide a linear relation between current and voltage, but after a particular voltage known the V_{TFL} , raising the voltage causes the current to rise nonlinearly. Hence, if the SCLC curves of hole-only devices display V_{TFL} characteristics that can be calculated, the trap density can be calculated using the formula below [190].

$$V_{TFL} = \frac{qn_tL^2}{2\varepsilon_0\varepsilon_r}$$
 (4-3)

The V_{TFL} results for pure and doped HTL used cells were obtained as 0.242 and 0.201 V, respectively, as depicted in Figure 4.11 (a) [170]. Therefore, the trap densities of the pristine and doped HTL-based cells were obtained as 0.95×10^{16} cm⁻³, and 0.79×10^{16} cm⁻³, respectively. Improved interfacial connection between the perovskite and the HTL leads to a decrease in the trap density for the devices employing doped HTLs, resulting in a reduced trap density [191].

The correlation between current and voltage is not linear throughout the high voltage zone (I α V²). The Mott-Gurney equation was used to calculate the mobility of hole for undoped and doped HTL-based cells.

$$J = \frac{9(\varepsilon_0)(\varepsilon_{PEDOT:PSS})(\mu)}{8L^3} V^2$$
 (4-4)

Here ε_0 , $\varepsilon_{\text{PEDOT:PSS}}$, L and μ are the vacuum permittivity, the relative dielectric constant of HTL (2.2 [192]), the thickness of the HTL (100 nm) and mobility, respectively.

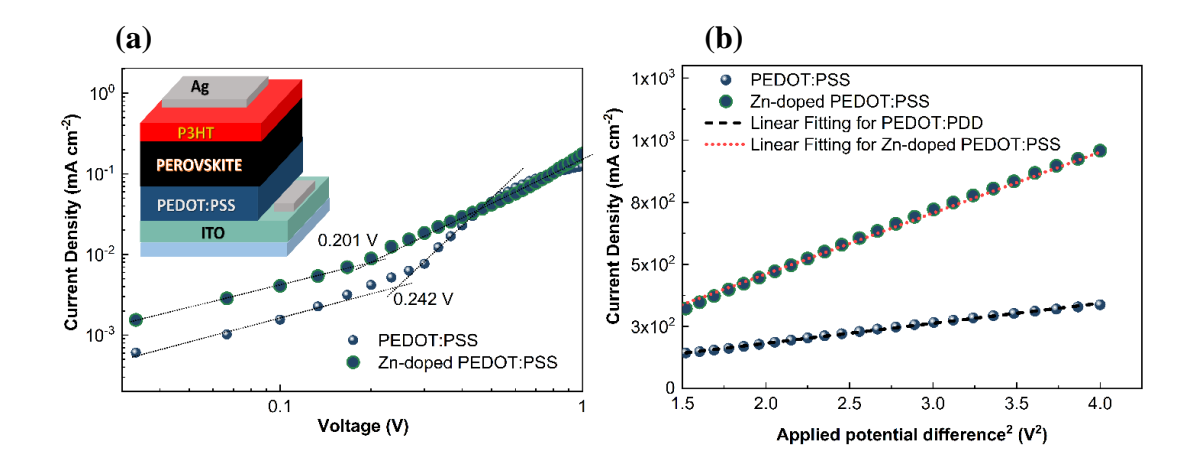


Figure 4.11 (a) Dark current density-voltage characteristics of the hole-only devices with ITO/HTL/perovskite/P3HT/Ag configuration, and (b) dark J-V² curves of high voltage region for hole mobility extraction [170].

The hole mobilities of the pristine and doped HTLs are calculated as 3.4×10^{-4} cm² V⁻¹ s⁻¹ and 1.1×10^{-3} cm² V⁻¹ s⁻¹, respectively, using the slope of J-V² from Figure 11 (b) [170]. The hole mobility of the doped HTL was greater than that of the pristine one, as anticipated, due to improvement in the electrical conductivity of doped HTL.

Figure 4.12 (a) [170] shows PL curves, supporting the enhanced carrier mobilities and reduced trap densities, and thus the PV performance of the doped HTL used cells. In other words, strongly quenching of PL intensity indicates the improved extraction of charge, transfer of carrier, and reduced recombination. To put it another way, strongly quenched intensity of PL indicates the extraction and transfer of charge increased while recombination rate decreased.

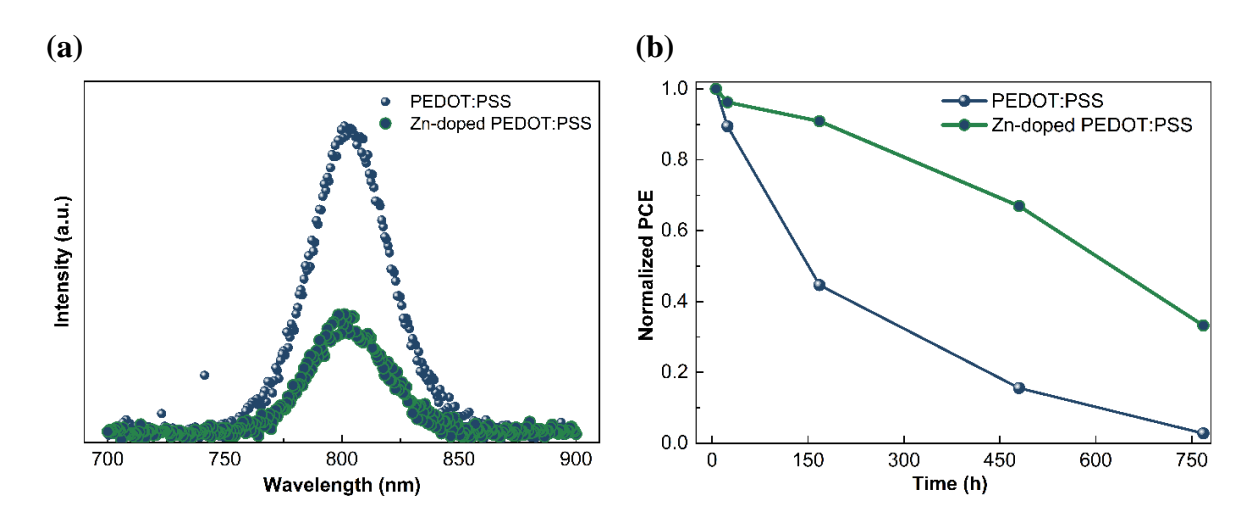


Figure 4.12 (a) Photoluminescence curves with a ITO/HTL/perovskite/PCBM/BCP configuration (b) normalized PCE values of the PSCs as a function of time [170]

Finally, the stability of the devices was studied, and the normalized results were displayed in Figure 4.12 (b) [170]. Cells were placed inside of a glove box without being encapsulated during the experiments. In 168 hours, the PCE values of devices employing pristine PEDOT: PSS cells declined to 45 % of their value at first, whereas doped HTL used devices preserved more than 90 % of it.

4.4 Conclusion

Perovskite solar cells employing pristine and Zn doped PEDOT:PSS HTLs have been fabricated and the effect of Zn doping of PEDOT:PSS layer on the performance of perovskite solar cells has been studied. A significant increase in efficiency and stability was observed for devices employing Zn doped PEDOT:PSS. The enhanced surface morphology of PEDOT:PSS layer upon Zn doping led to less rough and more homogeneous than the original one, suggesting that the high fill factor value is due to synergetic effects. SEM images disclosed that the use of a doped HTL results in homogeneous pin-hole free perovskite development, with an increase in grain sizes of perovskite and a reduction in grain boundaries. With doping of Zn, work function values derived from KPFM results increased slightly, leading to higher Voc values. Cyclic voltammetry experiments indicated an improvement in charge capacity of doped HTL, which can be interpreted as greater conductivity of the doped HTL, which is in excellent accordance with the current-density measurements. Optical transmittances were improved, which was supposed to result in enhanced lightharvesting efficiency for the doped PEDOT:PSS-based cells. Moreover, SCLC analyzes for hole-only devices indicated that at the interface the doped HTL has higher carrier mobility and lower trap density. Furthermore, photoluminescence quenching of doped HTL cells verified the findings. As a result, higher J_{SC} led to an improvement in device performance. Consequently, PEDOT: PSS HTLs doped with Zn are supposed to be attractive candidates for outstanding PSCs. Although we obtained high PCE of 13.2 %, we claim that efficiencies can be increased by enhancing the current densities by utilizing FTO-coated glass substrates instead of ITO-coated glass substrates inside of glove box.

THE ROLE OF BATHOCUPROINE CONCENTRATION ON THE PV PERFORMANCE OF NiO_x-BASED PSCs

5.1 Introduction

Nickel oxide (NiOx) has attracted a lot of attention in the p-i-n configuration because it has great stability and high hole mobility [193,194]. In the p-i-n configuration of perovskite solar cells, buffer layers including BCP [195–198], LiF [199,200], and PEIE [201] are commonly used to prevent recombination of charges between the electron transport layer and the cathode.

Vacuum or solvent processing may be used to process thin layers of BCP as buffer layers. While there are multiple reports focused on vacuum-processed BCP layers [202–205], the number of studies that use BCP layers prepared using a sol-gel method is relatively limited [206,207]. In this chapter, by varying the BCP concentration, prepared using the sol-gel process, we investigated the influence of BCP layers on the operation of PSCs. We have as well looked into the impact of spin coating rate of BCP film on the performance of a p-i-n perovskite solar cell as ITO/NiO_x/MAPbI₃/PCBM/BCP/Ag structure (Figure 5.1 [208]). All experiments were performed out of glove box under humidity around 60%. Unlike previous methods, this one does not involve the use of a high-vacuum setup.

5.2 Experimental procedure

5.2.1 Materials

Nickel (II) acetate tetrahydrate (Sigma, $\geq 99.0\%$), lead iodide (PbI₂, Sigma-Aldrich 99.0%), Bathocuproine (96%, Sigma), PCBM (Solenne, $\geq 99.0\%$), CH₃NH₃I (methylammonium iodide, Lumtec 99.99%), were bought and utilized without any additional refinement.

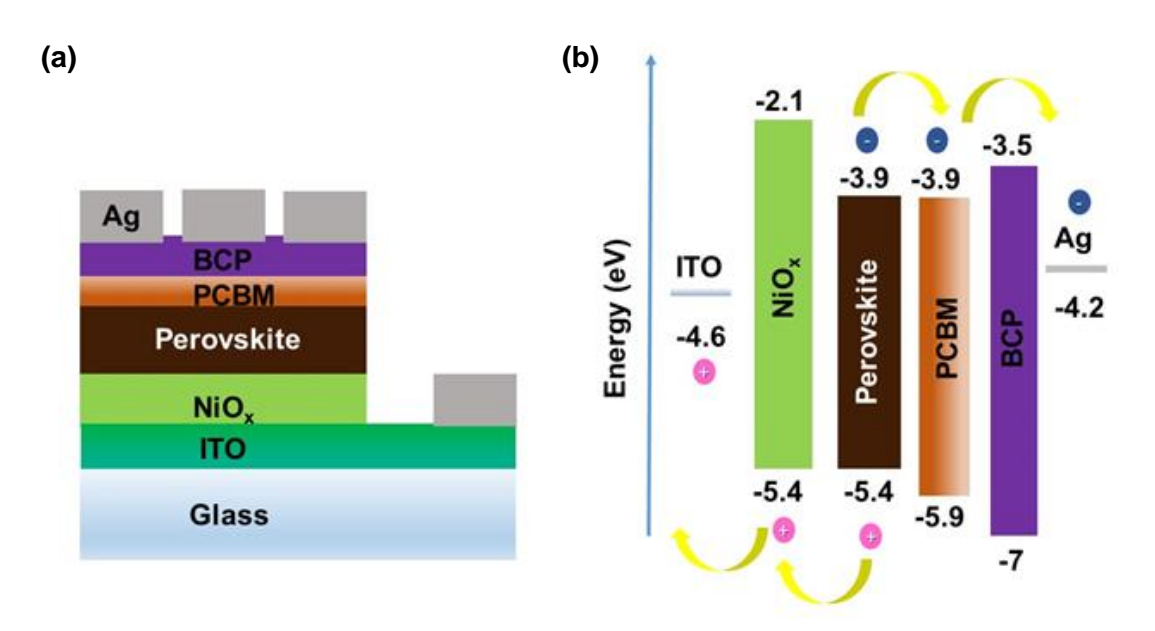


Figure 5.1 (a) Schematic description and (b) Energy level diagram for the device [208]

5.2.2 Device fabrication

At room temperature, 0.7 mM of nickel (II) acetate tetrahydrate was added into the mixture of IPA (5 ml) and ethanolamine (30 μ l). To obtain NiO_x solution, the blend was stirred for a few hours at 70 °C. Prior to coating, the solution was filtered with a PTFE filter (0.22 μ m). The solution of perovskite was achieved from a mixture of MAI:PbI2 in GBL at a molar ratio of 1.4:1.4 and agitated by a magnetic stirrer at

65 °C for one night before filtering with a PTFE filter (0.45 μ m). Bathocuproine (BCP) in various concentrations was solvated in absolute ethanol. PCBM solution was obtained by dissolving 20 mg PCBM in 1 ml chlorobenzene (CB) and agitating for 2 hours.

Initially, ITO coated substrates were etched and then washed with ethanol, acetone, and isopropanol, respectively, for device fabrication. In order to extract any impurities from the surface, substrates were sonicated in acetone and isopropanol for 20 and 45 minutes respectively. Ultimately, N₂ gas was used to dry the substrates. The solution of NiO_x was spin cast for 30 seconds at 1500 rpm at ambient air, and the coated substrates were heated at 80 °C for 15 min before being coated again. Afterward, NiO_x layers were annealed at 450°C for 30 minutes in a muffle furnace prior to use. By coating the solution of perovskite at 2500 rpm for 10 s and 4500 rpm for 20 s a perovskite layer was achieved. To obtain crystalline perovskite film, toluene washing was performed when the rotation speed reached 4000 rpm. Then, for 20 minutes at 100 °C, thermal annealing was performed. The PCBM solution was coated for 30 seconds at 1500 rpm, then thermal annealing for 90 seconds at 90 °C was applied. various concentrations of BCP solutions (0.325 mg/ml, 0.5 mg/ml, 1 mg/ml, 2 mg/l, and 4 mg/l) were spin coated for 40 seconds at two separate rotation speeds, 1500 rpm and 4000 rpm, individually. Finally, thermal evaporation was used to coat 110 nm thick Ag.

5.3 Result and discussion

The XRD spectrum of the obtained perovskite film is shown in the figure 5.2 [208]. The peaks are the characteristic crystalline MAPbI₃ structure peaks. The (110), (220), (310), (224), and (330) planes refer to $2\theta = 13.98^{\circ}$, 28.32° , 31.74° , 40.5° , and 42.5° , respectively, and represent the development of the tetragonal structure of perovskite [209].

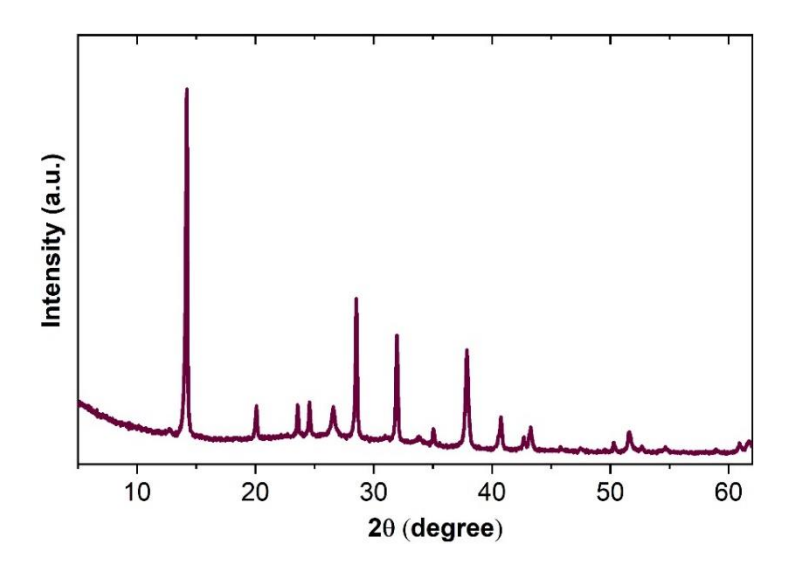


Figure 5.2 XRD graph of perovskite (MAPbI₃) film [208]

The photoluminescence and absorption spectra of the perovskite layer are demonstrated in the figure 5.3 [208]. The acquired optical band gap of MAPbI₃ is around 1.61 eV, which is consistent with the reported results [210,211].

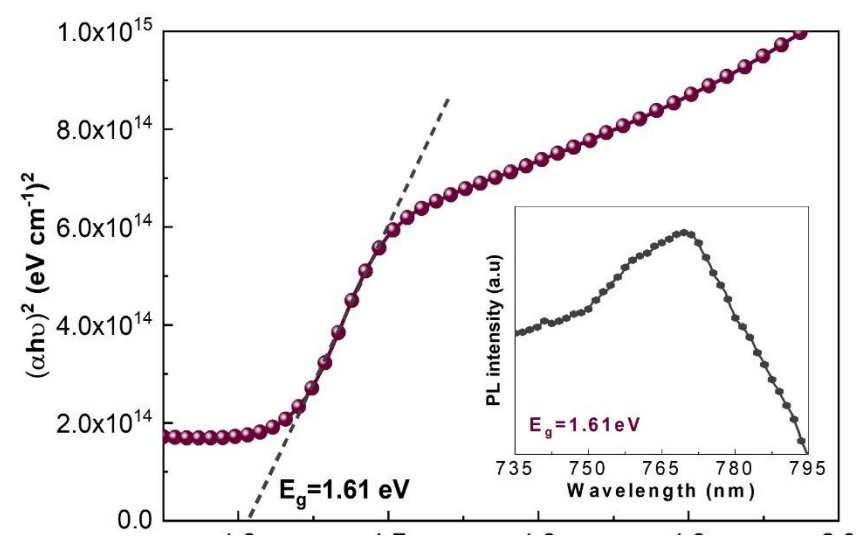


Figure 5.3 UV-Vis absorption spectra and photoluminescence (PL) of perovskite (MAPbI₃) film [208]

The FTIR pattern of the perovskite layer coated on an ITO surface is shown in Figure 5.4 [208]. The FTIR spectrum reveals the presence of various functional groups in the structure. The C–H band bending in the alkane group is primarily responsible for the IR band at 1465 cm⁻¹. The N–H stretching bond is represented by the infrared bands at 3180 cm⁻¹ and 3138 cm⁻¹ [212,213].

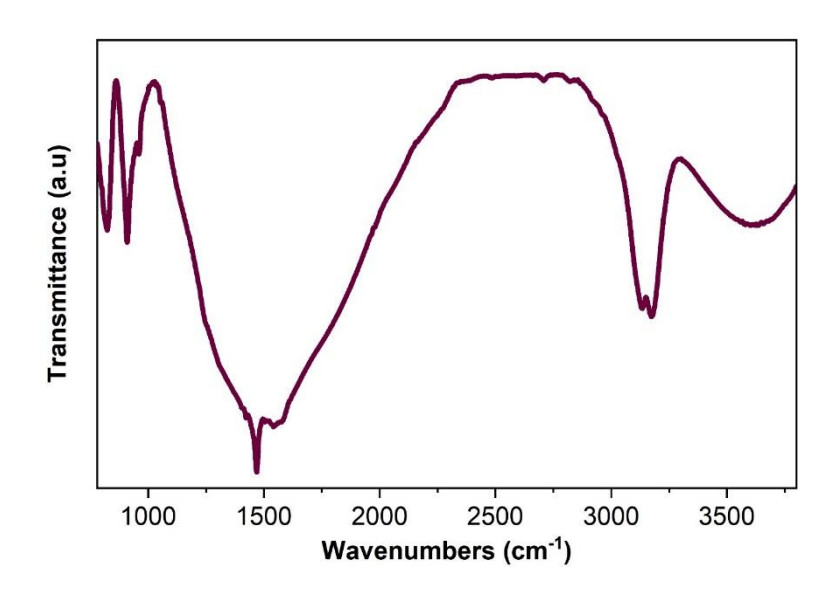


Figure 5.4 FTIR spectra of ITO/perovskite (MAPbI₃) film [208]

The J-V curves of devices employing BCP films, coated with various concentration and rotation speeds of 1500 rpm and 4000 rpm, respectively, are presented in Figure 5.5 (a)-(b) [208]. When the bathocuproine concentration was increased to 0.5 mg/ml, the J_{SC} of the devices increased. We noticed a decrease in the performance of PV devices as the BCP concentration was increased to 2 mg/ml. As an interlayer, BCP, Ca, and LiF are commonly employed in literature [214]. They assist in preventing an energy misalignment between the cathode and the electron selective layer, as well as cathode penetration into the conducting underlayers, which could result in charge recombination [214].

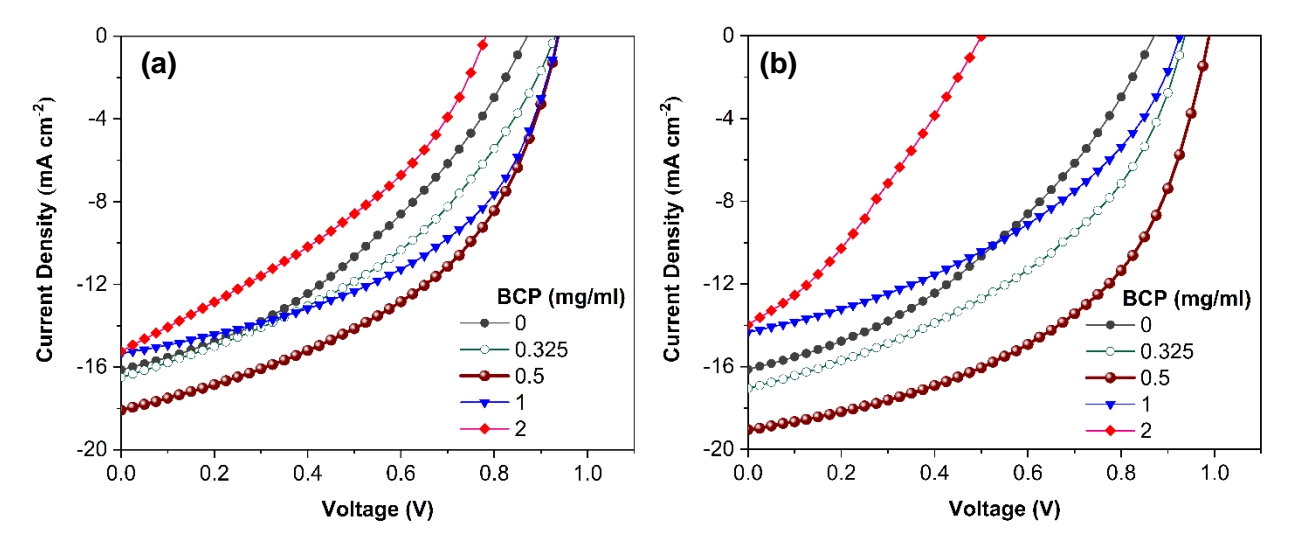


Figure 5.5 Current density-voltage curves of the solar cell devices as a function of BCP precursor concentration cast at (a) 1500 rpm and (b) 4000 rpm spinning speeds [208]

The PCE of devices employing BCP layers coated at 1500 and 4000 rpm are displayed at figure 5.6 (a) [208]. Spin coating is a technique for depositing thin and uniform films on flat underlying layers. A small proportion of coating material typically spreads to the substrate's center. Due to centrifugal force, coating material disperses when the layer is rotated at various speeds. The thin film thickness is directly affected by changes in spin coating speed. As the rotating speeds are raised, thinner layers can be formed. When the BCP solution is coated at higher rotating speeds of 4000 rpm, we have obtained a higher performance while holding the BCP concentration unchanged. Thinner films result from faster rotating speeds. As a result, for 4000 rpm, we anticipate a relatively thin layer of BCP than for 1500 rpm. It is important to remember that the BCP film functions as a interlayer between the electron transport layer and the cathode electrode. Consequently, aggregation can occur as a result of various mechanisms if the BCP coating is excessively thick or thin, resulting in system output degradation [197]. We selected 1500 rpm and 4000 rpm as moderate and high rotating speeds, respectively, and indicated that 4000 rpm is

the appropriate rotating speed for BCP films. The cells with bathocuproine films deposited at 4000 rpm from 0.5 mg/ml concentration have the highest performance of all. We noticed that the BCP concentration have a major impact on the performance of perovskite solar cells. The PCE of the perovskite solar cells enhanced at first and then reduced as concentration rose [197].

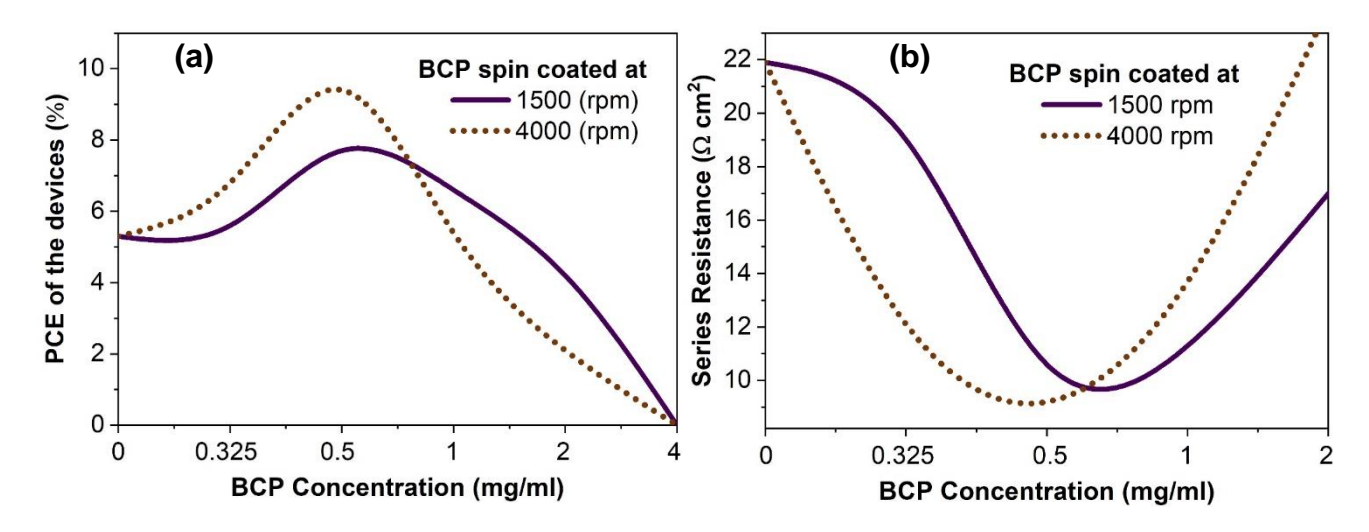


Figure 5.6 (a) Power conversion efficiency and (b) series resistance of the solar cell devices as a function BCP layer coating parameters [208]

The devices series resistance (Rs) is illustrated in Figure 5.6 (b) [208]. As illustrated, for the devices employing BCP films with 0.5 mg/ml concentration, the Rs is the lowest at both rotating speeds. A Schottky contact can be built between Ag and PCBM layers for devices that do not have a BCP layer [215]. Schottky contact prompt charge aggregation and strong series resistance, resulting in poor device performance. Rs is reduced when a thin layer of bathocuproine is inserted between Ag and PCBM, because of the development of an ohmic contact [196]. Since the concentration of dissolved materials affects the viscosity of a solutions, the BCP concentration has a major impact on the performance of PSCs [216], and the thickness of a deposited layer is influenced by its viscosity [217]. A high concentration of BCP can obstruct

charge transport at the interface due to its insulating properties. According to the literature, excessively thin or thick BCP films induce accumulation of charge via variety of mechanisms, resulting in poor device operation [218].

We manufactured electron-only cells (e-only) as ITO/TiO2/Perovskite/PCBM/BCP/Ag structure and also, we designed an electrononly cell without BCP as a reference. The J-V dark curves of PSCs and e-only cells with and without using BCP are displayed in Figures 5.7 (a) and (b) [208]. The leakage current density for PSCs with BCP layer is significantly low, as shown in Figure 5.7 (a) [208]. The inappropriate contact between two contact layers is the source of the leakage current [206]. The lower dark current means that BCP is doing a great job of interfacial improvement. The current rises linearly as voltage increase until a kink point, as shown in Figure 5.7 (b) [208] by increasing the voltage over the kink point, the current increases, indicating that the trap states are being filled by injected charge carriers [219]. The trap densities were calculated by utilization of the trap-filled limit voltage (V_{TFL}) and the formula

$$V_{TFL} = \frac{en_t L^2}{2\varepsilon\varepsilon_0}$$
 (5-1)

where e is elementary charge, n_t is trap state, L is the perovskite thickness, ϵ_0 and ϵ are the vacuum and perovskite permittivity, respectively. According to the literature, the perovskite's dielectric constant is 32 [220]. In this study, a perovskite film thickness around 240 nm was obtained. The e-only cell without BCP had a trap density of 5.71×10^{15} cm⁻³, while the e-only cell with BCP had a trap density of 4.65×10^{15} cm⁻³. As demonstrated, when BCP is added to the device setup, the trap density decreases, indicating that the quality of device improves.

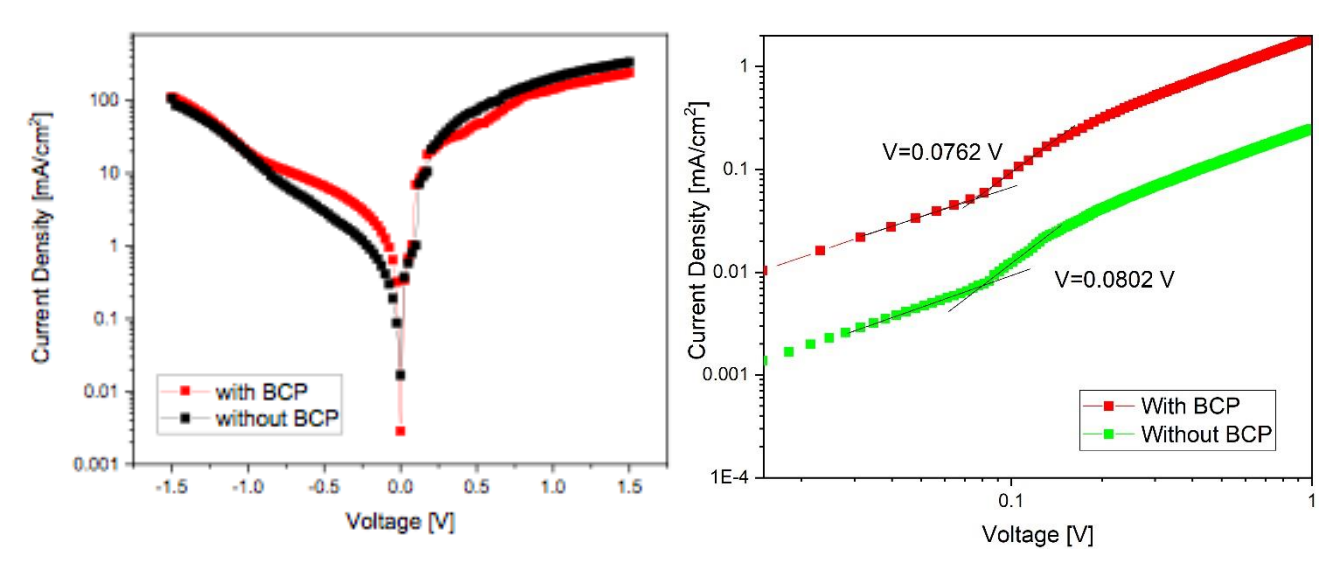


Figure 5.7 Dark current density-voltage characteristics of (a) perovskite solar cells (b) e-only devices (ITO/TiO₂/MAPbI₃/PCBM/BCP/Ag) with and without BCP (0.5 mg/ml, 4000 rpm) layers [208]

Table 5.1. Photovoltaic parameters of fabricated devices [208]

ВСР	Casting (rpm)	V _{oc} (mV)	J _{SC} (mAcm ⁻²)	FF	PCE (%)	R _S (Ωcm²)	R_{Sh} (Ωcm^2)
(mg/ml)	(тріті)	(1114)	(maom)		(70)	(12011)	(12011)
0		875	16.1	0.37	5.32	2.19 ×10 ¹	1.9×10^2
	1500	930	16.5	0.37	5.6	1.9 ×10 ¹	1.65 ×10 ²
0.325	4000	930	17	0.43	6.8	1.21 ×10¹	1.79 ×10 ²
	1500	930	18	0.46	7.7	1.06 ×10¹	1.82 ×10 ²
0.5	4000	990	19	0.50	9.4	0.92 ×10¹	2.95 ×10 ²
	1500	930	15.3	0.47	6.6	1.13 ×10¹	2.52 ×10 ²
1	4000	925	14.3	0.41	5.4	1.37 ×10 ¹	2.11 ×10 ²
	1500	780	15.2	0.36	4.2	1.7 ×10 ¹	8.84 ×10 ²
2	4000	510	13.9	0.30	2.1	2.4 ×10 ¹	6.88 ×10 ²

The PV parameters of the manufactured devices are listed in Table 5.1 [208]. It is certain that using the BCP reduces the series resistance of cells. Devices that do not use BCP demonstrated a $V_{\rm OC}$ of 0.875 V and a $J_{\rm SC}$ of 16.1 mA/cm² with a fill factor of 0.37, resulting in a PCE of 5.3%. For the devices with BCP layers prepared at a concentration of 0.5 mg/ml the FF, $V_{\rm OC}$, and $J_{\rm SC}$ have risen to 0.5, 0.99 V, and 19 mA/cm² respectively, which resulted in a PCE of 9.4 %. The FF, $J_{\rm SC}$, and $V_{\rm OC}$ of devices are significantly reduced with increasing concentration, resulting in a decreased PCE.

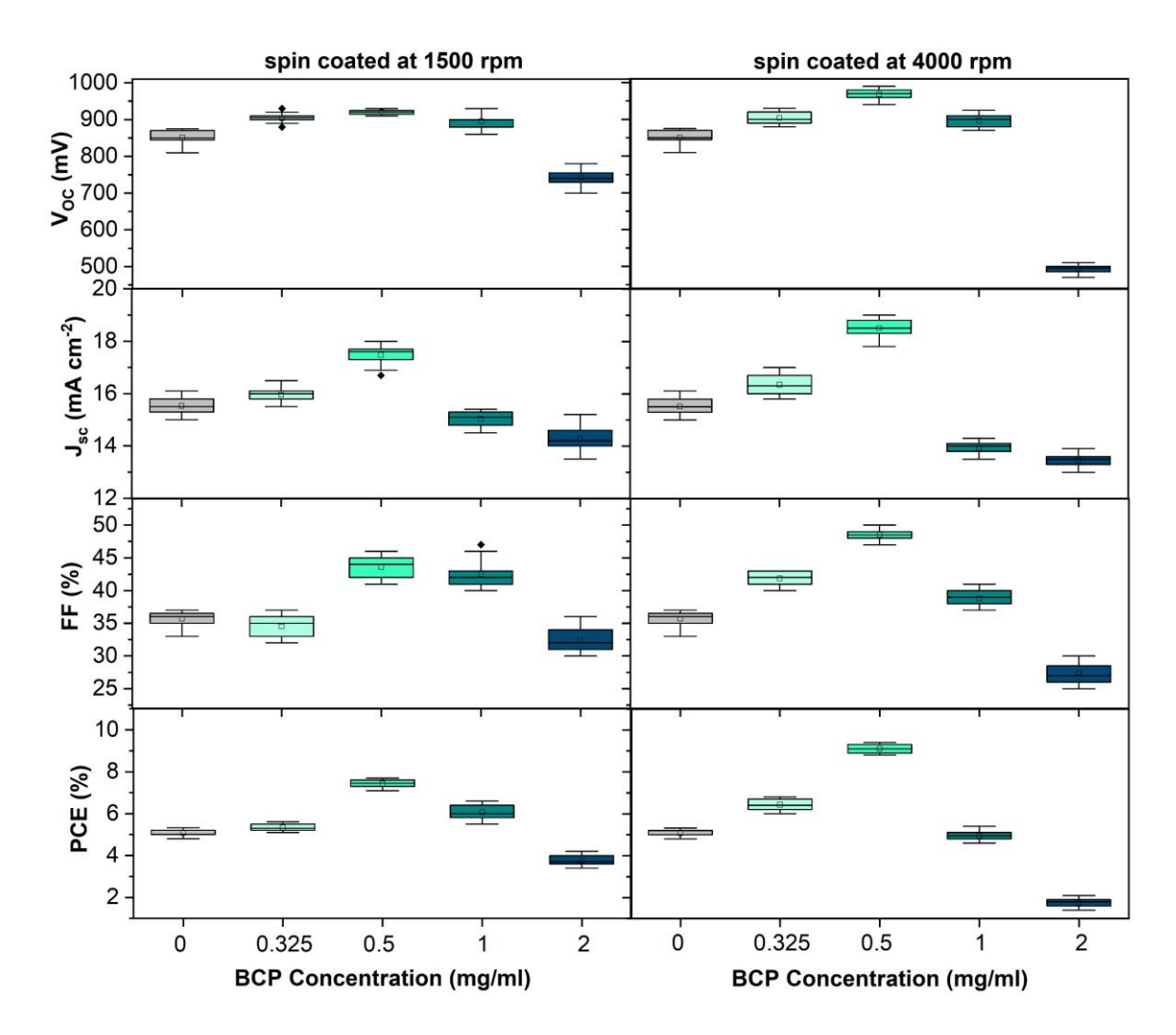


Figure 5.8 Distribution of the open circuit voltage, short circuit current density, fill factor and power conversion efficiency values over 15 solar cell devices as a function of different BCP concentrations cast at 1500 rpm and 4000 rpm [208]

Figure 5.8 [208] displays PV parameter (FF, V_{OC} , J_{SC} , PCE) statistics for 15 perovskite solar cells produced with different BCP concentration and rotation speeds. There is a relation between FF and V_{OC} with properties of the junction in perovskite solar cells [197] and consequently, the higher FF and V_{OC} , the higher PCE. J_{SC} relies on the passage of produced charge carriers from the perovskite film to the suitable transport layer. Charge carriers will be recombined or accumulated in the interface if the charge carrier transition does not go well [221]. The J_{SC} has been noticeably enhanced by increasing the concentration of bathocuproine to 0.5 (mg/ml), as displayed in Figure 5.7 [208]. These results revealed that the optimized BCP concentration, can minimize the recombination of charge carriers at the interface. Moreover, the devices show a great reproducibility.

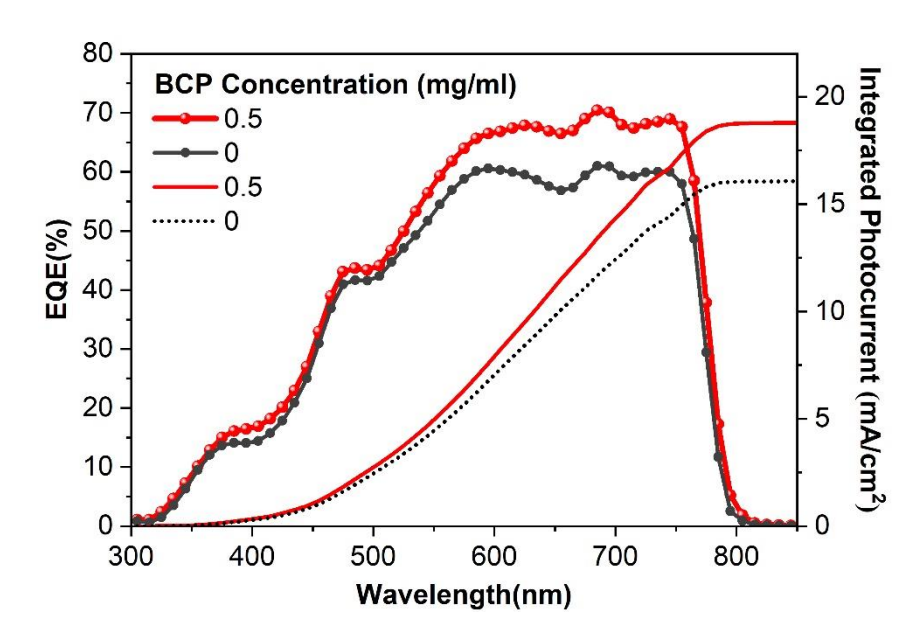


Figure 5.9 EQEs and corresponded integrated photocurrent densities of the solar cell devices with BCP (0.5 mg/ml, 4000 rpm) and without BCP layers [208]

Figure 5.9 [222] illustrates the EQE of PSCs with and without BCP films. The addition of BCP has an impact on EQE on both the short and long wavelength zones. PCBM/Ag configuration had an integrated photocurrent density (J_{SC}) of 16.05 mA/cm², while PCBM/BCP (0.5 mg/ml, 4000 rpm) /Ag configuration had an integrated

photocurrent density (J_{SC}) of 18.7 mA/cm² which are both achieved from EQE curves. The J_{SC} values obtained from EQE spectra were very close to the J_{SC} values obtained from J-V curves. The use of BCP as a hole-blocking layer reduces charge recombination at the interface, leading to a better external quantum efficiency in the PCBM/BCP(0.5 mg/ml)/Ag configuration.

5.4 Conclusion

In conclusion, applying a BCP as an interlayer between PCBM as a ETL and Ag as a cathode enhanced PV performance. By using 0.5 mg/ml BCP at 4000 rpm rotating speed, the champion device with high performance was obtained. Much more increases in BCP concentration resulted in thicker layers, which resulted in lower performance because of charge accumulation at the PCBM and the thick BCP interface, as reported in the literary works [196,197]. As the BCP concentration was optimized, the series resistance of the devices reduced, resulting in improved performance of device.

Ce AND Zn CO-DOPED NiO_x-BASED HTLs FOR USING IN PSCs

6.1 Introduction

Because of their easy of fabrication and low level of hysteresis, inverted planar PSCs have received a lot of attention. Inorganic hole transporters are preferred for p-i-n perovskite solar cells, where the device's structure begins with hole transport layer construction. They are cost - effective, easy to manufacture, have high hole mobility and better chemical stability. Because of its abundant supply, cost effectiveness, good stability, great transmittance of light, appropriate energy stage placement with perovskite, broad direct bandgap, and strong conduction band, non-stoichiometric NiO_x is a highly desirable and environmentally beneficial option [194]. Altering the concentration of oxygen interstices or nickel vacancies in NiO_x can change its work function (WF) [223]. With the addition of NiOOH and Ni₂O₃, stoichiometric nickel oxide becomes a p-type semiconductor [224], despite of having conductivity less than 10⁻¹¹ S cm⁻¹. Since excessive oxygen causes Ni vacancies and thus holes, increasing the amount of Ni₂O₃ in the Ni⁺³ structures can improve hole conductivity [225]. However, a higher proportion of Ni3+/Ni2+ states can result in an unfavorable decrease in resistivity. The poor conductivity of NiO_X is indeed a challenge to NiO_X HTL implementation in PSCs. Extrinsic doping has recently received a lot of attention as it is considered to be a viable option to change Ni vacancies/holes and increase conductivity of hole without raising NiOx's resistivity [226]. To improve electrical conductivity, Chen et al used magnesium and lithium co-doping and observed that co-doped HTLs had a conductivity that was 12 times higher [227]. To compensate for the unpleasant valence band change induced by lithium injection into the structure, Mg was added to the Li doped nickel oxide. This co-doping strategy produced rigid lattice stability with a small ionic radii discrepancy. This NiMg(Li)O HTL boosted the occurrence of ohmic contacts between the perovskite layer and transparent conducting oxide by decreasing the height of barrier in the energy states configuration. Cu-doping improves conductivity with a lower NiO_x lattice parameter, in accordance with Kim et al [94], despite the fact that Cu has a larger ionic radius than Ni. Although conductivity increased as Cu increased, transmittance decreased, limiting sunlight spectrum utilization and hence the performance. To boost the transmittance of Cu-treated nickel oxide films, Liu et al. employed Li and co-doped nickel oxide performed better than anticipated [228]. Chen et al. reported that doping nickel oxide with Cs resulted in greater hole extraction and much more acceptable band realignment [229]. In a paper on doping NiO_x with Ag, Wei et al. discovered that Ag prefers to fill the Ni locations and behaves as an acceptor in the nickel oxide composition. Furthermore, as compared to pure HTLs, Ag doping led to increased hole mobility, optical transparency, conductivity, and work function [230]. According to Xie et al., an optimum dose of Co will enhance the electrical conductivity and work function of NiO_x [231]. Xia et al. presented a paper about doped nickel oxide with lithium and silver, which enhanced hole mobility, electrical conductivity, and band adjustment in perovskite [232]. Teo et al. [233] demonstrated that the defects of NiO_x HTL are passivated by La doping. Chen et al recently reported a NiO_x HTL-based scarce earth ion treatment method [226]. Ce, Eu, Nd, Yb, and Tb ions were employed in NiO_X HTL. Inspired by the above reports, this chapter will present for the first time in the literature an investigation focused on doping of NiOx as a HTLs in inverted PSCs with Ce and Zn. Ni^{+2} , Ce^{+3} , and Zn^{+2} have ionic radius of 0.69, 1.14, and 0.74 Å, respectively. Zinc is suggested to enhance conductivity, whereas cerium is supposed to improve the stability of the perovskite film. The entire manufacturing process was done out of glovebox with humidity more than 55%, involving perovskite film coating employing a one-step toluene washing method.

In this thesis, for perovskite prepared using a GBL-containing precursor was used since DMF and DMSO-engaged equivalents are less stable in high humidity

conditions. According to our knowledge, only GBL-engaged procedures have PCEs that do not exceed 5% [191,234–239]. The ITO/NiO_x/CH₃NH₃PbI₃/PCBM/BCP/Ag arrangement attained record efficiencies of above 10%, and the PCEs of NiO_x-based devices were improved by the synergetic impact of Ce and Zn doping to 14.5 %.

6.2 Experimental

6.2.1 Materials

Methylammonium iodide was synthesized according to the literature. ITO substrates were bought from Sigma-Aldrich. Other Precursor materials which engaged in device manufacturing such as ethanolamine (MEA 99.5 % Sigma-Aldrich), PCBM (Nano-C purity 99.95 %), $Zn(CH_3CO_2)_2 \cdot 2H_2O$ (zinc acetate dihydrate, ACS Emsure), $Ce(CH_3CO_2)_3 \cdot xH_2O$ (cerium (III) acetate hydrate, Aldrich 99.99 %), nickel (II) acetate tetrahydrate (Aldrich > 99.0 %), BCP (96 %, Sigma), were bought and used without any further purification.

6.2.2 Precursor solutions

247 mg nickel acetate tetrahydrate was dissolved in 10 ml of isopropanol for 15 minutes to produce NiO_x precursor solution. Prior to heating, a 65 μ l ethanolamine (MEA) was added to the solution drop wisely. After adding MEA, the color of the mixture turned to dark green, and after dissolving the nickel salt at 75 °C, the color turns to clear green. The enclosed solution was magnetically stirred at 75 °C for a few hours. $Zn(CH_3COO)_2 \cdot 2H_2O$ and $Ce(CH_3CO_2)_3 \cdot xH_2O$ were added to the NiO_x precursor to produce cerium and zinc doped precursors. For $Zn(CH_3CO_2)_2 \cdot 2H_2O$ and $Ce(CH_3CO_2)_3 \cdot xH_2O$, the optimum values were determined to be 18 mmol % and 6 mmol %, respectively (Figure. 6.1 & 6.2 [240]). Doped solutions were stirred at 70 °C for 4 hours before being filtered through a 0.22 μ m filter at room temperature. Perovskite precursor solution achieved by combining 2.1 mM PbI₂ and 2.1 mM MAI

in 1.5 ml GBL at 65 $^{\circ}$ C for one night. The solution was filtered with 0.45 m PVDF filter before coating.

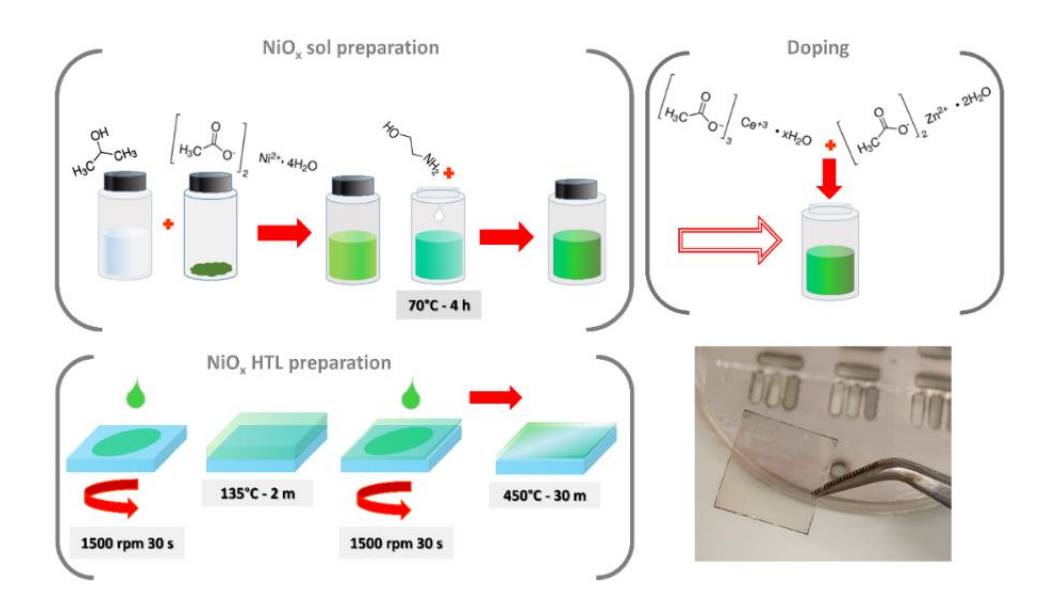


Figure 6.1 Precursor preparation and fabrication steps for NiO_x layers [240]

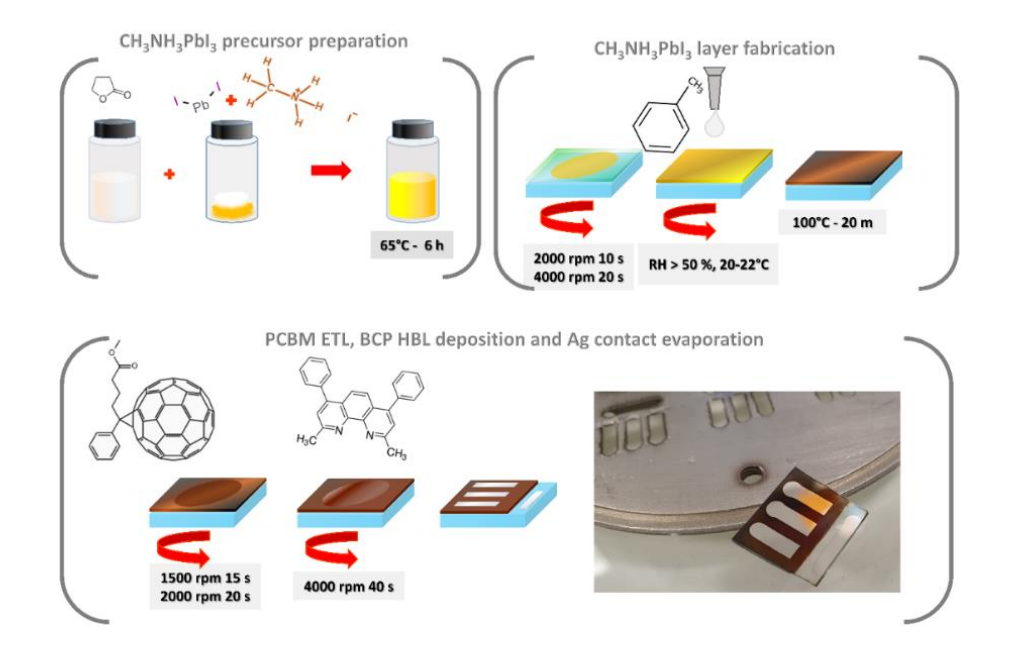


Figure 6.2 Perovskite precursor formation and solar cell fabrication steps [240]

6.2.3 Device fabrication

Ultrasonically washed ITO-coated glass slides in acetone for 21 minutes, then isopropanol at 65 °C for 45 minutes. N₂ gas was used to dry the substrates, then they were placed on a hot plate at 130 °C for 10 minutes and before being coated with hole transport layer, they were cooled. In ambient air, NiOx solutions were coated at 1550 rpm for 35 s. Cast HTLs were placed on a hot plate for 2 minutes at 135 °C, then the temperature of coated layer decreased to room temperature before being coated again with nickel oxide or doped-NiOx solutions. In a furnace, NiOx coated samples were sintered at 460 °C for 35 minutes. At 2001 rpm for 15 s and 4001 rpm for 25 s, the perovskite solution was spin coated on NiOx films. 65 µL of toluene were spurted on the rotating substrate. The samples were put on a hot-plate and annealed for 20 minutes at 100 °C. Instantly, a 20 mg/ml solution of PCBM in CB was used to develop the ETL. PCBM layers were coated at 1600 rpm for 20 s and 2500 rpm for 25 s, then heated at 95 ° C for 60 s. After that, a 0.5 mg/ml solution of BCP in ethanol was spin-coated for 40 s at 4000 rpm [222]. Ultimately, all of the cells were placed in a high-vacuum chamber and as a cathode contact, 110 nm thick Ag was vaporized.

6.3 Results and discussion

The AFM images which indicates morphological characteristics of doped and undoped NiO_x layers on ITO substrate are shown in Figure. 6.3 (a) [240].

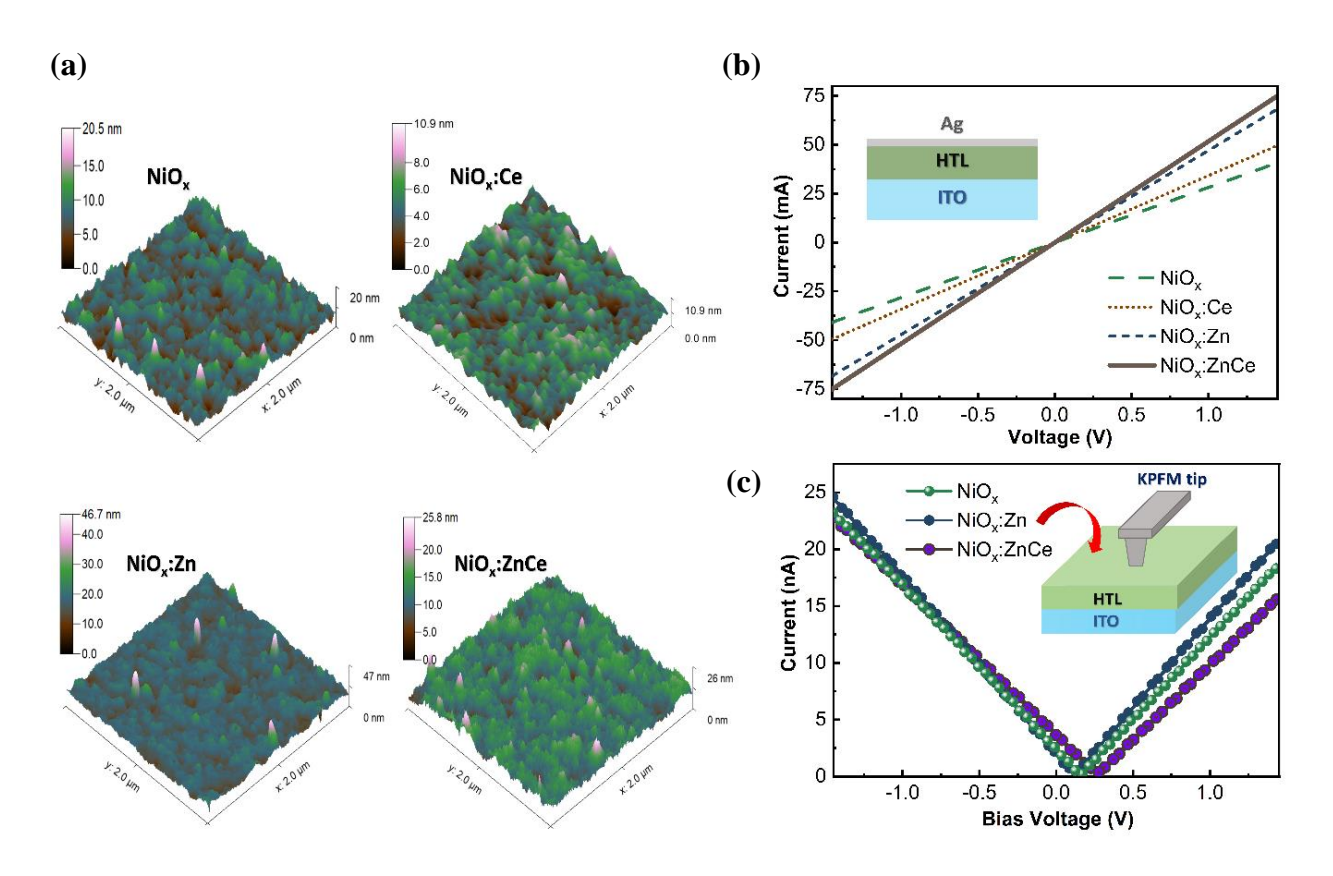


Figure 6.3 (a) AFM images (b) Current-voltage curves (c) KPFM measurements of NiO_x layers onto ITO coated glass substrates [240]

The pristine, Zn, Ce, and co-doped layers have RMS values of 2.023, 2.717, 1.802, and 2.373 nm, respectively. In comparison with the pristine films, doping the film with Ce (6 mmol %) the RMS is decreased whereas Zn (18 mmol %) doping substantially boosted it [241]. Nevertheless, zinc-cerium (18:6 mmol %) co-doping reduced the RMS as compared to that of the NiO_x film doped with Zn. This may be attributed to the fact that doping incorporation affects the formation and grain evolution of oxide semiconductors, which can either promote or prevent grain growth. Crystallization is determined by the atoms engaged in the phase transition, and impurity injection can influence deposition and grain development. Among many oxide semiconductors, the presence of impurities inhibits grain formation, resulting

in a smoother surface with the appropriate doping supply and dosage [226,228,229,242,243] or decrease of surface smoothness with the improper doping source and concentrations [228,232,244]. Doping nickel oxide with Ce at a specific doping proportion can impact the development process, leading to reduction in roughness of surface[245]. However, the roughness of Cu-doped NiO_X films is raised, according to Kim, et al. [246,247], since the radius of copper and nickel are nearly identical [248], it has been expressed that copper took the place of nickel and remained in the nickel oxide structure, which could have a beneficial influence [249].

In this study, since the ionic radii of Ni^{+2} and Zn^{+2} are similar to each other (0.69 and 0.74 Å, respectively), an improvement in the smoothness of Zn-doped films for various ratios of doping such as 18 mmol % may be anticipated [241]. NiO_X film's roughness has a significant impact on perovskite layers and interfacial stability. Despite that the surfaces with high roughness can lead to perovskite films with greater grain sizes [250], a smoother layer is preferable for efficient hole transport and facilitates a greater interface between HTL and the perovskite film, resulting in the formation of a perovskite layer with no pinholes. Therefore, the enhanced interface consistency between the perovskite and hole transport layer is thought to be a factor in the improvement of fill factor in comparison with devices that just used Zn doped HTL. As a result, co-doping was considered to be a significant approach to get low-roughness layers that are compact and homogeneous and a chance to get a surface that is not just smooth but also stable.

Current-voltage graphs with an ITO/HTL/Ag setup were used to investigate how conductivity varies due to doping, as displayed in Fig. 6.3 (b) [240]. The conductivity " σ " was derived using the 4-2 formula, with the layer thickness "L" determined using a profilometer. Conductivities for NiO_x, Ce, Zn, and co-doped NiO_x films were extracted to be 2.82 μ S cm⁻¹, 3.57 μ S cm⁻¹, 4.71 μ S cm⁻¹, and 5.18 μ S cm⁻¹, respectively, using the slopes of the graphs. Although it is possible that thickness fluctuates, it is obvious that the conductivity of nickel oxide films was enhanced

via doping of metal, as stated in previous studies [229,232,233,241,251]. Luckily, in comparison to that of only Zn doped films, co-doping resulted in a small rise. Low concentrations of Ce doping have been stated to function similarly to other metallic dopants in increasing electrical conductivity, as demonstrated by Dakhel et al. cerium improved the conductivity of metal oxide films [252].

The work function modification of nickel oxide layers by doping was investigated using KPFM and the results are shown in Figure 6.3 (c) [240]. Work function results for NiO_x, Zn, and co-doped nickel oxide films, were determined to be -5.26 eV, -5.22 eV, and -5.37 eV, respectively. Numerous analyzes on the work function values of NiO_x films over 5.5 eV have been released [229,241,253]. Our experimental work functions are comparatively high when compared to previously published work using UPS measurements, which yielded the smallest work function " φ_w " value on the surface. In this situation, KPFM was employed to achieve a work function based on the mean value of work function differences under the tip [254]. The V_{CPD} determines the φ_w difference, which is defined as 4-1 formula where "e" is the elementary charge. The development of NiOOH at top of the surface caused by UV-ozone treatment has been related to a powerful dipole, according to reports [255]. As illustrated in Figure 6.4 (a) [240], this favored improvement in work function of NiO_x results in better band alignment with the perovskite. Since improved band alignment facilitates hole collection from the perovskite film to the hole transport layer, successful extraction and transfer of holes are supposed to improve photovoltaic output and may be the explanation for the enhanced V_{OC} induced by co-doping.

In Figure 6.4 (b) [240], transmittance spectra and Tauc plots for nickel oxide films on ITO substrates are demonstrated.

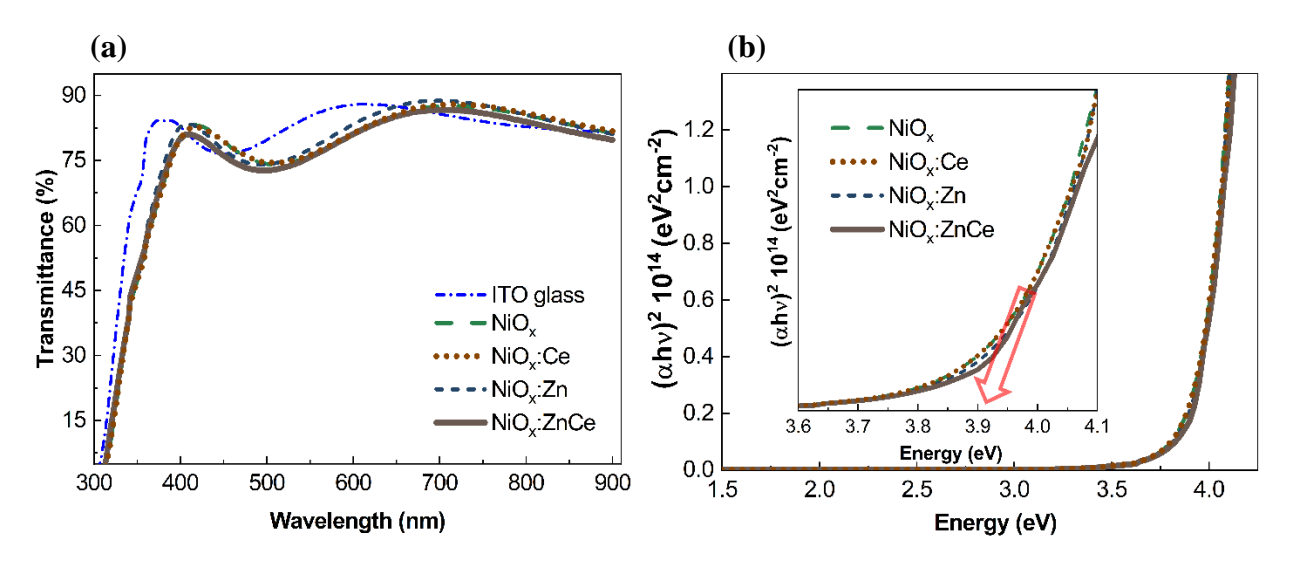


Figure 6.4 (a) UV-vis transmittance spectra (b) Tauc plots for NiO_x layers [240]

In the visible and near-infrared spectral zones, all of the $\rm NiO_{X}$ films provided strong transmittance of more than 80%. Doping-induced decreases in HTL transmittance are important for inverted PSCs because they are linked to optical losses, which lead to reduction in current and insufficient utilization of the solar spectrum. In this work, doping had no effect on the transmittance spectrum, indicating that photocurrent production generation was effective. Furthermore, for nickel oxide, Ce, Zn, and codoped nickel oxide films, the bandgaps ($\rm E_{g}$) derived from Tauc Plots were 3.96 eV, 3.93 eV, 3.96 eV, and 3.93 eV, respectively. The doping impact, which results in the creation of gap states, is said to be responsible for the slight drop in bandgap values caused by Ce incorporation [232,256,257].

The chemical compositions of the pristine and doped nickel oxide layers were determined using X-ray photoelectron spectroscopy. The survey spectra and identical high-resolution spectra of Ce, Ni, and Zn are indicated in Figure 6.5 (a)-(b) [240]. The non-stoichiometry and existence of Ni and O in NiO_x , as well as Ni, O, Zn, and Ce elements in Zn-Ce co-doped NiO_x films, are confirmed by the wide survey spectrums.

According to the Figure 6.5 (e) and (f), for Ce the $4p_{3/2}$ and $4p_{1/2}$ peaks are placed at 203.4 eV and 224.5 eV, respectively, while the $2p_{3/2}$ peaks for Zn are located at 1019.0 eV [241]. In the nickel oxide film, irrespective of doping treatment, the combined states of divalent and trivalent Ni charged particles are available, according to XPS data of the Ni 2p_{3/2} peaks in both NiO_x and Zn-Ce co-doped nickel oxide layers [230,243,258,259]. The three different peaks in the Ni 2p_{3/2} XPS spectra of pure and doped nickel oxide films are correlated with the NiO structure reorganization proceeding (860.9 - 861.6 eV), the vacancy induced Ni⁺³ ion (855.5 - 854.9 eV), and the cubic nickel oxide rock salt's typical Ni-O octahedral bonding characteristics (853.2 - 853.3 eV) [260,261]. Obviously, the Ni⁺³/Ni⁺² ratio grows with co-doping in this analysis, as illustrated in Figure 6.5 (c) and (d) [240]. Furthermore, Lee et al [241] identified XPS spectra of Zn-doped nickel oxide films, despite this fact that it was not noted the Ni3+/Ni2+ ratio, which shows no noticeable growth. We may conclude that co-doping resulted in a small growth in the ratio. The Ni⁺³ level, which is connected to Ni₂O₃, indicates that there is excess oxygen inside the NiO structure due to Ni vacancy [262]. That is to say, higher trivalent states, as opposed to divalent states, are analogous to the absence of one electron, which can significantly increase the number of hole carriers, causing hole transport easier. Then, according to previous reports [263–266], the moderately increased $\mathrm{Ni^{+3}/Ni^{+2}}$ ratio in Ce and Zn co-doped layers can supply an enhancement in conductivity of hole. However, Chen et al. suggested that nickel can be replaced and intercalated into the structure when nickel oxide is doped with the Cs. Since Cs has a larger atomic radius than Ni, incorporation into the lattice is assumed to be surrounded, resulting in a deformation of the lattice and a structure that is much more amorphous in comparison to pure layers. In addition, increases the trivalent acceptor ratio, as a result, the conductivity of hole improves. larger atomic radius of Ce (248 pm) may be linked to its improved conductivity in the same way [229].

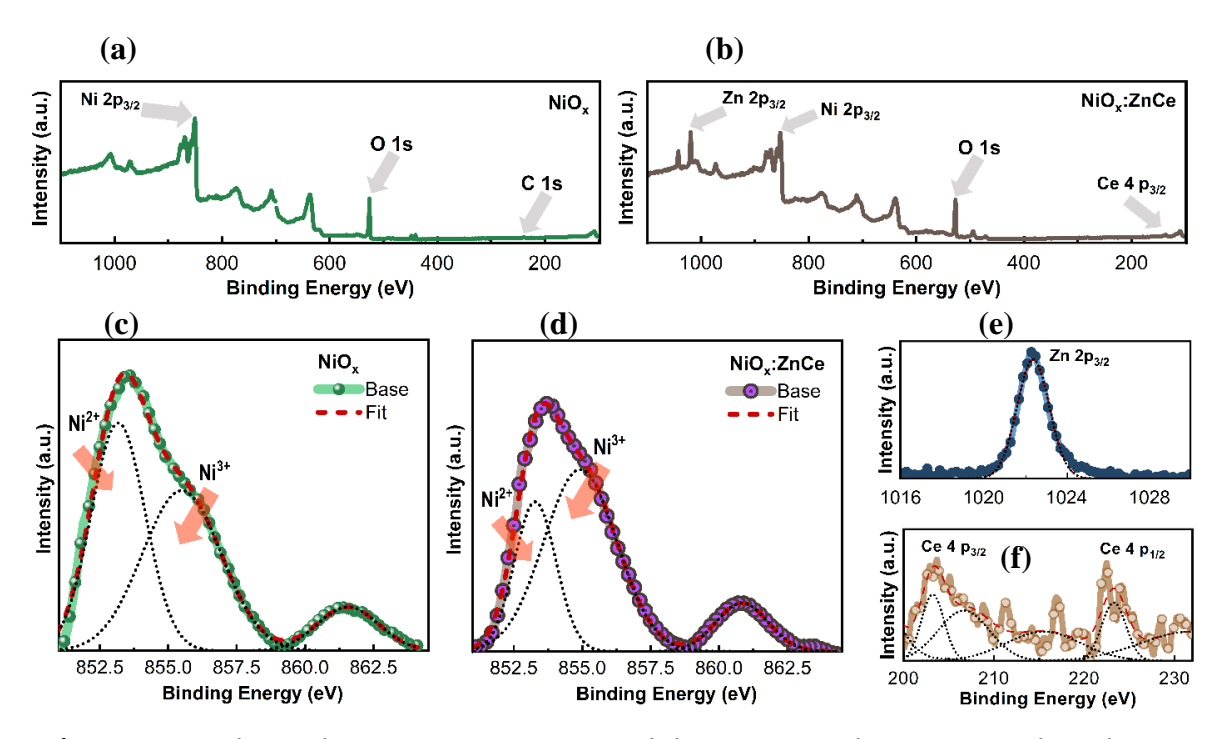


Figure 6.5 The wide survey XPS spectra of the (a) NiO_x (b) Zn-Ce co-doped NiO_x (c) deconvolution of Ni $2p_{3/2}$ for NiO_x and (d) Zn-Ce co-doped NiO_x (e) deconvolution of Zn $2p_{3/2}$ (f) deconvolution of Ce $4p_{3/2}$ and $4p_{1/2}$ for Zn-Ce co-doped layers [240]

SEM images with different resolutions of the perovskite films growing on undoped and co-doped NiO_X layers are shown in Figure 6.6(a)-(b) [240]. This should be noted that mirror-like perovskite formation occurs immediately following toluene washing and annealing. Both perovskite films have uniform, with pinhole-free surfaces, as can be seen in the low magnification illustration (left), implying a mirror-like surface.

The underlayer's surface chemistry, which is attributed to the doped materials, may indeed affect formation morphology [241,243], regardless of the fact that the precise reasoning behind perovskite development morphology is not fully understood. Nevertheless, SEM analysis shows that the surface morphology stayed consistent no matter what the HTLs used, which is consistent with previous reports [229,267,268]. Furthermore, the mean grain sizes of the perovskite films on pristine and co-doped

NiO_x films were about 306.3 nm and 339.5 nm, respectively, which were obtained employing image J program through a 3.45 \times 2.25 μ m² area.

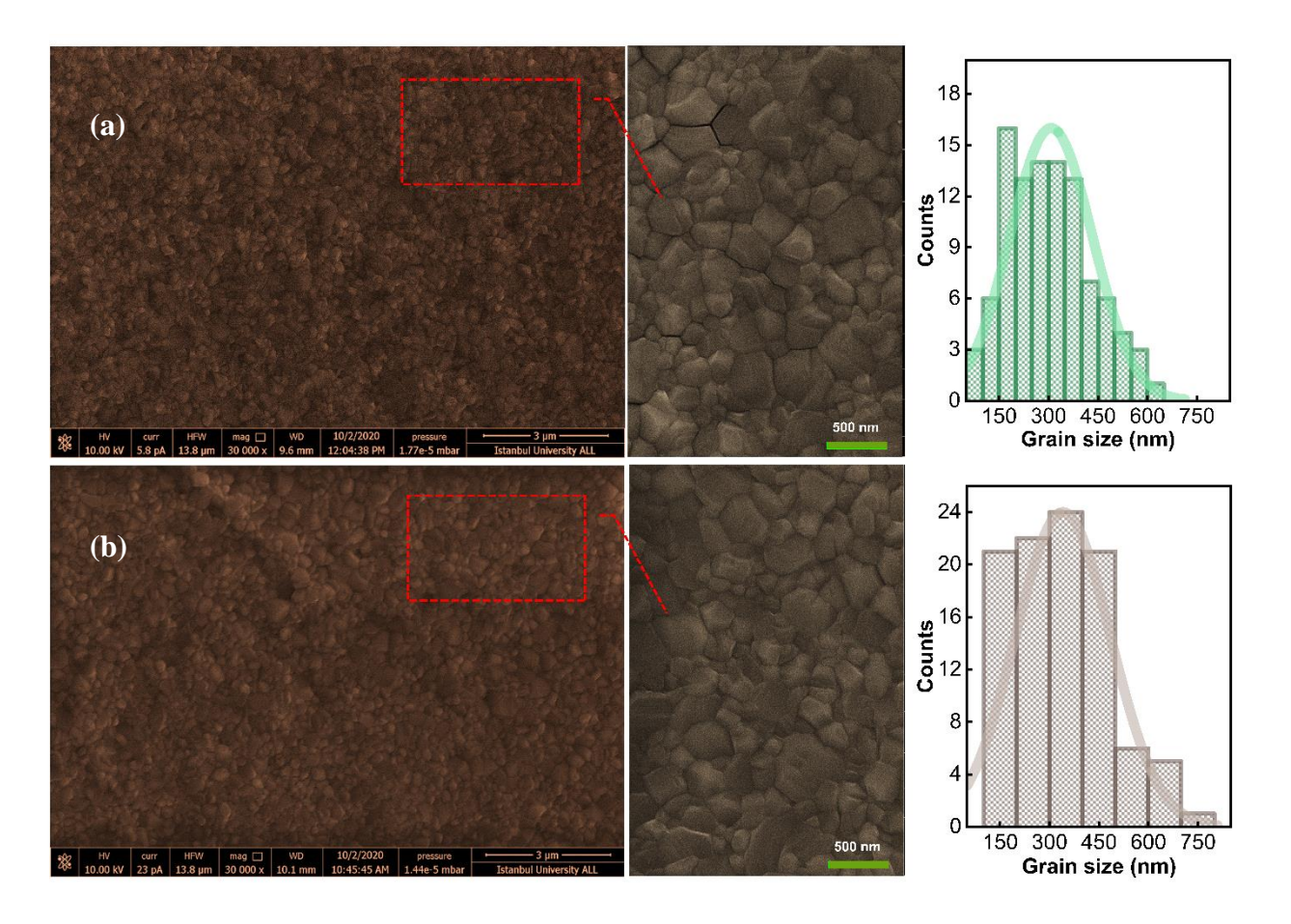


Figure 6.6 SEM surface images of the perovskite layers growth on (a) NiO_x and (b) Zn-Ce co-doped NiO_x HTLs under different magnifications and corresponded grain size distribution [240]

Figure 6.7 (b) [240] shows the J-V curves of devices with various HTLs under illumination, and Table 6.1 lists the photovoltaic parameter. Device employing pure NiO_X led to a J_{SC} of 20.7 mAcm⁻², V_{OC} of 970 mV, FF of 0.50 and PCE of 10.04%.

When compared to untreated cells with the identical quantity of optimal doping proportion, only cerium doped (6 mmol %) nickel oxide layer engaged devices showed an improvement in fill factor and V_{OC} values, however J_{SC} was marginally

reduced. The V_{OC} and FF values reduced while the J_{SC} increased for just Zn doped (18 mmol %) NiO_X used devices, which is related to the morphology characterized by AFM and electrical conductivity analyzes, respectively. As compared with the reference cells, the system that used co-doped (18:6 mmol) nickel oxide exhibited a significant enhancement. For NiO_X and co-doped NiO_X involved perovskite cells, the J_{SC} , FF, V_{OC} , and PCE quantities altered from 20.7 mA cm⁻² to 22.3 mA cm⁻², 0.50 to 0.63, 970 mV to 1030 mV, and 10.04 % to 14.47 %, respectively. Furthermore, for Zn-Ce co-doped and pure NiO_X, series resistance was examined to be 6.8 Ω cm⁻² and 10.6 Ω cm⁻², respectively. Enhanced conductivity in co-doped HTLs is assumed to be the reason for this. Furthermore, R_{shunt} was increased for the co-doped NiO_X that used perovskite devices, indicating current leakage is reduced and FF is increased.

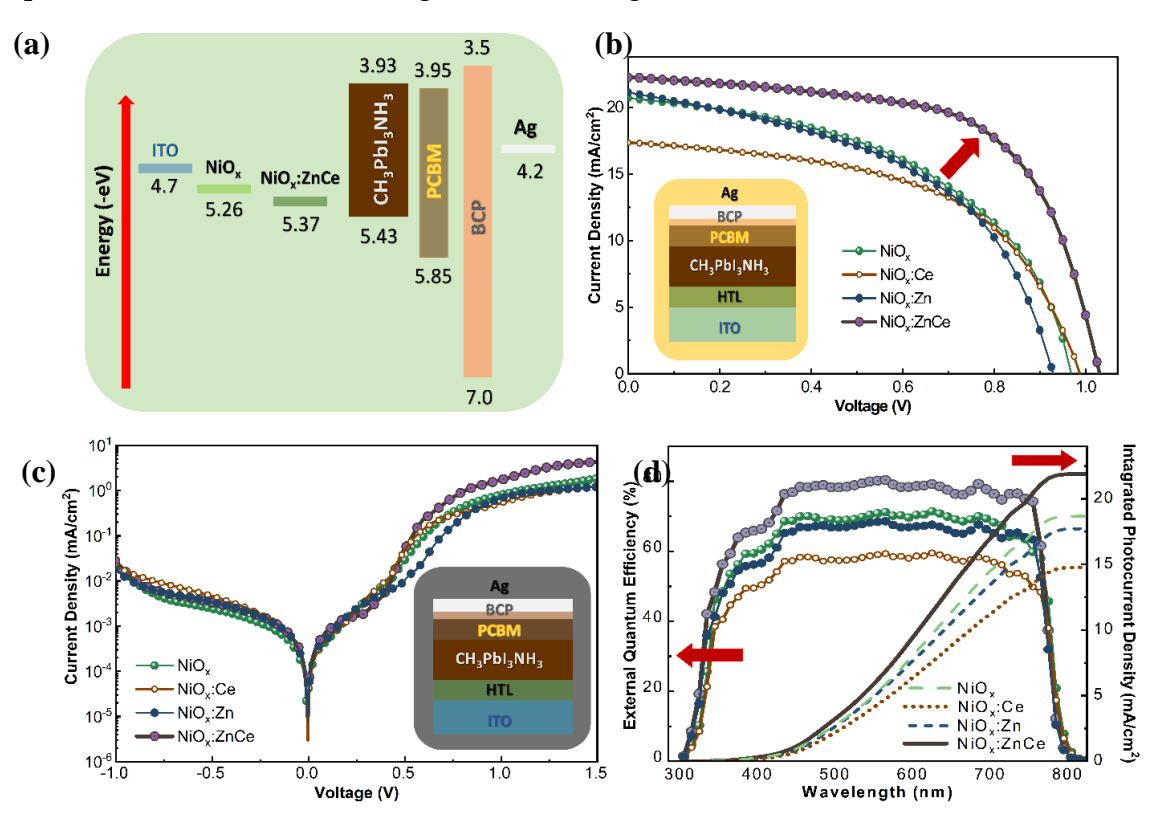


Figure 6.7 (a) Estimated energy level diagram of the devices (b) Illuminated J-V curves (c) Dark J-V curves (d) EQE spectra along with the corresponding integrated J_{SC} curves of the ITO/HTL/CH₃NH₃PbI₃/PCBM/BCP/Ag Solar Cells [240]

The dark J-V graphs of the perovskite devices with pure nickel oxide, Ce, Zn, and Zn-Ce co-doped NiO_X films are illustrated in Figure 6.7 (c) [240]. The rectifying ability of co-doped NiO_X films is improved. In addition, the decrease in leakage current could be attributed to less charge accumulation and recombination at the doped NiO_X /perovskite interface, leading to an improvement in device FF and J_{SC} [232,244,269,270].

Device's HTL	V_{OC} (mV)	J _{SC} (mA cm ⁻²)	1010	PCE (%)	R_{series} (Ω cm ⁻²)	R_{shunt} (k Ω cm ⁻²)
NiO _x	970	20.7	0.50	10.04	10.6	2.0
NiO _x :Ce (6)	990	17.4	0.55	9.47	10.9	2.7
NiO _x :Zn (18)	930	21.1	0.49	9.62	7.8	1.4
NiO _x :ZnCe (18:6)	1030	22.3	0.63	14.47	6.8	3.9

Table 6.1 Device Parameters of the PSCs Based on various NiO_x HTLs (doping: mmol %) [240]

To test the validity of the current density improvement by co-doped NiO_X films, EQE measurements were performed and the obtained IPCE spectra are shown in Figure 6.7 (d) [240]. Co-doped layer engaged devices have a larger external quantum efficiency, indicating a higher photon-to-current turning, as shown on the Figure 6.7 (d) [240]. This is assumed to be due to increased charge collection efficiency and improved perovskite development. For NiO_X, Ce, Zn, and co-doped NiO_X, integrated photocurrents of 18.7 mA cm⁻², 14.8 mA cm⁻², 17.7 mA cm⁻², and 21.9 mA cm⁻² were achieved, which were near to J_{SC} values [241,271].

The space charge limited current (SCLC) method was used to examine the trap density inside the perovskite using hole-only cells in an ITO/HTL/Perovskite/Ag arrangement. Figure 6.8 (a) [240] depicts the corresponding J-V plots, which indicate that the doped layer engaged devices have a higher current density than the undoped one appointed references at the exactly similar bias voltage, implying

greater hole conductivity. According to Mott-power Gurney's law, SCLC J-V plots show a linear relationship at low voltages, followed by a nonlinear increase at voltages above the V_{TFL} , where all trap states are occupied [270].

The perovskite trap density can be determined using the 4-3 equation. Where e, ε_o , ε_r , n_{trap} and D represent electrical charge, the perovskite dielectric constant [220], the vacuum permittivity, trap density and the thickness of perovskite film (430-450 nm). From Figure 6.8 (a), the V_{TFL} quantities for NiO_x, Ce, Zn, and co-doped nickel oxide utilized hole only cells were 585 mV, 454 mV, 492 mV, and 422 mV, respectively. Density of the trap for NiO_x, Ce, Zn, and co-doped NiO_x based cells were 1.02×10^{16} cm⁻³, 0.79×10^{16} cm⁻³, 0.86×10^{16} cm⁻³, and 0.74×10^{16} cm⁻³, respectively, which were consistent with the literature [264,270,272] and indicated that co-doping reduced the trap density [244,264,273]. The hole mobility of the pristine and modified NiO_x layers was also determined using the Mott-Gurney equation (4-4 equation), as shown in the inset in Figure 6.8 (a). where L, ε_{NiOx} , μ and ε_o are the thickness of the NiO_x, the dielectric constant of NiO_x [274], mobility and vacuum permittivity respectively.

For NiO_X, Ce, Zn, and co-doped NiO_X films, the hole mobilities were measured as 1.32×10^{-3} cm² V⁻¹s⁻¹, 4.92×10^{-3} cm² V⁻¹s⁻¹, 4.74×10^{-3} cm² V⁻¹s⁻¹, and 22.1×10^{-3} cm² V⁻¹s⁻¹, respectively, which are in a good agreement with the literature [244,275,276]. The hole mobility was substantially increased by Zn-Ce co-doping, as predicted and verified by XPS measurements.

By varying sample configuration and architecture, the Hall effect can be used to determine the charge mobility of semiconductors, which necessitates the use of an insulator substrate, resulting in a change in crystallinity, as well as an imperfect estimation of the factor of Hall scattering. The van der Pauw setup was used to analyze the Hall charge mobilities of the different hole transport layers at ambient air, as shown in Figure 6.8 (b) [240]. The measured charge mobilities for undoped, Ce, Zn, and co-doped NiO_x films were determined to be about 103.95 cm² V⁻¹s⁻¹, 181.20 cm² V⁻¹s⁻¹, 109.75 cm² V⁻¹s⁻¹, and 334.95 cm² V⁻¹s⁻¹, respectively [258,268,277].

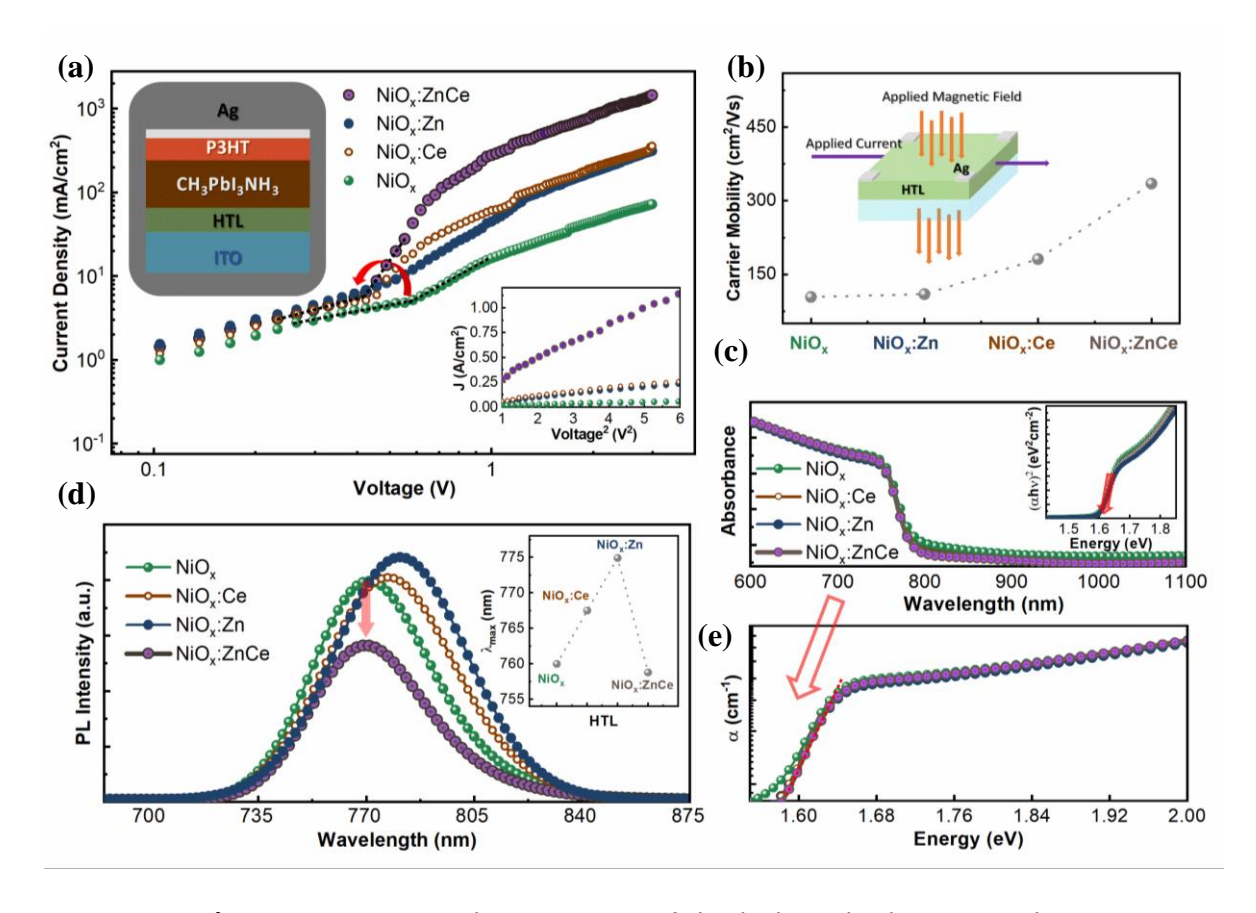


Figure 6.8 (a) Dark J-V curves of the hole-only devices with a ITO/HTL/CH₃NH₃PbI₃/P3HT/Ag configuration (b) Hall mobility measurements for various NiO_x HTLs (c) Photoluminescence spectra for the perovskite layers on various NiO_x HTLs (d) Absorbance spectra with Tauc plots (e) Urbach energy plots for various NiO_x HTLs [240]

Figure 6.8 (c) [240] shows PL spectra and peak maximum changes for perovskite films on different nickel oxide using an ITO/HTL/CH3NH3PbI3/PCBM structure. As compared to pure NiO_{X} , the co-doped NiO_{X} HTL configuration showed quenching action, suggesting facilitated hole extraction and carrier transfer at the interface between perovskite and hole transport layer. This finding demonstrated improved ptype conductivity and work function. However, the PL intensity of Zn doped HTL structures was significantly higher than that of pristine HTL structures, which could be clarified by the NiO_{X} :Zn layer's lowest p-type conductivity, lowest work function,

and coarsest morphology. When comparing the Ce doped HTL structures to the Zn doped ones, a more quenched behavior was found, suggesting improved p-type conductivity and reduced roughness. The λ_{max} of PL curves for undoped, Ce, Zn,and co-doped layers were 760 nm, 774 nm, 767 nm, and 758 nm, respectively, indicating a blue-shift for the co-doped layer engaged device, which could be connected to removed tail-states close band edges of CH₃NH₃PbI₃ [243].

The absorption spectra of perovskite films on different HTLs are displayed in Figure 6.8 (d) [240], and Tauc plots revealed a bandgap of 1.60 eV [278] irrespective of doping, as predicted for CH₃NH₃PbI₃. The slopes of Fig. 6.8 (e) [240] were used to calculate Urbach energies "E_U" by applying the following formula [279],

$$\log \alpha = \log \alpha_0 + (\frac{h\nu}{E_U}) \tag{6-1}$$

which were 113.9 meV, 93.9 meV, 98.3 meV, and 88.4 meV for NiO_x , Ce, Zn, and codoped NiO_x films, respectively. The measured energies were consistent with the SCLC study since the Urbach energies were linked to lattice distortion, defects, and trap states.

Finally, the stability and reproducibility were examined under high humidity conditions. Figure 6.9 [240] shows the change of PV parameters in a box chart for nickel oxide based utilized devices.

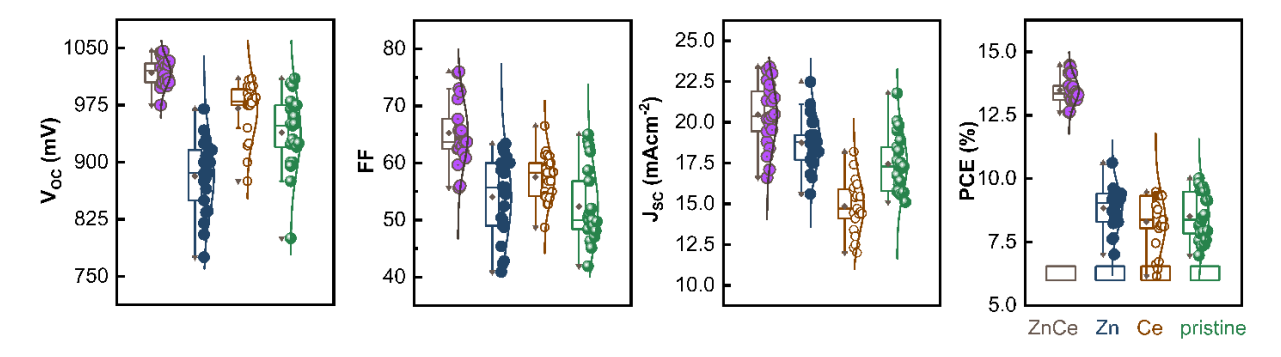


Figure 6.9 Box chart graphics of the photovoltaic parameters for various NiO_x HTL employed PSCs [240]

Mean $V_{\rm OC}$ values for pristine, Ce, Zn, and co-doped NiO_X engaged devices are 939 mV, 970 mV, 881 mV, and 1025 mV, respectively, although $J_{\rm SC}$ values for pristine, Ce, Zn, and co-doped NiO_X engaged devices are 17.4 mA cm⁻², 18.7 mA cm⁻², 14.9 mA cm⁻² for 21 best cells. Pristine, Ce, Zn, and co-doped NiO_X cells yielded FF average values of 52.5, 57.5, 54.1, and 65.2, respectively. Consequently, for pristine, Ce, Zn, and co-doped NiO_X devices, average PCE results ranged between 8.5, 8.3, and 13.5 %, respectively. In comparison to pure NiO_X devices, the PCE and $V_{\rm OC}$ values of co-doped NiO_X based devices show a significant progress. For the co-doped NiO_X based perovskite solar cells, $V_{\rm OC}$ and PCE have narrower ranges, resulting in greater reproducibility. Specifically, the increase in $V_{\rm OC}$ demonstrated the impact of doping, which results in improved energy level configuration. Furthermore, the box diagrams for co-doped NiO_X involved cells had a lower standard deviation, indicating greater reproducibility. In Figure 6.10 [240] the stability of the perovskite solar cells is shown. All of the devices were kept out of glove box, without encapsulation, at more than 60 % RH and 25.0 ° C.

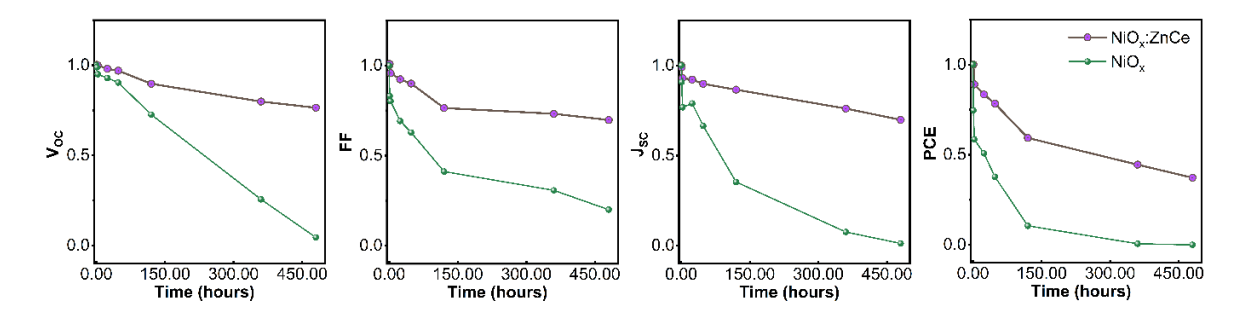


Figure 6.10 Short term device stability curves for NiO_x and Ce-Zn co-doped NiO_x employed PSCs stored under aging conditions with RH around 70 % and temperature; 23-25.0°C [240]

The efficiency values of NiO_x based perovskite devices dropped to 10% of their initial values in less than 120 hours, however co-doped NiO_x based PSCs maintained 60% of their initial PCEs over the similar time span. This increased short-term stability can

be attributed to the greater carrier extraction abilities of co-doped NiO_X films, and the improved interconnect between the hole transport layer and the perovskite film.

6.4 Conclusion

For the first time in the literature, this investigation showed a fast and easy sol-gel method for glove-box-free manufacturing of CH3NH3PbI3-based PSCs using Zn-Ce co-doped NiO $_{\rm X}$. The PV performance of the cells was improved when they were co-doped with Ce and Zn at a ratio of 6 and 18 mmol %, respectively, compared to undoped NiO $_{\rm X}$. The SCLC method, which indicates hole mobility and trap density inside the perovskite film, was performed to determine them. The hole mobilities of Zn-Ce co-doped NiO $_{\rm X}$ films were estimated to be 16.7 orders of magnitude stronger than those of pristine nickel oxide films, however trap densities of perovskite films formed on Zn-Ce co-doped NiO $_{\rm X}$ HTLs reduced by 27.4%. Zn-Ce co-doping improved the work function of NiO $_{\rm X}$ from 5.26 eV to 5.37 eV, which may be attributed to the substantially enhanced $V_{\rm OC}$ from 967 to 1030 mV. However, the increase in the FF from 0.50 to 0.63 is related to improved conductivity, hole extraction, and morphology of the interface between hole selective layer and perovskite film.

The PCE was successfully increased from 10.04 % to 14.47 % by using Zn-Ce codoping. According to our results, co-doped NiOx HTLs boost system stability, which may be due to improved carrier extraction abilities of HTLs, resulting in lower trap density in the perovskite film.

7.1 Conclusions

Organic-inorganic hybrid perovskites are a kind of semiconductor substances that has prompted a lot of interest in light-emitting diodes and PV systems. Within a decade of research, perovskite solar cells have experienced a tremendous increase in PCE from 3.9% to more than 25%, making them competitive with commercialized Sibased photovoltaic devices. This is due to its advantageous inherent features, which include a high absorption coefficient, high carrier mobility, long diffusion length, and tunable bandgap.

In Chapter 3 the impact of UV irradiation on ITO/PEDOT: PSS samples in p-i-n type of PSCs was studied. We demonstrated that UV radiation alters PEDOT: PSS morphology, which in turn alters the film forming features of perovskites on various PEDOT surfaces. Moreover, as a significant benefit, we revealed in our research that for observing the impact of UV light on the operation of the cells, a long UV radiation time is not required.

In Chapter 4 we prepared a zinc doped PEDOT: PSS as a hole transport layer for inverted PSCs, which resulted in a significant increase in efficiency and stability. The enhanced surface morphology of doped HTL revealed a surface that is less rough and more homogeneous than the original one, suggesting that the high fill factor value is due to synergetic effects.

In Chapter 5 we utilized the BCP as an interlayer between PCBM and Ag to enhance PV performance. As the BCP concentration was optimized, the series resistance of devices reduced, resulting in improved performance of device.

It was shown in chapter 6 that a fast and easy sol-gel method for manufacturing of CH3NH3PbI3-based PSCs out of glovebox using Zn-Ce co-doped NiO_x. The PV performance of cells was improved when they were co-doped with Ce and Zn at a ratio of 6 and 18 mmol %, respectively, compared to undoped NiO_x. According to our results, devices with co-doped NiO_x HTLs boost stability, which may be due to improved carrier extraction abilities of HTLs, resulting in lower trap density in the perovskite film. As a result, Zn-Ce co-doped NiOx HTL is supposed to be a promising hole extraction choice for p-i-n type perovskite solar cells that are both effective and stable.

7.2 Future work

It is found that using zinc acetate dihydrate as an additive in PEDOT:PSS solution resulted in a significant increase in efficiency and stability. Fabricating devices with comparable efficiencies will be advantageous using different salts to see if the same improvement in performance will be observed upon the same condition. This may give us some ideas on which salt can improve the performance of device better. The results will be valuable in the design of better and developed PSCs.

The effect of different buffer layers such as PEIE and LiF can also be studied. It will also be interesting to achieve more reduction in series resistance and further improvement by utilizing different interlayers.

we predict that efficiencies can be increased even more by utilizing FTO instead of ITO as substrates and implementing various perovskite precursors, especially other suitable perovskite choices within a glove box.

- [1] K. Branker, M.J.M. Pathak, J.M. Pearce, A review of solar photovoltaic levelized cost of electricity, Renew. Sustain. Energy Rev. 15 (2011) 4470–4482. https://doi.org/10.1016/j.rser.2011.07.104.
- [2] D.B. Mitzi, O. Gunawan, T.K. Todorov, K. Wang, S. Guha, The path towards a high-performance solution-processed kesterite solar cell, Sol. Energy Mater. Sol. Cells. 95 (2011) 1421–1436. https://doi.org/10.1016/j.solmat.2010.11.028.
- [3] I. Chung, B. Lee, J. He, R.P.H. Chang, M.G. Kanatzidis, All-solid-state dye-sensitized solar cells with high efficiency, Nature. 485 (2012) 486–489. https://doi.org/10.1038/nature11067.
- [4] C.J. Hibberd, E. Chassaing, W. Liu, D.B. Mitzi, D. Lincot, A.N. Tiwari, Non-vacuum methods for formation of Cu(In, Ga)(Se, S)2 thin film photovoltaic absorbers, Prog. Photovoltaics Res. Appl. 18 (2010) 434–452. https://doi.org/10.1002/pip.914.
- [5] Z.L. Wang, W. Wu, Nanotechnology-enabled energy harvesting for self-powered micro-/nanosystems, Angew. Chemie Int. Ed. 51 (2012) 11700–11721. https://doi.org/10.1002/anie.201201656.
- [6] M.L. Fraas, Low-cost solar electric power, Springer US, New York, 2014.
- [7] Saadi Lahlou, System Innovation for Sustainability 4: Case Studies in Sustainable Consumption and Production Energy Use and the Built Environment, (n.d.).
- [8] O. Ellabban, H. Abu-Rub, F. Blaabjerg, Renewable energy resources: Current status, future prospects and their enabling technology, Renew. Sustain. Energy Rev. 39 (2014) 748–764. https://doi.org/10.1016/j.rser.2014.07.113.

- [9] M. Gratzel, Photoelectrochemical cells, Nature. 414 (2001) 338.
- [10] M.I.A. Arafa, E.-S.S. A. Said, A different visions for uninterruptible load using hybrid solar-grid energy, Int. J. Power Electron. Drive Syst. 10 (2019) 381. https://doi.org/10.11591/ijpeds.v10.i1.pp381-387.
- [11] M.E. Becquerel, Mémoire sur les effets électriques produits sous l'influence des rayonssolaires", Comptes rendus hebdomadaires des séances de l'Académie des sciences, (1839) 561–567.
- [12] P. Gevorkian, Solar Power Generation Problems, Solutions, and Monitoring, Cambridge, n.d.
- [13] NREL. Efficiency Chart, (n.d.). http://www.nrel.gov/ncpv.
- [14] Y.S. Eo, H.W. Rhee, B.D. Chin, J.W. Yu, Influence of metal cathode for organic photovoltaic device performance, Synth. Met. 159 (2009) 1910–1913. https://doi.org/10.1016/j.synthmet.2009.05.036.
- [15] A. Le Donne, A. Scaccabarozzi, S. Tombolato, S. Marchionna, P. Garattini, B. Vodopivec, M. Acciarri, S. Binetti, State of the Art and Perspectives of Inorganic Photovoltaics, ISRN Renew. Energy. 2013 (2013) 1–8. https://doi.org/10.1155/2013/830731.
- [16] M. GREEN, K. EMERY, Y. HISHIKAWA, W. WARTA, E. DUNLOP, D. BARKHOUSE, O. GUNAWAN, T. GOKMEN, T. TODOROV, D. MITZI, Solar cell efficiency tables (version 40), Ieee Trans Fuzzy Syst. 20 (2012) 1114–1129. https://doi.org/10.1002/pip.
- [17] L. Meng, Y. Zhang, X. Wan, C. Li, X. Zhang, Y. Wang, X. Ke, Z. Xiao, L. Ding, R. Xia, H.L. Yip, Y. Cao, Y. Chen, Organic and solution-processed tandem solar cells with 17.3% efficiency, Science (80-.). 361 (2018) 1094–1098. https://doi.org/10.1126/science.aat2612.
- [18] M.E. De Graef, M. & McHenry, Structure of Materials: An Introduction to

- Crystallography, Diffraction and Symmetry, Cambridge University Press, 2012.
- [19] P. Gao, M. Grätzel, M.K. Nazeeruddin, Organohalide lead perovskites for photovoltaic applications, Energy Environ. Sci. 7 (2014) 2448–2463. https://doi.org/10.1039/c4ee00942h.
- [20] C.K. Møller, Crystal structure and photoconductivity of cæsium plumbohalides, Nature. 182 (1958) 1436. https://doi.org/10.1038/1821436a0.
- [21] D. Weber, CH 3 NH 3 PbX 3, einPb (II)-System mitkubischerPerowskitstruktur, Z Naturforsch C 33b. 1445 (1978) 1443–1445.
- [22] K. Chondroudis, D.B. Mitzi, Electroluminescence from an organic-inorganic perovskite incorporating a quaterthiophene dye within lead halide perovskite layers, Chem. Mater. 11 (1999) 3028–3030. https://doi.org/10.1021/cm990561t.
- [23] C.R. Kagan, D.B. Mitzi, C.D. Dimitrakopoulos, Organic-inorganic hybrid materials as semiconducting channels in thin- film field-effect transistors, Science (80-.). 286 (1999) 945–947. https://doi.org/10.1126/science.286.5441.945.
- [24] K. A, T. K, S. Y, M. T, Organometal halide perovskites as visible-light sensitizers for photovoltaic cells, J. Am. Chem. Soc. 131 (2009) 6050–1.
- [25] J.Y. Jeong, J., Kim, M., Seo, J., Lu, H., Ahlawat, P., Mishra, A., ... & Kim, Pseudo-halide anion engineering for α -FAPbI 3 perovskite solar cells, Nature. 592 (2021) 381–385.
- [26] RLE perovskite seminar series, in: MIT, n.d.
- [27] E.A. Katz, Perovskite: Name Puzzle and German-Russian Odyssey of Discovery, Helv. Chim. Acta. 103 (2020). https://doi.org/10.1002/hlca.202000061.
- [28] K. Liang, D.B. Mitzi, M.T. Prikas, <Cm970568F.Pdf>, Chem. Mater. 4756 (2013) 403–411.

- https://pubs.acs.org/sharingguidelines%0Ahttp://pubs.acs.org/doi/abs/10.1 021/cm970568f.
- [29] J.H. Burroughes, D.D.C. Bradley, A.R. Brown, R.N. Marks, K. Mackay, R.H. Friend, P.L. Burns, A.B. Holmes, Light-emitting diodes based on conjugated polymers, Nature. 347 (1990) 539–541. https://doi.org/10.1038/347539a0.
- [30] J.H. Im, C.R. Lee, J.W. Lee, S.W. Park, N.G. Park, 6.5% Efficient Perovskite Quantum-Dot-Sensitized Solar Cell, Nanoscale. 3 (2011) 4088–4093. https://doi.org/10.1039/c1nr10867k.
- [31] M.M. Lee, J. Teuscher, T. Miyasaka, T.N. Murakami, H.J. Snaith, Efficient hybrid solar cells based on meso-superstructured organometal halide perovskites, Science (80-.). 338 (2012) 643–647. https://doi.org/10.1126/science.1228604.
- [32] G.E. Eperon, V.M. Burlakov, P. Docampo, A. Goriely, H.J. Snaith, Morphological control for high performance, solution-processed planar heterojunction perovskite solar cells, Adv. Funct. Mater. 24 (2014) 151–157. https://doi.org/10.1002/adfm.201302090.
- [33] M. Saliba, K.W. Tan, H. Sai, D.T. Moore, T. Scott, W. Zhang, L.A. Estroff, U. Wiesner, H.J. Snaith, Influence of thermal processing protocol upon the crystallization and photovoltaic performance of organic-inorganic lead trihalide perovskites, J. Phys. Chem. C. 118 (2014) 17171–17177. https://doi.org/10.1021/jp500717w.
- [34] Z. Song, S.C. Watthage, A.B. Phillips, M.J. Heben, Pathways toward high-performance perovskite solar cells: review of recent advances in organo-metal halide perovskites for photovoltaic applications, J. Photonics Energy. 6 (2016) 022001. https://doi.org/10.1117/1.jpe.6.022001.
- [35] K.W. Tan, D.T. Moore, M. Saliba, H. Sai, L.A. Estroff, T. Hanrath, H.J. Snaith, U. Wiesner, Evolution and Performance of Solar Cells, ACS Nano. (2015) 4730–

4739.

- [36] H.S. Kim, C.R. Lee, J.H. Im, K.B. Lee, T. Moehl, A. Marchioro, S.J. Moon, R. Humphry-Baker, J.H. Yum, J.E. Moser, M. Grätzel, N.G. Park, Lead iodide perovskite sensitized all-solid-state submicron thin film mesoscopic solar cell with efficiency exceeding 9%, Sci. Rep. 2 (2012) 1–7. https://doi.org/10.1038/srep00591.
- [37] M. Liu, M.B. Johnston, H.J. Snaith, Efficient planar heterojunction perovskite solar cells by vapour deposition, Nature. 501 (2013) 395–398. https://doi.org/10.1038/nature12509.
- [38] H. Zhou, Q. Chen, G. Li, S. Luo, T.B. Song, H.S. Duan, Z. Hong, J. You, Y. Liu, Y. Yang, Interface engineering of highly efficient perovskite solar cells, Science (80-.). 345 (2014) 542–546. https://doi.org/10.1126/science.1254050.
- [39] N.J. Jeon, J.H. Noh, Y.C. Kim, W.S. Yang, S. Ryu, S. Il Seok, Solvent engineering for high-performance inorganic-organic hybrid perovskite solar cells, Nat. Mater. 13 (2014) 897–903. https://doi.org/10.1038/nmat4014.
- [40] N.J. Jeon, J.H. Noh, W.S. Yang, Y.C. Kim, S. Ryu, J. Seo, S. Il Seok, Compositional engineering of perovskite materials for high-performance solar cells, Nature. 517 (2015) 476–480. https://doi.org/10.1038/nature14133.
- [41] M.A. Green, A. Ho-Baillie, H.J. Snaith, The emergence of perovskite solar cells, Nat. Photonics. 8 (2014) 506–514. https://doi.org/10.1038/nphoton.2014.134.
- [42] C. Li, X. Lu, W. Ding, L. Feng, Y. Gao, Z. Guo, Formability of ABX 3 (X = F, Cl, Br, I) halide perovskites, Acta Crystallogr. Sect. B Struct. Sci. 64 (2008) 702–707. https://doi.org/10.1107/S0108768108032734.
- [43] N.G. Park, Perovskite solar cells: An emerging photovoltaic technology, Mater. Today. 18 (2015) 65–72. https://doi.org/10.1016/j.mattod.2014.07.007.

- [44] X. Ziang, L. Shifeng, Q. Laixiang, P. Shuping, W. Wei, Y. Yu, Y. Li, C. Zhijian, W. Shufeng, D. Honglin, Y. Minghui, G.G. Qin, Refractive index and extinction coefficient of CH_3NH_3PbI_3 studied by spectroscopic ellipsometry, Opt. Mater. Express. 5 (2015) 29. https://doi.org/10.1364/ome.5.000029.
- [45] PV Education, (n.d.). http://www.pveducation.org.
- [46] M. Samiee, S. Konduri, B. Ganapathy, R. Kottokkaran, H.A. Abbas, A. Kitahara, P. Joshi, L. Zhang, M. Noack, V. Dalal, Defect density and dielectric constant in perovskite solar cells, Appl. Phys. Lett. 105 (2014). https://doi.org/10.1063/1.4897329.
- [47] E.T. Hoke, D.J. Slotcavage, E.R. Dohner, A.R. Bowring, H.I. Karunadasa, M.D. McGehee, Reversible photo-induced trap formation in mixed-halide hybrid perovskites for photovoltaics, Chem. Sci. 6 (2015) 613–617. https://doi.org/10.1039/c4sc03141e.
- [48] C. Transport, Y. Zhao, A.M. Nardes, K. Zhu, Solid-State Mesostructured Perovskite CH 3 NH 3 PbI 3 Solar Cells: Charge Transport, Recombination, and Di ff usion Length, (2014) 3–7.
- [49] S.D. Stranks, G.E. Eperon, G. Grancini, C. Menelaou, M.J.P. Alcocer, T. Leijtens, L.M. Herz, A. Petrozza, H.J. Snaith, Electron-hole diffusion lengths exceeding 1 micrometer in an organometal trihalide perovskite absorber, Science (80-.). 342 (2013) 341–344. https://doi.org/10.1126/science.1243982.
- [50] C. La-O-Vorakiat, T. Salim, J. Kadro, M.T. Khuc, R. Haselsberger, L. Cheng, H. Xia, G.G. Gurzadyan, H. Su, Y.M. Lam, R.A. Marcus, M.E. Michel-Beyerle, E.E.M. Chia, Elucidating the role of disorder and free-carrier recombination kinetics in CH 3 NH 3 PbI 3 perovskite films, Nat. Commun. 6 (2015) 1–7. https://doi.org/10.1038/ncomms8903.
- [51] C.C. Stoumpos, C.D. Malliakas, M.G. Kanatzidis, Inorganic Chemistry Volume 52 issue 15 2013 [doi 10.1021%2Fic401215x] Stoumpos, Constantinos C.;

- Malliakas, Christos D.; Kanatzidis, M -- Semiconducting Tin and Lead Iodide Perovskites with Organic Ca.pdf, 2 (2013).
- [52] L. Zhang, Device physics of perovskite solar cells, Iowa State University, 2016.
- [53] N. Marinova, S. Valero, J.L. Delgado, Organic and perovskite solar cells: Working principles, materials and interfaces, J. Colloid Interface Sci. 488 (2017) 373–389. https://doi.org/10.1016/j.jcis.2016.11.021.
- [54] F. Hao, C.C. Stoumpos, D.H. Cao, R.P.H. Chang, M.G. Kanatzidis, Lead-free solid-state organic-inorganic halide perovskite solar cells, Nat. Photonics. 8 (2014) 489–494. https://doi.org/10.1038/nphoton.2014.82.
- [55] Q. Lin, A. Armin, R.C.R. Nagiri, P.L. Burn, P. Meredith, Electro-optics of perovskite solar cells, Nat. Photonics. 9 (2015) 106–112. https://doi.org/10.1038/nphoton.2014.284.
- [56] A. Miyata, A. Mitioglu, P. Plochocka, O. Portugall, J.T.W. Wang, S.D. Stranks, H.J. Snaith, R.J. Nicholas, Direct measurement of the exciton binding energy and effective masses for charge carriers in organic-inorganic tri-halide perovskites, Nat. Phys. 11 (2015) 582–587. https://doi.org/10.1038/nphys3357.
- [57] G. Xing, N. Mathews, S. Sun, S.S. Lim, Y.M. Lam, M. Gratzel, S. Mhaisalkar, T.C. Sum, Long-range balanced electron-and hole-transport lengths in organic-inorganic CH3NH3PbI3, Science (80-.). 342 (2013) 344–347. https://doi.org/10.1126/science.1243167.
- [58] Q. Dong, Y. Fang, Y. Shao, P. Mulligan, J. Qiu, L. Cao, J. Huang, Electron-hole diffusion lengths $> 175~\mu m$ in solution-grown CH3NH3PbI3 single crystals, Science (80-.). 347 (2015) 967–970. https://doi.org/10.1126/science.aaa5760.
- [59] N. Pellet, P. Gao, G. Gregori, T.Y. Yang, M.K. Nazeeruddin, J. Maier, M. Grätzel, Mixed-organic-cation perovskite photovoltaics for enhanced solar-light

- harvesting, Angew. Chemie Int. Ed. 53 (2014) 3151–3157. https://doi.org/10.1002/anie.201309361.
- [60] W.S. Yang, J.H. Noh, N.J. Jeon, Y.C. Kim, S. Ryu, J. Seo, S. Il Seok, High-performance photovoltaic perovskite layers fabricated through intramolecular exchange, Science (80-.). 348 (2015) 1234–1237. https://doi.org/10.1126/science.aaa9272.
- [61] Z.K. Tan, R.S. Moghaddam, M.L. Lai, P. Docampo, R. Higler, F. Deschler, M. Price, A. Sadhanala, L.M. Pazos, D. Credgington, F. Hanusch, T. Bein, H.J. Snaith, R.H. Friend, Bright light-emitting diodes based on organometal halide perovskite, Nat. Nanotechnol. 9 (2014) 687–692. https://doi.org/10.1038/nnano.2014.149.
- [62] G. Xing, N. Mathews, S.S. Lim, N. Yantara, X. Liu, D. Sabba, M. Grätzel, S. Mhaisalkar, T.C. Sum, Low-temperature solution-processed wavelength-tunable perovskites for lasing, Nat. Mater. 13 (2014) 476–480. https://doi.org/10.1038/nmat3911.
- [63] M. Saliba, S.M. Wood, J.B. Patel, P.K. Nayak, J. Huang, J.A. Alexander-Webber, B. Wenger, S.D. Stranks, M.T. Hörantner, J.T.W. Wang, R.J. Nicholas, L.M. Herz, M.B. Johnston, S.M. Morris, H.J. Snaith, M.K. Riede, Structured Organic-Inorganic Perovskite toward a Distributed Feedback Laser, Adv. Mater. 28 (2016) 923–929. https://doi.org/10.1002/adma.201502608.
- [64] N. Ahn, D.Y. Son, I.H. Jang, S.M. Kang, M. Choi, N.G. Park, Highly Reproducible Perovskite Solar Cells with Average Efficiency of 18.3% and Best Efficiency of 19.7% Fabricated via Lewis Base Adduct of Lead(II) Iodide, J. Am. Chem. Soc. 137 (2015) 8696–8699. https://doi.org/10.1021/jacs.5b04930.
- [65] D. Liu, T.L. Kelly, Perovskite solar cells with a planar heterojunction structure prepared using room-temperature solution processing techniques, Nat. Photonics. 8 (2014) 133–138. https://doi.org/10.1038/nphoton.2013.342.

- [66] K. Domanski, W. Tress, T. Moehl, M. Saliba, M.K. Nazeeruddin, M. Grätzel, Working Principles of Perovskite Photodetectors: Analyzing the Interplay between Photoconductivity and Voltage-Driven Energy-Level Alignment, Adv. Funct. Mater. 25 (2015) 6936–6947. https://doi.org/10.1002/adfm.201503188.
- [67] L. Wang, G.D. Yuan, R.F. Duan, F. Huang, T.B. Wei, Z.Q. Liu, J.X. Wang, J.M. Li, Tunable bandgap in hybrid perovskite CH3NH3Pb(Br3-yXy) single crystals and photodetector applications, AIP Adv. 6 (2016). https://doi.org/10.1063/1.4948312.
- [68] T.A. Berhe, W.N. Su, C.H. Chen, C.J. Pan, J.H. Cheng, H.M. Chen, M.C. Tsai, L.Y. Chen, A.A. Dubale, B.J. Hwang, Organometal halide perovskite solar cells: Degradation and stability, Energy Environ. Sci. 9 (2016) 323–356. https://doi.org/10.1039/c5ee02733k.
- [69] J.A. Christians, J.S. Manser, P. V. Kamat, Best practices in perovskite solar cell efficiency measurements. Avoiding the error of Making Bad Cells Look Good, J. Phys. Chem. Lett. 6 (2015) 852–857. https://doi.org/10.1021/acs.jpclett.5b00289.
- [70] B. Chen, M. Yang, S. Priya, K. Zhu, Origin of J-V Hysteresis in Perovskite Solar
 Cells, J. Phys. Chem. Lett. 7 (2016) 905–917.
 https://doi.org/10.1021/acs.jpclett.6b00215.
- [71] W. Tress, N. Marinova, T. Moehl, S.M. Zakeeruddin, M.K. Nazeeruddin, M. Grätzel, Understanding the rate-dependent J-V hysteresis, slow time component, and aging in CH3NH3PbI3 perovskite solar cells: The role of a compensated electric field, Energy Environ. Sci. 8 (2015) 995–1004. https://doi.org/10.1039/c4ee03664f.
- [72] R.S. Sanchez, V. Gonzalez-Pedro, J.W. Lee, N.G. Park, Y.S. Kang, I. Mora-Sero, J. Bisquert, Slow dynamic processes in lead halide perovskite solar cells.

- Characteristic times and hysteresis, J. Phys. Chem. Lett. 5 (2014) 2357–2363. https://doi.org/10.1021/jz5011187.
- [73] B. Chen, M. Yang, X. Zheng, C. Wu, W. Li, Y. Yan, J. Bisquert, G. Garcia-Belmonte, K. Zhu, S. Priya, Impact of Capacitive Effect and Ion Migration on the Hysteretic Behavior of Perovskite Solar Cells, J. Phys. Chem. Lett. 6 (2015) 4693–4700. https://doi.org/10.1021/acs.jpclett.5b02229.
- [74] E.L. Unger, E.T. Hoke, C.D. Bailie, W.H. Nguyen, A.R. Bowring, T. Heumüller, M.G. Christoforo, M.D. McGehee, Hysteresis and transient behavior in current-voltage measurements of hybrid-perovskite absorber solar cells, Energy Environ. Sci. 7 (2014) 3690–3698. https://doi.org/10.1039/c4ee02465f.
- [75] H.S. Kim, N.G. Park, Parameters affecting I-V hysteresis of CH3NH3PbI3 perovskite solar cells: Effects of perovskite crystal size and mesoporous TiO2 layer, J. Phys. Chem. Lett. 5 (2014) 2927–2934. https://doi.org/10.1021/jz501392m.
- [76] J. Wei, Y. Zhao, H. Li, G. Li, J. Pan, D. Xu, Q. Zhao, D. Yu, Hysteresis analysis based on the ferroelectric effect in hybrid perovskite solar cells, J. Phys. Chem. Lett. 5 (2014) 3937–3945. https://doi.org/10.1021/jz502111u.
- [77] H.J. Snaith, A. Abate, J.M. Ball, G.E. Eperon, T. Leijtens, N.K. Noel, S.D. Stranks, J.T.W. Wang, K. Wojciechowski, W. Zhang, Anomalous hysteresis in perovskite solar cells, J. Phys. Chem. Lett. 5 (2014) 1511–1515. https://doi.org/10.1021/jz500113x.
- [78] Y. Shao, Z. Xiao, C. Bi, Y. Yuan, J. Huang, Origin and elimination of photocurrent hysteresis by fullerene passivation in CH3NH3PbI3 planar heterojunction solar cells, Nat. Commun. 5 (2014) 1–7. https://doi.org/10.1038/ncomms6784.
- [79] J. Xu, A. Buin, A.H. Ip, W. Li, O. Voznyy, R. Comin, M. Yuan, S. Jeon, Z. Ning, J.J. McDowell, P. Kanjanaboos, J.P. Sun, X. Lan, L.N. Quan, D.H. Kim, I.G. Hill,

- P. Maksymovych, E.H. Sargent, Perovskite-fullerene hybrid materials suppress hysteresis in planar diodes, Nat. Commun. 6 (2015) 1–8. https://doi.org/10.1038/ncomms8081.
- [80] S. Van Reenen, M. Kemerink, H.J. Snaith, Modeling Anomalous Hysteresis in Perovskite Solar Cells, J. Phys. Chem. Lett. 6 (2015) 3808–3814. https://doi.org/10.1021/acs.jpclett.5b01645.
- [81] A. Al Mamun, Y. Mohammed, T.T. Ava, G. Namkoong, A.A. Elmustafa, Influence of air degradation on morphology, crystal size and mechanical hardness of perovskite film, Mater. Lett. 229 (2018) 167–170. https://doi.org/10.1016/j.matlet.2018.06.126.
- [82] T.T. Ava, A. Al Mamun, S. Marsillac, G. Namkoong, A review: Thermal stability of methylammonium lead halide based perovskite solar cells, Appl. Sci. 9 (2019). https://doi.org/10.3390/app9010188.
- [83] Z. Messegee, A. Al Mamun, T.T. Ava, G. Namkoong, T.M. Abdel-Fattah, Characterization of perovskite (CH3NH3PbI3) degradation with the integration of different polymers for increased stability, Mater. Lett. 236 (2019) 159–162. https://doi.org/10.1016/j.matlet.2018.10.064.
- [84] Scientists discover why next-gen solar cells break down in days", Imp. Coll. London. (2015). https://www.imperial.ac.uk/news/165809/scientists-discover-next-gen-solar-cells-break/.
- [85] G. Niu, X. Guo, L. Wang, Review of recent progress in chemical stability of perovskite solar cells, J. Mater. Chem. A. 3 (2015) 8970–8980. https://doi.org/10.1039/c4ta04994b.
- [86] K. Miyano, M. Yanagida, N. Tripathi, Y. Shirai, Hysteresis, Stability, and Ion Migration in Lead Halide Perovskite Photovoltaics, J. Phys. Chem. Lett. 7 (2016) 2240–2245. https://doi.org/10.1021/acs.jpclett.6b00579.
- [87] F. Sani, S. Shafie, H.N. Lim, A.O. Musa, Advancement on lead-free organic-

- inorganic halide perovskite solar cells: A review, Materials (Basel). 11 (2018) 1–17. https://doi.org/10.3390/ma11061008.
- [88] E. Edri, S. Kirmayer, A. Henning, S. Mukhopadhyay, K. Gartsman, Y. Rosenwaks, G. Hodes, D. Cahen, Why lead methylammonium tri-iodide perovskite-based solar cells require a mesoporous electron transporting scaffold (but not necessarily a hole conductor), Nano Lett. 14 (2014) 1000–1004. https://doi.org/10.1021/nl404454h.
- [89] Q. Chen, N. De Marco, Y. Yang, T. Bin Song, C.C. Chen, H. Zhao, Z. Hong, H. Zhou, Y. Yang, Under the spotlight: The organic-inorganic hybrid halide perovskite for optoelectronic applications, Nano Today. 10 (2015) 355–396. https://doi.org/10.1016/j.nantod.2015.04.009.
- [90] K.C. Wang, J.Y. Jeng, P.S. Shen, Y.C. Chang, E.W.G. Diau, C.H. Tsai, T.Y. Chao, H.C. Hsu, P.Y. Lin, P. Chen, T.F. Guo, T.C. Wen, P-type mesoscopic nickel oxide/organometallic perovskite heterojunction solar cells, Sci. Rep. 4 (2014) 1–8. https://doi.org/10.1038/srep04756.
- [91] J. Burschka, N. Pellet, S.J. Moon, R. Humphry-Baker, P. Gao, M.K. Nazeeruddin, M. Grätzel, Sequential deposition as a route to high-performance perovskite-sensitized solar cells, Nature. 499 (2013) 316–319. https://doi.org/10.1038/nature12340.
- [92] T. Leijtens, B. Lauber, G.E. Eperon, S.D. Stranks, H.J. Snaith, The importance of perovskite pore filling in organometal mixed halide sensitized TiO2-based solar cells, J. Phys. Chem. Lett. 5 (2014) 1096–1102. https://doi.org/10.1021/jz500209g.
- [93] S.S. Shin, E.J. Yeom, W.S. Yang, S. Hur, M.G. Kim, J. Im, J. Seo, J.H. Noh, S. Il Seok, **胶体制**备的La掺杂BaSnO 3电极·用于高效·光稳定的钙钛矿太阳能电池, Science (80-.). 356 (2017) 167–171.

- http://www.sciencemag.org/lookup/doi/10.1126/science.aam6620.
- [94] W. Chen, Y. Wu, Y. Yue, J. Liu, W. Zhang, X. Yang, H. Chen, E. Bi, I. Ashraful, M. Grätzel, L. Han, Efficient and stable large-area perovskite solar cells with inorganic charge extraction layers, Science (80-.). 350 (2015) 944–948. https://doi.org/10.1126/science.aad1015.
- [95] J. You, L. Meng, T. Bin Song, T.F. Guo, W.H. Chang, Z. Hong, H. Chen, H. Zhou, Q. Chen, Y. Liu, N. De Marco, Y. Yang, Improved air stability of perovskite solar cells via solution-processed metal oxide transport layers, Nat. Nanotechnol. 11 (2016) 75–81. https://doi.org/10.1038/nnano.2015.230.
- [96] Q. Chen, H. Zhou, Z. Hong, S. Luo, Q. Chen, H. Zhou, Z. Hong, S. Luo, H. Duan, H. Wang, <Planar heterojunction perovskite solar.pdf>, (2013).
- [97] Y. Deng, E. Peng, Y. Shao, Z. Xiao, Q. Dong, J. Huang, Scalable fabrication of efficient organolead trihalide perovskite solar cells with doctor-bladed active layers, Energy Environ. Sci. 8 (2015) 1544–1550. https://doi.org/10.1039/c4ee03907f.
- [98] A.T. Barrows, A.J. Pearson, C.K. Kwak, A.D.F. Dunbar, A.R. Buckley, D.G. Lidzey, Efficient planar heterojunction mixed-halide perovskite solar cells deposited via spray-deposition, Energy Environ. Sci. 7 (2014) 2944–2950. https://doi.org/10.1039/c4ee01546k.
- [99] Z. Song, S.C. Watthage, B.L. Tompkins, G.K. Liyanage, A.B. Phillips, R.J. Ellingson, M.J. Heben, Spatially resolved characterization of solution processed perovskite solar cells using the LBIC technique, 2015 IEEE 42nd Photovolt. Spec. Conf. PVSC 2015. (2015) 0–4. https://doi.org/10.1109/PVSC.2015.7355676.
- [100] C.G. Wu, C.H. Chiang, Z.L. Tseng, M.K. Nazeeruddin, A. Hagfeldt, M. Grätzel, High efficiency stable inverted perovskite solar cells without current hysteresis, Energy Environ. Sci. 8 (2015) 2725–2733.

- https://doi.org/10.1039/c5ee00645g.
- [101] Y. Wu, A. Islam, X. Yang, C. Qin, J. Liu, K. Zhang, W. Peng, L. Han, Retarding the crystallization of PbI2 for highly reproducible planar-structured perovskite solar cells via sequential deposition, Energy Environ. Sci. 7 (2014) 2934–2938. https://doi.org/10.1039/c4ee01624f.
- [102] F. Hao, C.C. Stoumpos, Z. Liu, R.P.H. Chang, M.G. Kanatzidis, Hole Conductor-Free Solar Cells with Steady Power Conversion, J. Am. Chem. Soc. 136 (2014) 16411–16419.
- [103] D.B. Mitzi, M.T. Prikas, K. Chondroudis, Thin film deposition of organic-inorganic hybrid materials using a single source thermal ablation technique, Chem. Mater. 11 (1999) 542–544. https://doi.org/10.1021/cm9811139.
- [104] O. Malinkiewicz, A. Yella, Y.H. Lee, G.M. Espallargas, M. Graetzel, M.K. Nazeeruddin, H.J. Bolink, Perovskite solar cells employing organic charge-transport layers, Nat. Photonics. 8 (2014) 128–132. https://doi.org/10.1038/nphoton.2013.341.
- [105] P. Qin, M. Paulose, M.I. Dar, T. Moehl, N. Arora, P. Gao, O.K. Varghese, M. Grätzel, M.K. Nazeeruddin, Stable and Efficient Perovskite Solar Cells Based on Titania Nanotube Arrays, Small. 11 (2015) 5533–5539. https://doi.org/10.1002/smll.201501460.
- [106] M. Salado, M. Oliva-Ramirez, S. Kazim, A.R. González-Elipe, S. Ahmad, 1-dimensional TiO2 nano-forests as photoanodes for efficient and stable perovskite solar cells fabrication, Nano Energy. 35 (2017) 215–222. https://doi.org/10.1016/j.nanoen.2017.03.034.
- [107] D. Bryant, N. Aristidou, S. Pont, I. Sanchez-Molina, T. Chotchunangatchaval, S. Wheeler, J.R. Durrant, S.A. Haque, Light and oxygen induced degradation limits the operational stability of methylammonium lead triiodide perovskite solar cells, Energy Environ. Sci. 9 (2016) 1655–1660.

- https://doi.org/10.1039/c6ee00409a.
- [108] F. Fu, T. Feurer, T. Jäger, E. Avancini, B. Bissig, S. Yoon, S. Buecheler, A.N. Tiwari, Low-temperature-processed efficient semi-transparent planar perovskite solar cells for bifacial and tandem applications, Nat. Commun. 6 (2015) 1–9. https://doi.org/10.1038/ncomms9932.
- [109] Q. Bao, X. Liu, S. Braun, M. Fahlman, Oxygen- and water-based degradation in [6,6]-phenyl-C61-butyric acid methyl ester (PCBM) films, Adv. Energy Mater. 4 (2014). https://doi.org/10.1002/aenm.201301272.
- [110] D. Zhang, B. Bin Cui, C. Zhou, L. Li, Y. Chen, N. Zhou, Z. Xu, Y. Li, H. Zhou, Q. Chen, Reduction of intrinsic defects in hybrid perovskite films: Via precursor purification, Chem. Commun. 53 (2017) 10548–10551. https://doi.org/10.1039/c7cc05590k.
- [111] K. Mahmood, S. Sarwar, M.T. Mehran, Current status of electron transport layers in perovskite solar cells: materials and properties, RSC Adv. 7 (2017) 17044–17062. https://doi.org/10.1039/c7ra00002b.
- [112] G. Yang, H. Tao, P. Qin, W. Ke, G. Fang, Recent progress in electron transport layers for efficient perovskite solar cells, J. Mater. Chem. A. 4 (2016) 3970–3990. https://doi.org/10.1039/c5ta09011c.
- [113] X. Yang, H. Wang, B. Cai, Z. Yu, L. Sun, Progress in hole-transporting materials for perovskite solar cells, J. Energy Chem. 27 (2018) 650–672. https://doi.org/10.1016/j.jechem.2017.12.017.
- [114] Z.H. Bakr, Q. Wali, A. Fakharuddin, L. Schmidt-Mende, T.M. Brown, R. Jose, Advances in hole transport materials engineering for stable and efficient perovskite solar cells, Nano Energy. 34 (2017) 271–305. https://doi.org/10.1016/j.nanoen.2017.02.025.
- [115] W.S. Yang, B.W. Park, E.H. Jung, N.J. Jeon, Y.C. Kim, D.U. Lee, S.S. Shin, J. Seo, E.K. Kim, J.H. Noh, S. Il Seok, Iodide management in formamidinium-

- lead-halide-based perovskite layers for efficient solar cells, Science (80-.). 356 (2017) 1376–1379. https://doi.org/10.1126/science.aan2301.
- [116] S.N. Habisreutinger, T. Leijtens, G.E. Eperon, S.D. Stranks, R.J. Nicholas, H.J. Snaith, Carbon nanotube/polymer composites as a highly stable hole collection layer in perovskite solar cells, Nano Lett. 14 (2014) 5561–5568. https://doi.org/10.1021/nl501982b.
- [117] N. Arora, M.I. Dar, A. Hinderhofer, N. Pellet, F. Schreiber, S.M. Zakeeruddin, M. Grätzel, Perovskite solar cells with CuSCN hole extraction layers yield stabilized efficiencies greater than 20%, Science (80-.). 358 (2017) 768–771. https://doi.org/10.1126/science.aam5655.
- [118] Adopted from PVeducation website., (n.d.). https://www.pveducation.org/pvcdrom/characterisation/double-diodemodel.
- [119] Adopted from, (n.d.). http://www.pveducation.org/pvcdrom/solar-cell-operation/fill-factor.
- [120] L. Zhang, Phd Thesis, Iowa State University, 2017.
- [121] Adoped from, (n.d.). https://ecee.colorado.edu/~bart/book/book/chapter4/ch4_4.htm.
- [122] B.G.S. and S.K. Banerjee, Solid state electronic devices, 6 ed, Pearson Education, New Jersey, 2006.
- [123] M. Samiee, Phd Thesis, Iowa State University, 2015.
- [124] Adoped from, (n.d.). http://www.pveducation.org/pvcdrom/solar-cell-operation/quantumefficiency.
- [125] A.L.F. and R.H. Bube, Fundamentals of solar cells, Academic Press, New York, 1983.
- [126] M.A. Green, A. Ho-Baillie, Perovskite Solar Cells: The Birth of a New Era in

- Photovoltaics, ACS Energy Lett. 2 (2017) 822–830. https://doi.org/10.1021/acsenergylett.7b00137.
- [127] G. Yang, C. Wang, H. Lei, X. Zheng, P. Qin, L. Xiong, X. Zhao, Y. Yan, G. Fang, Interface engineering in planar perovskite solar cells: Energy level alignment, perovskite morphology control and high performance achievement, J. Mater. Chem. A. 5 (2017) 1658–1666. https://doi.org/10.1039/c6ta08783c.
- [128] W. Zhang, X. Zhang, T. Wu, W. Sun, J. Wu, Z. Lan, Interface engineering with NiO nanocrystals for highly efficient and stable planar perovskite solar cells, Electrochim. Acta. 293 (2019) 211–219. https://doi.org/10.1016/j.electacta.2018.10.032.
- [129] Z. Yuan, Y. Yang, Z. Wu, S. Bai, W. Xu, T. Song, X. Gao, F. Gao, B. Sun, Approximately 800-nm-Thick Pinhole-Free Perovskite Films via Facile Solvent Retarding Process for Efficient Planar Solar Cells, ACS Appl. Mater. Interfaces. 8 (2016) 34446–34454. https://doi.org/10.1021/acsami.6b12637.
- [130] B. El Cohen, L. Etgar, Parameters that control and influence the organo-metal halide perovskite crystallization and morphology, Front. Optoelectron. 9 (2016) 44–52. https://doi.org/10.1007/s12200-016-0630-3.
- [131] Y. Guo, H. Lei, L. Xiong, B. Li, G. Fang, An integrated organic-inorganic hole transport layer for efficient and stable perovskite solar cells, J. Mater. Chem. A. 6 (2018) 2157–2165. https://doi.org/10.1039/c7ta09946k.
- [132] Y. Zhang, G. Grancini, Y. Feng, A.M. Asiri, M.K. Nazeeruddin, Optimization of Stable Quasi-Cubic FAxMA1-xPbI3 Perovskite Structure for Solar Cells with Efficiency beyond 20%, ACS Energy Lett. 2 (2017) 802–806. https://doi.org/10.1021/acsenergylett.7b00112.
- [133] O.P. Dimitriev, D.A. Grinko, Y. V. Noskov, N.A. Ogurtsov, A.A. Pud, PEDOT:PSS films-Effect of organic solvent additives and annealing on the film conductivity, Synth. Met. 159 (2009) 2237–2239.

- https://doi.org/10.1016/j.synthmet.2009.08.022.
- [134] C. Song, Z. Zhong, Z. Hu, Y. Luo, L. Wang, J. Wang, Y. Cao, The effect of solvent treatment on the buried PEDOT:PSS layer, Org. Electron. 43 (2017) 9–14. https://doi.org/10.1016/j.orgel.2016.12.057.
- [135] Z. Hu, J. Zhang, Y. Zhu, Effects of solvent-treated PEDOT: PSS on organic photovoltaic devices, Renew. Energy. 62 (2014) 100–105. https://doi.org/10.1016/j.renene.2013.06.042.
- [136] L.J. J. Zhou, D.H. Anjum, L. Chen, X. Xu, I.A. Ventura, G. Lubineau, Temperature-dependent microstructure of PEDOT/PSS films: insights from morphological, mechanical and electrical analyses, J. Mater. Chem. C 2 (2014).
- [137] G. Adam, M. Kaltenbrunner, E.D. Głowacki, D.H. Apaydin, M.S. White, H. Heilbrunner, S. Tombe, P. Stadler, B. Ernecker, C.W. Klampfl, N.S. Sariciftci, M.C. Scharber, Solution processed perovskite solar cells using highly conductive PEDOT:PSS interfacial layer, Sol. Energy Mater. Sol. Cells. 157 (2016) 318–325. https://doi.org/10.1016/j.solmat.2016.05.011.
- [138] H.M. Alishah, M. Kazici, F. Ongül, S. Bozar, M. Cantürk Rodop, C. Kahveci, M.B. Arvas, Y. Sahin, M. Gencten, M. Kaleli, S. Akyürekli, H.U. Yilmaz, A.B. Bayram, S. Günes, Effect of UV exposure of ITO/PEDOT:PSS substrates on the performance of inverted-type perovskite solar cells, J. Mater. Sci. Mater. Electron. 31 (2020) 7968–7980. https://doi.org/10.1007/s10854-020-03336-4.
- [139] R.R.L. De Oliveira, D.A.C. Albuquerque, T.G.S. Cruz, AFM_badic, (n.d.). www.intechopen.com.
- [140] Y.C.K. K. Lim, J. Kang, S. Jung, S. Lee, J. Park, D.G. Kim, Bull, No Title, Korean Chem. Soc. 39 (2018).
- [141] H. Kim, J. Hong, C. Kim, E.Y. Shin, M. Lee, Y.Y. Noh, B. Park, I. Hwang, Impact of Hydroxyl Groups Boosting Heterogeneous Nucleation on Perovskite Grains

- and Photovoltaic Performances, J. Phys. Chem. C. 122 (2018) 16630–16638. https://doi.org/10.1021/acs.jpcc.8b05374.
- [142] M. Ameri, E. Mohajerani, M. Ghafarkani, N. Safari, S.A. Alavi, The investigation of the unseen interrelationship of grain size, ionic defects, device physics and performance of perovskite solar cells, J. Phys. D. Appl. Phys. 52 (2019). https://doi.org/10.1088/1361-6463/aafea9.
- [143] H. Choi, C.K. Mai, H.B. Kim, J. Jeong, S. Song, G.C. Bazan, J.Y. Kim, A.J. Heeger, Conjugated polyelectrolyte hole transport layer for inverted-type perovskite solar cells, Nat. Commun. 6 (2015) 1–6. https://doi.org/10.1038/ncomms8348.
- [144] Microscopical investigations of PEDOT: PSS thin films, Adv. Funct. Mater. 19 (2009) 1215–1220. https://doi.org/10.1002/adfm.200801258.
- [145] Y.J. Lin, F.M. Yang, C.Y. Huang, W.Y. Chou, J. Chang, Y.C. Lien, Increasing the work function of poly(3,4-ethylenedioxythiophene) doped with poly(4-styrenesulfonate) by ultraviolet irradiation, Appl. Phys. Lett. 91 (2007). https://doi.org/10.1063/1.2777147.
- [146] C. Tengstedt, A. Kanciurzewska, M.P. de Jong, S. Braun, W.R. Salaneck, M. Fahlman, Ultraviolet light-ozone treatment of poly(3,4-ethylenedioxy-thiophene)-based materials resulting in increased work functions, Thin Solid Films. 515 (2006) 2085–2090. https://doi.org/10.1016/j.tsf.2006.07.005.
- [147] H.K. Lee, J.K. Kim, O.O. Park, Effects of UV light-irradiated buffer layer on the performance of polymer solar cells, Org. Electron. 10 (2009) 1641–1644. https://doi.org/10.1016/j.orgel.2009.09.010.
- [148] V. Singh, S. Arora, M. Arora, V. Sharma, R.P. Tandon, Characterization of doped PEDOT: PSS and its influence on the performance and degradation of organic solar cells, Semicond. Sci. Technol. 29 (2014). https://doi.org/10.1088/0268-1242/29/4/045020.

- [149] L.M. Campos, A.J. Mozer, S. Günes, C. Winder, H. Neugebauer, N.S. Sariciftci, B.C. Thompson, B.D. Reeves, C.R.G. Grenier, J.R. Reynolds, Photovoltaic activity of a PolyProDOT derivative in a bulk heterojunction solar cell, Sol. Energy Mater. Sol. Cells. 90 (2006) 3531–3546. https://doi.org/10.1016/j.solmat.2006.06.051.
- [150] J.F. Li, C. Zhao, H. Zhang, J.F. Tong, P. Zhang, C.Y. Yang, Y.J. Xia, D.W. Fan, Improving the performance of perovskite solar cells with glycerol-doped PEDOT:PSS buffer layer, Chinese Phys. B. 25 (2015). https://doi.org/10.1088/1674-1056/25/2/028402.
- [151] A.P. Wanninayake, S. Li, B.C. Church, N. Abu-Zahra, Electrical and optical properties of hybrid polymer solar cells incorporating Au and CuO nanoparticles, AIMS Mater. Sci. 3 (2016) 35–50. https://doi.org/10.3934/matersci.2016.1.35.
- [152] T. Park, C. Park, B. Kim, H. Shin, E. Kim, Flexible PEDOT electrodes with large thermoelectric power factors to generate electricity by the touch of fingertips, Energy Environ. Sci. 6 (2013) 788–792. https://doi.org/10.1039/c3ee23729j.
- [153] Y.J. Lin, Y.M. Chin, C.Y. Wu, D.S. Liu, Electron-phonon coupling modification and carrier mobility enhancement in poly(3,4-ethylenedioxythiophene) doped with poly(4-styrenesulfonate) films by ultraviolet irradiation, J. Appl. Phys. 116 (2014). https://doi.org/10.1063/1.4894836.
- [154] M. Gençten, K.B. Dönmez, Y. Şahin, K. Pekmez, E. Suvacı, Voltammetric and electrochemical impedimetric behavior of silica-based gel electrolyte for valve-regulated lead-acid battery, J. Solid State Electrochem. 18 (2014) 2469–2479. https://doi.org/10.1007/s10008-014-2507-y.
- [155] S.K. Swami, N. Chaturvedi, A. Kumar, N. Chander, V. Dutta, D.K. Kumar, A. Ivaturi, S. Senthilarasu, H.M. Upadhyaya, Spray deposited copper zinc tin sulphide (Cu2ZnSnS4) film as a counter electrode in dye sensitized solar cells,

- Phys. Chem. Chem. Phys. 16 (2014) 23993–23999. https://doi.org/10.1039/c4cp03312d.
- [156] H. Gürsu, M. Gençten, Y. Şahin, One-step electrochemical preparation of graphene-coated pencil graphite electrodes by cyclic voltammetry and their application in vanadium redox batteries, Electrochim. Acta. 243 (2017) 239–249. https://doi.org/10.1016/j.electacta.2017.05.065.
- [157] J. C. Kim, B. Lee, H.J. Yang, H.M. Lee, J.G. Lee, H. Shin, No Title, Korean Phys. Soc. 47 (2005).
- [158] F.P. Gokdemir Choi, H. Moeini Alishah, S. Bozar, C. Doyranli, S. Koyuncu, N. San, C. Kahveci, M. Cantürk Rodop, M.B. Arvas, M. Gencten, Y. Sahin, S. Gunes, A novel interface layer for inverted perovskite solar cells fabricated in ambient air under high humidity conditions, Sol. Energy. 209 (2020) 400–407. https://doi.org/10.1016/j.solener.2020.08.013.
- [159] K. Dericiler, H.M. Alishah, S. Bozar, S. Güneş, F. Kaya, A novel method for graphene synthesis via electrochemical process and its utilization in organic photovoltaic devices, Appl. Phys. A Mater. Sci. Process. 126 (2020). https://doi.org/10.1007/s00339-020-04091-3.
- [160] J.Y. Jeng, Y.F. Chiang, M.H. Lee, S.R. Peng, T.F. Guo, P. Chen, T.C. Wen, CH3NH3PbI3 perovskite/fullerene planar-heterojunction hybrid solar cells, Adv. Mater. 25 (2013) 3727–3732. https://doi.org/10.1002/adma.201301327.
- [161] P. Docampo, J.M. Ball, M. Darwich, G.E. Eperon, H.J. Snaith, Efficient organometal trihalide perovskite planar-heterojunction solar cells on flexible polymer substrates, Nat. Commun. 4 (2013). https://doi.org/10.1038/ncomms3761.
- [162] C. Roldán-Carmona, O. Malinkiewicz, A. Soriano, G. Mínguez Espallargas, A. Garcia, P. Reinecke, T. Kroyer, M.I. Dar, M.K. Nazeeruddin, H.J. Bolink,

- Flexible high efficiency perovskite solar cells, Energy Environ. Sci. 7 (2014) 994–997. https://doi.org/10.1039/c3ee43619e.
- [163] S.I. Na, S.S. Kim, J. Jo, D.Y. Kim, Efficient and flexible ITO-free organic solar cells using highly conductive polymer anodes, Adv. Mater. 20 (2008) 4061–4067. https://doi.org/10.1002/adma.200800338.
- [164] A.M. Nardes, R.A.J. Janssen, M. Kemerink, A morphological model for the solvent-enhanced conductivity of PEDOT:PSS thin films, Adv. Funct. Mater. 18 (2008) 865–871. https://doi.org/10.1002/adfm.200700796.
- [165] D. Huang, T. Goh, J. Kong, Y. Zheng, S. Zhao, Z. Xu, A.D. Taylor, Perovskite solar cells with a DMSO-treated PEDOT:PSS hole transport layer exhibit higher photovoltaic performance and enhanced durability, Nanoscale. 9 (2017) 4236–4243. https://doi.org/10.1039/c6nr08375g.
- [166] X. Huang, K. Wang, C. Yi, T. Meng, X. Gong, Efficient Perovskite Hybrid Solar Cells by Highly Electrical Conductive PEDOT:PSS Hole Transport Layer, Adv. Energy Mater. 6 (2016). https://doi.org/10.1002/aenm.201501773.
- [167] J. Chang, Y. Kuga, I. Mora-Seró, T. Toyoda, Y. Ogomi, S. Hayase, J. Bisquert, Q. Shen, High reduction of interfacial charge recombination in colloidal quantum dot solar cells by metal oxide surface passivation, Nanoscale. 7 (2015) 5446–5456. https://doi.org/10.1039/c4nr07521h.
- [168] M. Qian, M. Li, X.B. Shi, H. Ma, Z.K. Wang, L.S. Liao, Planar perovskite solar cells with 15.75% power conversion efficiency by cathode and anode interfacial modification, J. Mater. Chem. A. 3 (2015) 13533–13539. https://doi.org/10.1039/c5ta02265g.
- [169] L. Hu, K. Sun, M. Wang, W. Chen, B. Yang, J. Fu, Z. Xiong, X. Li, X. Tang, Z. Zang, S. Zhang, L. Sun, M. Li, Inverted Planar Perovskite Solar Cells with a High Fill Factor and Negligible Hysteresis by the Dual Effect of NaCl-Doped PEDOT:PSS, ACS Appl. Mater. Interfaces. 9 (2017) 43902–43909.

- https://doi.org/10.1021/acsami.7b14592.
- [170] H.M. Alishah, F.P.G. Choi, F. Kuruoglu, A. Erol, S. Gunes, Improvement of fill factor by the utilization of Zn-doped PEDOT:PSS hole-transport layers for p-in planar type of perovskite solar cells, Electrochim. Acta. 388 (2021) 138658. https://doi.org/10.1016/j.electacta.2021.138658.
- [171] Z. Zhao, Q. Wu, F. Xia, X. Chen, Y. Liu, W. Zhang, J. Zhu, S. Dai, S. Yang, Improving the conductivity of PEDOT:PSS Hole transport layer in polymer solar cells via copper(II) bromide salt doping, ACS Appl. Mater. Interfaces. 7 (2015) 1439–1448. https://doi.org/10.1021/am505387q.
- [172] H. Yan, H. Okuzaki, Effect of solvent on PEDOT/PSS nanometer-scaled thin films: XPS and STEM/AFM studies, Synth. Met. 159 (2009) 2225–2228. https://doi.org/10.1016/j.synthmet.2009.07.032.
- [173] A. Yaseen, D. Maestre, E.S. Marstein, S.Z. Karazhanov, A. Cremades, Journal of Nanosciences: Current Research Characterization of Pedot: Pss Functionalized by Dimethyl Sulfoxide and Triton X-100 and Tio 2 Nanoparticles Characterization Methods, 5 (2020) 3–7. https://doi.org/10.4172/jncr.2020.05.133.
- [174] X. Zhang, B. Zhang, X. Ouyang, L. Chen, H. Wu, Polymer Solar Cells Employing Water-Soluble Polypyrrole Nanoparticles as Dopants of PEDOT:PSS with Enhanced Efficiency and Stability, J. Phys. Chem. C. 121 (2017) 18378–18384. https://doi.org/10.1021/acs.jpcc.7b05767.
- [175] Y. Xia, J. Ouyang, Salt-induced charge screening and significant conductivity enhancement of conducting poly(3,4-ethylenedioxythiophene): Poly(styrenesulfonate), Macromolecules. 42 (2009) 4141–4147. https://doi.org/10.1021/ma900327d.
- [176] J. Chen, J.A. Heitmann, M.A. Hubbe, Dependency of polyelectrolyte complex stoichiometry on the order of addition. 1. Effect of salt concentration during

- streaming current titrations with strong poly-acid and poly-base, Colloids Surfaces A Physicochem. Eng. Asp. 223 (2003) 215–230. https://doi.org/10.1016/S0927-7757(03)00222-X.
- [177] P. Fan, D. Zheng, Y. Zheng, J. Yu, Efficient and stable planar p-i-n perovskite solar cells by doping tungsten compound into PEDOT:PSS to facilitate perovskite crystalline, Electrochim. Acta. 283 (2018) 922–930. https://doi.org/10.1016/j.electacta.2018.07.029.
- [178] H. He, J. Ouyang, Enhancements in the Mechanical Stretchability and Thermoelectric Properties of PEDOT:PSS for Flexible Electronics Applications, Accounts Mater. Res. 1 (2020) 146–157. https://doi.org/10.1021/accountsmr.0c00021.
- [179] L. Ouyang, C. Musumeci, M.J. Jafari, T. Ederth, O. Inganäs, Imaging the Phase Separation between PEDOT and Polyelectrolytes during Processing of Highly Conductive PEDOT:PSS Films, ACS Appl. Mater. Interfaces. 7 (2015) 19764–19773. https://doi.org/10.1021/acsami.5b05439.
- [180] Y. Wu, Z. Wang, M. Liang, H. Cheng, M. Li, L. Liu, B. Wang, J. Wu, R. Prasad Ghimire, X. Wang, Z. Sun, S. Xue, Q. Qiao, Influence of Nonfused Cores on the Photovoltaic Performance of Linear Triphenylamine-Based Hole-Transporting Materials for Perovskite Solar Cells, ACS Appl. Mater. Interfaces. 10 (2018) 17883–17895. https://doi.org/10.1021/acsami.8b02090.
- [181] D. Liu, Y. Li, J. Yuan, Q. Hong, G. Shi, D. Yuan, J. Wei, C. Huang, J. Tang, M.K. Fung, Improved performance of inverted planar perovskite solar cells with F4-TCNQ doped PEDOT:PSS hole transport layers, J. Mater. Chem. A. 5 (2017) 5701–5708. https://doi.org/10.1039/C6TA10212C.
- [182] P. Kumar, Z. Yi, S. Zhang, A. Sekar, F. Soavi, F. Cicoira, Effect of channel thickness, electrolyte ions, and dissolved oxygen on the performance of organic electrochemical transistors, Appl. Phys. Lett. 107 (2015).

- https://doi.org/10.1063/1.4927595.
- [183] S.R.S. Prabaharan, R. Vimala, Z. Zainal, Nanostructured mesoporous carbon as electrodes for supercapacitors, J. Power Sources. 161 (2006) 730–736. https://doi.org/10.1016/j.jpowsour.2006.03.074.
- [184] D. Antiohos, G. Folkes, P. Sherrell, S. Ashraf, G.G. Wallace, P. Aitchison, A.T. Harris, J. Chen, A.I. Minett, Compositional effects of PEDOT-PSS/single walled carbon nanotube films on supercapacitor device performance, J. Mater. Chem. 21 (2011) 15987–15994. https://doi.org/10.1039/c1jm12986d.
- [185] I.U.S. Shohibuddin, W.W.A. Wan Salim, Tailoring the Electrochemical and Morphological Properties of Electropolymerized and Dropcast rGO:PSS-PEDOT:PSS Transducers for Ion-Selective Sensors, (2020) 7058. https://doi.org/10.3390/iecb2020-07058.
- [186] Y. Wu, Y. Yang, C. Li, Y. Li, W. Chen, Flexible and Electroactive Textile Actuator Enabled by PEDOT:PSS/MOF-Derivative Electrode Ink, Front. Bioeng. Biotechnol. 8 (2020) 1–12. https://doi.org/10.3389/fbioe.2020.00212.
- [187] D. Levasseur, I. Mjejri, T. Rolland, A. Rougier, Color tuning by oxide addition in PEDOT:PSS-based electrochromic devices, Polymers (Basel). 11 (2019). https://doi.org/10.3390/polym11010179.
- [188] H.S. Kim, I. Mora-Sero, V. Gonzalez-Pedro, F. Fabregat-Santiago, E.J. Juarez-Perez, N.G. Park, J. Bisquert, Mechanism of carrier accumulation in perovskite thin-absorber solar cells, Nat. Commun. 4 (2013). https://doi.org/10.1038/ncomms3242.
- [189] L. Cojocaru, S. Uchida, P.V.V. Jayaweera, H. Kaneko, J. Nakazaki, T. Kubo, H. Segawa, Origin of the hysteresis in I-V curves for planar structure perovskite solar cells rationalized with a surface boundary-induced capacitance model, Chem. Lett. 44 (2015) 1750–1752. https://doi.org/10.1246/cl.150933.
- [190] J.H. Heo, M.S. You, M.H. Chang, W. Yin, T.K. Ahn, S.J. Lee, S.J. Sung, D.H.

- Kim, S.H. Im, Hysteresis-less mesoscopic CH3NH3PbI3 perovskite hybrid solar cells by introduction of Li-treated TiO2 electrode, Nano Energy. 15 (2015) 530–539. https://doi.org/10.1016/j.nanoen.2015.05.014.
- [191] P.H. Huang, Y.H. Wang, J.C. Ke, C.J. Huang, The effect of solvents on the performance of CH3NH3PbI3 perovskite solar cells, Energies. 10 (2017). https://doi.org/10.3390/en10050599.
- [192] S.A. Rutledge, A.S. Helmy, Carrier mobility enhancement in poly(3,4-ethylenedioxythiophene)- poly(styrenesulfonate) having undergone rapid thermal annealing, J. Appl. Phys. 114 (2013). https://doi.org/10.1063/1.4824104.
- [193] R. Singh, P.K. Singh, B. Bhattacharya, H.W. Rhee, Review of current progress in inorganic hole-transport materials for perovskite solar cells, Appl. Mater. Today. 14 (2019) 175–200. https://doi.org/10.1016/j.apmt.2018.12.011.
- [194] S. Sajid, A.M. Elseman, H. Huang, J. Ji, S. Dou, H. Jiang, X. Liu, D. Wei, P. Cui, M. Li, Breakthroughs in NiOx-HTMs towards stable, low-cost and efficient perovskite solar cells, Nano Energy. 51 (2018) 408–424. https://doi.org/10.1016/j.nanoen.2018.06.082.
- [195] N.N. Som, P.M.W.P. Sampath, S.D. Dabhi, V. Mankad, S. Shinde, M.L.C. Attygalle, P.K. Jha, Strain and layer modulated electronic and optical properties of low dimensional perovskite methylammonium lead iodide: Implications to solar cells, Sol. Energy. (2018) 1315–1322. https://doi.org/10.1016/j.solener.2018.06.052.
- [196] N. Shibayama, H. Kanda, T.W. Kim, H. Segawa, S. Ito, Design of BCP buffer layer for inverted perovskite solar cells using ideal factor, APL Mater. 7 (2019). https://doi.org/10.1063/1.5087796.
- [197] C. Chen, S. Zhang, S. Wu, W. Zhang, H. Zhu, Z. Xiong, Y. Zhang, W. Chen, Effect of BCP buffer layer on eliminating charge accumulation for high

- performance of inverted perovskite solar cells, RSC Adv. 7 (2017) 35819–35826. https://doi.org/10.1039/c7ra06365b.
- [198] B.R. Patil, M. Ahmadpour, G. Sherafatipour, T. Qamar, A.F. Fernández, K. Zojer, H.G. Rubahn, M. Madsen, Area dependent behavior of bathocuproine (BCP) as cathode interfacial layers in organic photovoltaic cells, Sci. Rep. 8 (2018) 1–9. https://doi.org/10.1038/s41598-018-30826-7.
- [199] J. Seo, S. Park, Y. Chan Kim, N.J. Jeon, J.H. Noh, S.C. Yoon, S. Il Seok, Benefits of very thin PCBM and LiF layers for solution-processed p-i-n perovskite solar cells, Energy Environ. Sci. 7 (2014) 2642–2646. https://doi.org/10.1039/c4ee01216j.
- [200] X. Liu, H. Yu, L. Yan, Q. Dong, Q. Wan, Y. Zhou, B. Song, Y. Li, Triple cathode buffer layers composed of PCBM, C60, and LiF for high-performance planar perovskite solar cells, ACS Appl. Mater. Interfaces. 7 (2015) 6230–6237. https://doi.org/10.1021/acsami.5b00468.
- [201] F. Guo, H. Azimi, Y. Hou, T. Przybilla, M. Hu, C. Bronnbauer, S. Langner, E. Spiecker, K. Forberich, C.J. Brabec, High-performance semitransparent perovskite solar cells with solution-processed silver nanowires as top electrodes, Nanoscale. 7 (2015) 1642–1649. https://doi.org/10.1039/c4nr06033d.
- [202] C. He, F. Zhang, X. Zhao, C. Lin, M. Ye, Interface engineering of BCP buffer layers in planar heterojunction perovskite solar cells with NiOx hole transporting layers, Front. Phys. 6 (2018). https://doi.org/10.3389/fphy.2018.00099.
- [203] Q. Wang, Y. Shao, Q. Dong, Z. Xiao, Y. Yuan, J. Huang, Large fill-factor bilayer iodine perovskite solar cells fabricated by a low-temperature solution-process, Energy Environ. Sci. 7 (2014) 2359–2365. https://doi.org/10.1039/c4ee00233d.

- [204] C. Hanmandlu, C.Y. Chen, K.M. Boopathi, H.W. Lin, C.S. Lai, C.W. Chu, Bifacial Perovskite Solar Cells Featuring Semitransparent Electrodes, ACS Appl. Mater. Interfaces. 9 (2017) 32635–32642. https://doi.org/10.1021/acsami.7b06607.
- [205] A. Babaei, C. Dreessen, M. Sessolo, H.J. Bolink, High voltage vacuum-processed perovskite solar cells with organic semiconducting interlayers, RSC Adv. 10 (2020) 6640–6646. https://doi.org/10.1039/d0ra00214c.
- [206] D.X. Yuan, X.D. Yuan, Q.Y. Xu, M.F. Xu, X.B. Shi, Z.K. Wang, L.S. Liao, A solution-processed bathocuproine cathode interfacial layer for high-performance bromine-iodine perovskite solar cells, Phys. Chem. Chem. Phys. 17 (2015) 26653–26658. https://doi.org/10.1039/c5cp03995a.
- [207] D. Di Girolamo, F. Matteocci, E. Lamanna, E. Calabrò, A. Di Carlo, D. Dini, Inverted perovskite solar cells with transparent hole transporting layer based on semiconducting nickel oxide, AIP Conf. Proc. 1990 (2018). https://doi.org/10.1063/1.5047765.
- [208] H.M. Alishah, F.P.G. Choi, U.D. Menda, C. Kahveci, M.C. Rodop, M.J. Mendes, S. Gunes, Effect of Bathocuproine Concentration on the Photovoltaic Performance of NiOx-Based Perovskite Solar Cells, J. Mex. Chem. Soc. 65 (2021) 149–160. https://doi.org/10.29356/jmcs.v65i2.1461.
- [209] X. Guo, C. McCleese, C. Kolodziej, A.C.S. Samia, Y. Zhao, C. Burda, Identification and characterization of the intermediate phase in hybrid organic-inorganic MAPbI3 perovskite, Dalt. Trans. 45 (2016) 3806–3813. https://doi.org/10.1039/c5dt04420k.
- [210] A.M.A. Leguy, P. Azarhoosh, M.I. Alonso, M. Campoy-Quiles, O.J. Weber, J. Yao, D. Bryant, M.T. Weller, J. Nelson, A. Walsh, M. Van Schilfgaarde, P.R.F. Barnes, Experimental and theoretical optical properties of methylammonium lead halide perovskites, Nanoscale. 8 (2016) 6317–6327. https://doi.org/10.1039/c5nr05435d.

- [211] A. Kojima, K. Teshima, Y. Shirai, T. Miyasaka, Organometal halide perovskites as visible-light sensitizers for photovoltaic cells, J. Am. Chem. Soc. 131 (2009) 6050–6051. https://doi.org/10.1021/ja809598r.
- [212] J.B. Patel, R.L. Milot, A.D. Wright, L.M. Herz, M.B. Johnston, Formation Dynamics of CH3NH3PbI3 Perovskite Following Two-Step Layer Deposition, J. Phys. Chem. Lett. 7 (2016) 96–102. https://doi.org/10.1021/acs.jpclett.5b02495.
- [213] M.A. Pérez-Osorio, R.L. Milot, M.R. Filip, J.B. Patel, L.M. Herz, M.B. Johnston, F. Giustino, Vibrational Properties of the Organic-Inorganic Halide Perovskite CH3NH3PbI3 from Theory and Experiment: Factor Group Analysis, First-Principles Calculations, and Low-Temperature Infrared Spectra, J. Phys. Chem. C. 119 (2015) 25703–25718. https://doi.org/10.1021/acs.jpcc.5b07432.
- [214] H. Hu, K.K. Wong, T. Kollek, F. Hanusch, S. Polarz, P. Docampo, L. Schmidt-Mende, Highly efficient reproducible perovskite solar cells prepared by low-temperature processing, Molecules. 21 (2016) 1–10. https://doi.org/10.3390/molecules21040542.
- [215] K. Yan, Z. Wei, J. Li, H. Chen, Y. Yi, X. Zheng, X. Long, Z. Wang, J. Wang, J. Xu, S. Yang, High-performance graphene-based hole conductor-free perovskite solar cells: Schottky junction enhanced hole extraction and electron blocking, Small. 11 (2015) 2269–2274. https://doi.org/10.1002/smll.201403348.
- [216] P. Yimsiri, M.R. MacKley, Spin and dip coating of light-emitting polymer solutions: Matching experiment with modelling, Chem. Eng. Sci. 61 (2006) 3496–3505. https://doi.org/10.1016/j.ces.2005.12.018.
- [217] A. Calleja, S. Ricart, M. Aklalouch, N. Mestres, T. Puig, X. Obradors, Thickness-concentration-viscosity relationships in spin-coated metalorganic ceria films containing polyvinylpyrrolidone, J. Sol-Gel Sci. Technol. 72 (2014) 21–29. https://doi.org/10.1007/s10971-014-3417-2.

- [218] J. Dong, X. Xu, J.J. Shi, D.M. Li, Y.H. Luo, Q.B. Meng, Q. Chen, Suppressing Charge Recombination in ZnO-Nanorod-Based Perovskite Solar Cells with Atomic-Layer-Deposition TiO2, Chinese Phys. Lett. 32 (2015). https://doi.org/10.1088/0256-307X/32/7/078401.
- [219] X. Wu, H. Li, K. Wang, X. Sun, L. Wang, CH3NH3Pb1-: XEuxI3 mixed halide perovskite for hybrid solar cells: The impact of divalent europium doping on efficiency and stability, RSC Adv. 8 (2018) 11095–11101. https://doi.org/10.1039/c7ra12754e.
- [220] W. Zhu, L. Kang, T. Yu, B. Lv, Y. Wang, X. Chen, X. Wang, Y. Zhou, Z. Zou, Facile Face-Down Annealing Triggered Remarkable Texture Development in CH3NH3PbI3 Films for High-Performance Perovskite Solar Cells, ACS Appl. Mater. Interfaces. 9 (2017) 6104–6113. https://doi.org/10.1021/acsami.6b15563.
- [221] P. Ch, N.H. Pbi, C. Applications, Y. Yamada, T. Nakamura, M. Endo, A. Wakamiya, Y. Kanemitsu, Photocarrier Recombination Dynamics in Photocarrier Recombination Dynamics in Perovskite CH 3 NH 3 PbI 3 for Solar Cell Applications, J Am Chem Soc. 136 (2014) 11610–11613.
- [222] H. Moeini Alishah, F.P. Gokdemir Choi, U.D. Menda, C. Kahveci, M. Canturk Rodop, M. J. Mendes, S. Gunes, Effect of Bathocuproine Concentration on the Photovoltaic Performance of NiOx-Based Perovskite Solar Cells, J. Mex. Chem. Soc. 65 (2021). https://doi.org/10.29356/jmcs.v65i2.1461.
- [223] W.L. Jang, Y.M. Lu, W.S. Hwang, T.L. Hsiung, H.P. Wang, Point defects in sputtered NiO films, Appl. Phys. Lett. 94 (2009). https://doi.org/10.1063/1.3081025.
- [224] C.M. Osburn, R.W. Vest, Defect structure and electrical properties of Nio-II. Temperatures below equilibration, J. Phys. Chem. Solids. 32 (1971) 1343–1354. https://doi.org/10.1016/S0022-3697(71)80192-0.

- [225] J.G. Aiken, A.G. Jordan, Electrical transport properties of single crystal nickel oxide, J. Phys. Chem. Solids. 29 (1968) 2153–2167. https://doi.org/10.1016/0022-3697(68)90011-5.
- [226] X. Chen, L. Xu, C. Chen, Y. Wu, W. Bi, Z. Song, X. Zhuang, S. Yang, S. Zhu, H. Song, Rare earth ions doped NiOx hole transport layer for efficient and stable inverted perovskite solar cells, J. Power Sources. 444 (2019). https://doi.org/10.1016/j.jpowsour.2019.227267.
- [227] J.H. Kim, P.W. Liang, S.T. Williams, N. Cho, C.C. Chueh, M.S. Glaz, D.S. Ginger, A.K.Y. Jen, High-performance and environmentally stable planar heterojunction perovskite solar cells based on a solution-processed copperdoped nickel oxide hole-transporting layer, Adv. Mater. 27 (2015) 695–701. https://doi.org/10.1002/adma.201404189.
- [228] M.-H. Liu, Z.-J. Zhou, P.-P. Zhang, Q.-W. Tian, W.-H. Zhou, D.-X. Kou, S.-X. Wu, p-type Li, Cu-codoped NiOx hole-transporting layer for efficient planar perovskite solar cells, Opt. Express. 24 (2016) A1349. https://doi.org/10.1364/oe.24.0a1349.
- [229] W. Chen, F.Z. Liu, X.Y. Feng, A.B. Djurišić, W.K. Chan, Z.B. He, Cesium Doped NiOx as an Efficient Hole Extraction Layer for Inverted Planar Perovskite Solar Cells, Adv. Energy Mater. 7 (2017). https://doi.org/10.1002/aenm.201700722.
- [230] Y. Wei, K. Yao, X. Wang, Y. Jiang, X. Liu, N. Zhou, F. Li, Improving the efficiency and environmental stability of inverted planar perovskite solar cells via silver-doped nickel oxide hole-transporting layer, Appl. Surf. Sci. 427 (2018) 782–790. https://doi.org/10.1016/j.apsusc.2017.08.184.
- [231] Y. Xie, K. Lu, J. Duan, Y. Jiang, L. Hu, T. Liu, Y. Zhou, B. Hu, Enhancing Photovoltaic Performance of Inverted Planar Perovskite Solar Cells by Cobalt-Doped Nickel Oxide Hole Transport Layer, ACS Appl. Mater. Interfaces. 10

- (2018) 14153–14159. https://doi.org/10.1021/acsami.8b01683.
- [232] X. Xia, Y. Jiang, Q. Wan, X. Wang, L. Wang, F. Li, Lithium and Silver Co-Doped Nickel Oxide Hole-Transporting Layer Boosting the Efficiency and Stability of Inverted Planar Perovskite Solar Cells, ACS Appl. Mater. Interfaces. 10 (2018) 44501–44510. https://doi.org/10.1021/acsami.8b16649.
- [233] S. Teo, Z. Guo, Z. Xu, C. Zhang, Y. Kamata, S. Hayase, T. Ma, The Role of Lanthanum in a Nickel Oxide-Based Inverted Perovskite Solar Cell for Efficiency and Stability Improvement, ChemSusChem. 12 (2019) 518–526. https://doi.org/10.1002/cssc.201802231.
- [234] S.A. Fateev, A.A. Petrov, V.N. Khrustalev, P. V. Dorovatovskii, Y. V. Zubavichus, E.A. Goodilin, A.B. Tarasov, Solution Processing of Methylammonium Lead Iodide Perovskite from γ-Butyrolactone: Crystallization Mediated by Solvation Equilibrium, Chem. Mater. 30 (2018) 5237–5244. https://doi.org/10.1021/acs.chemmater.8b01906.
- [235] Y.H. Seo, E.C. Kim, S.P. Cho, S.S. Kim, S.I. Na, High-performance planar perovskite solar cells: Influence of solvent upon performance, Appl. Mater. Today. 9 (2017) 598–604. https://doi.org/10.1016/j.apmt.2017.11.003.
- [236] S. Lin, W. Li, H. Sun, W. Xu, W. Guo, M. Xia, K. Yang, Effects of Different Solvents on the Planar Hetero-junction Perovskite Solar Cells, in: MATEC Web Conf., 2015. https://doi.org/10.1051/matecconf/20152205002.
- [237] H.L. Yue, H.H. Sung, F.C. Chen, Seeded Space-Limited Crystallization of CH3NH3PbI3 Single-Crystal Plates for Perovskite Solar Cells, Adv. Electron. Mater. 4 (2018). https://doi.org/10.1002/aelm.201700655.
- [238] S.H. Huang, K.Y. Tian, H.C. Huang, C.F. Li, W.C. Chu, K.M. Lee, K.M. Lee, Y.C. Huang, W.F. Su, Controlling the Morphology and Interface of the Perovskite Layer for Scalable High-Efficiency Solar Cells Fabricated Using Green Solvents and Blade Coating in an Ambient Environment, ACS Appl. Mater. Interfaces.

- 12 (2020) 26041–26049. https://doi.org/10.1021/acsami.0c06211.
- [239] J. Song, Y. Yang, Y.L. Zhao, M. Che, L. Zhu, X.Q. Gu, Y.H. Qiang, Morphology modification of perovskite film by a simple post-treatment process in perovskite solar cell, Mater. Sci. Eng. B Solid-State Mater. Adv. Technol. 217 (2017) 18–25. https://doi.org/10.1016/j.mseb.2017.01.004.
- [240] F.P. Gokdemir Choi, H. Moeini Alishah, S. Gunes, Cerium and zinc co-doped nickel oxide hole transport layers for gamma-butyrolactone based ambient air fabrication of CH3NH3PbI3 perovskite solar cells, Appl. Surf. Sci. 563 (2021) 150249. https://doi.org/10.1016/j.apsusc.2021.150249.
- [241] J.H. Lee, Y.W. Noh, I.S. Jin, J.W. Jung, Efficient planar heterojunction perovskite solar cells employing a solution-processed Zn-doped NiOX hole transport layer, Electrochim. Acta. 284 (2018) 253–259. https://doi.org/10.1016/j.electacta.2018.07.178.
- [242] Z. Saki, K. Sveinbjörnsson, G. Boschloo, N. Taghavinia, The Effect of Lithium Doping in Solution-Processed Nickel Oxide Films for Perovskite Solar Cells, ChemPhysChem. 20 (2019) 3322–3327. https://doi.org/10.1002/cphc.201900856.
- [243] J.H. Lee, Y.W. Noh, I.S. Jin, S.H. Park, J.W. Jung, A solution-processed cobalt-doped nickel oxide for high efficiency inverted type perovskite solar cells, J. Power Sources. 412 (2019) 425–432. https://doi.org/10.1016/j.jpowsour.2018.11.081.
- [244] J. Zhang, W. Mao, X. Hou, J. Duan, J. Zhou, S. Huang, W. Ou-Yang, X. Zhang, Z. Sun, X. Chen, Solution-processed Sr-doped NiOx as hole transport layer for efficient and stable perovskite solar cells, Sol. Energy. 174 (2018) 1133–1141. https://doi.org/10.1016/j.solener.2018.10.004.
- [245] M. Yousefi, M. Amiri, R. Azimirad, A.Z. Moshfegh, Enhanced photoelectrochemical activity of Ce doped ZnO nanocomposite thin films under

- visible light, J. Electroanal. Chem. 661 (2011) 106–112. https://doi.org/10.1016/j.jelechem.2011.07.022.
- [246] K.H. Kim, C. Takahashi, Y. Abe, M. Kawamura, Effects of Cu doping on nickel oxide thin film prepared by sol-gel solution process, Optik (Stuttg). 125 (2014) 2899–2901. https://doi.org/10.1016/j.ijleo.2013.11.074.
- [247] S. Nag, K. Banerjee, D. Datta, Estimation of the van der Waals radii of the d-block elements using the concept of bond valence, New J. Chem. 31 (2007) 832–834. https://doi.org/10.1039/b701197k.
- [248] M. Rahm, R. Hoffmann, N.W. Ashcroft, Atomic and Ionic Radii of Elements 1–96, Chem. A Eur. J. 22 (2016) 14625–14632. https://doi.org/10.1002/chem.201602949.
- [249] Cu-doped nickel oxide hole-transporting layer via efficient low-temperature spraying combustion method for perovskite solar cells, (n.d.).
- [250] E. Climent-Pascual, B.C. Hames, J.S. Moreno-Ramírez, A.L. Álvarez, E.J. Juarez-Perez, E. Mas-Marza, I. Mora-Seró, A. De Andrés, C. Coya, Influence of the substrate on the bulk properties of hybrid lead halide perovskite films, J. Mater. Chem. A. 4 (2016) 18153–18163. https://doi.org/10.1039/c6ta08695k.
- [251] X. Wan, Y. Jiang, Z. Qiu, H. Zhang, X. Zhu, I. Sikandar, X. Liu, X. Chen, B. Cao, Zinc as a New Dopant for NiOx-Based Planar Perovskite Solar Cells with Stable Efficiency near 20%, ACS Appl. Energy Mater. 1 (2018) 3947–3954. https://doi.org/10.1021/acsaem.8b00671.
- [252] A.A. Dakhel, Effect of cerium doping on the structural and optoelectrical properties of CdO nanocrystallite thin films, Mater. Chem. Phys. 130 (2011) 398–402. https://doi.org/10.1016/j.matchemphys.2011.06.060.
- [253] P.H. Lee, B.T. Li, C.F. Lee, Z.H. Huang, Y.C. Huang, W.F. Su, High-efficiency perovskite solar cell using cobalt doped nickel oxide hole transport layer

- fabricated by NIR process, Sol. Energy Mater. Sol. Cells. 208 (2020). https://doi.org/10.1016/j.solmat.2019.110352.
- [254] C. Kim, B. Lee, H.J. Yang, H.M. Lee, J.G. Lee, H. Shin, Effects of surface treatment on work function of ITO (Indium Tin Oxide) films, in: J. Korean Phys. Soc., 2005.
- [255] S.D. Chavhan, R. Hansson, L.K.E. Ericsson, P. Beyer, A. Hofmann, W. Brütting, A. Opitz, E. Moons, Low temperature processed NiOx hole transport layers for efficient polymer solar cells, Org. Electron. 44 (2017) 59–66. https://doi.org/10.1016/j.orgel.2017.01.040.
- [256] S.R. Gul, M. Khan, Y. Zeng, M. Lin, B. Wu, C.T. Tsai, Electronic band structure variations in the Ceria Doped Zirconia: A first principles study, Materials (Basel). 11 (2018). https://doi.org/10.3390/ma11071238.
- [257] Z. Qiu, H. Gong, G. Zheng, S. Yuan, H. Zhang, X. Zhu, H. Zhou, B. Cao, Enhanced physical properties of pulsed laser deposited NiO films via annealing and lithium doping for improving perovskite solar cell efficiency, J. Mater. Chem. C. 5 (2017) 7084–7094. https://doi.org/10.1039/c7tc01224a.
- [258] Z. Hu, D. Chen, P. Yang, L. Yang, L. Qin, Y. Huang, X. Zhao, Sol-gel-processed yttrium-doped NiO as hole transport layer in inverted perovskite solar cells for enhanced performance, Appl. Surf. Sci. 441 (2018) 258–264. https://doi.org/10.1016/j.apsusc.2018.01.236.
- [259] Y.S. Chen, J.F. Kang, B. Chen, B. Gao, L.F. Liu, X.Y. Liu, Y.Y. Wang, L. Wu, H.Y. Yu, J.Y. Wang, Q. Chen, E.G. Wang, Microscopic mechanism for unipolar resistive switching behaviour of nickel oxides, J. Phys. D. Appl. Phys. 45 (2012). https://doi.org/10.1088/0022-3727/45/6/065303.
- [260] E.L. Ratcliff, J. Meyer, K.X. Steirer, A. Garcia, J.J. Berry, D.S. Ginley, D.C. Olson, A. Kahn, N.R. Armstrong, Evidence for near-surface NiOOH species in solution-processed NiO x selective interlayer materials: Impact on energetics and the

- performance of polymer bulk heterojunction photovoltaics, Chem. Mater. 23 (2011) 4988–5000. https://doi.org/10.1021/cm202296p.
- [261] S. Uhlenbrock, C. Scharfschwerdt, M. Neumann, G. Illing, H.J. Freund, The influence of defects on the Ni 2p and O 1s XPS of NiO, J. Phys. Condens. Matter. 4 (1992) 7973–7978. https://doi.org/10.1088/0953-8984/4/40/009.
- [262] P. Dubey, N. Kaurav, R.S. Devan, G.S. Okram, Y.K. Kuo, The effect of stoichiometry on the structural, thermal and electronic properties of thermally decomposed nickel oxide, RSC Adv. 8 (2018) 5882–5890. https://doi.org/10.1039/c8ra00157j.
- [263] J. Sun, J. Lu, B. Li, L. Jiang, A.S.R. Chesman, A.D. Scully, T.R. Gengenbach, Y.B. Cheng, J.J. Jasieniak, Inverted perovskite solar cells with high fill-factors featuring chemical bath deposited mesoporous NiO hole transporting layers, Nano Energy. 49 (2018) 163–171. https://doi.org/10.1016/j.nanoen.2018.04.026.
- [264] G. Niu, S. Wang, J. Li, W. Li, L. Wang, Oxygen doping in nickel oxide for highly efficient planar perovskite solar cells, J. Mater. Chem. A. 6 (2018) 4721–4728. https://doi.org/10.1039/c8ta00161h.
- [265] L.J. Tang, X. Chen, T.Y. Wen, S. Yang, J.J. Zhao, H.W. Qiao, Y. Hou, H.G. Yang, A Solution-Processed Transparent NiO Hole-Extraction Layer for High-Performance Inverted Perovskite Solar Cells, Chem. A Eur. J. 24 (2018) 2845–2849. https://doi.org/10.1002/chem.201705658.
- [266] Z. Zhu, Y. Bai, T. Zhang, Z. Liu, X. Long, Z. Wei, Z. Wang, L. Zhang, J. Wang, F. Yan, S. Yang, High-performance hole-extraction layer of sol-gel-processed nio nanocrystals for inverted planar perovskite solar cells, Angew. Chemie Int. Ed. 53 (2014) 12571–12575. https://doi.org/10.1002/anie.201405176.
- [267] J. Zheng, L. Hu, J.S. Yun, M. Zhang, C.F.J. Lau, J. Bing, X. Deng, Q. Ma, Y. Cho, W. Fu, C. Chen, M.A. Green, S. Huang, A.W.Y. Ho-Baillie, Solution-Processed,

- Silver-Doped NiOx as Hole Transporting Layer for High-Efficiency Inverted Perovskite Solar Cells, ACS Appl. Energy Mater. 1 (2018) 561–570. https://doi.org/10.1021/acsaem.7b00129.
- [268] A.B. Huang, J.T. Zhu, J.Y. Zheng, Y. Yu, Y. Liu, S.W. Yang, S.H. Bao, L. Lei, P. Jin, Achieving high-performance planar perovskite solar cells with co-sputtered Co-doping NiOx hole transport layers by efficient extraction and enhanced mobility, J. Mater. Chem. C. 4 (2016) 10839–10846. https://doi.org/10.1039/c6tc03624d.
- [269] P. Liao, X. Zhao, G. Li, Y. Shen, M. Wang, A new method for fitting current–voltage curves of planar heterojunction perovskite solar cells, Nano-Micro Lett. 10 (2018) 1–8. https://doi.org/10.1007/s40820-017-0159-z.
- [270] X. Cao, L. Zhi, Y. Li, F. Fang, X. Cui, L. Ci, K. Ding, J. Wei, Fabrication of Perovskite Films with Large Columnar Grains via Solvent-Mediated Ostwald Ripening for Efficient Inverted Perovskite Solar Cells, ACS Appl. Energy Mater. 1 (2018) 868–875. https://doi.org/10.1021/acsaem.7b00300.
- [271] J. an Yang, A. Xiao, L. Xie, K. Liao, X. Deng, C. Li, A. Wang, Y. Xiang, T. Li, F. Hao, Precise control of PbI2 excess into grain boundary for efficacious charge extraction in off-stoichiometric perovskite solar cells, Electrochim. Acta. 338 (2020). https://doi.org/10.1016/j.electacta.2020.135697.
- [272] Z. Xiao, Q. Dong, C. Bi, Y. Shao, Y. Yuan, J. Huang, Solvent Annealing of Perovskite-Induced Crystal Growth for Photovoltaic-Device Efficiency Enhancement, Adv. Mater. 26 (2014) 6503–6509. https://doi.org/10.1002/adma.201401685.
- [273] P. Zhou, B. Li, Z. Fang, W. Zhou, M. Zhang, W. Hu, T. Chen, Z. Xiao, S. Yang, Nitrogen-Doped Nickel Oxide as Hole Transport Layer for High-Efficiency Inverted Planar Perovskite Solar Cells, Sol. RRL. 3 (2019). https://doi.org/10.1002/solr.201900164.

- [274] K. V. Rao, A. Smakula, Dielectric properties of alkaline earth fluoride single crystals, J. Appl. Phys. 37 (1966) 319–323. https://doi.org/10.1063/1.1707834.
- [275] S. Wang, B. Zhang, D. Feng, Z. Lin, J. Zhang, Y. Hao, X. Fan, J. Chang, Achieving high performance and stable inverted planar perovskite solar cells using lithium and cobalt co-doped nickel oxide as hole transport layers, J. Mater. Chem. C. 7 (2019) 9270–9277. https://doi.org/10.1039/c9tc02526j.
- [276] P.C. Chen, S.H. Yang, Potassium-Doped Nickel Oxide as the Hole Transport Layer for Efficient and Stable Inverted Perovskite Solar Cells, ACS Appl. Energy Mater. 2 (2019) 6705–6713. https://doi.org/10.1021/acsaem.9b01200.
- [277] S.S. Mali, J. V. Patil, H. Kim, R. Luque, C.K. Hong, Highly efficient thermally stable perovskite solar cells via Cs:NiOx/CuSCN double-inorganic hole extraction layer interface engineering, Mater. Today. 26 (2019) 8–18. https://doi.org/10.1016/j.mattod.2019.01.017.
- [278] J. Emara, T. Schnier, N. Pourdavoud, T. Riedl, K. Meerholz, S. Olthof, Impact of Film Stoichiometry on the Ionization Energy and Electronic Structure of CH3NH3PbI3 Perovskites, Adv. Mater. 28 (2016) 553–559. https://doi.org/10.1002/adma.201503406.
- [279] C. Ayik, I. Studenyak, M. Kranjec, M. Kurik, Urbach Rule in Solid State Physics, Int. J. Opt. Appl. 4 (2014) 76–83. https://doi.org/10.5923/j.optics.20140403.02.

PUBLICATIONS FROM THE THESIS

Journal Papers:

- **1. Hamed Moeini Alishah**, Fatma Pinar Gokdemir Choi, Furkan Kuruoglu, Ayse Erol, Serap Gunes. "Improvement of fill factor by the utilization of Zn-doped PEDOT:PSS hole-transport layers for p-i-n planar type of perovskite solar cells." Electrochimica Acta (2021):138658.
- **2**. Fatma Pinar Gokdemir Choi, **Hamed Moeini Alishah**, Serap Gunes. "Cerium and zinc co-doped nickel oxide hole transport layers for gamma-butyrolactone based ambient air fabrication of CH3NH3PbI3 perovskite solar cells. "Applied Surface Science (2021): 150249.
- **3. Hamed Moeini Alishah**, Fatma Pinar Gokdemir Choi, Serap Gunes. "Investigation of various commercial PEDOT: PSS (poly(3,4-ethylenedioxythiophene)polystyrene sulfonate) as a hole transport layer in lead iodide based inverted planar perovskite solar cells." Journal of Materials Science: Materials in Electronics (2021).
- **4.** Fatma Pinar Gokdemir choi, **Hamed Moeini Alishah**, Sinem Bozar, Cihangir Kahveci, Macide Canturk Rodop, and Serap Gunes. "First demonstration of lithium, cobalt and magnesium introduced nickel oxide hole transporters for inverted methylammonium lead triiodide-base perovskite solar cells." Solar Energy 215 (2021): 434-442.
- **5. Hamed Moeini Alishah**., Mehmet Kazici., Fatih Ongul., Sinem Bozar., Macide Canturk Rodop., Cihangir Kahveci., Melih Besir Arvas, Sahin Yucel, Metin Gencten, Murat Kaleli, Salih Akyurekli, Huseyin Utku Yilmaz, Ahmet Bugrahan Bayram, Serap Gunes. "Effect of UV exposure of ITO/PEDOT: PSS substrates on the performance of inverted-type perovskite solar cells." Journal of Materials Science: Materials in Electronics (2020): 1-13.
- **6**. Fatma Pinar Gokdemir Choi, **Hamed Moeini Alishah**, Sinem Bozar, Ceylan Doyranli, Sermet Koyuncu, Nevim San, Cihangir Kahveci, Macide Canturk Rodop, Melih Besir Arvas, Metin Gencten, Yucel Sahin, Serap Gunes. "A novel interface layer for inverted perovskite solar cells fabricated in ambient air under high humidity conditions. "Solar Energy (2020). 209,400-407.

- **7**. Kuray Dericiler, **Hamed Moeini Alishah**, Sinem Bozar, Serap Gunes, Figen Kaya. "A novel method for graphene synthesis via electrochemical process and its utilization in organic photovoltaic devices. "Applied Physics A, 126(11), 1-9.
- **8**. **Hamed Moeini Alishah**, Fatma Pinar Gokdemir Choi, Ugur Deneb Mende, Cihangir Kahveci, Macide Canturk Rodop, Manuel J. Mendes, Serap Gunes. " Effect of Bathocuproine concentration on the photovoltaic performance of NiOX -based perovskite solar cells. " Journal of Mexican Chemical society" 65.2 (2021)

Conference Presentation:

Li modified PCBM electron transport layers for CH3NH3PbI3 based inverted solar cells. 4th International Conference on Physical Chemistry & Functional Materials. (PCFM2021, Elazig, Turkey), April 2021 (oral).

Posters presented at national and international assemblies:

- **1**. Menda, U.D., Choi, F.P., Kazici M., **Alishah M. H**., and Gunes, S. "Inverted organic/inorganic halide perovskite solar cells: A precursor concentration study". 14th Nanoscience and Nanotechnology Conference (NANOTR-14). TURKEY, (September 22-25, 2018).
- **2**. Yorur-Goreci Cigdem, Kazici Mehmet, Bozar Sinem, Nilisaz Sinem, **Moeini Alishah Hamed**, Gunes Serap (2019). "Novel Small Molecules for Organic Solar Cell Applications", 8th International Conference on Advanced Technologies (ICAT'19), August 26-30, 2019 Sarajevo/ BOSNIA